Theoretical and Computational Analysis of Airfoils in Steady and Unsteady Flows

by

Mohammed Abdo

Department of Mechanical Engineering
McGill University
Montreal, Quebec, Canada.

June, 2004

A thesis submitted to McGill University in partial fulfillment of the requirements of the degree of Doctor of Philosophy.

Library and
Archives Canada

Published Heritage
Branch

395 Wellington Street
Ottawa ON K1A 0N4
Canada

Bibliothèque et
Archives Canada

Direction du
Patrimoine de l'édition

395, rue Wellington
Ottawa ON K1A 0N4
Canada

Your file Votre référence
ISBN: 0-494-06262-2
Our file Notre référence
ISBN: 0-494-06262-2

NOTICE:
The author has granted a non-exclusive license allowing Library and Archives Canada to reproduce, publish, archive, preserve, conserve, communicate to the public by telecommunication or on the Internet, loan, distribute and sell theses worldwide, for commercial or non-commercial purposes, in microform, paper, electronic and/or any other formats.

The author retains copyright ownership and moral rights in this thesis. Neither the thesis nor substantial extracts from it may be printed or otherwise reproduced without the author's permission.

AVIS:
L'auteur a accordé une licence non exclusive permettant à la Bibliothèque et Archives Canada de reproduire, publier, archiver, sauvegarder, conserver, transmettre au public par télécommunication ou par l'Internet, prêter, distribuer et vendre des thèses partout dans le monde, à des fins commerciales ou autres, sur support microforme, papier, électronique et/ou autres formats.

L'auteur conserve la propriété du droit d'auteur et des droits moraux qui protège cette thèse. Ni la thèse ni des extraits substantiels de celle-ci ne doivent être imprimés ou autrement reproduits sans son autorisation.

In compliance with the Canadian Privacy Act some supporting forms may have been removed from this thesis.

While these forms may be included in the document page count, their removal does not represent any loss of content from the thesis.

Conformément à la loi canadienne sur la protection de la vie privée, quelques formulaires secondaires ont été enlevés de cette thèse.

Bien que ces formulaires aient inclus dans la pagination, il n'y aura aucun contenu manquant.

Canada

Abstract

This dissertation studies three aspects of airfoil flows: (i) second-order theoretical solutions of airfoils in steady flows; (ii) unsteady solutions for oscillating flexible airfoils; and (iii) numerical analysis of airfoil flows at low Reynolds numbers.

The first part presents simple and efficient analytical solutions in closed form for the velocity and pressure distributions on airfoils of arbitrary shapes in steady flows, which are obtained using special singularities in the expression of the fluid velocity. A second-order accurate method is first developed for airfoils in inviscid incompressible flows to simultaneously solve the symmetric and anti-symmetric flow components defined by coupled boundary conditions. Then, the method is extended to take into account the viscous and compressibility effects on the pressure distribution. The resulting solutions were found to be in very good agreement with the available exact solutions (for specific airfoils), and with numerical and experimental results at various Mach and Reynolds numbers and moderate angles of attack.

The second part presents a new method of solution for the analysis of unsteady incompressible flows past oscillating rigid and flexible airfoils. The method has been successfully validated by comparison with the results obtained by Theodorsen and by Postel and Leppert for rigid airfoil and aileron oscillations in translation and rotation. The aerodynamic stiffness, damping and virtual mass contributions are specifically determined, as required in the aeroelastic studies. In all cases studied, this method led to very efficient and simple analytical solutions in closed form.

The third part presents an efficient numerical method for the incompressible flows past airfoils at low Reynolds numbers, which are of interest for micro-aircraft applications. The present analysis is based on a pseudo-time integration method using artificial compressibility to accurately solve the Navier-Stokes equations. Solutions are obtained with this method for airfoils at various incidences and very low Reynolds numbers between 400 and 6000. A detailed analysis is presented for the influence of the Reynolds number, incidence and airfoil shape on the pressure distribution, lift and drag coefficients. The flow separation is especially studied; the separation and reattachment positions are compared for various airfoil shapes, incidences and Reynolds numbers.

Résumé

Cette thèse étudie trois aspects des écoulements autour des profils aérodynamiques: (i) solutions analytiques pour profils en écoulements stationnaires; (ii) solutions instationnaires pour profils flexibles en mouvement oscillatoire; et (iii) analyse numérique d'écoulements autour des profils à faible nombre de Reynolds.

La première partie présente des solutions analytiques pour les distributions de vitesse et de pression sur des profils de forme arbitraire en écoulement stationnaire. Ces solutions sont obtenues à l'aide de singularités spéciales dans l'expression de la vitesse. Une méthode précise au second ordre permettant de résoudre simultanément les composantes symétriques et anti-symétriques, telles que définies par les conditions aux frontières couplées, est d'abord développée pour des écoulements incompressibles et non-visqueux. Un développement de la méthode permet ensuite de tenir compte des effets de la viscosité et de la compressibilité sur la distribution de pression. Les solutions obtenues pour des profils spécifiques sont en très bon accord avec les résultats théoriques, numériques et expérimentaux disponibles pour plusieurs nombres de Mach, de Reynolds et angles d'incidence modérés.

Le deuxième partie présente une nouvelle méthode pour l'analyse des écoulements instationnaires autour de profils rigides et flexibles en oscillation. Cette méthode a été validée avec succès en comparaison avec les résultats obtenus par Theodorsen et par Postel et Leppert pour un profil rigide en rotation et translation muni ou non d'un aileron oscillant. Les contributions dues à la rigidité et l'amortissement aérodynamiques, et à la masse virtuelle sont déterminées de façon spécifique, tel que requis pour les études d'aéroélasticité. Pour tous les cas considérés, cette méthode a permis d'obtenir des solutions très simples et pratiques.

La troisième partie de la thèse décrit une méthode numérique efficace pour la résolution d'écoulements incompressibles à bas nombre de Reynolds autour de profils. Ces écoulements sont d'intérêt dans la conception de micro-avions. L'analyse présentée est basée sur une méthode d'intégration pseudo-temporelle utilisant la compressibilité artificielle pour résoudre avec précision les équations de Navier-Stokes. Des solutions ont été obtenues pour des profils à plusieurs incidences et à de très bas nombres de Reynolds variant entre 400 et 6000. Une analyse détaillée de l'influence du nombre de Reynolds, de l'incidence et de la forme du profil sur la distribution de pression ainsi que sur la portance et la traînée est présentée. La séparation de l'écoulement est spécialement étudiée et les positions de séparation et de réattachement de l'écoulement sont comparées pour divers incidences, nombres de Reynolds et types de profils.

Acknowledgements

I would like to thank my thesis supervisor, Professor Dan Mateescu, for his guidance, knowledge, dedication, encouragement and support throughout this research.

The support of the Natural Sciences and Engineering Research Council of Canada and the Fonds pour la Formation de Chercheurs et l'Aide à la Recherche is gratefully acknowledged.

I would also like to thank all my supervisors and friends at Bombardier Aerospace for their continuous encouragement, especially my colleagues in the Advanced Aerodynamics, Advanced Design, Stress, Loads and Dynamics, Structures and Weights departments.

I owe special thanks for my best friends and their wives for their confidence in me.

Finally, I would like to dedicate this work to my parents, Iftikhar Abdo and Afaf Abdo, my brother and three sisters, Rami, Rawya, Diana and Hadeel for all their love and support over the years. I would like also to express my appreciation to my uncle and aunt, Akram and Kawthar, for their unconditional support.

Contents

List of figures

List of tables

Chapter 1

Introduction

1.1 Analysis of steady flows past airfoils

The steady flows around airfoils (or *wing sections*) have been extensively studied during the last seven decades for their aeronautical applications in the aerodynamic design. Initially, the method of conformal transformations has been used to obtain exact steady flow solutions for particular airfoil shapes, such as Joukowski, Karman-Trefftz, Betz-Keune, Müller, Von Mises and Carafoli airfoils [7, 21, 22, 98, 142, 188]. Since it is in general difficult to develop an exact solution for the ideal flow past an airfoil of arbitrary shape, approximate methods have been developed to solve this problem. The classical thin airfoil theory developed by Glauert and Birnbaum [7, 21, 65, 98, 142, 188] established the foundation of aerodynamics of thin airfoils of arbitrary shapes in incompressible steady flows, by using a modified Fourier series for the distributed vortex intensity on the chord. Based on a truncated Fourier series representation of the camberline shape (sometimes requiring a large number of terms), this linear method permitted the calculation of the steady aerodynamic forces and pressure distribution on the airfoil. Willcox and Megretski [205] used Fourier series for reduced-order linear computational applications. However, the Fourier series are not convenient to aerodynamically model the airfoils with discontinuities in the boundary conditions, such as the flapped airfoils [124].

In order to overcome some of the deficiencies of the methods based on Fourier series expansions, several authors, such as Weber [201, 202], have developed linear methods using velocity singularities, and others, such as Munk [147] and Cheng and Rott [28] mathematically derived inversion formulae for the analysis of thin airfoils in steady flows. The generalized inversion formula of thin airfoil theory, developed by Cheng and Rott [28], permits to obtain linear analytical solutions for the camberline problems of thin airfoils in the small perturbation assumption. When the inversion formulae are applied to symmetrical airfoils at zero angle of attack, the steady solution obtained gives infinite velocity at the leading and trailing edges, in contrast to the actual velocity behavior characterized by the fact that the leading and trailing edges are stagnation points in inviscid flows. The unphysical behavior of these linear solutions has to be corrected by discarding the small perturbation assumption (on which the linear theories are based) and considering rigorously the correct boundary conditions.

An efficient method using velocity singularities leading to simple analytical solution in closed form has been developed by Mateescu [115], Mateescu and Newman [124] and Mateescu and Nadeau [123] for thin airfoils in steady incompressible flow. The method based on velocity singularities (name used in Ref. [116] for the study of wings in supersonic flows) consists in the determination of the specific contributions in the expression of the fluid velocity (instead of the velocity potential) related to the singular points on the airfoil or wing, such as the leading edge and ridges, where the boundary conditions display sudden changes. These contributions are determined by taking into account the singular behavior of the fluid velocity at these points and satisfy all other boundary conditions, including Kutta condition at the trailing edge. These methods were proven to be also suitable to solve problems of unspecified geometry, such as flexible-membrane and jet-flapped airfoils [124]. More recently, methods using velocity singularities in subsonic flow have been developed for the nonlinear analysis of airfoils of arbitrary shapes [119] and for the finite-span wings of arbitrary shapes [127].

Other solutions for steady flows past airfoils involving intensive numerical calculations have been obtained using conformal mappings (Sells [171], Halsey [73], Ives [81] and Bauer *et al.* [14]), or using boundary element methods based on source, doublet and vortex panels (see Kuethe and Chow [98], Hess and Smith [78], Hunt [80], Katz and Plotkin [91], Mavriplis [131] and Mateescu [114]). These panel methods are based on distributed singularities in the expression of the potential (in contrast to the present method which uses different type of singularities in the expression of the velocity) and use geometrical discretization of the airfoil contour into numerous small panels (not needed in the present method).

More recently, computational solutions have been obtained using various numerical methods for solving the Euler or Navier-Stokes equations, such as those based on finite-difference or finite-volume formulations (for examples see Anderson [6], Drela and Giles

[43, 44], Jameson *et al.* [85], Jameson and Yoon [86], Elrefaee *et al.* [53], Nelson *et al.* [149] and Mateescu and Stanescu [128]). A finite element approach to solve several subsonic aerodynamics problems has been developed by Habashi [68]. Various aspects of airfoil design and analysis have been obtained by several authors such as Jiang *et al.* [88], Walsh and Zingg [197], and Liebeck [107, 108]. Deiwert and Bailey [37] solved numerically the compressible Navier-Stokes equations for a variety of airfoil configurations using McCormack [5, 112] predictor-corrector explicit/implicit method and Beam and Warming [5, 15] implicit method. Freuler and Gregorek [59] compared the solutions of four different airfoil analysis methods while Dvorak and Kind [49] developed a method for the viscous flow over circulation-controlled airfoils. More recently, Harris [77] compared and analyzed the aerodynamic characteristics of various NASA supercritical airfoils in steady flows.

A great effort has been made to come up with computational methods that can accurately predict the aerodynamic characteristics of airfoils. Unfortunately, in most of the cases these methods require a great amount of set-up and computer time which limit their practical use as shown by Pueyo [159]. Many challenges in computational aerodynamics were demonstrated by Jameson [82-84] and McMullen [138]. Habashi *et al.* [69, 70] addressed several aspects of solver-independent numerical solutions including developing efficient flow solvers. Dutto and Habashi [46] and Dutto *et al.* [47, 48] developed a multilevel parallel method for the compressible Navier-Stokes equations in order to reduce the time required to perform the numerical analysis. Multigrid techniques with preconditioners dramatically accelerated the numerical solution of the flow past airfoils. Ni [151], Jameson [82], and Martinelli *et al.* [113] have developed similar methods based on the multigrid approach. Unfortunately, multigrid acceleration is cell dependent and can slow down if high aspect ratio cells are present. More recently, several authors have considered using Newton's method as a possible alternative for steady flows due to its robustness and speed. Zingg [209], Pueyo and Zingg [160] and Nemec [150] developed an efficient solver based on Newton's method for aerodynamic applications and addressed many of the issues related to convergence acceleration. In order to overcome some of the difficulties involved with solving numerically the Navier-Stokes equations, several authors solved numerically the steady viscous flows past airfoils (or wings) by combining the inviscid Euler solvers or the panel method with the analysis of the boundary layer developed along the airfoil contour (see Cebeci [23-25] and Drela and Giles [43, 44]). Hafez *et al.* [71] used a finite element method for analyzing the viscous-inviscid interaction.

The solution of the Euler or Navier-Stokes equations requires the availability of a structured or unstructured grid generation method which also in many cases renders the numerical methods into a time consuming analysis tool, which is user dependent, for examples see Kinsey and Barth [97], Merriam [141], Sorenson [177], Vinokur [193] and Thompson *et al.* [187]. However, advances in technology have reduced the significance of these issues, but the scarcity of efficient theoretical closed form methods of solution for airfoils of arbitrary shapes remains to be addressed.

In the past, the development of airfoil aerodynamics had to rely heavily on experimental work. Testing and modifying airfoils of various shapes in the wind-tunnel was the primary design tool before building flying prototypes [159, 160]. However, experimental design and analysis is extremely expensive. Several airfoils in steady subsonic flows have been tested in the low speed wind-tunnel by Abbott and Doenhoff [2] and Selig and Guglielmo [169]. Experimental studies of the boundary layer development on airfoils have been conducted by Kerho [95] and Kerho and Bragg [96]. The aerodynamic characteristics of a high-lift airfoil have been tested in the NASA low-turbulence pressure tunnel by Lin and Dominic [109]. An experimental database of high-lift airfoils is given by Fidders *et al.* [56] and Valarezo *et al.* [190]. More recently, experimental pressure distribution on various airfoils for analytical and numerical methods validation has been reported by Vidal *et al.* [192] and Thibert *et al.* [186]. An extensive experimental database for low-speed airfoils has been developed by Lyon *et al.* [111] and Selig *et al.* [170].

The theoretical solutions based on linear analyses are very efficient, but their accuracy is not very good, especially in considering the effect of the airfoil thickness near the leading and trailing edges. For example, in the linear solutions for the symmetric airfoils at zero angle of attack, the fluid velocity tends to infinity at the leading and trailing edges, although physically the airfoil edges are stagnation points in the inviscid flow. This unphysical behavior of the linear solution in the vicinity of the airfoil edges has to be corrected by considering the nonlinear effects in the flow past airfoils.

The first objective of this study is to present accurate and efficient analytical solutions for the velocity and pressure distributions on airfoils of arbitrary shapes in steady flows, which are based on the correct formulation of the boundary conditions (without resorting to the small perturbation assumption). These solutions are obtained by a method based on specific singular contributions in the expression of the fluid velocity which are associated to special points on the airfoil: the leading edge and ridges (where the boundary conditions, expressed using Heaviside functions, are changing). These singular contributions satisfy all boundary conditions on the airfoil and outside it, including Kutta condition at the trailing edge. This second-order accurate method (as opposed to the linear methods based on the small perturbation assumption), simultaneously solve the symmetric (with respect to the airfoil chord) and anti-symmetric flow components which are defined by *coupled boundary conditions* (i.e. the boundary condition for the anti-symmetric flow component contains also the unknown velocity of the symmetric flow component, and vice-versa). The solution of each of these flow components (anti-symmetric or symmetric) is derived using velocity singularities, by considering formal expressions (with *a priori* unknown coefficients) for the other flow component solution (symmetric or anti-symmetric, respectively) in the coupling terms of the boundary conditions. These formal expressions used for the two flow components are derived to satisfy the corresponding singularities and the form of the boundary conditions. The *a priori* unknown coefficients in these formal solutions are then determined by collocation, by imposing that the actual solution derived in this process for each flow component is equal to the formal solution considered for the corresponding flow component at a convenient number (usually between 6 to 10) of collocation points along the chord.

Accurate analytical solutions are first derived for inviscid incompressible steady flows. These solutions are successfully validated by comparison with exact solutions for special airfoils obtained by conformal transformation (such as Joukowski and Karman-Trefftz airfoils), and with numerical results obtained by panel methods [98] and by inviscid Euler solvers [43, 44].

The second-order accurate method developed for inviscid incompressible flows is then modified to take into account the viscous effects on the pressure distribution on airfoils without flow separation regions. The viscous effects are taken into account in this modified method in two ways: (i) by considering the real physical behavior of the velocity at the trailing edge (which is different than that in the inviscid flows where the trailing edge is a stagnation point), and (ii) indirectly, by including the displacement thickness of the boundary layer developed on the airfoil contour and the wake. An equivalent modified expression has been used in (ii) instead of the known theoretical solution for the displacement thickness of the turbulent boundary layer on a flat plate (see Schlichting [166], Schlichting and Gersten [167] and White [204]), in order to permit the derivation of closed form analytical solutions. These new analytical solutions including viscous effects for the pressure distribution are then successfully validated by comparison with experimental results and with numerical viscous results at moderate angles of attack.

Finally, these viscous and inviscid nonlinear solutions derived for incompressible flows are extended for compressible subsonic flows past airfoils, by using the Karman-Tsien compressibility correction [7, 8]. The resulting inviscid and viscous solutions are validated in comparison with numerical [43, 44] and experimental [186] results for various Mach and Reynolds numbers.

1.2 Unsteady aerodynamics of oscillating flexible airfoils

The analysis of the unsteady flows past oscillating airfoils has been mostly motivated by the efforts made to avoid or reduce undesirable unsteady effects in aeronautics, such as flutter, buffeting and dynamic stall. Potentially beneficial effects of these unsteady flows have been also studied, such as propulsive efficiency of flapping motion, controlled periodic vortex generation, stall delay, and optimal control of unsteady forces to improve the performance of turbomachinery, helicopter rotors and wind turbines. Studies of unsteady airfoil flows require predicting the unsteady aerodynamic loads acting on thin lifting surfaces such as those inspired by biological systems (insects, birds, bats, etc.). Most of these studies concern either periodic motion of a rigid airfoil in a uniform stream or periodic fluctuations in the approaching flow.

In the last few years, interest in small, unmanned air vehicles (UAV) and micro aerial vehicles (MAV) has stimulated research in biologically inspired flight and flapping-wing propulsion. The ability of micro flight vehicles to fly inside buildings, tunnels and confined spaces has significant military and civilian applications. These vehicles can be used in various environments without human involvement. Micro flight vehicles can include communication micro-devices, video cameras and chemical sensors which have many industrial applications. The biologically inspired flight is extremely challenging and pushes the limits of our understanding of flapping flexible-airfoil aerodynamics. The flexible nature of airfoils can provide several non-obvious advantages over classical rigid ones. For a rigid airfoil, the aerodynamic characteristics are determined by the airfoil shape and flow properties. For a flexible or membrane airfoil, its shape changes under unsteady loads and consequently the angle of attack and pressure distribution will change along with the flow behavior. This problem involves complex unsteady flow with the oscillating flexible airfoil generating vortices and interacting with them.

The foundations of the unsteady aerodynamics of oscillating rigid airfoils have been established by Theodorsen [184], Theodorsen and Garrick [185], Wagner [196], Karman and Sears [195] and Küssner [100, 101], who considered the unsteady flow past a thin flat plate and a trailing flat wake of vorticity in incompressible flows. Further studies involving detailed unsteady flow solutions of oscillating airfoils have been performed by Postel and Leppert [158], Fung [62], McCroskey [134, 135], Kemp and Homicz [94], Basu and Hancock [12], Dowell *et al.* [40, 41], Katz and Weihs [92, 93] and others [9, 21]. A method to analyze an airfoil undergoing high-frequency unsteady motion has been developed by Landahl [104] and extended by Amiet [4]. Mehta [139, 140] studied the dynamic stall of an oscillating rigid airfoil. Studies of the methods in frequent use to solve unsteady subsonic problems have been performed by Hancock and Doe [75] and Geissler [63].

Some of the recent studies used computational methods and panel methods for these unsteady aerodynamic problems; Katz and Plotkin [91] have done an interesting analysis of unsteady flows past airfoils using panel methods. A discrete vortex method has been recently used by Han *et al.* [74] to analyze the fluid propulsion mechanism of two pitching rigid flat plates. The small-disturbance aerodynamic theory was used by Guruswamy and Goorjian [67] to investigate the aeroelastic characteristics of oscillating airfoils. Other authors such as Kandil and Chuang [90] solved the unsteady Euler equations for an oscillating rigid airfoil using an implicit finite-volume scheme. However, this scheme requires adding implicit and explicit dissipation terms which dramatically reduces the efficiency of the method. For predicting unsteady flows, Edwards and Thomas [50] have reviewed the significant advances of computational methods. Batina [13] developed two numerical finite-volume algorithms for the solution of the time-dependent Euler equations for the analysis of oscillating airfoils using unstructured grids. A similar method has been developed by Azevedo and Oliveira [10] by using a cell-centered unstructured grid made up of triangles. These methods require moving-meshes to conform to the new position of the oscillating airfoil which makes the solution process very lengthy. Acharya and Metwally [3] studied and quantified the sources of vorticity of a pitching rigid airfoil. Chandrashekhara and Carr [26] studied the effects of Mach number on the dynamic stall of an oscillating airfoil. Also, Visbal [194] described the dynamic stall process of a pitching NACA 0015 airfoil and employed the implicit Beam and Warming [15] method to solve the unsteady Navier-Stokes equations on an O-grid topology. The two-dimensional unsteady leading-edge separation on a pitching NACA 0012 airfoil has been studied numerically by Choudhuri *et al.* [33] using structured and unstructured grids. An implicit finite-difference solver with an automatic grid generation procedure was used by Chyu *et al.* [34] to calculate the transonic flow over a NACA 64A010 pitching airfoil. Two finite-volume schemes were developed by Venkatakrishnan and Jameson [191] to solve the unsteady Euler equations for a pitching and plunging airfoil.

Despite the advances in algorithms and computer hardware, time-accurate solutions of the Euler or Navier-Stokes equations remain a computationally intensive problem. Several authors used the viscous-inviscid interaction methods to improve the computational efficiency in computing unsteady flows past oscillating airfoils. Among the pioneering works are those by Cebeci *et al.* [25] and Summa *et al.* [179]. A viscous-inviscid interaction procedure to calculate the unsteady airloads for oscillating rigid airfoils using the full potential and integral boundary layer equations has been developed by Coiro and Pagano [35]. However, the conventional approach has the well-known limitations of the boundary layer equations and needs an unsteady wake model. A simplified zonal approach has been developed by Singh and Wu [174] for the unsteady aerodynamics of bodies undergoing large amplitude time-dependent motions. Tuncer *et al.* [189] ingeniously employed a Navier-Stokes/potential flow interactive method to solve the unsteady flow past a pitching NACA 0012 airfoil. However, the application of the mixed boundary conditions is one of the limitations of this approach.

Several investigators have developed various techniques to reduce the complexity of the unsteady aerodynamic models. Hall *et al.* [72], Florea and Hall [58], Romanowski and Dowell [165], Dowell *et al.* [41, 42], Nadarajah *et al.* [148] and McMullen [138] have developed reduced-order unsteady aerodynamic models of flows past airfoils. These methods depend on splitting the solution variable into steady and unsteady components with the assumption that the magnitude of the unsteady component is much smaller than that of the steady one.

More recently, a method that uses the added mass of vortex sheets was developed by Sunada and Ellington [181] to estimate the induced power in flapping flight for birds and insects. Several studies have investigated the unsteady aerodynamics of animals such as birds, dragonflies and insects in flight. Different biologically inspired unsteady lift generation mechanisms such as the 'clap and fling' and 'hovering' have been the subject of considerable experimental and theoretical investigations (for examples see Weis-Fogh [203], Ellington [51, 52], Maxworthy [132], Ennos [54], Zanker [206], Zanker and Götz [207], Dickinson and Götz [39], and Dickinson [38]).

Various aspects of the unsteady flows past oscillating rigid airfoils such as the dynamic stall have been investigated in the wind-tunnel. An experimental study of an oscillating NACA 0012 airfoil was presented by McAlister *et al.* [133]. Experimental results by Ericsson and Reding [55] revealed how the mode of oscillation for the airfoil determines which unsteady flow effect will dominate. A detailed flow field visualization of an airfoil pitched sinusoidally over a wide range of reduced frequencies was carried out by Panda and Zaman [153], who also measured the evolution of vorticity and airfoil wake structure. Similar flow field measurements at low-frequency oscillations have been obtained by Bragg *et al.* [18] and Broeren and Bragg [20]. Other researchers such as

Oshima and Ramaprian [152] presented the results obtained in an open-surface water tunnel for a pitching NACA 0015 airfoil. The unsteady boundary layer developed on an oscillating airfoil was experimentally investigated in a low-speed wind tunnel by Lee and Basu [105] and Du and Lee [45].

In the aeroelastic studies, the unsteady aerodynamic analysis has to be performed, in conjunction with the analysis of the related structural motion, involving flexural and torsional deformations. A complete numerical approach to simultaneously solve the unsteady Euler and Navier-Stokes equations governing the unsteady flows (which involves numerous iterations for each time step) and the structural equations of motion requires a large computational effort in terms of computing time and memory, even with the present computing capabilities. For this reason, there is still a need for efficient unsteady aerodynamic solutions to be used in the aeroelastic studies.

The second objective of the present thesis is to present a new method of solution in closed form for the analysis of unsteady flows past oscillating flexible and rigid airfoils, which are obtained by a method using velocity singularities (previous results where mainly obtained for the case of rigid airfoil oscillations in translation and rotation). This method is based on the derivation of specific contributions associated to the singular points on the oscillating airfoil, the leading edge and ridges (where the unsteady boundary conditions are changing) as well as the unsteady shedding free vortices in the wake, in the expression of the fluid velocity and unsteady pressure coefficient. These singular contributions satisfy all boundary conditions on the airfoil and outside it, including the Kutta condition at the trailing edge (Mateescu and Abdo [117, 118]).

The method has been successfully validated by comparison with the results obtained by Theodorsen [184] and by Postel and Leppert [158] for rigid airfoil and aileron oscillations in translation and rotation. This method has then been used to obtain solutions for the flexural oscillations of the flexible airfoils, fitted or not with oscillating flexible ailerons, which is of interest for the aeroelastic studies. The aerodynamic stiffness, damping and virtual (or added) mass contributions in the solutions of the unsteady pressure distribution, lift coefficient, and moment coefficient are specifically determined. An analysis of the relative magnitude of the quasi-steady and vortex shedding contributions in the aerodynamic coefficients is also presented. In all cases studied, this method led to very efficient and simple analytical solutions in closed form.

1.3 Airfoil aerodynamics at very low Reynolds numbers

A special interest has been recently devoted to the aerodynamics of airfoils at low and very low Reynolds numbers. This interest is driven by a variety of applications ranging from domestic windmills to special military aircraft and unmanned air vehicles (UAV). Very small aircrafts called micro aerial vehicles (MAV) can operate in various environments including tunnels, desert and jungle (for examples see Davis *et al.* [36] and Mueller [144, 145]). These applications have shown that many questions are unanswered regarding the airfoil aerodynamics at low and very low Reynolds numbers. The flows past airfoils at low Reynolds numbers are dominated by viscous effects, transitional and flow separation phenomena and increased boundary layer thickness, which complicate the understanding of airfoil aerodynamics.

Recently, research on micro-rotorcraft or Meso-Scale Flight Vehicles (a device that is much smaller than a conventional aircraft) has been initiated at Stanford University by Kunz and Kroo [99] (funded by the NASA Institute for Advanced Concepts). A comprehensive presentation of the NASA Morphing research project to explore the flight technologies inspired by natural fliers such as insects and hummingbirds was prepared by McGowan [136] and Raney and Waszak [162]. A detailed review of MAV concept and Reynolds number range for biological and mechanical flight vehicles ranging from Butterfly to Boeing-747 was performed by Mueller [144, 145]. The study of the flight of MAV is very challenging and is motivated by the revolution in microelectronics and MEMS, which made the micro flight vehicles feasible. Besides, vehicles at this scale would be capable to fly indoors or outdoors in groups to provide sensor information over a wide area at a specific time, as indicated by Kunz and Kroo [99]. Various successful designs and aerodynamic studies of Micro Aerial Vehicles at low Reynolds numbers are presented by Grasmeyer and Keennon [66], Morris and Holden [143], Shyy *et al.* [172] and Jenkins *et al.* [87]. Many researchers tended to use conventional thick airfoils (10%-12%) in their studies of flows at low Reynolds numbers (for examples see Sun and Tang [180], Wang [199], Freymuth *et al.* [60], Freymuth [61], Anderson [9] and Jones and

Platzer [89]). Others used more realistic thin plates (for examples see Liu *et al.* [110] and Ramamurti and Sandberg [161]). Several researchers proved that the thick airfoils will be outperformed by thin cambered airfoils (which are more representative of biological wing sections). Among the recent works are those by Laitone [103], Kunz and Kroo [99], Simons [173], Mueller and Balill [146] and Lentink and Gerritsma [106]. In addition, most of the biological systems (such as small insects) have thin cambered membrane-like wing sections (for various examples see Brackenbury [17] and Brodsky [19]).

For micro flight vehicles of very small size (ranging in mass from 10 to 20 g) flying at very low speeds, the Reynolds numbers are as low as 1000. There is very little aerodynamic research available on very small mechanical flying vehicles or biological ones (such as insects which fly at very low Reynolds numbers). Aerodynamics at very low Reynolds numbers in the range of 400 to 6000 is very challenging and different from those of conventional aircraft. Some of the aerodynamic characteristics at this flow regime are poorly understood, and few methods of analysis and design tools are available for the low and very low Reynolds number flows. An important issue to be addressed is the lack of computational or experimental results, which could provide a reasonable basis for comparison and validation (for details see Mueller [144] and Kunz and Kroo [99]). Experimental measurements of aerodynamic pressures are further complicated by the low magnitude of these pressures at low Reynolds numbers, hence creating the potential for large experimental error.

The airfoil aerodynamics at very low Reynolds numbers, which is dominated by viscous effects, flow separation and increased boundary layer thickness, requires careful investigation. It is misleading to analyze these flows based on the research results and experiments obtained for higher Reynolds numbers. The flow analysis at very low Reynolds numbers has to be done considering that the flow is incompressible (which is computationally more challenging than the compressible flows), since the Mach numbers are in this case considerably below 0.3 (the Mach number is extremely low in small insect flight as shown by Azuma [11] and Wang [198, 199]).

Kunz and Kroo [99] based their computational work on the INS2D code from NASA Ames (developed by Rogers and Kwak [164]), after experimenting with FLO103 developed by Jameson [85] and MSES by Drela and Giles [43, 44] with limited success.

More recently, Lentink and Gerritsma [106] found out that the incompressible code ISNAS developed by Segal *et al.* [168] did not converge well for this challenging flow regime.

For the study of incompressible flows, several researchers such as Patankar and Spalding [154] and Patankar [155] developed solvers based on the pressure correction methods using the Poisson equation. However, some of these methods require the addition of artificial dissipation terms to avoid the odd-and-even points decoupling problem. Other methods are characterized by large numerical dissipation being based on upwind discretization procedures (for examples see Fletcher [57] and Hirsch [79]). Harlow and Welch [76] used a set of marker particles which move with the fluid and upwind finite-differencing to solve the Navier-Stokes equations, this technique is called the marker and cell method. A finite-difference scheme for incompressible flows using primitive variables has been proposed by Ghia *et al.* [64]. In this method, central second-order formulas are used for discretization. However, the odd-and-even points decoupling problem still remains. Perić *et al.* [156] used the colocated methods, but it is not clear how these methods avoid the odd-and-even points decoupling problem. More recently, Zdanski *et al.* [208] developed a second-order accurate method based on colocated central differencing with the aid of the Poisson pressure equation. This method requires artificial dissipation terms added explicitly by the user. However, the solution of an extra equation for the pressure (the Poisson equation) reduces the computational efficiency of the method.

Several authors applied the pseudo-compressibility method (which was initially introduced by Chorin [30-32]) to the computation of incompressible flows, which avoids most of the difficulties of the previous methods; among them are Temam [182], Steger and Kutler [178], Peyret and Taylor [157], Chang and Kwak [27], Choi and Merkle [29], Rizzi and Eriksson [163], Kwak *et al.* [102], Soh [175] and Fletcher [57].

The third objective of this work is to present a numerical method that is able to adequately analyze the flows past airfoils at low and very low Reynolds numbers in the incompressible regime. A similar method has been developed by Mateescu and Venditti [129] for the analysis of the unsteady confined flows with oscillating boundaries and with multiple separation regions.

The present analysis of airfoils in incompressible laminar flows at very low Reynolds numbers is based on a pseudo-time integration method using artificial compressibility to accurately solve the Navier-Stokes equations. This is done in a rectangular computational domain obtained by a coordinate transformation from the physical flow domain around the airfoil. The method uses a central differencing approach on a stretched staggered grid in the computational domain (for examples see Chorin [30-32], Soh and Goodrich [176], Mateescu *et al.* [125, 126], Mateescu and Abdo [120, 121] and Abdo and Mateescu [1]). In the present method, the governing equations are recast in delta form after the introduction of the pseudo-time relaxation procedure (not before, as done by Soh and Goodrich [176]), which simplifies the approach considerably and increase the implicit coupling in the solution. A factored alternating direction implicit (ADI) scheme and a special decoupling procedure in each sweep using the continuity equation is used finally to reduce the problem to the computationally efficient solution of scalar tridiagonal systems of equations (algorithms for the solution of cyclic tridiagonal systems were developed by Temperton [183]).

The method is first used to obtain the pressure distributions, lift and drag coefficients for several NACA airfoils at very low Reynolds numbers between 400 and 6000. The present airfoil solutions are validated by comparison with the numerical results obtained by Kunz and Kroo [99] for Reynolds numbers between 1000 and 6000 (no results were available for Reynolds numbers smaller than 1000).

The present method has then been used to study the effects of varying the Reynolds number, angle of attack and airfoil maximum thickness and camber (along with the maximum camber position along the chord) on the pressure distribution, lift and drag coefficients and the onset of the flow separation. The variation of the lift and drag coefficients with angle of attack as well as the drag polars has been determined for several flow conditions and airfoils.

In order to better understand the complex flow separation phenomena in viscous laminar flows past airfoils at very low Reynolds numbers, the onset of separation and reattachment positions as well as the separation length have been calculated, analyzing the effect of various parameters (such as the Reynolds number, incidence, relative maximum thickness and camber, and the relative position along the chord) affecting the flow separation. The streamline contours for several airfoils at various Reynolds numbers and angles of attack have been generated and compared.

1.4 Thesis organization

After the introduction, in Chapter 2, nonlinear analytical solutions are first derived for inviscid incompressible steady flows and then modified to take into account the viscous and compressibility effects on the pressure distribution on airfoils without flow separation regions. This chapter outlines the validation of the method by comparison with previously obtained exact, numerical and experimental results.

Chapter 3 is devoted to the development and validation of a new method for the analysis of unsteady incompressible flows past oscillating rigid and flexible airfoils. This chapter compares the present solutions with previous results obtained by classical theories for rigid airfoil and aileron oscillations in translation and rotation. The goal is to verify the accuracy of the present solutions. This method has then been used to obtain solutions for the flexural oscillations of the flexible airfoils, fitted or not with oscillating flexible ailerons. In this chapter, an analysis of the relative magnitude of the quasi-steady and vortex shedding contributions in the aerodynamic coefficients is also presented.

Chapter 4 is devoted to the development of a pseudo-time integration method using artificial compressibility to accurately solve the Navier-Stokes equations. The coordinate transformation, the stretched staggered grid generation process, the spatial discretization and a special alternating direction implicit procedure are presented in this chapter. This is followed by a presentation of the solutions obtained for several airfoils at incidences and very low Reynolds numbers between 400 and 6000. The pressure coefficient distribution, lift and drag coefficients as well as the streamline contours around these airfoils are calculated and presented. Then a detailed analysis for the influence of the Reynolds number, incidence and airfoil shape on the pressure distribution, lift and drag coefficients is presented. The flow separation phenomena is especially studied and compared for various airfoil shapes, incidences and Reynolds numbers. In certain cases, when previous numerical results were available, the present solutions were compared with these previous results. The goal is to validate the present method.

Chapter 5 is devoted to the conclusions, followed by research contributions.

Chapter 2

Nonlinear Analytical Solutions for Steady Airfoil Aerodynamics

2.1 Problem formulation

Consider an airfoil of chord c placed at an incidence α in a uniform inviscid and incompressible flow of velocity U_∞ as shown in Figure 2.1. The fluid flow past this airfoil is referred to a Cartesian reference system cx, cy, where x and y are nondimensional coordinates, with the x-axis along the airfoil chord and its origin at the airfoil leading edge.

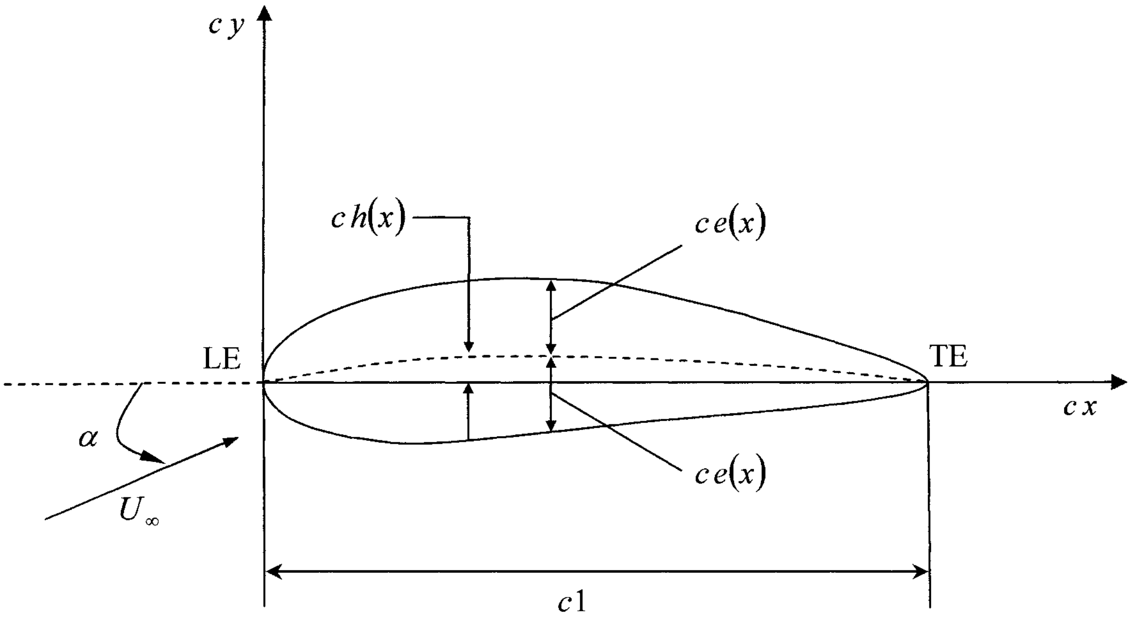

Figure 2.1 Geometry of a general airfoil placed in a uniform flow at incidence.

Let $\mathbf{V} = U_\infty\left[(\cos\alpha + u)\mathbf{i} + (\sin\alpha + v)\mathbf{j}\right]$ denote the fluid velocity around the airfoil, where $u(x,y)$ and $v(x,y)$ are the nondimensional perturbation velocity components (nondimensionalized with respect to U_∞), which in incompressible irrotational flows are harmonic functions, satisfying the Laplace equation. Thus, a complex conjugate velocity $w(z)=u(x,y)-i\,v(x,y)$ can be defined in function of the complex variable $z=x+i\,y$. The upper and lower surfaces of this airfoil are described in nondimensional coordinates using the common notation

$$y_u(x)=h(x)+e(x)\ , \tag{2.1}$$

$$y_l(x)=h(x)-e(x)\ . \tag{2.2}$$

where $h(x)$ and $e(x)$ define, respectively, the camberline and the airfoil thickness variation along the airfoil chord. For a general point on the upper surface, the exact expression of the boundary conditions on this surface is,

$$\frac{\sin\alpha+v_u}{\cos\alpha+u_u}=h'(x)+e'(x)\ , \tag{2.3}$$

while for a point on the lower surface, the same condition is

$$\frac{\sin\alpha+v_l}{\cos\alpha+u_l}=h'(x)-e'(x)\ , \tag{2.4}$$

where u_u, v_u and u_l, v_l are the perturbation velocity components on the upper and lower surfaces, respectively.

The boundary conditions on the upper and lower surfaces of the airfoil can be expressed in complex form as

$$-\mathrm{IMAG}\{w(z)\}=-\sin\alpha+[\cos\alpha+u(x)][h'(x)\pm e'(x)]\ . \tag{2.5}$$

where the plus and minus signs (±) refer to the upper and lower surfaces of the airfoil, respectively.

The flow around the cambered airfoil at incidence can be decomposed into two flow components in the form

$$w(z)=w_A(z)+w_S(z)\ , \tag{2.6}$$

where $w_A(z)=u_A(x,y)-i\,v_A(x,y)$ represents the complex conjugate velocity of an anti-symmetric flow with respect to the airfoil chord, and $w_S(z)=u_S(x,y)-i\,v_S(x,y)$ is the complex conjugate velocity of a symmetric flow with respect to the chord. It is important to realize that this division of the flow field is performed regardless of the airfoil geometrical characteristics.

These flow components are defined by the following boundary conditions on the airfoil derived from (2.5)

$$\mathrm{IMAG}\{w_A(z)\} = -V_A(x) \ , \tag{2.7a}$$

$$\mathrm{IMAG}\{w_S(z)\} = \mp V_S(x) \ , \tag{2.7b}$$

where

$$\mathrm{V}_A(x) = -\sin\alpha + [\cos\alpha + u_S(x)]\, h'(x) + u_A(x)\, e'(x) \ , \tag{2.8a}$$

$$\mathrm{V}_S(x) = [\cos\alpha + u_S(x)]\, e'(x) + u_A(x)\, h'(x) \ . \tag{2.8b}$$

In these anti-symmetric and symmetric flows (denoted respectively by the subscripts A and S), the velocity components at symmetrical points with respect to the chord (with $y = b > 0$ and $y = -b < 0$) are related as

$$u_A(x,b) = -u_A(x,-b), \qquad v_A(x,b) = v_A(x,-b) \ , \tag{2.8c}$$

$$u_S(x,b) = u_S(x,-b), \qquad v_S(x,b) = -v_S(x,-b) \ , \tag{2.8d}$$

$$u_{u,l} = \pm u_A + u_S, \qquad v_{u,l} = v_A \pm v_S \ , \tag{2.8e}$$

Due to the flow anti-symmetry and symmetry with respect to the chord, the boundary conditions on the x-axis outside the airfoil ($x < 0$ and $x > 1$) are respectively

$$\mathrm{REAL}\{w_A(z)\} = 0 \ , \tag{2.9a}$$

$$\mathrm{IMAG}\{w_S(z)\} = 0 \ . \tag{2.9b}$$

One can notice that the nonlinear boundary conditions (2.7a,b) and (2.8a,b) are coupled, each containing both unknown perturbation velocity components u_A and u_S. Hence, both the anti-symmetric and symmetric flow components have to be solved simultaneously in order to obtain the complete nonlinear solution of the flow past the airfoil. The nonlinear nature of the boundary conditions is evidenced by the above relations, which indicate that the normal disturbance velocities v_A and v_S are both functions of the associated chordwise disturbance velocities u_A and u_S. It is also noted that the nonlinearities are proportional to both the flow quantities u_A and u_S and the geometrical quantities $e'(x)$ and $h'(x)$. In fact, the problem is truly linear in the case of a flat plate only, for which $h'(x) = 0$ and $e'(x) = 0$.

In the linear analysis, based on the small perturbations assumption (implying small incidence, relative camber and airfoil thickness, and hence small perturbation velocity components u and v), the nonlinear terms can be neglected in equations (2.8a,b), which become in this case

$$\mathrm{V}_A(x) = -\sin\alpha + h'(x)\cos\alpha \ , \tag{2.10a}$$

$$\mathrm{V}_S(x) = e'(x)\cos\alpha \ . \tag{2.10b}$$

Thus in the linear analysis of thin airfoils, the boundary conditions (2.7a,b), (2.10a,b) are decoupled, and the anti-symmetric flow past the thin-cambered airfoil at incidence and the symmetric flow around the airfoil of symmetrical thickness at zero angle of attack can be studied separately.

2.2 Linear method of solution

2.2.1 Velocity and pressure distributions for thin-cambered airfoils

Consider the prototype problem of a flapped thin airfoil, $y = h(x)$, placed at an incidence α in a uniform inviscid flow of velocity U_∞ (as shown in Figure 2.2). The airfoil is defined by a ridge situated at $x = s$ where the airfoil slope suddenly changes due to the deflection angle β of the flap. The slope of the airfoil, $h'(x)$, is given by

$$h'(x) = \begin{cases} h'(0) = \tan\tau & \text{for} \quad 0 < x < s \\ \tan(\tau - \beta) = h'(0) + \Delta h' & \text{for} \quad s < x < 1 \end{cases} \ , \tag{2.11}$$

where $\Delta h' = \tan(\tau - \beta) - \tan\tau$.

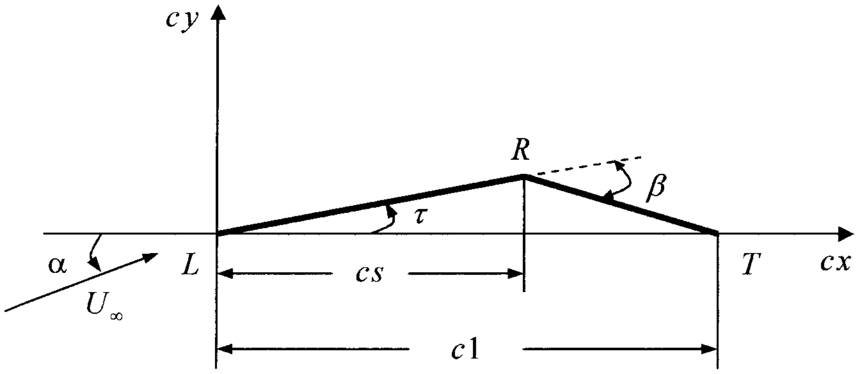

Figure 2.2 Prototype problem of a flapped thin airfoil.

The velocity and pressure solutions of this problem based on the method of velocity singularities have been first obtained by Mateescu [116], Mateescu and Nadeau [123] and Mateescu and Newman [124] in the complex form

$$w_A(z) = -[V_A(0) + \Delta V_A\, C(s)]\sqrt{\frac{1-z}{z}} - \Delta V_A\, \tilde{G}(s,z)\ , \tag{2.12}$$

where $V_A(0) = -\sin\alpha + h'(0)\cos\alpha$, $\Delta V_A = \Delta h' \cos\alpha$ and $C(s) = (2/\pi)\cos^{-1}\sqrt{s}$. The first right-hand-side term is the singular contribution of the airfoil leading edge (at $x = 0$), and $\tilde{G}(s,z) = \frac{2}{\pi}\cosh^{-1}\sqrt{\frac{(1-z)s}{s-z}}$ represents the singular contribution of the ridge situated at $x = s$. Note that these singular contributions satisfy all boundary conditions on the airfoil and outside it, including the Kutta condition at the trailing edge. The axial perturbation velocity on the airfoil ($z = x$) can be easily obtained by taking the real part of equation (2.12)

$$u_A(x) = -[V_A(0) + \Delta V_A\, C(s)]\sqrt{\frac{1-x}{x}} - \Delta V_A\, G(s,x)\ , \tag{2.13}$$

where $G(s,x) = \text{REAL}\{\tilde{G}(s,z)\}$ is

$$G(s,x) = \begin{cases} \frac{2}{\pi}\cosh^{-1}\sqrt{\frac{(1-x)s}{s-x}} & \text{for } x \in (0,s) \\ \frac{2}{\pi}\sinh^{-1}\sqrt{\frac{(1-x)s}{x-s}} & \text{for } x \in (s,1) \\ 0 & \text{for } x < 0 \text{ and } x > 1 \end{cases} \tag{2.14}$$

For a continuously cambered airfoil, the solution is obtained by considering a continuous distribution of elementary ridges [124], defined by $\Delta h' = h''(s)\,ds$, or $\Delta V_A = V_A'(s)\,ds$ where $V_A'(s) = h''(s)\cos\alpha$, in the form

$$u_A(x) = -\left[V_A(0) + \int_0^1 V_A'(s)\, C(s)\, ds\right]\sqrt{\frac{1-x}{x}} - \int_0^1 V_A'(s)\, G(s,x)\, ds\ . \tag{2.15}$$

A polynomial representation is used for the camberline slope, as in the case of NACA airfoils, in the form

$$h'(x) = \sum_{k=0}^{n} h_k \, x^k \,, \tag{2.16}$$

which corresponds to the camberline equation $h(x) = \sum_{k=0}^{n} \left[h_k / (k+1)\right] x^{k+1}$, where the coefficients h_k are specified. A very simple expression in closed form is obtained for $u_A(x)$, as well as for the pressure difference coefficient $\Delta C_p(x) = 4\, u_A(x)$, as

$$u_A(x) = \left[\sin\alpha - 2\cos\alpha \sum_{k=0}^{n} h_k \sum_{j=0}^{k} g_{k-j} \, x^j \right] \sqrt{\frac{1-x}{x}} \,, \tag{2.17}$$

where the coefficients $g_j = (2j)! / \left[2^{2j} (j!)^2\right]$ are also defined by the recurrence formula $g_j = g_{j-1} (2j-1)/(2j)$, with $g_0 = 1$.

This velocity singularity method has proven to be very efficient in solving the aerodynamic problems involving adaptive surfaces, such as flexible-membrane and jet-flapped airfoils [124].

2.2.2 Velocity and pressure distributions for airfoils of symmetrical thickness

Consider the prototype problem of a symmetric double-wedge airfoil (as shown in Figure 2.3), $y = \pm\, e(x)$, at zero angle of attack ($\alpha = 0$), defined by a sudden change of its upper surface slope at $x = s$ (and that of its lower surface slope, which is symmetric).

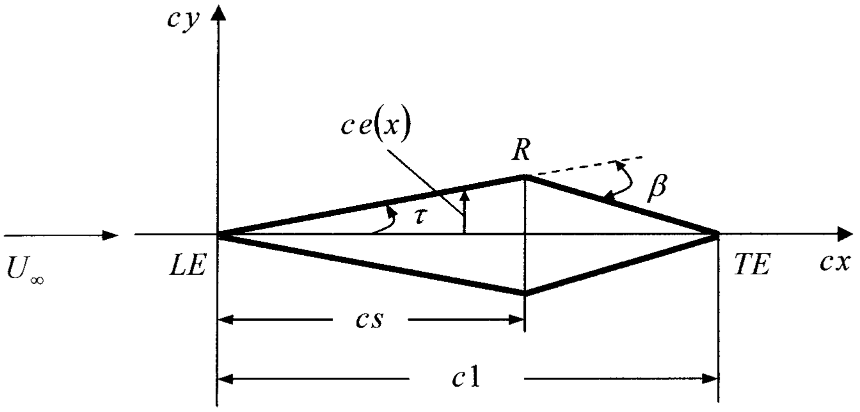

Figure 2.3 Prototype problem of symmetric double-wedge airfoil at zero incidence.

The slope of the upper surface $e'(x)$ is given by

$$e'(x)=\begin{cases} e'(0)=\tan\tau & \text{for} \quad 0<x<s \\ e'(0)+\Delta e'=\tan(\tau-\beta) & \text{for} \quad s<x<1 \end{cases} \tag{2.18}$$

where $\Delta e'=\tan(\tau-\beta)-\tan\tau$.

Similarly to the thin airfoil case, the solution of the perturbation velocity for this symmetrical flow problem can be expressed in the complex form as

$$w_S(z)=V_S(0)\frac{1}{\pi}\ln\frac{-z}{1-z}+\Delta V_S\,\frac{1}{\pi}\ln\frac{s-z}{1-z} \ , \tag{2.19}$$

where $V_S(0)=e'(0)$ and $\Delta V_S=\Delta e'$, and where $(1/\pi)\ln(s-z)$ represents the singular contribution of the ridge situated at $x=s$, while $(1/\pi)\ln(-z)$ and $(1/\pi)\ln(1-z)$ represent the contribution of the leading and trailing edges, which in this case have the same singular behavior as ridges.

The chordwise perturbation velocity on the airfoil is obtained by taking the real part of equation (2.19), noticing that $\mathrm{REAL}\{\ln(s-z)\}=\ln|s-x|$, in the form

$$u_S(x)=V_S(0)\frac{1}{\pi}\ln\frac{x}{1-x}+\Delta V_S\,\frac{1}{\pi}\ln\frac{|s-x|}{1-x} \ , \tag{2.20}$$

For an airfoil with a continuously variable slope, the corresponding velocity solution is also obtained by considering a continuous distribution of elementary ridges, defined by $\Delta e'=e''(s)ds$, or $\Delta V_S=V_S'(s)ds$, in the form

$$u_S(x)=V_S(0)\frac{1}{\pi}\ln\frac{x}{1-x}+\int_0^1 V_S'(s)\frac{1}{\pi}\ln\frac{s-x}{1-x}ds \ , \tag{2.21}$$

or, after integrating by parts,

$$u_S(x)=-\frac{1}{\pi}\int_0^1 V_S(s)\frac{ds}{s-x} \ , \tag{2.22}$$

where for this case $V_S(s)=e'(s)$.

For a polynomial representation of the contour slope in the form

$$e'(x)=\sum_{k=0}^{m} e_k\,x^k \ , \tag{2.23}$$

where the coefficients e_k are specified, a very simple expression in closed form is obtained for $u_S(x)$, as well as for the pressure coefficient $C_p(x) = -2\, u_S(x)$, in the form

$$u_S(x) = (1/\pi)\sum_{k=0}^{m} e_k \left\{ x^k \ln\frac{1-x}{x} + \sum_{j=0}^{k-1} \frac{x^j}{k-j} \right\} . \tag{2.24}$$

A similar linear solution can be obtained by considering a continuous distribution of elementary sources on the airfoil chord in the expression of the velocity potential.

The linear solution (2.24) provides a reasonable engineering accuracy for most part of the airfoil chord, except near the leading and trailing edges. However, at both edges of the airfoil the fluid velocity provided by (2.24) becomes infinite, instead of being zero, although physically both leading and trailing edges of symmetric airfoils at zero angle of attack are stagnation points in inviscid flows. This is in contrast to the linear solution (2.17) for the thin airfoils, in which the physical behavior of the velocity at the leading and trailing edges is correctly respected (that is, theoretically infinite at the leading edge and $u_A(1) = 0$ at the trailing edge, according to Kutta condition). This unphysical behavior of the fluid velocity at the edges of the symmetric airfoils provided by the linear solution (2.24) has to be corrected in the nonlinear aerodynamic analysis of airfoils.

2.3 Second-order analysis of symmetric airfoils in inviscid flow

2.3.1 Velocity behavior in the inviscid flows past airfoils

In the previous section, a linear theory has been presented for the solution of the inviscid flows past airfoils, which is based on the assumption of small disturbances implying small incidence, relative camber and airfoil thickness, and hence small perturbation velocity components u and v. As a result, the boundary conditions of the problem are only satisfied in an approximate manner. While this hypothesis may lead to a satisfactory first approximation, it is clearly inappropriate when the angle of incidence become large or in certain regions of the airfoil such as the leading and trailing edges.

The special case of symmetrical airfoils (such as lenticular airfoils) at zero incidence provides a valuable insight into the problem; in particular it illustrates the importance of considering the nonlinearity of the boundary conditions in the vicinity of the leading edge. It is interesting to note how the linear theory can be misleading in this case. A representation of the behavior of the linear solution for the case of the flow past a lenticular airfoil (circular arc airfoil) at zero incidence is shown in Figure 2.4.

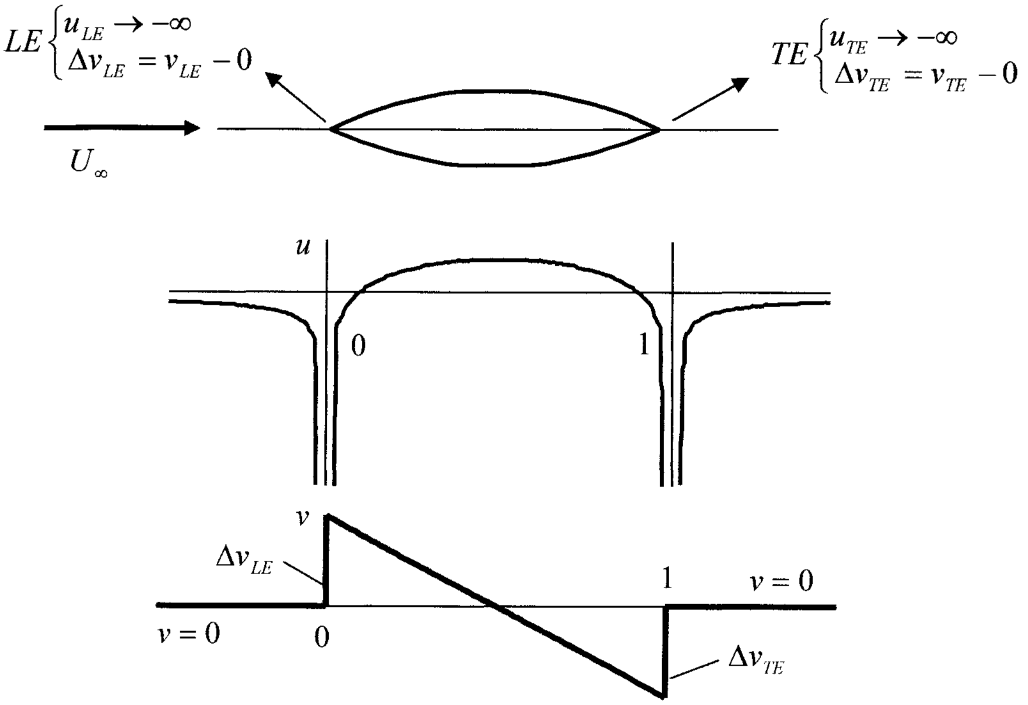

Figure 2.4 Unphysical behavior of the linear inviscid solution for the case of the flows past circular arc airfoils at zero incidence.

In this case, the chordwise perturbation velocity, u, (shown in Figure 2.4) tends asymptotically to negative infinity ($-\infty$) at both the leading and trailing edges of the airfoil which violates the real inviscid behavior (both edges are stagnation points). The maximum chordwise velocity is reached for lenticular arc airfoils at the mid-chord of the airfoil, shown also in the same Figure. The normal-to-chord perturbation velocity, v, is characterized by a jump Δv at the leading and trailing edges of the airfoil (from a zero value outside the airfoil at $x < 0$ and $x > 1$), instead of being zero at these points.

Another interesting unphysical and misleading behavior of the linear solution is demonstrated in Figure 2.5 for the case of the inviscid flows past symmetrical airfoils with rounded leading edges (such as the NACA four digits airfoils) at zero angle of attack.

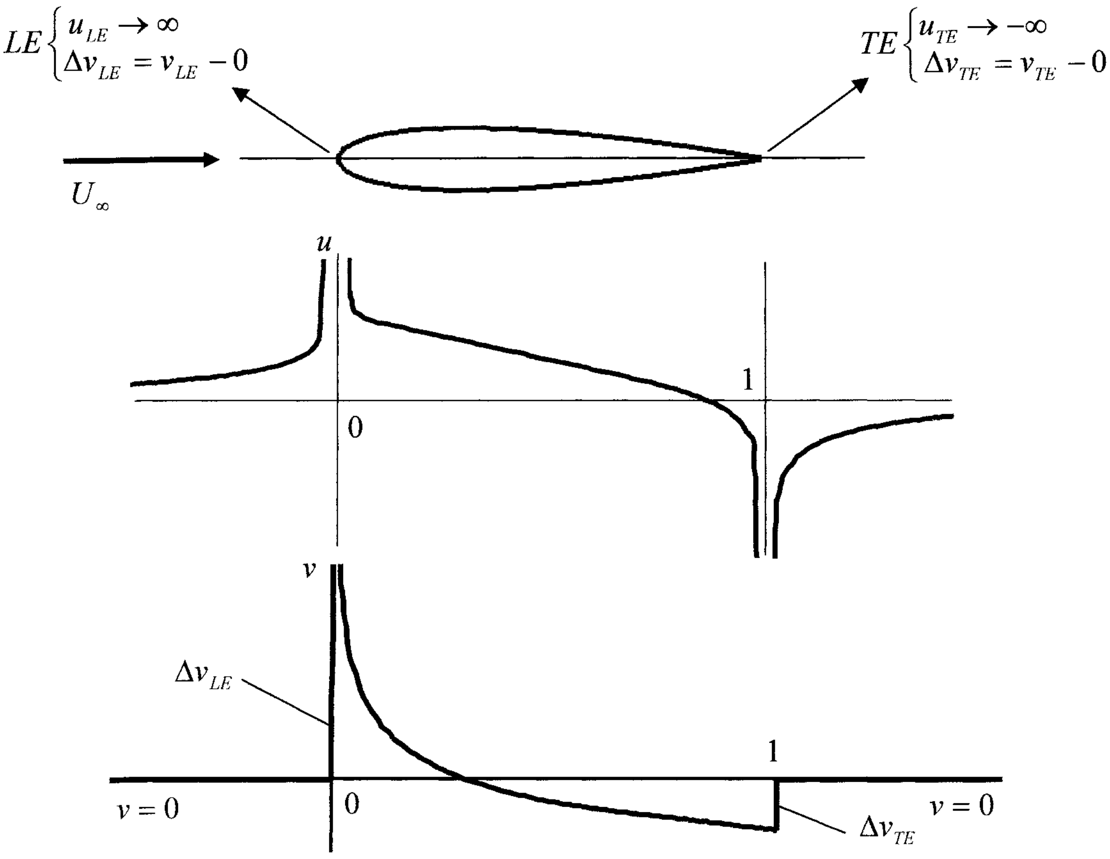

Figure 2.5 Unphysical behavior of the linear inviscid solution for the case of the flows past symmetric airfoils with rounded leading edges at zero incidence.

In this case of linear analysis, the chordwise perturbation velocity tends unphysically to infinity at the leading edge ($u_{LE} \to \infty$) from a zero value at $x \to -\infty$, which contradicts the real inviscid flow behavior (the leading edge is a stagnation point). Also this velocity decreases asymptotically to the negative infinity at the trailing edge of the airfoil ($u_{TE} \to -\infty$) and then tends asymptotically to zero as $x \to \infty$, as shown in Figure 2.5. It is noted also in this case the unequal jumps in the normal-to-chord perturbation velocity at the airfoil edges. This behavior is different for the case of the inviscid flow past lenticular airfoils at zero incidence (characterized by symmetric and equal velocity components at the edges of the airfoil, shown in Figure 2.4).

The real behavior of the inviscid flow past symmetrical airfoils is shown in Figure 2.6.

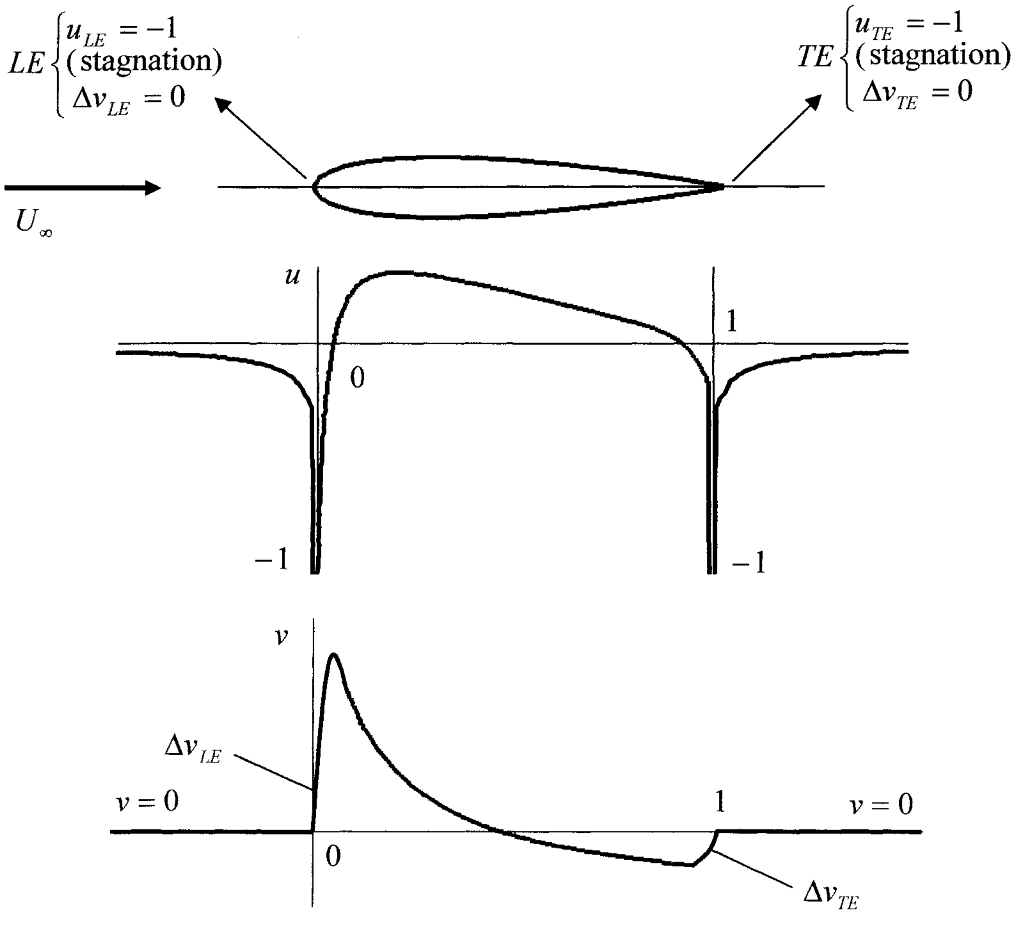

Figure 2.6 Physical behavior of the real inviscid flows past symmetric airfoils with rounded leading edges at zero incidence.

Physically both the leading and trailing edges are stagnation points in real inviscid flows past symmetrical airfoils at zero angle of attack. As shown in Figure 2.6, the chordwise perturbation velocity changes in value from zero at infinity ($x \to \pm\infty$) to that of the uniform stream velocity at both edges of the airfoil and the jump in the normal-to-chord perturbation velocity becomes zero at these points. Although the linear theory provides a good first approximation for most part of the airfoil chord, it fails to predict the real inviscid behavior at the leading and trailing edges. As a consequence of the small perturbation assumption (u and v are so small which implies that their squares and products may be neglected), the pressure coefficient becomes infinite at the leading and trailing edges of the airfoil since it depends only on the chordwise perturbation velocity (which is infinite in the linear analysis).

This unphysical behavior of the fluid velocity (as well as the pressure) at the edges of the symmetric airfoils provided by the linear theory would not appear in an exact solution. In the present nonlinear method of solution, no assumption has been made on the size of the perturbation velocities and the rigorous form of the boundary conditions is used.

2.3.2 Present method of solution for symmetric airfoils

In the case of the uncambered symmetric airfoils at zero angle of attack ($\alpha = 0$ and $h'(x) = 0$), the flow is symmetric with respect to the airfoil chord, and hence $V_A(x) = 0$ and

$$V_S(x) = [1 + u_S(x)]e'(x) \; . \tag{2.25}$$

Since the leading and trailing edges are physically stagnation points (that is $u_S(0) = u_S(1) = -1$ and $v_S(0) = v_S(1) = 0$), one can assume for $u_S(x)$ the expression

$$u_S(x) = -1 + \sqrt{x(1-x)} \sum_{j=0}^{M} b_j \, x^j \; , \tag{2.26}$$

where the coefficients b_j are *a priori* unknown.

In general, the variation of the airfoil thickness can be defined (as in the case of NACA airfoils) by the modified polynomial expression $e(x) = 2e_L\sqrt{x} + \sum_{k=0}^{m} \left[e_k/(k+1)\right] x^{k+1}$, where the coefficients e_L and e_k ($k = 0, 1, \cdots m$) are specified. This leads to the airfoil slope equation

$$e'(x) = \frac{e_L}{\sqrt{x}} + \sum_{k=0}^{m} e_k \, x^k \; . \tag{2.27}$$

The square root term associated to e_L corresponds to the airfoils with rounded leading edges, while $e_L = 0$ for the airfoils with a pointed leading edge (such as the lenticular or double-wedge airfoils). In general, for the airfoils with rounded leading edges, the value of e_L is specified in the equation of the airfoil contour $y(x)$, as in the case of NACA airfoils. For the special airfoils generated by conformal transformation, e_L can be calculated as $e_L = \sqrt{2R_L}$ from the radius of curvature at the leading edge, $R_L = \left\{\left(1 + [y'(x)]^2\right)^{3/2} / y''(x)\right\}_{x=0}$.

Thus, taking into account (2.26) and (2.27), the expression (2.25) of $V_S(x)$ becomes in this case

$$V_S(x) = \sqrt{x(1-x)} \sum_{j=0}^{M} b_j \, x^j \left[\frac{e_L}{\sqrt{x}} + \sum_{k=0}^{m} e_k \, x^k \right] \; . \tag{2.28}$$

By introducing equation (2.28) into equation (2.22) for the chordwise perturbation velocity, one obtains

$$u_S(x)=-\frac{e_L}{\pi}\sum_{j=0}^{M} b_j \int_0^1 \frac{(1-s)s^j}{\sqrt{1-s}}\frac{ds}{s-x}-\frac{1}{\pi}\sum_{j=0}^{M} b_j \sum_{k=0}^{m} e_k \int_0^1 \sqrt{s(1-s)}\, s^{k+j}\frac{ds}{s-x}, \tag{2.29a}$$

where the power terms (s^j and s^{k+j}) in equation (2.29a) are then replaced by

$$s^j = x^j + (s-x)\sum_{q=0}^{j-1} x^q\, s^{j-1-q} \ , \tag{2.29b}$$

$$s^{k+j} = x^{k+j} + (s-x)\sum_{q=0}^{k+j-1} s^q\, x^{k+j-1-q} \ . \tag{2.29c}$$

By also noting that the term $(1-s)=(1-x)-(s-x)$, one obtains the following equation for the chordwise symmetric perturbation velocity, $u_S(x)$

$$u_S(x)=-\frac{2e_L}{\pi}\sum_{j=0}^{M} b_j \left\{ (1-x)x^j\, \xi_1 + (1-x)\sum_{q=0}^{j-1} x^q\, L_{j-1-q} - L_j \right\}$$

$$-\sum_{j=0}^{M} b_j \sum_{k=0}^{m} e_k \left\{ x^{k+j}\, \xi_2 + \sum_{q=0}^{k+j-1} x^{k+j-1-q}\, H_q \right\}, \tag{2.30a}$$

where,

$$L_j = \int_0^1 \frac{s^j}{2\sqrt{1-s}} ds \ , \tag{2.30b}$$

$$H_q = \frac{1}{\pi}\int_0^1 s^q \sqrt{s(1-s)}\, ds \ , \tag{2.30c}$$

$$\xi_1 = \int_0^1 \frac{ds}{2(s-x)\sqrt{1-s}} \ , \tag{2.30d}$$

$$\xi_2 = \frac{1}{\pi}\int_0^1 \frac{\sqrt{s(1-s)}}{s-x} ds \ . \tag{2.30e}$$

The detailed derivations of L_j, H_q, ξ_1 and ξ_2 are given in Appendix A.

The nonlinear solution for symmetric airfoils can then be easily obtained from (2.30), after integration, as

$$u_S(x)=\sum_{j=0}^{M} b_j\, F_j(x) \ , \tag{2.31}$$

$$F_j(x) = -\frac{2e_L}{\pi}\left[x^j\sqrt{1-x}\,\sinh^{-1}\sqrt{\frac{1-x}{x}} - L_j + (1-x)\sum_{q=0}^{j-1} x^q L_{j-1-q}\right]$$

$$-\sum_{k=0}^{m} e_k\left[\left(\frac{1}{2}-x\right)x^{k+j} + \sum_{q=0}^{k+j-1} x^{k+j-1-q} H_q\right], \tag{2.32}$$

where $L_j = \frac{2j}{2j+1}L_{j-1}$, $L_0 = 1$, $H_q = \frac{1}{2(q+2)}g_{q+1}$, in which g_q are defined in Section 2.2.1 and derived in detail in Appendix A.

The unknown coefficients b_j are determined by requiring the expressions (2.31) and (2.26) for $u_S(x)$ to be equal at a specified number $M+1$ of collocation points conveniently distributed along the airfoil chord (usually M=6 to 10). As a result of the collocation process, one thus obtains the following simple system of linear equations

$$\sum_{j=0}^{M} b_j\left[x_i^j\sqrt{x_i(1-x_i)} - F_j(x_i)\right] = 1 \tag{2.33}$$

where x_i is the x-position of the collocation point and i is the number of that point along the airfoil chord (i varies from 0 to M).

The normal-to-chord velocity component can be calculated based on the solution for $u_S(x)$ from the boundary condition $v_S(x) = V_S(x) = [1+u_S(x)]e'(x)$, and the pressure coefficient on the airfoil can be calculated as

$$C_p = -2u_S - \left(u_S^{\,2} + v_S^{\,2}\right). \tag{2.34}$$

Thus, a very simple expression (2.31) has been obtained for the nonlinear solution of the flow past a symmetric airfoil. This nonlinear solution is validated in the following sections by comparison with the exact solution for special airfoils, with the results given by Abbott and Doenhoff [2] and with numerical results obtained using a panel method.

2.3.3 Method validation for Karman-Trefftz airfoils

The Karman-Trefftz airfoils [7, 142] are generated by the conformal transformation

$$\frac{z-\kappa b}{z+\kappa b} = \left(\frac{\zeta - b}{\zeta + b}\right)^{\kappa}, \quad \kappa = 2 - \gamma_T/\pi, \tag{2.35}$$

from a circle of radius r situated in the complex plane $\zeta = \xi + i\eta$, with the centre at $\zeta_0 = b(-e_0 + i f_0)$. In equation (2.35), γ_T represents the dihedral angle at the trailing edge of the airfoil, and b defines the position of the trailing edge. By considering convenient values for r/b, e_0 and f_0 one can obtain symmetric Karman-Trefftz airfoils (for $f_0 = 0$) and general cambered Karman-Trefftz airfoils, or other special airfoils, such as lenticular symmetrical airfoils with pointed leading and trailing edges (also for $f_0 = 0$) and half-moon cambered airfoils. Joukowski airfoils represent a special class of Karman-Trefftz airfoils with zero dihedral angle at the trailing edge (cusped trailing edge), that is $\gamma_T = 0$ and $\kappa = 2$.

In Figures 2.7 and 2.8, the present nonlinear solutions of the pressure coefficients for symmetric Karman-Trefftz airfoils at zero angle of attack and relative thickness $t = 0.08$, $t = 0.09$, $t = 0.10$ and $t = 0.12$ are validated by comparison with the exact solutions obtained by conformal transformation. A very good agreement can be observed between the two sets of results, even in the case of thicker airfoils.

2.3.4 Method validation for NACA airfoils

The present solution (2.31) is also validated for NACA 0009 and NACA 0012 airfoils at zero angle of attack by comparison with the results presented by Abbott and Doenhoff [2] as shown in Figures 2.9 and 2.10. Figure 2.9 shows that the present nonlinear solution for the fluid velocity on the airfoil contour, $V = \sqrt{(1+u)^2 + v^2}$, is in very good agreement with Abbott and Doenhoff data, while the linear solution (which tends unphysically to infinity at the leading edge) displays large errors on the first part of the airfoil. A very good agreement was also found for the pressure coefficients as shown in Figure 2.10.

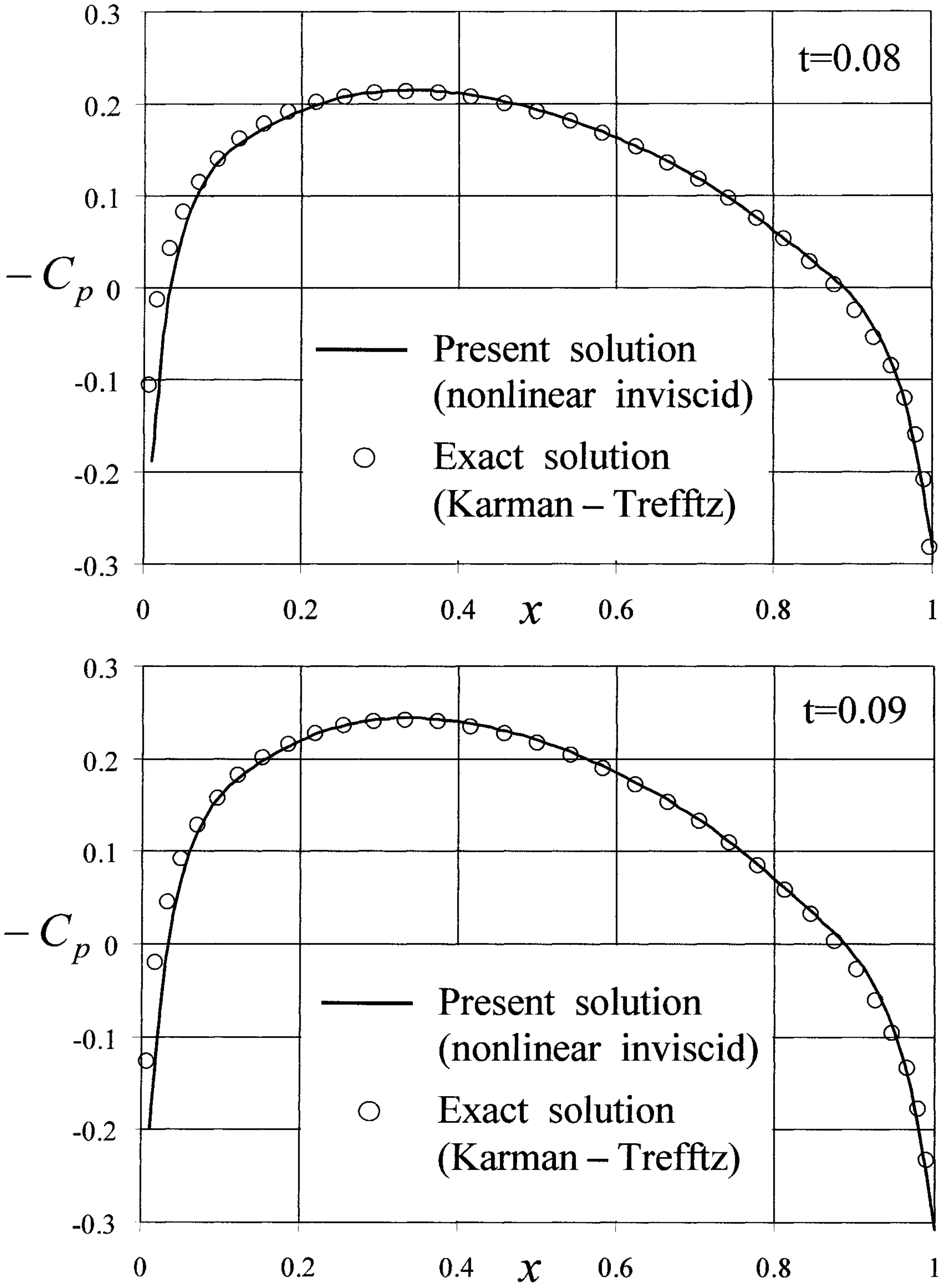

Figure 2.7 Symmetric Karman-Trefftz airfoils at zero incidence; present nonlinear solutions compared with the exact solutions based on conformal transformation for the pressure coefficient distribution, $C_p(x)$.

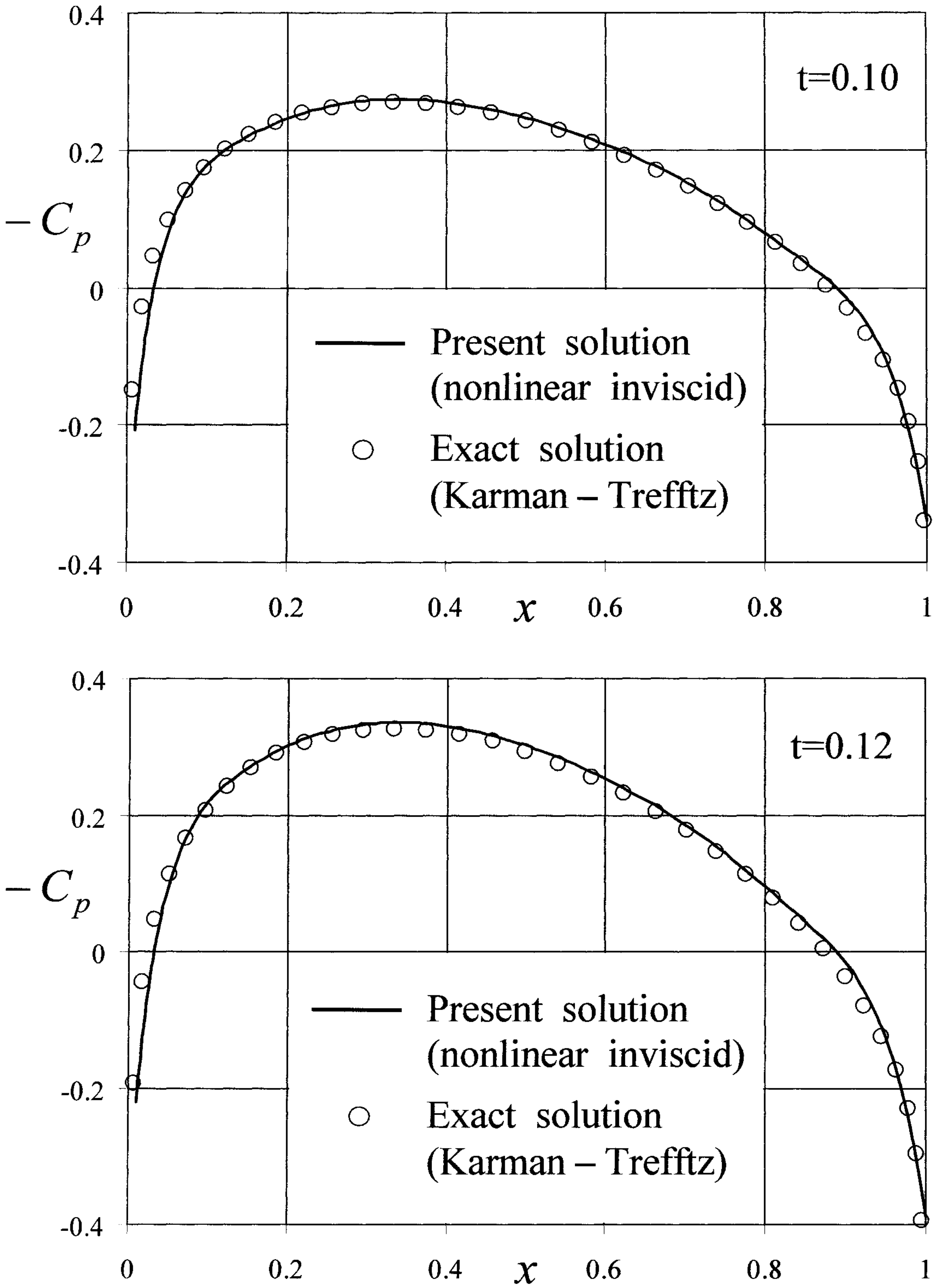

Figure 2.8 Symmetric Karman-Trefftz airfoils at zero incidence; present nonlinear solutions compared with the exact solutions based on conformal transformation.

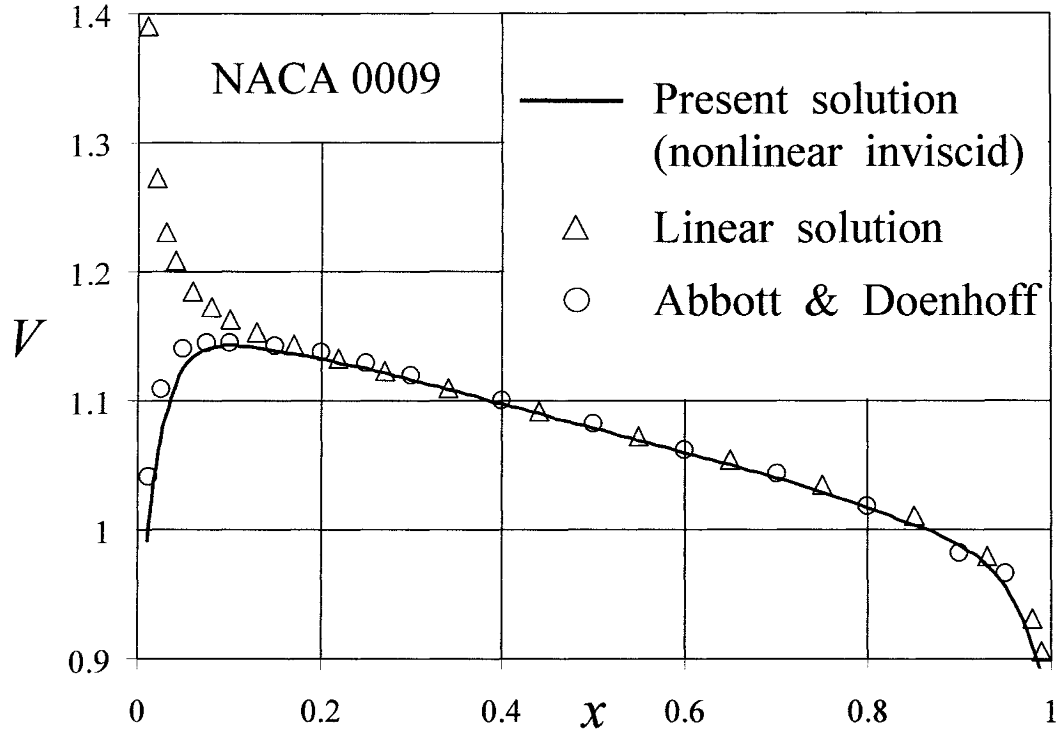

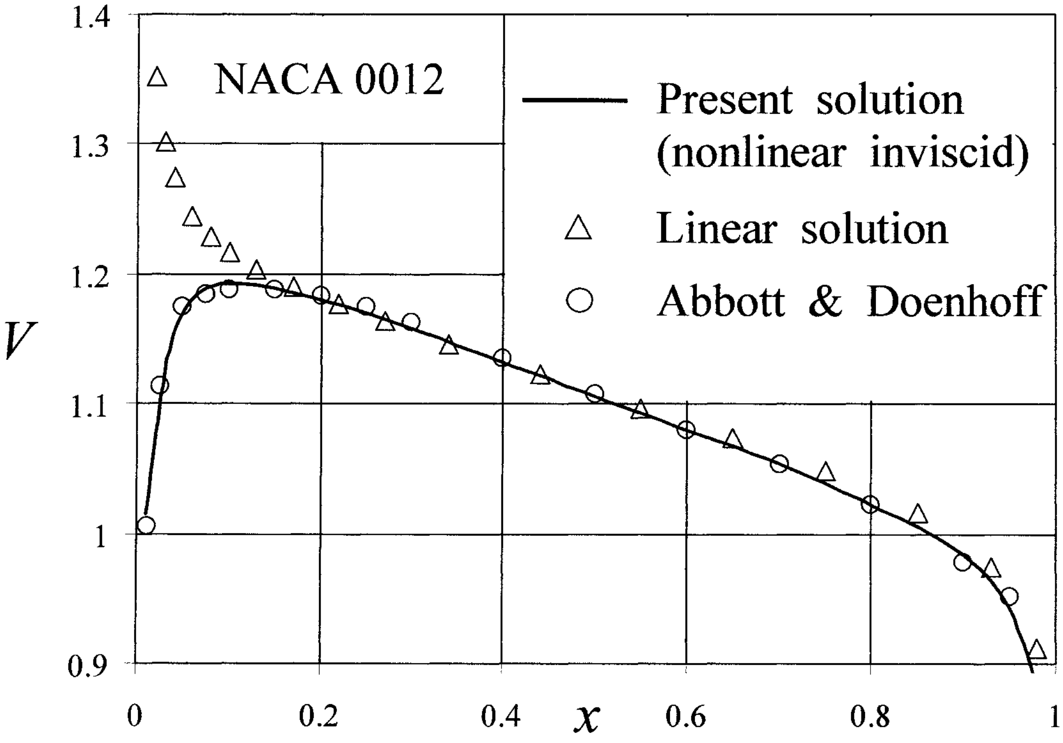

Figure 2.9 NACA 0009 and NACA 0012 airfoils at zero incidence; present nonlinear solutions for the fluid velocity distribution, $V(x)$, compared with Abbott and Doenhoff data and with the linear solutions.

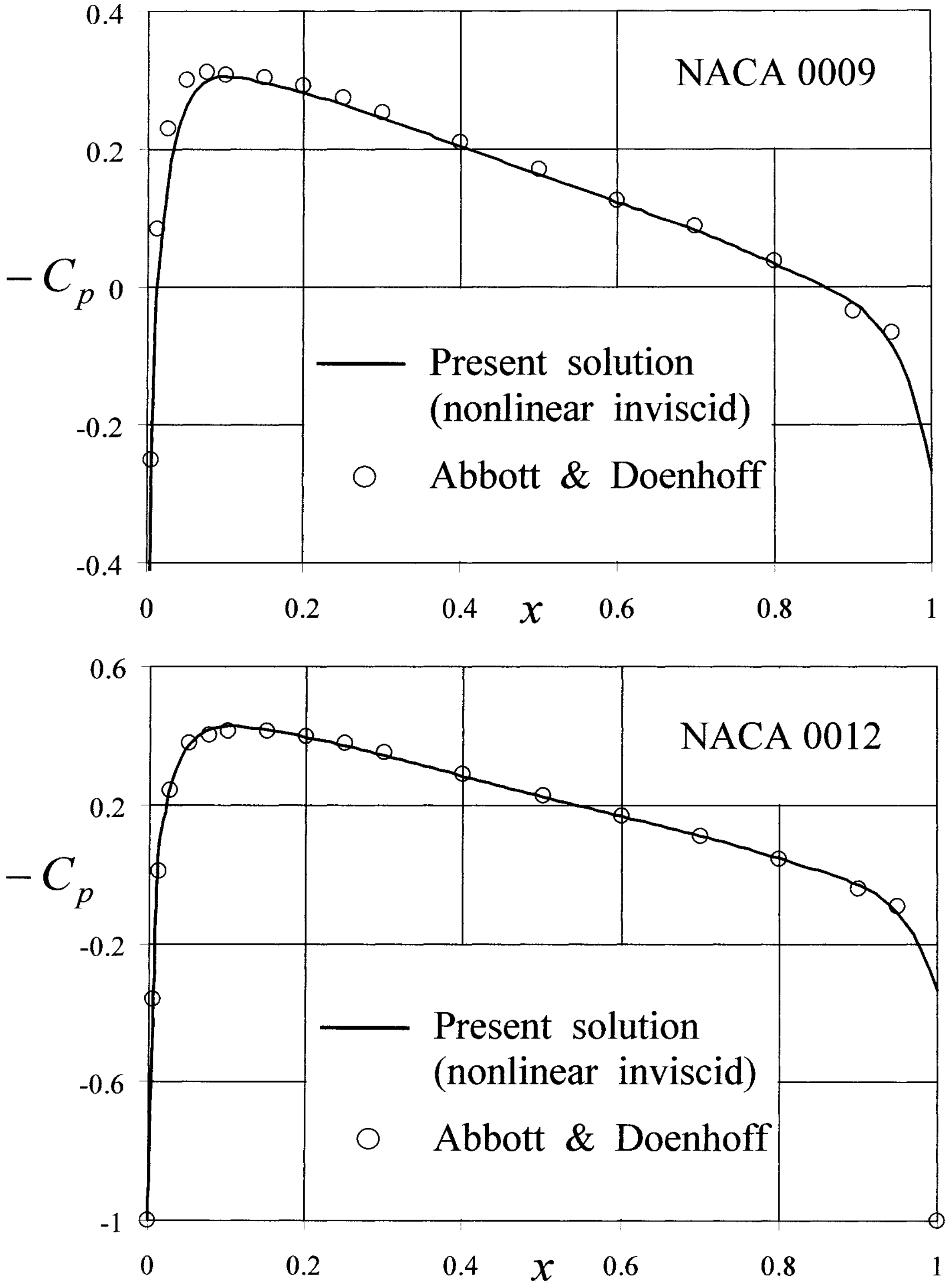

Figure 2.10 NACA 0009 and NACA 0012 airfoils at zero incidence; present nonlinear solutions for the pressure coefficient distribution, $C_p(x)$, compared with Abbott and Doenhoff data.

2.3.5 Comparison with symmetric airfoils with pointed leading edges

The symmetric airfoils with pointed leading and trailing edges represents a particular case of symmetric airfoils for which $e_L = 0$. This particularization has to be introduced in equations (2.31), (2.32) in order to obtain the nonlinear solution for these airfoils. This solution is validated for the Karman-Trefftz lenticular airfoils (with the upper and lower sides represented by circular arcs) by comparison with the exact solution obtained by conformal transformation.

Figures 2.11a and 2.11b show a comparison for the chordwise perturbation velocity distribution between the present solution and the exact solution obtained by conformal transformation for two symmetric lenticular Karman-Trefftz airfoils of relative thickness $t = 0.02$ and $t = 0.10$ at zero angle of attack. The present nonlinear solutions were found to be in very good agreement with the exact solutions even in the case of thicker airfoils.

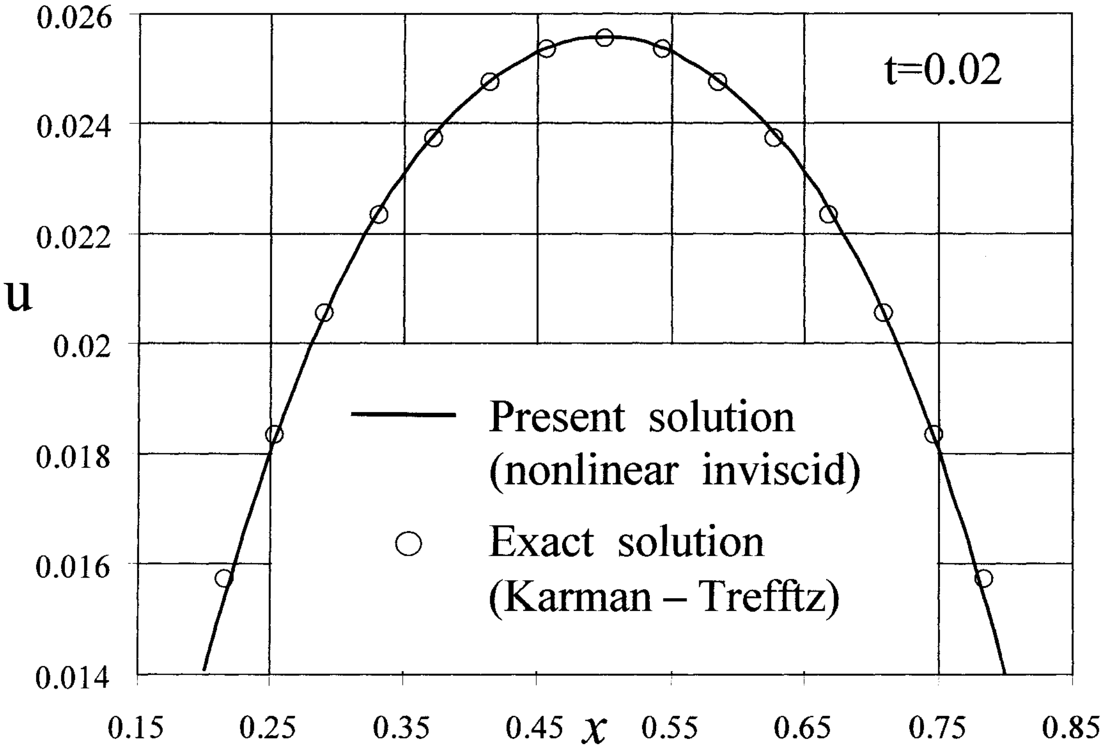

Figure 2.11a Symmetric airfoils with pointed leading edges; present nonlinear solution for Karman-Trefftz lenticular airfoil ($t = 0.02$) compared with the exact linear solution.

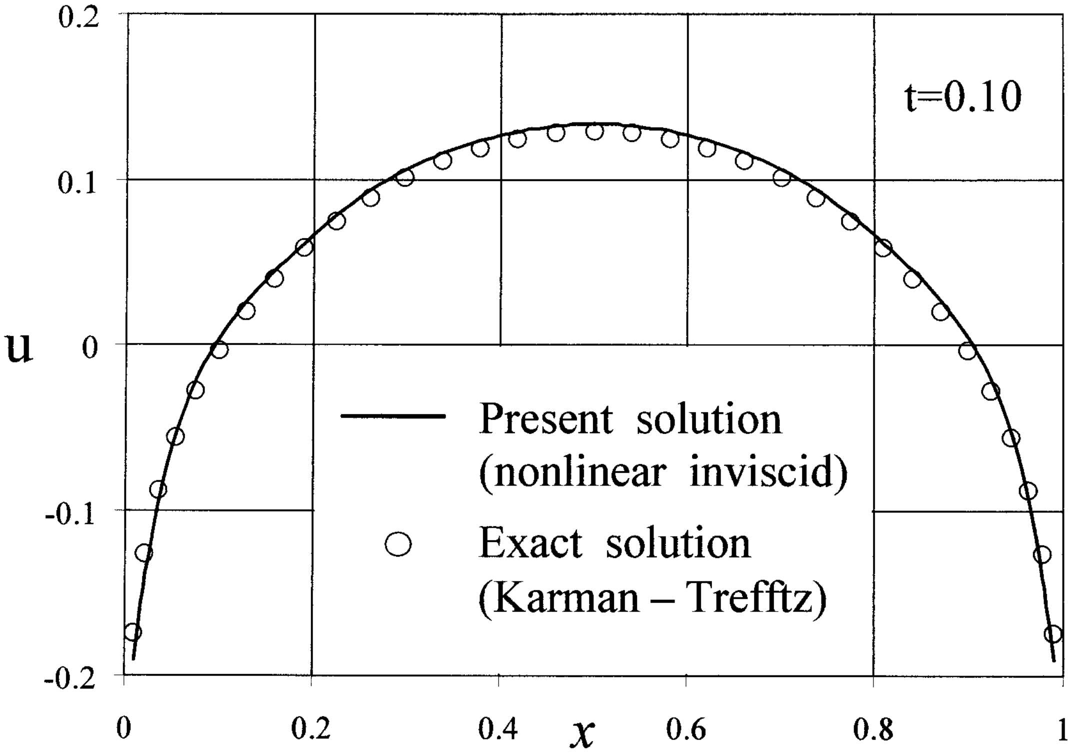

Figure 2.11b Symmetric airfoils with pointed leading edges; present nonlinear solution for Karman-Trefftz lenticular airfoil ($t = 0.10$) compared with the exact linear solution.

2.3.6 Accurate nonlinear solutions for symmetric double wedge airfoils

Consider the inviscid incompressible uniform flow of velocity U_∞ past a symmetric double-wedge airfoil, $y = \pm e(x)$, at zero angle of attack (as shown in Figure 2.3). The slope of the airfoil is defined by

$$e'(x) = \begin{cases} \tan\tau & \text{for } 0 < x < s \\ \tan(\tau - \beta) & \text{for } s < x < 1 \end{cases} \tag{2.36}$$

where s defines the position of the ridge, τ is the surface slope angle between the leading edge and the ridge, and $\tau - \beta$ is the slope angle between the ridge and the trailing edge. Consider the following formal expression for the chordwise perturbation velocity $u_S(x)$, which has been also used in Section 2.3.2.

$$u_S(x) = -1 + \sqrt{x(1-x)} \sum_{j=0}^{M} b_j x^j , \tag{2.37}$$

where the coefficients b_j are *a priori* unknown. By introducing the formal expression for $u_S(x)$ into the expression (2.25) for $V_S(x)$, one obtains

$$V_S(x) = \tan\tau \,\sqrt{x(1-x)}\sum_{j=0}^{M} b_j\, x^j + \tan(\tau-\beta)\sqrt{x(1-x)}\sum_{j=0}^{M} b_j\, x^j \ . \tag{2.38}$$

By introducing equation (2.38) into equation (2.22) for the chordwise perturbation velocity, one obtains

$$u_S(x) = -\frac{\tan\tau}{\pi}\sum_{j=0}^{M} b_j \int_0^s \frac{\sqrt{s(1-s)}\, s^j}{s-x}\, ds - \frac{\tan(\tau-\beta)}{\pi}\sum_{j=0}^{M} b_j \int_s^1 \frac{\sqrt{s(1-s)}\, s^j}{s-x}\, ds \ , \tag{2.39a}$$

where the power terms (s^j) in equation (2.39a) are then replaced by

$$s^j = x^j + (s-x)\sum_{q=0}^{j-1} s^q\, x^{j-1-q} \ , \tag{2.39b}$$

and the integrals of equation (2.39a) are hence given by

$$\int_0^s \frac{\sqrt{s(1-s)}\, s^j}{s-x}\, ds = x^j Q(x) + \sum_{q=0}^{j-1} x^{j-1-q}\left(J_{q+1} - J_{q+2}\right), \tag{2.40a}$$

$$\int_s^1 \frac{\sqrt{s(1-s)}\, s^j}{s-x}\, ds = x^j\, \overline{Q}(x) + \sum_{q=0}^{j-1} x^{j-1-q}\left(\overline{J}_{q+1} - \overline{J}_{q+2}\right), \tag{2.40b}$$

where

$$Q(x) = \int_0^s \frac{\sqrt{s(1-s)}}{s-x}\, ds \ , \tag{2.40c}$$

$$\overline{Q}(x) = \int_s^1 \frac{\sqrt{s(1-s)}}{s-x}\, ds \ , \tag{2.40d}$$

$$J_k = \int_0^s \frac{s^k}{\sqrt{s(1-s)}}\, ds \ , \tag{2.40e}$$

$$\overline{J}_k = \int_s^1 \frac{s^k}{\sqrt{s(1-s)}}\, ds \ . \tag{2.40f}$$

The detailed derivations of $Q(x)$, $\overline{Q}(x)$, J_k and $\overline{J}_k$ are given in Appendix A.

The accurate chordwise perturbation velocity is obtained after integration as

$$u_S(x) = \sum_{j=0}^{M} b_j\, \hat{F}_j(x) \ , \tag{2.41}$$

where

$$\hat{F}_j(x) = -\frac{\tan\tau}{\pi}\left[x^j Q(x) + \sum_{q=0}^{j-1} x^{j-1-q}\left(J_{q+1} - J_{q+2}\right)\right]$$

$$-\frac{\tan(\tau-\beta)}{\pi}\left[x^j\,\overline{Q}(x) + \sum_{q=0}^{j-1} x^{j-1-q}\left(\overline{J}_{q+1} - \overline{J}_{q+2}\right)\right], \tag{2.42}$$

in which

$$Q(x) = (1-x)J_0 - J_1 - 2\sqrt{(1-x)x}\;G(s,x), \tag{2.43a}$$

$$\overline{Q}(x) = (1-x)\overline{J}_0 - \overline{J}_1 + 2\sqrt{(1-x)x}\;G(s,x), \tag{2.43b}$$

$$J_k = -\frac{s^{k-1}}{k}\sqrt{(1-s)s} + \frac{2k-1}{2k}J_{k-1}\,, \quad J_0 = \pi - 2\cos^{-1}\sqrt{s}\,, \tag{2.43c}$$

$$\overline{J}_k = \frac{s^{k-1}}{k}\sqrt{(1-s)s} + \frac{2k-1}{2k}\overline{J}_{k-1}\,, \quad \overline{J}_0 = 2\cos^{-1}\sqrt{s}\,, \tag{2.43d}$$

$$G(s,x) = \begin{cases} \dfrac{2}{\pi}\cosh^{-1}\sqrt{\dfrac{(1-x)s}{s-x}} & \text{for } x \in (0,s) \\[2ex] \dfrac{2}{\pi}\sinh^{-1}\sqrt{\dfrac{(1-x)s}{x-s}} & \text{for } x \in (s,1)\,. \\[2ex] 0 & \text{for } x<0 \text{ and } x>1 \end{cases} \tag{2.43e}$$

The unknown coefficients b_j are determined (by collocation) from the following simple system of linear equations

$$\sum_{j=0}^{M} b_j\left[x_i^j\sqrt{x_i(1-x_i)} - \hat{F}_j(x_i)\right] = 1\,. \tag{2.44}$$

where x_i is the x-position of the collocation point and i is the number of that point along the airfoil chord (i varies from 0 to M). The present second-order accurate solution for the pressure coefficient distribution on the symmetric double-wedge airfoils is validated in Figure 2.12 by comparison with results obtained by a panel method (Kuethe and Chow [98]) for three airfoils with different relative thickness and ridge position: (i) $t = 0.05$ and $s = 0.5$; (ii) $t = 0.05$ and $s = 0.7$; (iii) $t = 0.10$ and $s = 0.5$. A matrix of 120 x 120 was solved using the panel method compared to an 8 x 8 matrix using the present method. A good agreement can be noticed between the two sets of results for all cases.

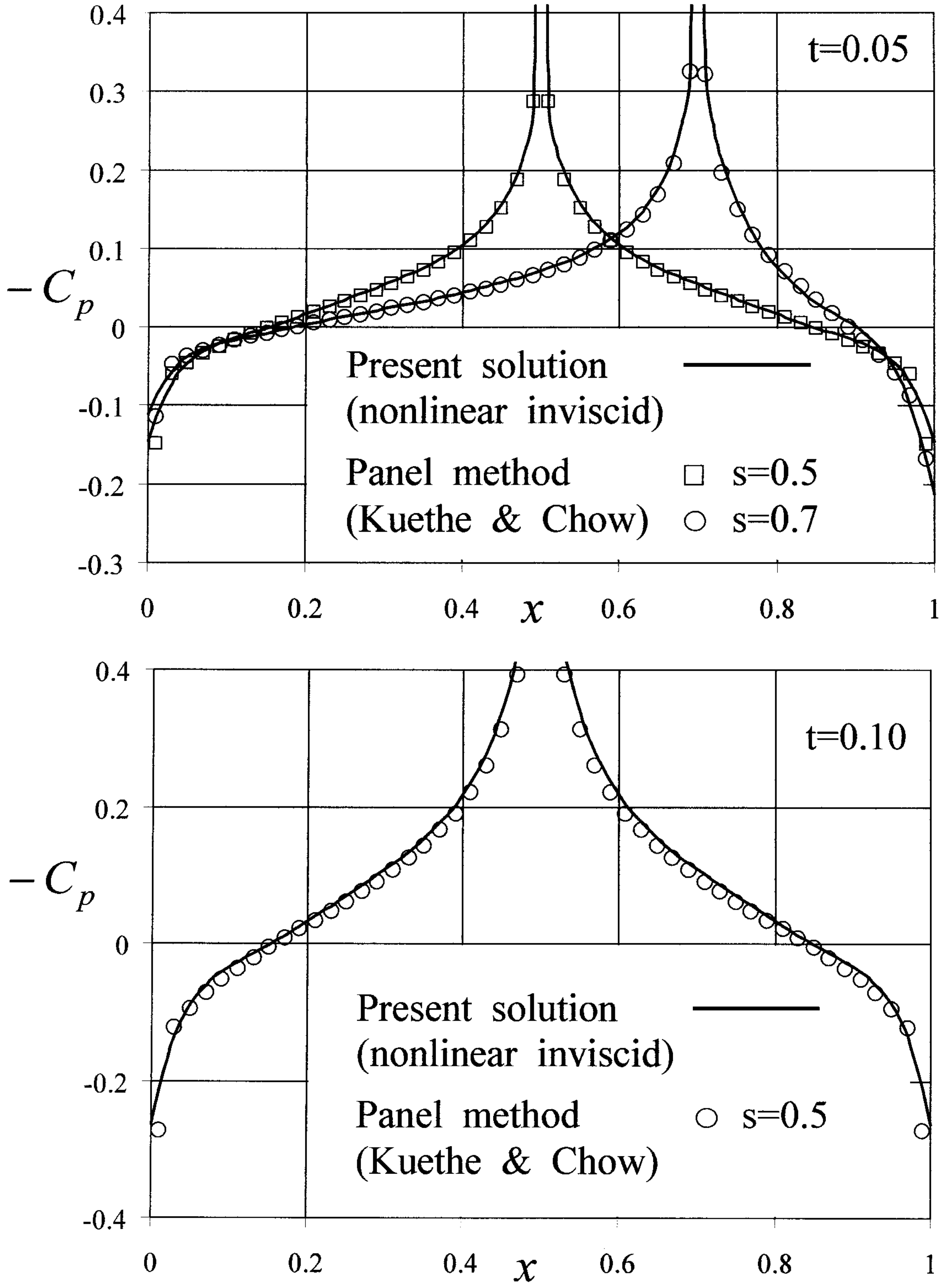

Figure 2.12 Symmetric double-wedge airfoils; present nonlinear solutions compared with panel method results (Kuethe and Chow [98]), for $t = 0.05$ and 0.10, and $s = 0.5$ and 0.7.

2.4 Present analysis of general cambered airfoils at incidence

2.4.1 General accurate method of solution

In the general case of thick cambered airfoils placed in a uniform inviscid and incompressible flow at incidence, the anti-symmetric and symmetric flow components are defined by the boundary conditions (2.7a,b), (2.8a,b) on the airfoil, in which $h'(x)$ and $e'(x)$ are defined by equations (2.16) and (2.27).

As discussed in sections 2.2 and 2.3, in inviscid flow the physical behavior of the flow velocity at the leading and trailing edges can be summarized as follows:

(i) Both edges are stagnation points for the symmetrical flow component, that is $u_S(0)=u_S(1)=-1$ and $v_S(0)=v_S(1)=0$, and hence the following expression is assumed for $u_S(x)$ in equations (2.8a,b)

$$u_S(x)=-\cos\alpha+\sqrt{x(1-x)}\sum_{j=0}^{M} b_j\, x^j \ , \tag{2.45}$$

where the coefficients b_j are *a priori* unknown.

(ii) In the anti-symmetrical flow component, the velocity is theoretically infinite at the leading edge ($x=0$) and at the trailing edge $u_A(1)=0$, according to Kutta condition, and hence the following expression is assumed for $u_A(x)$ in equations (2.8a,b)

$$u_A(x)=\sqrt{\frac{1-x}{x}}\sum_{j=0}^{N} a_j\, x^j \ , \tag{2.46}$$

where the coefficients a_j are *a priori* unknown.

The camberline and symmetric slope relations given by equations (2.16) and (2.27) are

$$h'(x)=\sum_{k=0}^{n} h_k\, x^k \ ,$$

$$e'(x)=\frac{e_L}{\sqrt{x}}+\sum_{k=0}^{m} e_k\, x^k \ .$$

where the coefficients h_k and e_k are specified by the airfoil geometry.

Thus, taking into account (2.45) and (2.46), the expression (2.8b) of $V_S(x)$ becomes in this case

$$V_S(x) = \sqrt{x(1-x)}\sum_{j=0}^{M} b_j\,x^j\left[\frac{e_L}{\sqrt{x}}+\sum_{k=0}^{m} e_k\,x^k\right]+\sqrt{\frac{1-x}{x}}\sum_{k=0}^{n} h_k x^k\sum_{j=0}^{N} a_j\,x^j \;. \tag{2.47}$$

Similarly, the expression (2.8a) of $V_A(x)$ for this case becomes

$$V_A(x) = -\sin\alpha + \sqrt{(1-x)x}\sum_{j=0}^{M} b_j\,x^j\sum_{k=0}^{n} h_k\,x^k + \sqrt{\frac{1-x}{x}}\sum_{j=0}^{N} a_j\,x^j\left[\frac{e_L}{\sqrt{x}}+\sum_{k=0}^{m} e_k\,x^k\right] , \tag{2.48}$$

The complex nature of the boundary conditions is evidenced by the above relations, which indicate that the normal disturbance velocities v_A and v_S are both functions of the associated chordwise disturbance velocities u_A and u_S . It is also noted that the non-linearities in the boundary conditions are proportional to both the flow quantities u_A and u_S and the geometrical quantities $e'(x)$ and $h'(x)$.

In order to obtain the solutions for the symmetric and anti-symmetric flow components $u_S(x)$ and $u_A(x)$, the resulting expressions of $V_S(x)$ and $V_A(x)$ are then introduced in the integral form of the perturbation flow components, equations (2.22) and (2.15), respectively

$$u_S(x) = -\frac{1}{\pi}\int_0^1 V_S(s)\frac{ds}{s-x} \;,$$

$$u_A(x) = -\left[V_A(0) + \int_0^1 V_A'(s)\,C(s)\,ds\right]\sqrt{\frac{1-x}{x}} \;-\; \int_0^1 V_A'(s)\,G(s,x)\,ds \;.$$

Hence, one obtains

$$\begin{aligned} u_S(x) = &-\frac{e_L}{\pi}\sum_{j=0}^{M} b_j\int_0^1 \frac{(1-s)s^j}{\sqrt{1-s}}\,\frac{ds}{s-x} - \frac{1}{\pi}\sum_{j=0}^{M} b_j\sum_{k=0}^{m} e_k\int_0^1 \sqrt{s(1-s)}\;s^{k+j}\,\frac{ds}{s-x} \\ &-\frac{1}{\pi}\sum_{j=0}^{N} a_j\sum_{k=0}^{n} h_k\int_0^1 \sqrt{\frac{(1-s)}{s}}\;s^{k+j}\,\frac{ds}{s-x} \;. \end{aligned} \tag{2.49}$$

The integrals in the expression of $u_A(x)$ are performed by integrating by parts. These integrals are hence rewritten as

$$\int_0^1 V_A'(s)\,C(s)\,ds = C(s)V_A(s)\Big|_{s=0}^{s=1} + \int_0^1 V_A(s)\,C'(s)\,ds \;, \tag{2.50a}$$

$$\int_0^1 V_A'(s)\,G(s,x)\,ds = V_A(s)\,G(s,x)\Big|_{s=0}^{s=1} + \int_0^1 V_A(s)\,G'(s,x)\,ds \;, \tag{2.50b}$$

in which

$$C(s) = (2/\pi)\cos^{-1}\sqrt{s} \;, \tag{2.50c}$$

$$C'(s) = (2/\pi)\left[\frac{1}{2\sqrt{(1-s)s}}\right], \tag{2.50d}$$

$$G(s,x) = \frac{2}{\pi}\cosh^{-1}\sqrt{\frac{(1-x)s}{s-x}} \;, \tag{2.50e}$$

$$G'(s,x) = \frac{2}{\pi}\left[\frac{\sqrt{(1-x)x}}{2(s-x)\sqrt{(1-s)s}}\right]. \tag{2.50f}$$

Thus the integral form of $u_A(x)$ becomes

$$\begin{aligned} u_A(x) = &-\left[-\sin\alpha + \frac{1}{\pi}\sum_{j=0}^{M} b_j \sum_{k=0}^{n} h_k \int_0^1 s^{k+j}\, ds\right]\sqrt{\frac{1-x}{x}} - \frac{1}{\pi}\sqrt{(1-x)x}\sum_{j=0}^{M} b_j \sum_{k=0}^{n} h_k \left[\int_0^1 \frac{s^{k+j}}{s-x} ds\right] \\ &-\left[\frac{1}{\pi} e_L \sum_{j=0}^{N} a_j \int_0^1 s^{j-3/2} ds + \sum_{j=0}^{N} a_j \sum_{k=0}^{m} e_k \int_0^1 s^{k+j-1} ds\right]\sqrt{\frac{1-x}{x}} \\ &-\frac{1}{\pi}\left[e_L \sum_{j=0}^{N} a_j \sqrt{(1-x)x}\int_0^1 \frac{s^{j-1}}{(s-x)\sqrt{s}} ds + \sqrt{(1-x)x}\sum_{j=0}^{N} a_j \sum_{k=0}^{m} e_k \int_0^1 \frac{s^{k+j-1}}{(s-x)} ds\right]. \end{aligned} \tag{2.51}$$

The power terms (such as s^j, s^{k+j} and s^{j-1}) in equations (2.49) and (2.51) are then replaced by $s^j = x^j + (s-x)\sum_{q=0}^{j-1} s^q\, x^{j-1-q}$. The resulting recurrence integrals that appear in equations (2.49) and (2.51) are derived in detail in Appendix A.

After performing the integrations and rearranging the terms one thus obtains the solutions for the symmetric and anti-symmetric flow components

$$u_S(x) = \sum_{j=0}^{M} b_j F_j(x) + \sum_{j=0}^{N} a_j T_j(x), \tag{2.52}$$

$$u_A(x) = \sqrt{\frac{1-x}{x}}\left[\sin\alpha + \sum_{j=0}^{M} b_j P_j(x) + \sum_{j=0}^{N} a_j R_j(x)\right], \tag{2.53}$$

where $F_j(x)$ is defined by (2.32), and

$$P_j(x) = -\sum_{k=0}^{n} \frac{h_k}{\pi}\left[\frac{1}{k+j+1} + x^{k+j+1}\ln\frac{1-x}{x} + \sum_{q=0}^{k+j-1}\frac{x^{k+j-q}}{q+1}\right], \tag{2.54a}$$

$$T_j(x) = -\sum_{q=0}^{N-j} h_j \left[\sum_{l=0}^{q+j-1} (1-x) x^{q+j-1-l} g_l - g_{q+j} \right], \tag{2.54b}$$

$$R_j(x) = -\frac{2e_L}{\pi} \left[\frac{1}{2j-1} + x^{j-1/2} \cosh^{-1} \sqrt{\frac{1}{1-x}} - \sum_{q=0}^{j-2} \frac{x^{j-1-q}}{2q+1} \right]$$

$$-\frac{1}{\pi} \sum_{k=0}^{m} e_k \left[\frac{1}{k+j} + x^{k+j} \ln \frac{1-x}{x} + \sum_{q=0}^{k+j-2} \frac{x^{k+j-1-q}}{q+1} \right]. \tag{2.54c}$$

The unknown coefficients a_j and b_j are determined by requiring the expressions (2.45) and (2.52) for $u_S(x)$, and respectively (2.46) and (2.53) for $u_A(x)$, to be equal at a specified number $M+1$, and respectively $N+1$, collocation points conveniently distributed along the airfoil chord (M and N are usually taken between 6 and 10). This is done by solving the following linear system of $M+N+2$ algebraic equations

$$\sum_{j=0}^{M} b_j \left[F_j(x_i) - x_i^j \sqrt{(1-x_i)x_i} \right] + \sum_{j=0}^{N} a_j T_j(x_i) = -\cos\alpha \ , \tag{2.55}$$

$$\sum_{j=0}^{M} b_j P_j(x_i) + \sum_{j=0}^{N} a_j \left[R_j(x_i) - x_i^j \right] = -\sin\alpha \ . \tag{2.56}$$

where x_i is the x-position of the collocation point and i is the number of that point along the airfoil chord (i varies from 0 to $M+N+1$).

The perturbation velocity components on the airfoil are

$$u(x) = \pm u_A(x) + u_S(x) \ , \tag{2.57a}$$

$$v(x) = V_A(x) \pm V_S(x) \ , \tag{2.57b}$$

where the upper (+) and lower (−) signs refer to the upper and lower sides, respectively, and where $V_A(x)$ and $V_S(x)$ are calculated from (2.8a,b) with the solutions (2.52), (2.53). The pressure coefficient on the airfoil can be calculated as

$$C_p = -2\left(u\cos\alpha + v\sin\alpha\right) - \left(u^2 + v^2\right) . \tag{2.58}$$

The present nonlinear solutions are validated in the following section by comparison with exact solutions for special airfoils obtained by conformal transformation and with numerical results for NACA airfoils.

2.4.2 Validation for symmetric Karman-Trefftz airfoils at incidence

In Figure 2.13 the present nonlinear solutions of the pressure coefficient distribution, $C_p(x)$, for two Karman-Trefftz airfoils are compared with the exact solutions obtained by conformal transformation. In both cases, defined by the relative thickness $t = 0.03$ and incidence $\alpha = 5°$, and respectively $t = 0.05$ and $\alpha = 10°$, the present nonlinear solutions were found in excellent agreement with the exact solutions.

The chordwise variation of the pressure difference coefficient between the two sides of the airfoil, $\Delta C_p(x)$, is presented in Figure 2.14 for a Karman-Trefftz airfoil of relative thickness $t = 0.09$ at incidences $\alpha = 2°$ and $\alpha = 5°$. The present nonlinear solutions were again found in excellent agreement with the exact solutions. By contrast, the linear solutions (also shown in the same figure) display larger differences with respect to the exact solutions.

2.4.3 Case of general cambered Karman-Trefftz airfoils at incidence

The pressure coefficient distributions, $C_p(x)$, for two general Karman-Trefftz airfoils at two angles of attack, $\alpha = 5°$ and $\alpha = 10°$, are shown in Figures 2.15 and 2.16. The relative thickness, t, and the relative camber, f, of the two airfoils are: (i) $t = 0.03$ and $f = 0.02$, and (ii) $t = 0.05$ and $f = 0.05$. A very good agreement can be noticed between the present nonlinear solutions and the exact solutions obtained by conformal transformation.

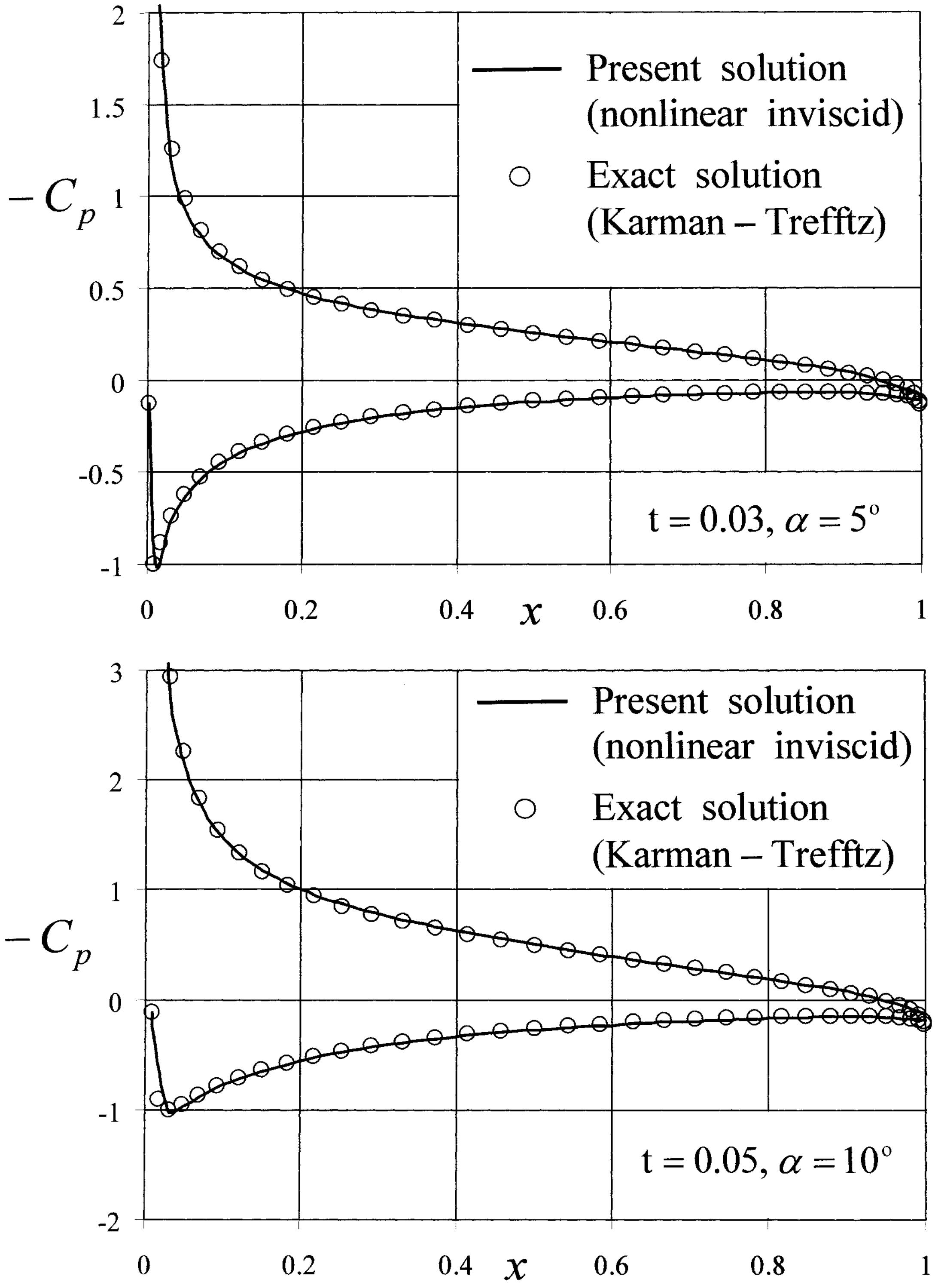

Figure 2.13 Symmetric Karman-Trefftz airfoils at incidence; present nonlinear solutions for the pressure coefficient distribution, $C_p(x)$, compared with exact solutions ($t = 0.03$, $\alpha = 5°$ and $t = 0.05$, $\alpha = 10°$).

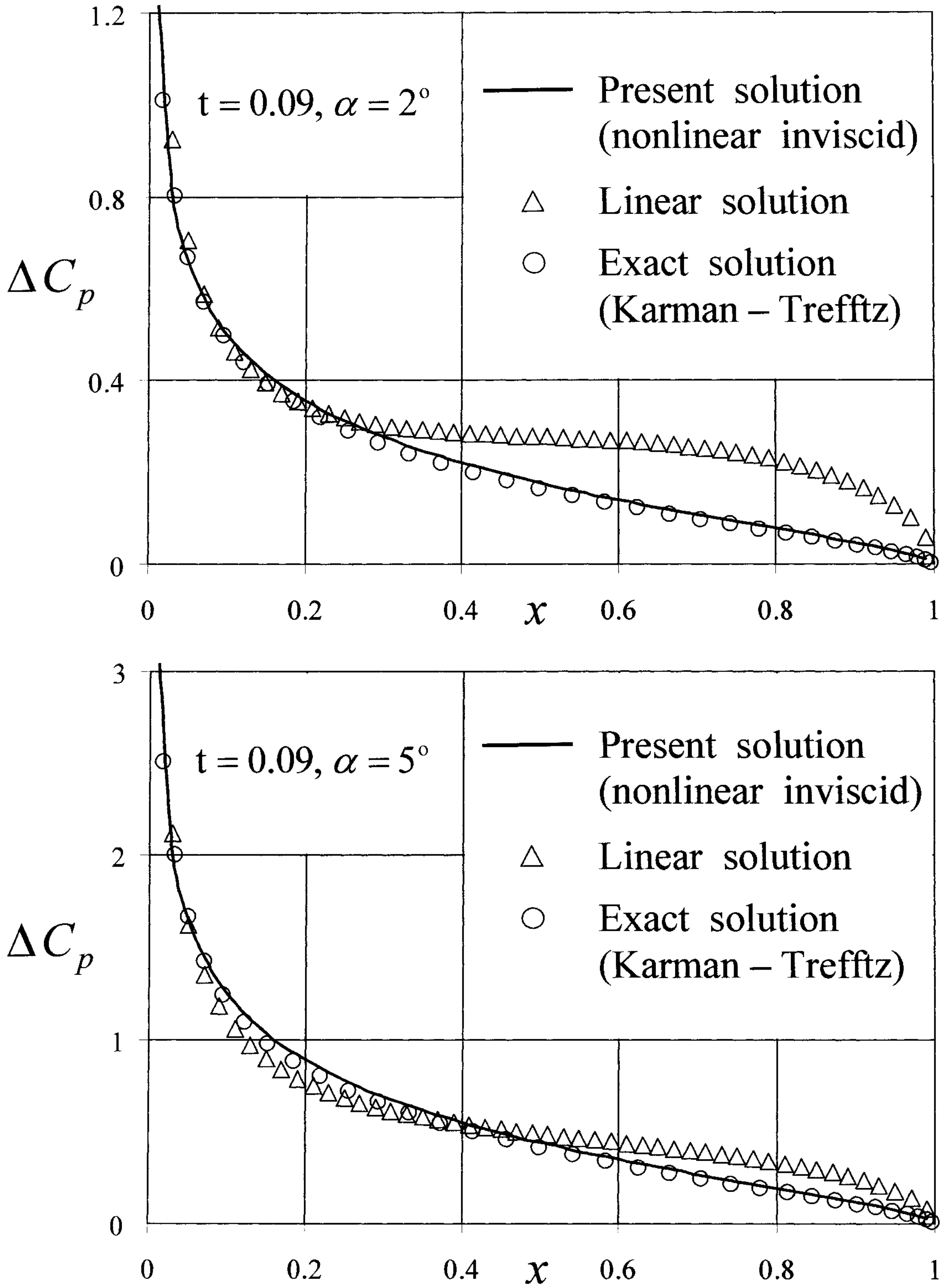

Figure 2.14 Symmetric Karman-Trefftz airfoils at incidence; present nonlinear solutions for the pressure difference coefficient, $\Delta C_p(x)$, compared with the exact solutions ($t = 0.09$, $\alpha = 2°$ and $\alpha = 5°$).

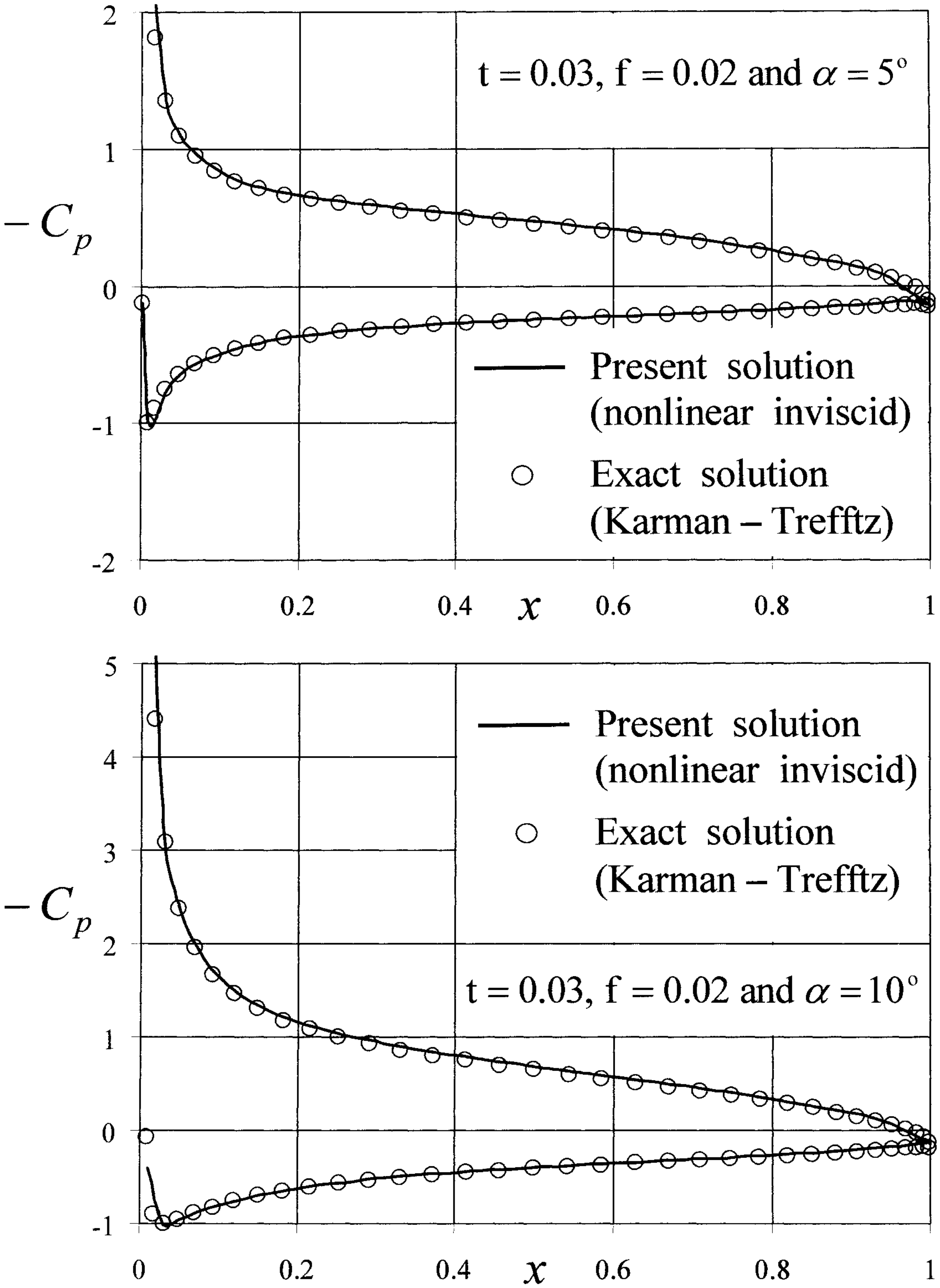

Figure 2.15 General cambered Karman-Trefftz airfoils at incidence; present nonlinear solutions compared with the exact solutions ($t = 0.03$, $f = 0.02$, $\alpha = 5°$ and $\alpha = 10°$).

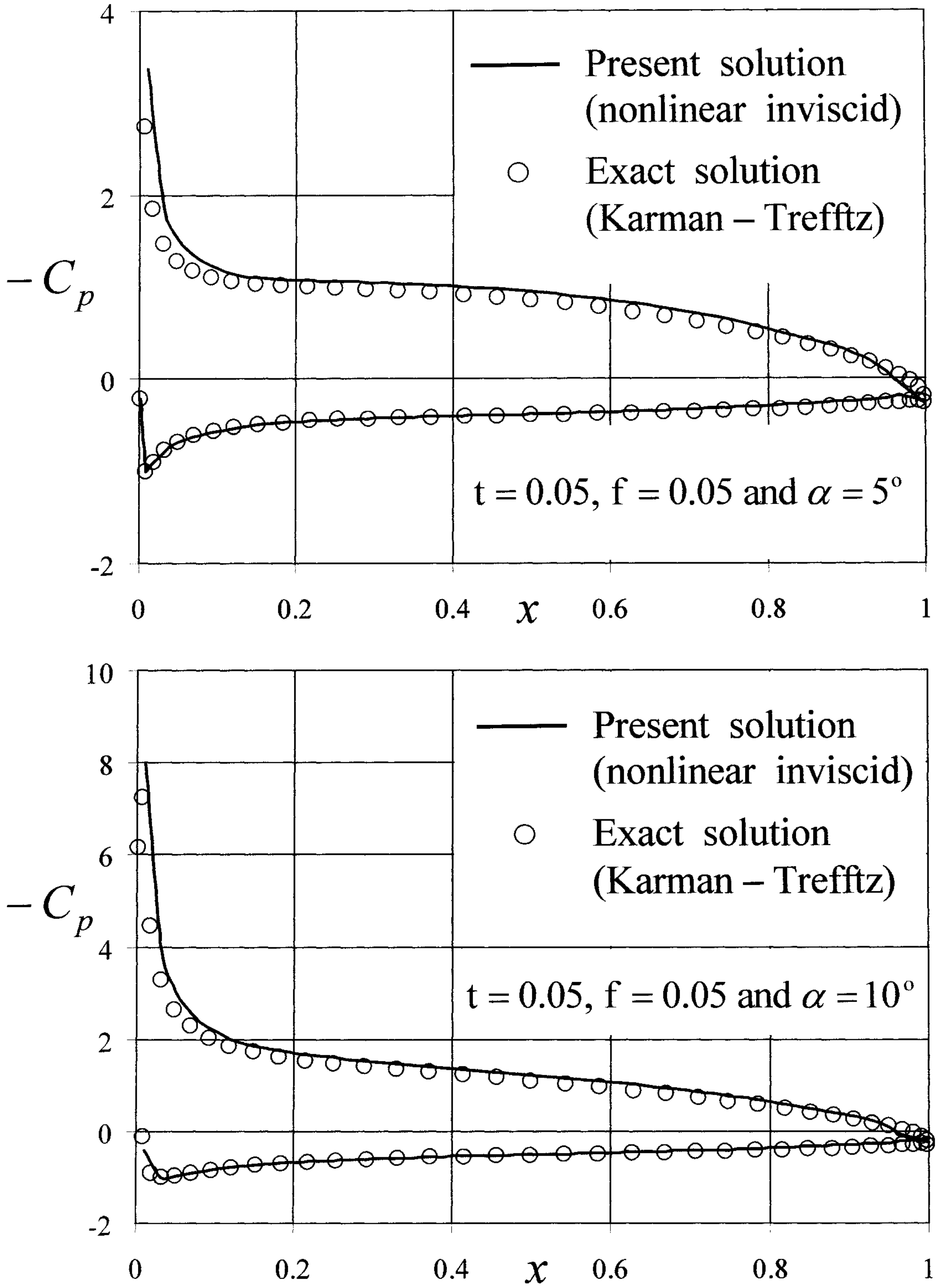

Figure 2.16 General cambered Karman-Trefftz airfoils at incidence; present nonlinear solutions compared with the exact solutions ($t = 0.05$, $f = 0.05$, $\alpha = 5^{\circ}$ and $\alpha = 10^{\circ}$).

2.4.4 Case of thin cambered airfoils at incidence

The case of thin cambered airfoils is illustrated here by a thin circular-arc airfoil represented by a thin Joukowski airfoil obtained by the conformal transformation (2.35) for $\gamma_T = 0$ and $\kappa = 2$, and with $e_0 = 0$, $r/b = \sqrt{1+f_0^2}$ and $f_0 = 2f$, where f is the relative camber of the airfoil.

The pressure coefficient distribution, $C_p(x)$, is shown in Figures 2.17a,b for two circular-arc airfoils of relative camber $f = 0.02$ and $f = 0.05$ at the angles of attack $\alpha = 10°$ and $\alpha = 5°$, respectively. The present nonlinear solutions were found to be in a very good agreement with the exact solutions obtained by conformal transformation. The accuracy of the linear solution (also shown in Figure 2.17b for the pressure coefficient on the lower side of the airfoil) is obviously not good.

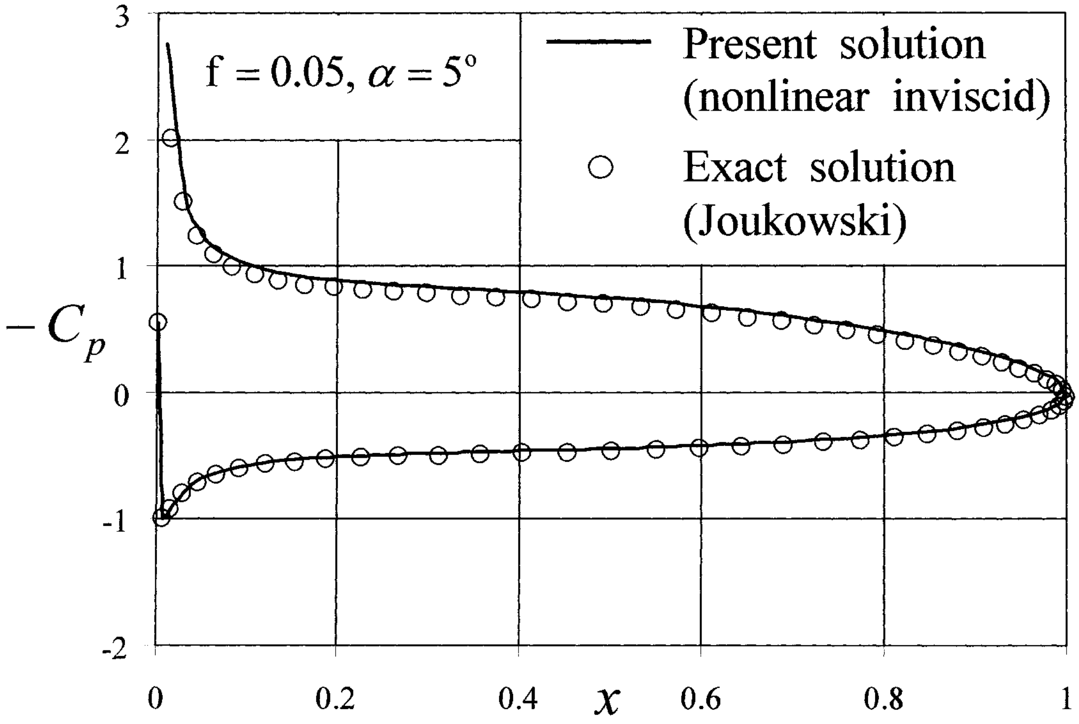

Figure 2.17a Thin cambered airfoils at incidence; present nonlinear solution for the pressure coefficient, $C_p(x)$, on a circular-arc airfoil ($f = 0.05$ at $\alpha = 5°$) compared with the exact solution.

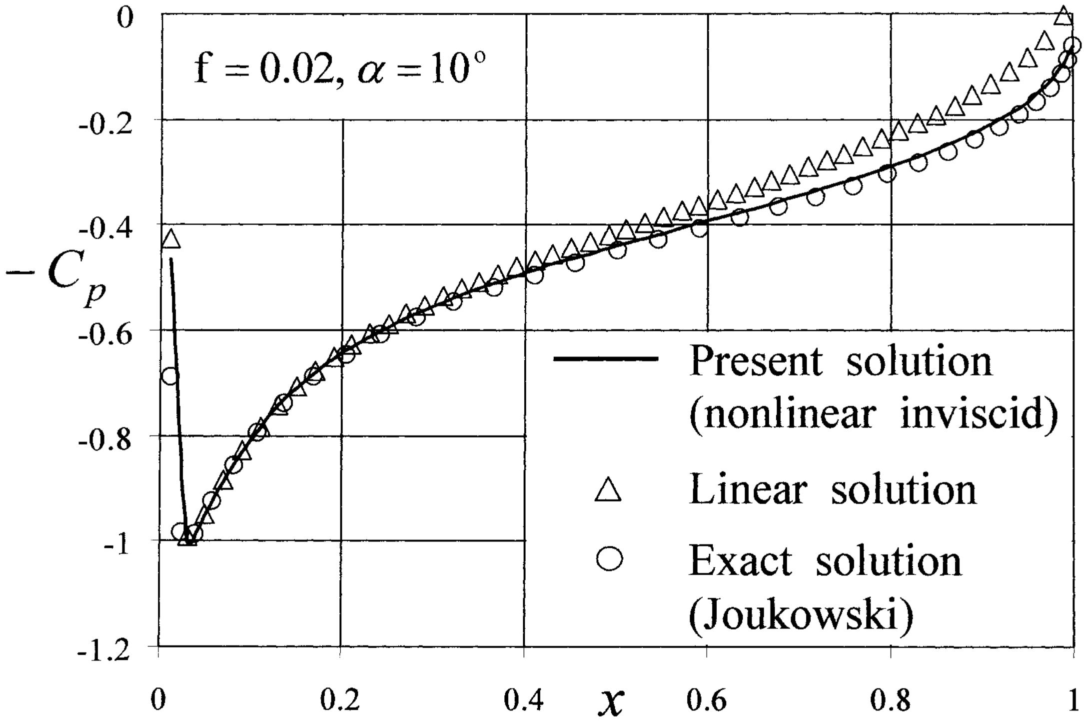

Figure 2.17b Thin cambered airfoils at incidence; present nonlinear solution for the pressure coefficient, $C_p(x)$, on the lower surface of a circular-arc airfoil (f=0.02 at $\alpha = 10°$) compared with the exact and linear solutions.

2.4.5 Extension of the nonlinear solutions for compressible flows

The present accurate solutions derived for incompressible flows can be extended for compressible flows using the Karman-Tsien compressibility correction

$$C_p = C_{p\text{in}} / \beta_{\text{KT}} \ , \qquad \beta_{\text{KT}} = \sqrt{1-M_\infty{}^2} + \frac{1}{2} C_{p\text{in}} \left(1 - \sqrt{1-M_\infty{}^2} \right) \ , \qquad (2.59)$$

where β_{KT} is the Karman-Tsien compressibility correction factor, C_p is the pressure coefficient on the airfoil at Mach number M_∞ and $C_{p\text{in}}$ is the nonlinear solution of the pressure coefficient calculated in Sections 2.3 and 2.4 for incompressible inviscid flows. The same compressibility correction will also used to extend to compressible flows the solutions derived in Section 2.5 for incompressible viscous flow.

The present nonlinear solutions extended to compressible flows for NACA 0008 and NACA 0009 airfoils at zero incidence are shown in Figure 2.18 in comparison with the numerical results obtained with the inviscid MSES code [43, 44] based on the integration of the compressible Euler equations. A good agreement was found between these results for $M_\infty = 0.3$ and $M_\infty = 0.6$ (MSES required a grid of 7740 points compared to 8 points using the present method). More validations of this compressibility correction are presented in Section 2.5 for the present viscous solutions in comparison with experimental results for NACA airfoils at Mach numbers $M_\infty = 0.3$ and $M_\infty = 0.503$.

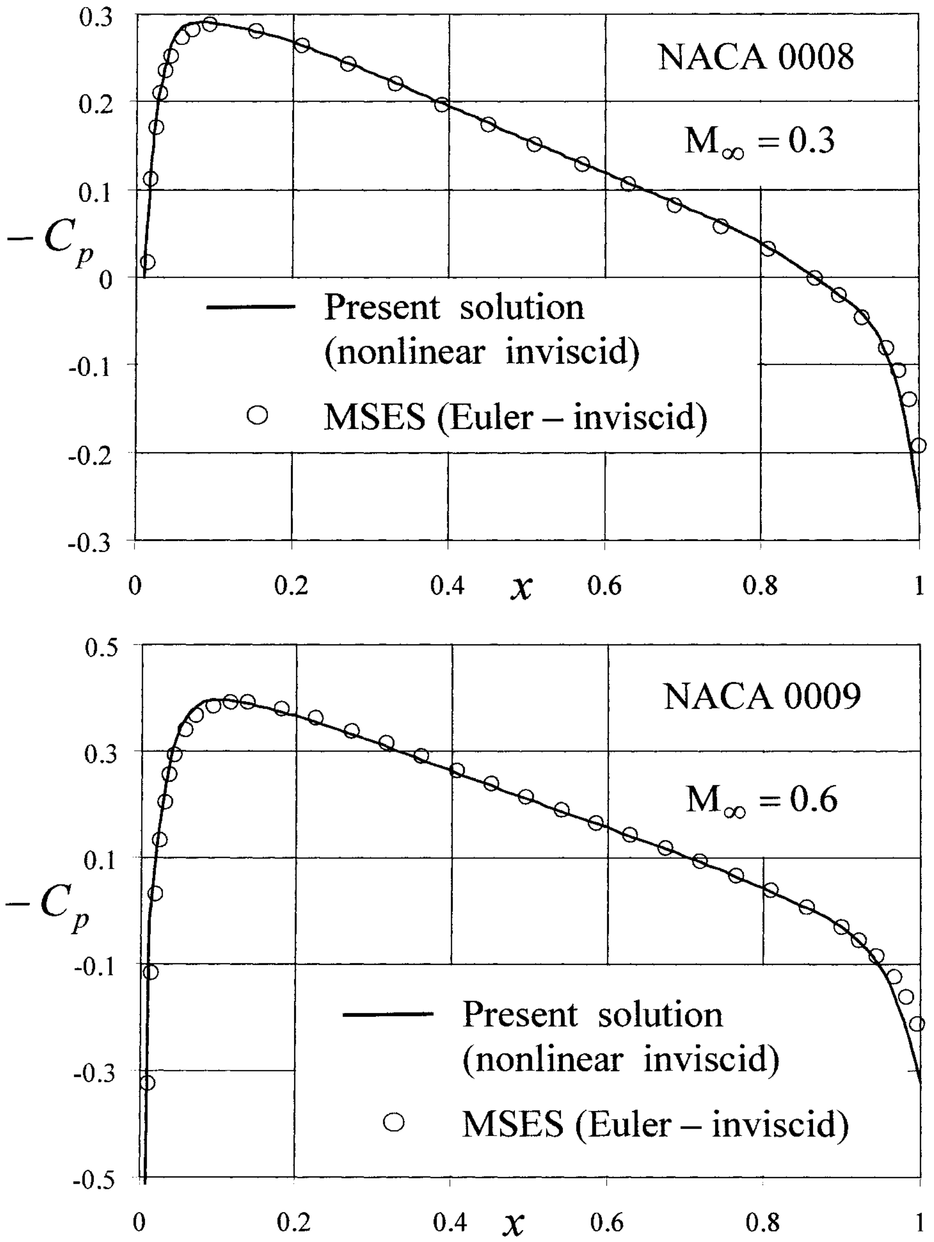

Figure 2.18 NACA 0008 and NACA 0009 airfoils in compressible flows; present nonlinear solutions for $\alpha = 0$, compared with the inviscid MSES code results.

2.5 Extension of the present method to include viscous effects

2.5.1 Velocity behavior in viscous attached flows past airfoils

The effect of viscous and boundary layer displacement effects on the velocity distribution on airfoils placed in attached viscous flows (without separation regions) is shown in Figure 2.19.

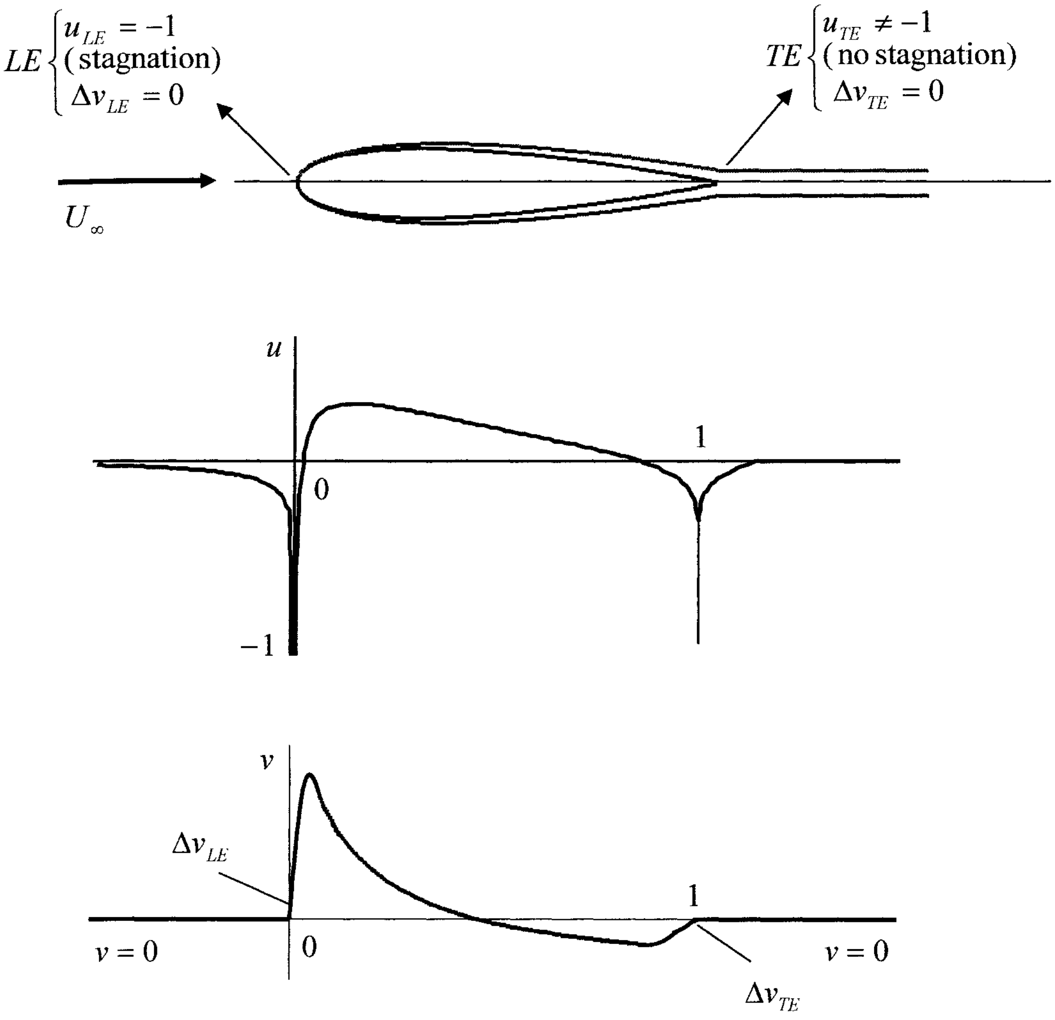

Figure 2.19 Real physical behavior of the viscous attached flows past symmetric airfoils.

In the viscous flows (without separation) past airfoils, the trailing edge is no longer a stagnation point in the symmetric flow component, as in the case of inviscid flows. The boundary layers developed on the two sides of the airfoil are continued downstream, beyond the trailing edge, by the viscous wake trailing the airfoil. As a result, the expression (2.45), which implies that both leading and trailing edges are stagnation points, has to be replaced by the expression

$$u_S(x) = -\cos\alpha + \sqrt{x} \sum_{j=0}^{M} b_j x^j \ , \tag{2.60}$$

which implies that only the leading edge is a stagnation point in the symmetric flow component.

The viscous effects in the real flow past airfoils are taken into account by many authors [23, 43, 44] by considering the development of the boundary layer along the airfoil contour and the wake in the numerical analysis of the inviscid flows based on Euler or boundary element (panel) methods.

As shown by Cebeci [23], a simple and efficient approach to consider these viscous effects is to modify the geometrical shape of the airfoil (or wing) by adding the displacement thickness of the boundary layer, $\delta(x)$. In the usual case of airfoils (not very thick or excessively cambered), one can consider the same boundary layer development as that on a flat plate. For turbulent flows, the boundary layer displacement thickness can be expressed in the form (see Schlichting [166], Schlichting and Gersten [167] and White [204])

$$\delta(x) = \sigma\, x^{(n-1)/n} \ , \tag{2.61}$$

where $n = 5$ and $\sigma = 0.04625 / \mathrm{Re}^{1/n}$ (for Re>10^5).

Thus, in the case of the flow without separation past an airfoil, the geometrical equations (2.1) and (2.2) have to be modified by adding the displacement thickness $\delta(x)$ of the boundary layer in the form

$$y = g_{\pm}(x) = h(x) \pm [e(x) + \delta(x)] \ . \tag{2.62}$$

The effect of the boundary layer on the airfoil can be thus introduced in the expression of $V_S(x)$, defining the symmetric flow component, in the form

$$\mathrm{V_S}(x) = [\cos\alpha + u_S(x)]\,[e'(x) + \delta'(x)] + u_A(x)\,h'(x) \ . \tag{2.63}$$

For convenience of the analytical derivations, $\delta'(x) = \sigma / x^{1/5}$ is replaced in the following derivations by an equivalent modified polynomial representation similar to (2.27) in the form

$$\delta'(x)=\frac{\delta_L}{\sqrt{x}}+\delta_0+\delta_1 x \ , \tag{2.64}$$

where $\delta_L=0.2003767\ \bar{\sigma}$, $\delta_0=0.9310225\ \bar{\sigma}$, $\delta_1=-0.1313991\bar{\sigma}$ and $\bar{\sigma}=4\sigma/5$.

2.5.2 General analytical solution including viscous effects

The analytical solutions of the velocity and pressure distributions including viscous effects for the general case of thick cambered airfoils at incidence can be determined in a similar way as that presented in Section 2.4.1. However, the function $V_S(x)$, from the boundary condition (2.7b) for the symmetric flow component, is defined in this case by equation (2.63) instead of (2.8b). Also, the expression assumed for $u_S(x)$ in the functions $V_A(x)$ and $V_S(x)$ is in this case (2.60) instead of (2.45), since in the viscous flow the trailing edge is no longer a stagnation point for the symmetric flow component. The expression for $V_A(x)$ and the assumed expression for $u_A(x)$ remain the same as in the inviscid flow case, that is (2.8a) and (2.46).

The solution for the anti-symmetric flow component, based on the resulting expression of $V_A(x)$ is derived using the same velocity singularity solution (2.15). However, the velocity singularity solution (2.22) for the symmetric flow component is not valid anymore for the viscous case, since it assumes that $v_S(x)$ suddenly changes at the trailing edge from $V_S(1)$ to zero. In the viscous flow case, because the boundary layer is continued behind the trailing edge by the viscous wake, one can consider that $v_S(x)$ remains practically unchanged at the trailing edge.

For this case, the complex symmetric perturbation velocity is expressed as

$$w_S(z)=\frac{1}{\pi}V_S(0)\ln(-z)+\frac{1}{\pi}\int_0^1 V_S'(s)\ln(s-z)ds+\frac{1}{\pi}\int_1^{1+\varepsilon} V_S'(s)\ln(s-z)ds \ , \tag{2.65}$$

where ε is a small nondimensional distance behind the trailing edge beyond which $v_S(x)$ is assumed constant, $(1/\pi)\ln(s-z)$ represents the singular contribution of the ridge situated at $x=s$, while $(1/\pi)\ln(-z)$ represent the contribution of the leading edge, which in this case have the same singular behavior as ridges.

By integrating equation (2.65) by parts, one obtains

$$w_S(z)=\frac{1}{\pi}V_S(0)\ln(-z)+\frac{1}{\pi}\left\{V_S(s)\ln(s-z)\Big|_{s=0}^{s=1}-\int_0^1 V_S(s)\frac{ds}{(s-z)}\right\}$$

$$+\frac{1}{\pi}\left\{V_S(s)\ln(s-z)\Big|_{s=1}^{s=1+\varepsilon}-\int_1^{1+\varepsilon} V_S(s)\frac{ds}{(s-z)}\right\}, \tag{2.66}$$

As a result, the velocity singularity solution in complex form is

$$w_S(z)=-\frac{1}{\pi}\int_0^1 V_S(s)\frac{ds}{s-z}-\frac{1}{\pi}\frac{V_S(1)}{\varepsilon}\left[1+\varepsilon-z\right]\ln\frac{1+\varepsilon-z}{1-z}\ , \tag{2.67}$$

The solution for $u_S(x)$ is obtained by taking the real part of the expression resulting after integration. By taking into account (2.60), the expression (2.63) for $V_S(x)$ becomes in this case

$$V_S(x)=\sqrt{x}\sum_{j=0}^{M}b_j\,x^j\left[\frac{e_L+\delta_L}{\sqrt{x}}+\sum_{k=0}^{m}(e_k+\delta_k)x^k\right]+\sqrt{\frac{1-x}{x}}\sum_{k=0}^{n}h_kx^k\sum_{j=0}^{N}a_j\,x^j\ . \tag{2.68}$$

Similarly, the expression (2.8a) for $V_A(x)$ for this case becomes

$$V_A(x)=-\sin\alpha+\sqrt{x}\sum_{j=0}^{M}b_j\,x^j\sum_{k=0}^{n}h_k\,x^k+\sqrt{\frac{1-x}{x}}\sum_{j=0}^{N}a_j\,x^j\left[\frac{e_L+\delta_L}{\sqrt{x}}+\sum_{k=0}^{m}(e_k+\delta_k)x^k\right], \tag{2.69}$$

The resulting expressions of $V_S(x)$ and $V_A(x)$ are then introduced in equations (2.67) and (2.15), respectively.

One obtains thus, after performing the integrations of equations (2.67) and (2.15), the solutions for the symmetric and anti-symmetric perturbation velocity components

$$u_S(x)=\sum_{j=0}^{M}b_j\breve{F}_j(x)+\sum_{j=0}^{N}a_jT_j(x), \tag{2.70}$$

$$u_A(x)=\sqrt{\frac{1-x}{x}}\left[\sin\alpha+\sum_{j=0}^{M}b_j\breve{P}_j(x)+\sum_{j=0}^{N}a_jR_j(x)\right]. \tag{2.71}$$

where $T_j(x)$ and $R_j(x)$ are defined by (2.54b,c) with e_L and e_k now replaced by $e_L+\delta_L$ and $e_k+\delta_k$, respectively. While,

$$
\begin{aligned}
\breve{F}_j(x) = &-\frac{e_L+\delta_L}{\pi}\left[x^j \ln\frac{1-x}{x}+\sum_{q=0}^{j-1}\frac{x^q}{j-q}-1+\frac{1+\varepsilon-x}{\varepsilon}\ln\frac{1+\varepsilon-x}{1-x}\right] \\
&-\frac{1}{\pi}\sum_{k=0}^{m}\left(e_k+\delta_k\right)\left[2x^{k+j+1/2}\cosh^{-1}\sqrt{\frac{1}{1-x}}\right. \\
&\left.-\sum_{q=0}^{k+j}\frac{x^q}{k+j-q+1/2}-1+\frac{1+\varepsilon-x}{\varepsilon}\ln\frac{1+\varepsilon-x}{1-x}\right] ,
\end{aligned}
\tag{2.72a}
$$

$$
\breve{P}_j(x) = -\sum_{k=0}^{n}\frac{2h_k}{\pi}\left[L_{k+j}+\frac{x^{k+j+1}}{\sqrt{1-x}}\sinh^{-1}\sqrt{\frac{1-x}{x}}+\sum_{q=0}^{k+j-1}x^{k+j-q}L_q\right] .
\tag{2.72b}
$$

where $L_j = \dfrac{2j}{2j+1}L_{j-1}$, $L_0 = 1$ is derived in detail in Appendix A.

The unknown coefficients a_j and b_j are determined by requiring the expressions (2.70) and (2.60) for $u_S(x)$, and respectively (2.71) and (2.46) for $u_A(x)$, to be equal at a specified number $M+1$, and respectively $N+1$, collocation points conveniently distributed along the airfoil chord (*M* and *N* are usually taken between 6 and 10). This is done by solving the following linear system of $M+N+2$ algebraic equations

$$
\sum_{j=0}^{M} b_j\left[\breve{F}_j(x_i)-x_i^j\sqrt{x_i}\right]+\sum_{j=0}^{N} a_j T_j(x_i) = -\cos\alpha \ ,
\tag{2.73}
$$

$$
\sum_{j=0}^{M} b_j \breve{P}_j(x_i)+\sum_{j=0}^{N} a_j\left[R_j(x_i)-x_i^j\right] = -\sin\alpha \ .
\tag{2.74}
$$

where x_i is the *x*-position of the collocation point and i is the number of that point along the airfoil chord (i varies from 0 to $M+N+1$).

The present analytical solutions including viscous effects are validated in the following section by comparison with numerical and experimental results for NACA airfoils.

2.5.3 Method validation for viscous attached flows past NACA airfoils

The present nonlinear solution including viscous effects, extended for compressible flows as shown in Section 2.4.5, is validated in Figures 2.20-2.22 in comparison with numerical results obtained with the viscous MSES code developed by Drela and Giles [43, 44] (integration of Euler equations coupled with boundary layer analysis) and with experimental results [186] for NACA 0008, 0009 and 0012 airfoils at Mach numbers $M_\infty = 0.3$ and $M_\infty = 0.503$.

The present viscous solutions for NACA 0008 and NACA 0009 at zero incidence are compared in Figure 2.20 with the numerical results obtained with the viscous MSES code for $M_\infty = 0.3$ at the Reynolds number $\mathrm{Re} = 1.85 \times 10^6$. A very good agreement can be noticed between the two sets of results.

Figures 2.21 and 2.22 show the pressure coefficient distribution on the NACA 0012 airfoil for various angles of attack, Mach numbers and Reynolds numbers. A very good agreement can be seen between the present second-order accurate solutions including viscous effects and the experimental results.

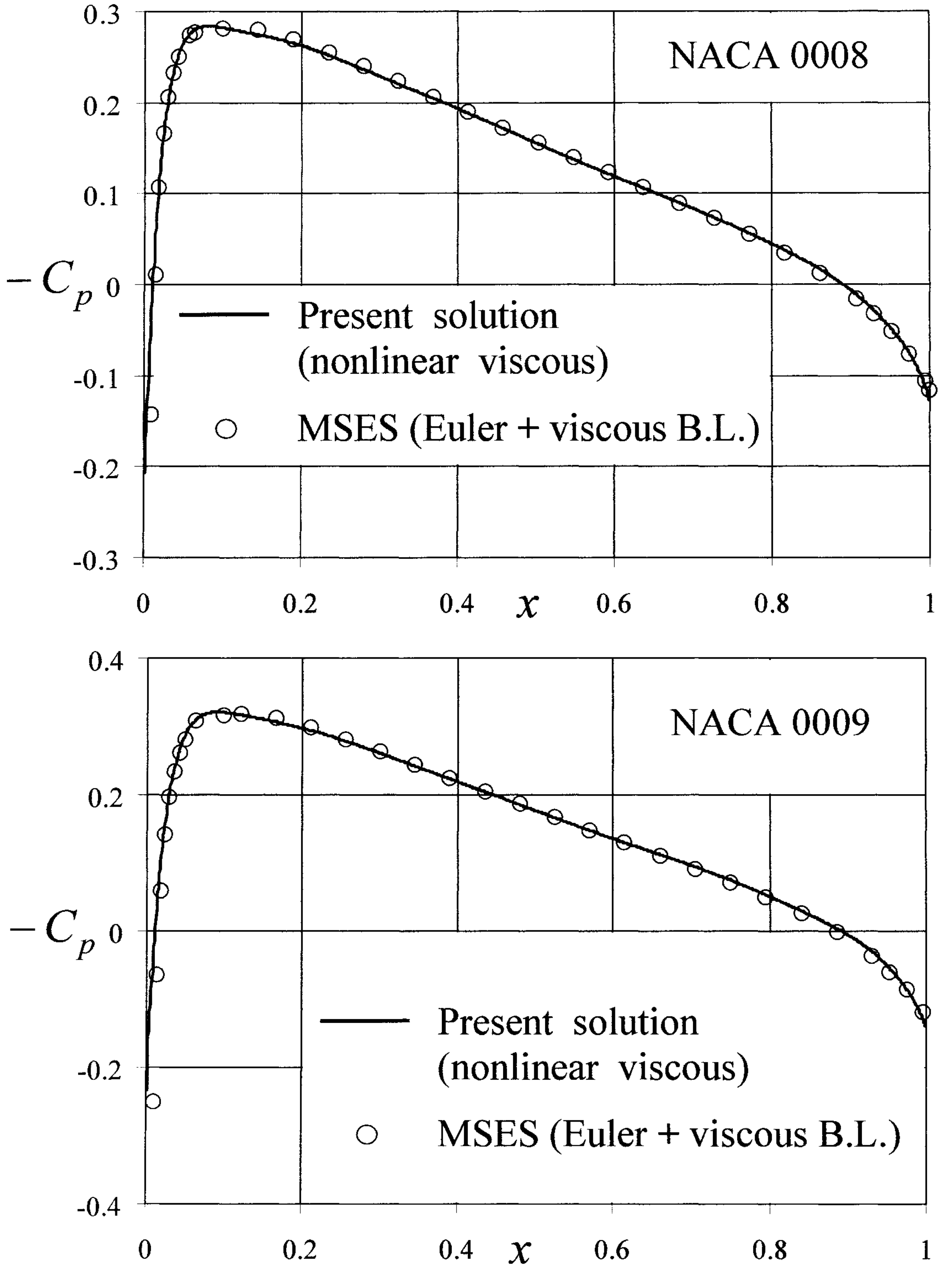

Figure 2.20 NACA 0008 and NACA 0009 airfoils in compressible viscous flows; present viscous solutions compared with the viscous MSES code results for $\alpha = 0$, $M_\infty = 0.3$ and $\mathrm{Re} = 1.85 \times 10^6$.

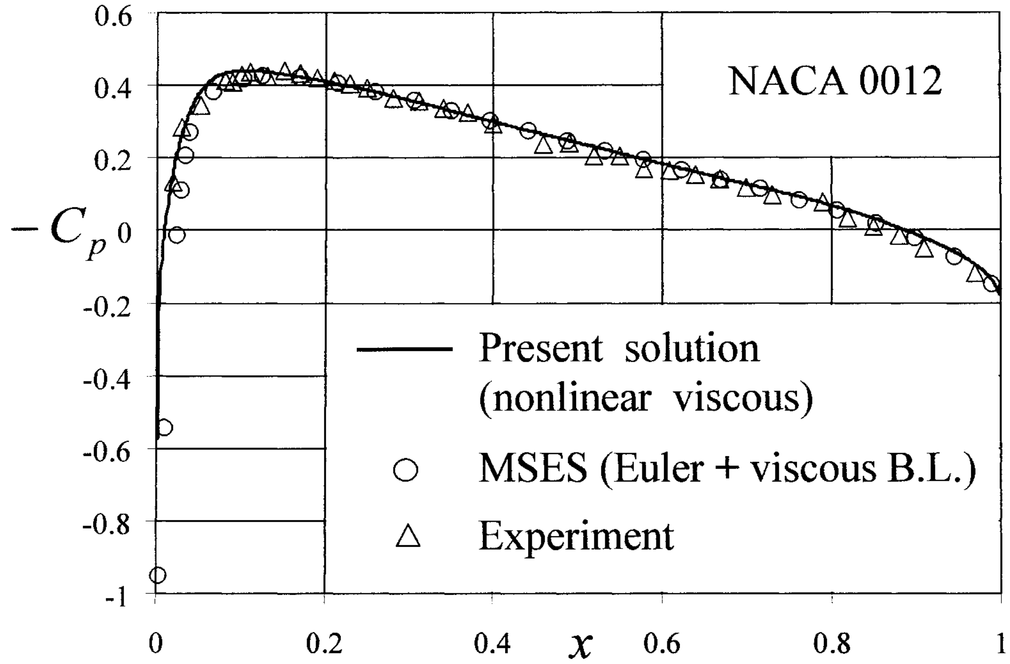

a) $\alpha = 0$, $M_\infty = 0.3$ and $\mathrm{Re} = 1.85 \times 10^6$

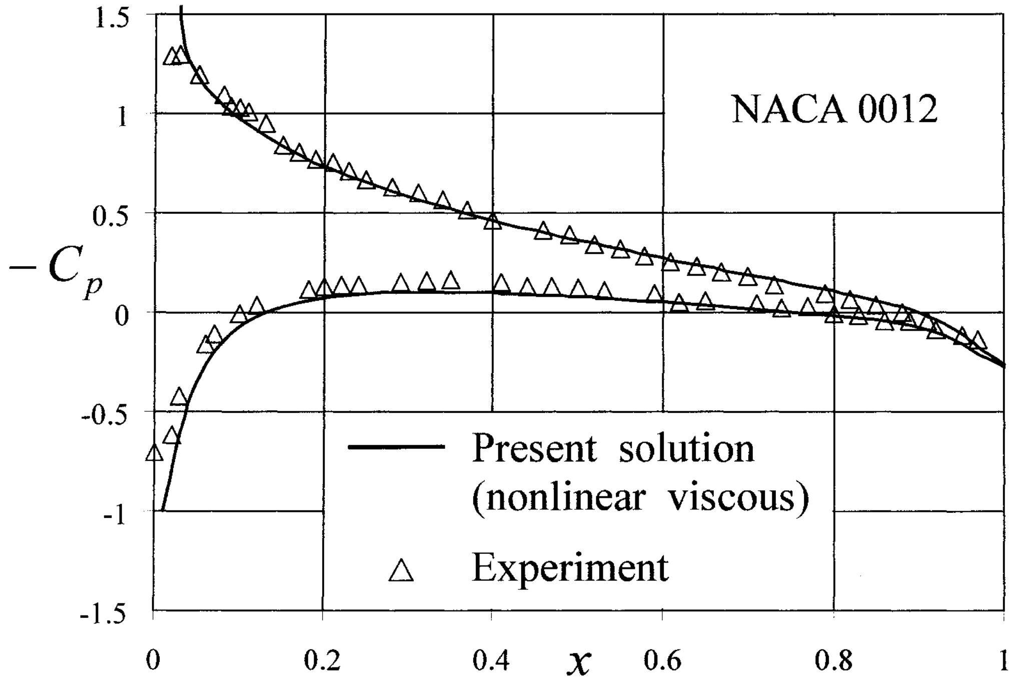

b) $\alpha = 4.04^o$, $M_\infty = 0.3$ and $\mathrm{Re} = 1.86 \times 10^6$

Figure 2.21 NACA 0012 airfoil in compressible viscous flows; present nonlinear solutions compared with the viscous MSES code and with experimental results [186].

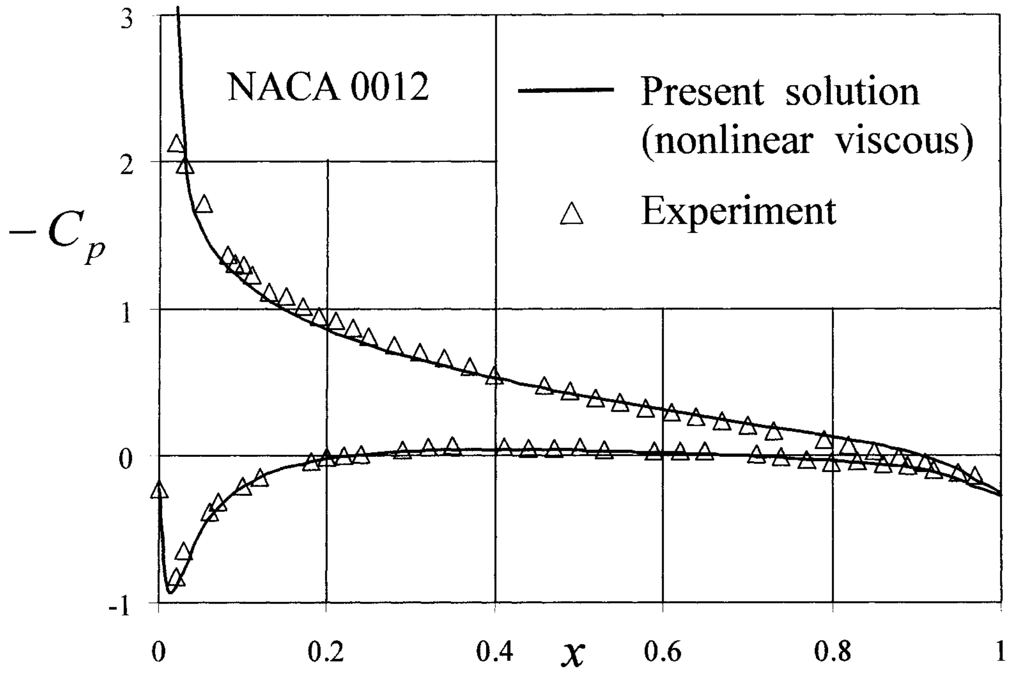

a) $\alpha = 6.05^o$, $M_\infty = 0.503$ and $\mathrm{Re} = 2.93 \times 10^6$

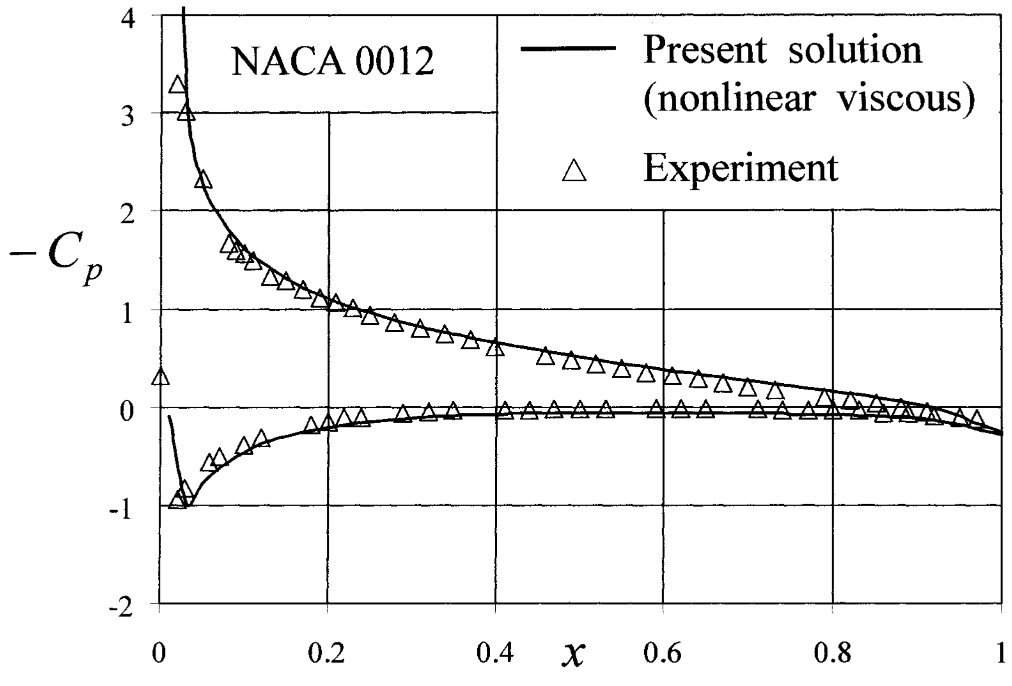

b) $\alpha = 8.02^o$, $M_\infty = 0.503$ and $\mathrm{Re} = 2.85 \times 10^6$

Figure 2.22 NACA 0012 airfoil in compressible viscous flows; present nonlinear solutions compared with experimental results [186].

Chapter 3

Unsteady Flow Solutions for Oscillating Flexible Airfoils

3.1 Previous classical method of solution (Theodorsen's theory)

For the unsteady flow past an oscillating rigid plate, Theodorsen [184] and Theodorsen and Garrick [185] have developed a method to determine the aerodynamic forces on an oscillating airfoil. The theory was based on the potential flow and the Kutta condition. In this classical method, the perturbation velocity potential around the oscillating airfoil is decomposed into two parts: (i) the perturbation potential corresponding to the motion without circulation around the airfoil, and, (ii) the potential corresponding to the motion with circulation due to the shedding vortices.

By adding the potential corresponding to the motion without circulation around the flat plate, due to the normal velocity jump $W(x_1,t)$ on the plate at $x = x_1$, and the potential corresponding to the pure circulatory motion, produced by the shedding free vortices in the wake of the airfoil, one obtains the total perturbation velocity potential for the complete motion around the oscillating plate or airfoil. The resulting equation of the pressure difference across the airfoil in integral form is given by,

$$\begin{aligned}\Delta p(x,t) = &\frac{2}{\pi}\rho U_\infty \sqrt{\frac{1-x}{1+x}} \int_{-1}^{1} W(x_1,t)\sqrt{\frac{1+x_1}{1-x_1}}\,\frac{dx_1}{x-x_1} \\ &+ \frac{1}{\pi}\rho b \int_{-1}^{1} \frac{\partial W(x_1,t)}{\partial t} L(x,x_1)\,dx_1 \qquad , \\ &+ \frac{2}{\pi}\rho U_\infty [1-C(k)] \sqrt{\frac{1-x}{1+x}} \int_{-1}^{1} W(x_1,t)\sqrt{\frac{1+x_1}{1-x_1}}\,dx_1\end{aligned} \tag{3.1}$$

where b is half the chord and the reduced frequency k is given by,

$$k = \frac{\omega b}{U_\infty} \ . \tag{3.2}$$

while Theodorsen's function $C(k)$, is defined as,

$$C(k)=\frac{H_1^{(2)}(k)}{H_1^{(2)}(k)+iH_0^{(2)}(k)}=F(k)+iG(k)\ , \tag{3.3}$$

where $H_0^{(2)}(k)$, $H_1^{(2)}(k)$ represent the Hankel functions of second kind of orders zero and one [137, 200]. See Appendix B for details.

The function $L(x,x_1)$ is obtained as,

$$L(x,x_1)=\ln\frac{(x-x_1)^2+\left(\sqrt{1-x^2}-\sqrt{1-x_1^2}\right)^2}{(x-x_1)^2+\left(\sqrt{1-x^2}+\sqrt{1-x_1^2}\right)^2}\ . \tag{3.4}$$

Theodorsen's results are presented for the following oscillatory motions of the airfoil, as shown in Figure 3.1.

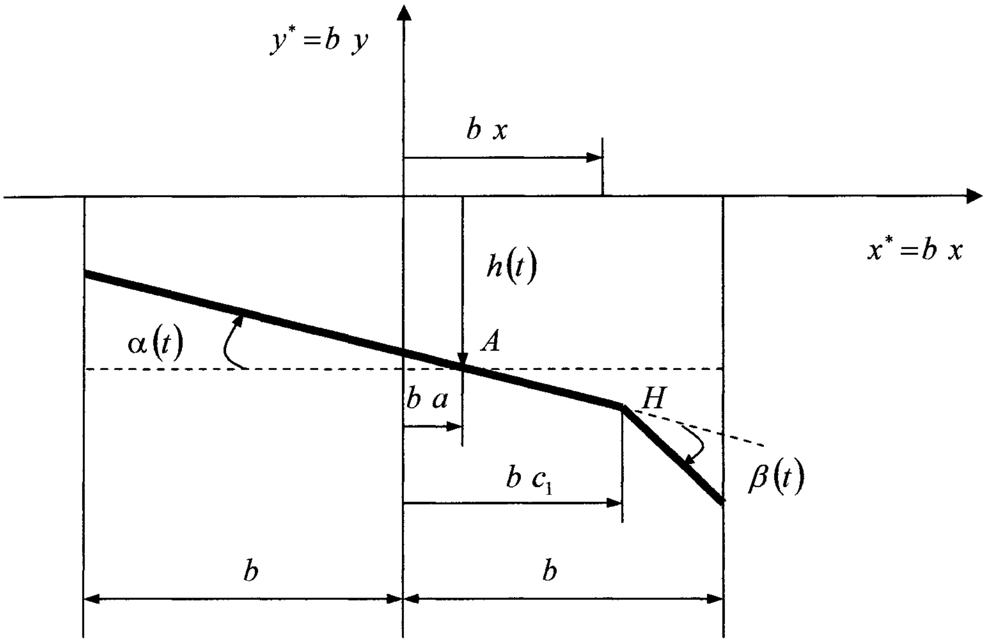

Figure 3.1 Flat plate geometry as presented in Theodorsen's solution.

The harmonic oscillations of the airfoil are denoted as,

$$h(t)=\hat{h}e^{i\omega t}\ , \tag{3.5}$$

$$\alpha(t)=\hat{\alpha}\,e^{i\omega t}\ , \tag{3.6}$$

$$\beta(t)=\hat{\beta}\,e^{i\omega t}\ . \tag{3.7}$$

where $h(t)$, $\alpha(t)$ and $\beta(t)$ represent harmonic plunging, pitching and aileron rotation, respectively.

The boundary conditions on the airfoil-aileron combination are defined as,

$$W(x,t) = -\alpha U_{\infty} - \dot{h} - b(x-a)\dot{\alpha} \qquad \text{for } x \in (-1, c_1)\,, \tag{3.8}$$

$$W(x,t) = -\alpha U_{\infty} - \dot{h} - b(x-a)\dot{\alpha} - b(x-c_1)\dot{\beta} - \beta U_{\infty} \qquad \text{for } x \in (c_1, 1)\,. \tag{3.9}$$

The lift force is given by,

$$L = \pi \rho b^3 \omega^2 \left\{ P_{\omega} \frac{h}{b} + \left[P_{\varphi} - \left(\frac{1}{2} + a \right) P_{\omega} \right] \alpha + P_{\beta}\, \beta \right\}, \tag{3.10}$$

The pitching moment equation is,

$$M_A = \pi \rho b^4 \omega^2 \left\{ \left[M_{\omega} - \left(\frac{1}{2} + a \right) P_{\omega} \right] \frac{h}{b} + \left[M_{\varphi} - \left(\frac{1}{2} + a \right)\left(P_{\varphi} + M_{\omega} \right) + \left(\frac{1}{2} + a \right)^2 P_{\omega} \right] \alpha \right.$$

$$\left. + \left[M_{\beta} - \left(\frac{1}{2} + a \right) P_{\beta} \right] \beta \right\}, \tag{3.11}$$

The hinge moment equation is given by,

$$M_H = \pi \rho b^4 \omega^2 \left\{ T_{\omega} \frac{h}{b} + \left[T_{\varphi} - \left(\frac{1}{2} + a \right) T_{\omega} \right] \alpha + T_{\beta}\, \beta \right\}. \tag{3.12}$$

where a in (3.8)-(3.12) is the point about which the airfoil is rotating. A list of the terms that appear in the above formulas is given in Appendix B.

Theodorsen's classical solutions are restricted to the special cases of oscillatory translation and rotation of an airfoil. These formulas for the aerodynamic forces are complicated and are obtained only for airfoils oscillating as rigid bodies without considering the flexural oscillations.

In the following sections, a new analytical method of solution for the analysis of the unsteady flow past rigid and flexible airfoils and ailerons executing various harmonic motions is developed and validated.

3.2 Method of solution for unsteady flows past oscillating airfoils

Consider a thin flexible airfoil of chord c executing harmonic oscillations about its mean position situated along the x-axis, as shown in Figure 3.2.

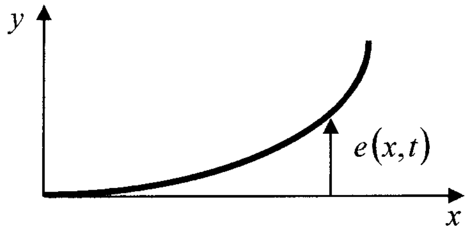

Figure 3.2 Thin flexible airfoil with a boundary condition $e(x,t)$.

The harmonic oscillations executed by the airfoil are defined by the equation

$$y = e(x,t) = \hat{e}(x)\, e^{i\omega t} \quad , \qquad e^{i\omega t} = \cos\omega t + i\sin\omega t \ . \tag{3.13}$$

where x and y represent the nondimensional Cartesian coordinates with respect to the chord c, with the origin placed at the airfoil leading edge in its mean position, t is the time, ω is the radian frequency of oscillations, and $\hat{e}(x)$ defines the modal amplitude of oscillations in flexure or as a rigid plate. In the complex form convention used to define the oscillations, the reduced quantities marked by a hat, ^, are complex numbers.

The oscillating airfoil is placed in an undisturbed and incompressible uniform flow of velocity U_∞ parallel to the x-axis, and the unsteady perturbation velocity components generated by the airfoil oscillations are denoted by $u(x,y,t)$ and $v(x,y,t)$.

The equation of the body surface $f(x,y,t)$ is hence

$$f(x,y,t) = y - e(x,t) = 0 \ , \tag{3.14}$$

The boundary condition on the surface of the airfoil is defined by

$$\frac{\partial f}{\partial t} + \left[(U_\infty + u)\mathbf{i} + \mathbf{j}v\right]\cdot\nabla f = 0 \ , \tag{3.15}$$

where u and v are the perturbation velocities in the x and y directions, respectively. By performing the derivatives and inserting them into the boundary equation (3.15), one obtains the perturbation velocity v on the surface in terms of $e(x,t)$,

$$v = \frac{\partial e}{\partial t} + (U_\infty + u)\frac{\partial e}{\partial x} \ , \tag{3.16}$$

$$v = \left[i\omega\,\hat{e}(x) + (U_\infty + u)\frac{\partial \hat{e}}{\partial x} \right] e^{i\omega t} \; . \tag{3.17}$$

Thus, the boundary condition on the oscillating airfoil can be expressed as

$$v(x,0,t) = \hat{V}(x) e^{i\omega t} \; , \tag{3.18a}$$

where,

$$\hat{V}(x) = \left[i\omega\,\hat{e}(x) + (U_\infty + u)\frac{\partial \hat{e}}{\partial x} \right] \; , \tag{3.18b}$$

In the small perturbation assumption u/U_∞ is smaller than unity and hence can be neglected in the above equations.

In view of the form of this boundary condition, one can introduce the reduced perturbation velocity components

$$\hat{u}(x,y) = u(x,y,t) e^{-i\omega t} \; , \tag{3.19a}$$

and

$$\hat{v}(x,y) = v(x,y,t) e^{-i\omega t} \; . \tag{3.19b}$$

Since in incompressible flows the velocity components are harmonic functions, satisfying the Laplace equation, one can introduce the complex conjugate reduced velocity $\hat{w}(z)$ expressed as

$$\hat{w}(z) = \hat{u}(x,y) - j\,\hat{v}(x,y) \, , \qquad z = x + j\,y \; , \tag{3.20}$$

where $j = \sqrt{-1}$, and thus the boundary condition (3.18) on the oscillating airfoil can be expressed in the complex form

$$\mathrm{IMAG}_j \left\{ \hat{w}(z) \right\}_{z=x} = -\hat{V}(x) \;\; \text{for} \;\; 0 < z = x < 1 \; , \tag{3.21}$$

where the subscript j indicates an imaginary part taken with respect to the complex variable $z = x + j\,y$ (not with respect to i from the complex representation of the oscillatory motion).

The elementary circulation along an infinitesimal control volume placed around an airfoil portion of length $c\,dx$ is $d\Gamma = 2u(x,0,t)\,c\,dx$, which leads to the distributed circulation on the airfoil

$$\gamma(x,t) = \frac{d\Gamma}{c\,dx} = 2\;\hat{u}(x,0) e^{i\omega t} \; . \tag{3.22}$$

By integrating this relation over the chord, one obtains the unsteady circulation around the airfoil

$$\Gamma_C(t) = 2\int_0^1 u(x,0,t)\; c\,dx = 2e^{i\omega t}\int_0^1 \hat{u}(x,0)\; c\,dx\,, \tag{3.23}$$

and hence the reduced circulation around the airfoil $\hat{\Gamma}_C$ can be expressed in the complex form

$$\hat{\Gamma}_C = \mathrm{REAL}_j\left\{2\int_0^1 \hat{w}(z)\; c\,dz\right\}, \qquad \hat{\Gamma}_C = \Gamma_C(t)e^{-i\omega t}\,. \tag{3.24}$$

Since the circulation around the airfoil varies in time, at each instant in time an elementary free vortex is shed at the trailing edge ($x = 1$) through a complex process involving viscous effects, as shown in Figure 3.3.

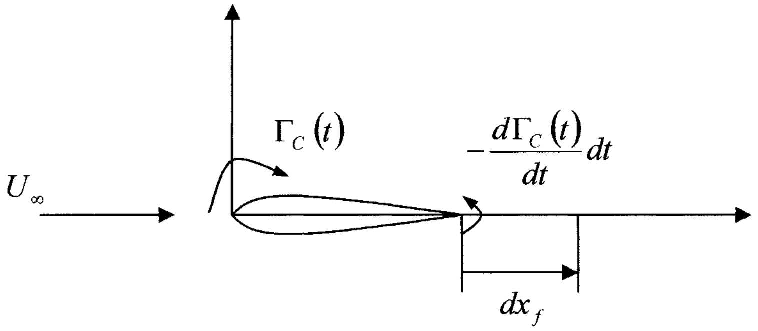

Figure 3.3 Free vortices shedding at the trailing edge of the airfoil.

The intensity of such a free vortex shed at the trailing edge, $d\Gamma_f(1,t)$, can be determined from Kelvin' s circulation theorem for a material contour K which includes the airfoil, $d\Gamma_K/dt = 0$, as

$$d\Gamma_f(1,t) = -\left[\frac{d\Gamma_C}{dt}\right]dt = -i\omega\hat{\Gamma}_C\, e^{i\omega t}\,dt\ . \tag{3.25}$$

These shedding free vortices move downstream with the fluid flow velocity ($c\,dx = U_\infty\,dt$), and their distributed vortex intensity just behind the trailing edge is

$$\gamma_f(1,t) = \frac{d\Gamma_f(1,t)}{c\,dx} = -\left(\frac{i\omega}{U_\infty}\right)\hat{\Gamma}_C\, e^{i\omega t}\ . \tag{3.26}$$

The intensity of the elementary shedding vortices remains constant in time while they are moving downstream with the fluid velocity, according to Helmholtz' circulation theorem [22, 98, 188]. Such a shedding vortex situated at time t in the airfoil wake at the location $x=\sigma$ has been generated at the trailing edge at a previous time $t-\Delta t$, where the time lag $\Delta t = c(\sigma-1)/U_\infty$ represents the time needed by this vortex to travel from the trailing edge to its present location, as shown in Figure 3.4.

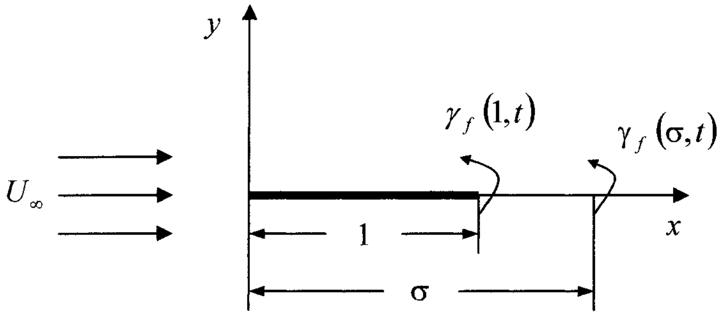

Figure 3.4 Geometry of a flat plate airfoil indicating the free vortex distribution.

Thus, the intensity of the distributed vortex sheet in the wake at the location $x=\sigma$ can be calculated as

$$\gamma_f(\sigma,t) = -i\left(\frac{2k}{c}\right)\hat{\Gamma}_C\ e^{i\omega t - i2k(\sigma-1)}\ , \tag{3.27}$$

where k is the reduced frequency of oscillations and is given by

$$k = \frac{\omega c}{2U_\infty}\ . \tag{3.28}$$

The reduced intensity of the free wake vortices $\hat{\gamma}_f(\sigma)$, is then

$$\hat{\gamma}_f(\sigma) = \gamma_f(\sigma,t)e^{-i\omega t}\ , \tag{3.29}$$

where

$$\hat{\gamma}_f(\sigma) = 2\hat{U}(\sigma), \qquad \hat{U}(x) = -i\left(\frac{k}{c}\right)\hat{\Gamma}_C\ e^{-i2k(x-1)}\ . \tag{3.30}$$

Similarly to (3.22), one can express $\hat{u}(x,0)$ in terms of $\hat{\gamma}_f(\sigma)$ by considering the circulation along an elementary control volume placed around a portion of the wake of length $c\,d\sigma$ in the form

$$\hat{u}(\sigma,0) = \hat{\gamma}_f(\sigma)/2 = \hat{U}(\sigma)\ . \tag{3.31}$$

Thus, in addition to the boundary condition (3.21) on the oscillating airfoil, the complete unsteady problem formulation has to also include the following boundary conditions upstream (where $\hat{\gamma} = 0$) and downstream of the airfoil, expressed in complex form as

$$\text{REAL}_j \{\hat{w}(z)\}_{z=x} = H_1(x)\,\hat{U}(x) \ . \tag{3.32}$$

for $x < 0$ and $x > 1$, where $H_1(x)$ ($H_1(x) = 1$ for $x > 1$ and 0 for $x < 0$) and $\hat{U}(x)$ are defined by (3.34b) and (3.30), respectively.

3.2.1 Prototype unsteady problem solution

To solve the complete problem of the oscillating flexible or rigid airfoil, consider first the prototype problem characterized by the jumps of velocities due to the bound vortices on the airfoil, represented by a constant b_0 and a variable $\delta\hat{V}$ (which is a sudden change in the normal to chord velocity component). The jump or sudden change of velocity due to the free vortices behind the trailing edge of the airfoil is represented by $\delta\hat{U}$, as depicted in Figure 3.5.

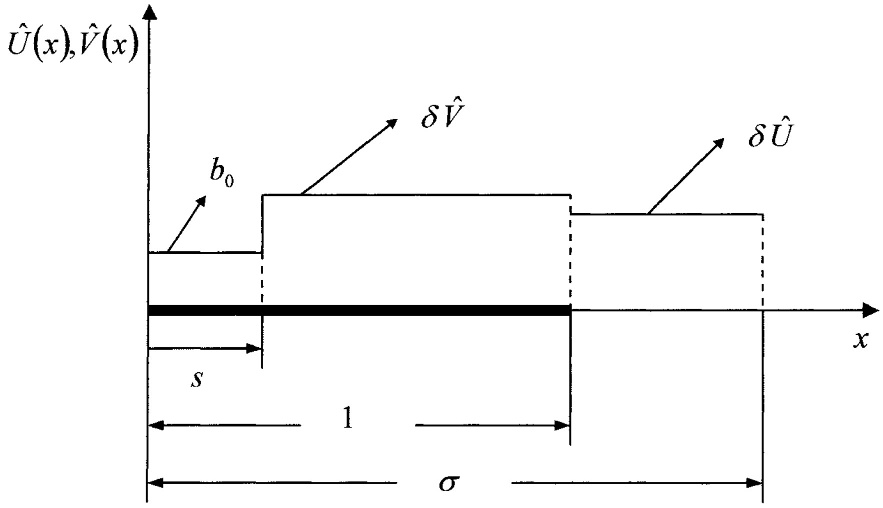

Figure 3.5 Representation of the velocity jumps in the boundary conditions of the prototype problem of an oscillating airfoil.

The prototype problem is defined by the boundary conditions,

$$\text{IMAG}_j \{\delta\hat{W}(s,z)\}_{z=x} = b_0 - H(s,x)\,\delta\hat{V} \ , \tag{3.33a}$$

$$\text{REAL}_j \{\delta\hat{W}(s,z)\}_{z=x} = H_1(x)\,\hat{U}(x) \ . \tag{3.33b}$$

where

$$H(s,x)=\begin{cases} 1 & \text{for } s<x<1 \\ 0 & \text{for } x<s \text{ or } x>1 \end{cases}, \tag{3.34a}$$

$$H_1(x)=\begin{cases} 1 & \text{for } x>1 \\ 0 & \text{for } x<0 \end{cases}. \tag{3.34b}$$

Complex singularity functions

Special singularities are used to determine the complex perturbation velocity (rather than the complex potential) in the airfoil plane (see Figure 3.5). The perturbation velocity displays the following singular behavior at the leading edge and at the ridges (where the velocity has sudden change):

At the leading edge, $z = 0$

$$\sqrt{\frac{1-z}{z}}, \tag{3.35}$$

At the velocity jump on the airfoil, $s \le z \le 1$

$$\cosh^{-1}\sqrt{\frac{(1-z)s}{(s-z)}}, \tag{3.36}$$

At the velocity jump due to the free vortices outside the airfoil, $1 < z \le \sigma$

$$\cos^{-1}\sqrt{\frac{(1-z)\sigma}{(\sigma-z)}}. \tag{3.37}$$

The general behavior and the derivations of the above special complex singularities are given in Appendix C. The velocity jump $\delta\hat{U}$ due to an elementary free vortex behind the trailing edge is defined by

$$\delta\hat{U}=\frac{d\hat{U}}{d\sigma}\delta\sigma, \tag{3.38}$$

The prototype complex conjugate velocity $\delta\hat{W}(s,z)$ is expressed in terms of the velocity jumps, due to the bound and free vortices, and special singularities related to the complex variable $z = x + jy$. The singular contributions associated to the sudden changes in velocity and satisfying the boundary conditions (3.33) are hence $\delta\hat{V}\,\tilde{G}(s,z)$ and $\left[\hat{U}'(z)\,dz\right]_{z=\sigma}\tilde{H}(\sigma,z)$, where

$$\tilde{G}(s,z)=\frac{2}{\pi}\cosh^{-1}\sqrt{\frac{(1-z)s}{(s-z)}}\ , \tag{3.39}$$

$$\hat{U}'(\sigma)=\frac{d\hat{U}(\sigma)}{d\sigma}=-\left(\frac{2k^2}{c}\right)\hat{\Gamma}_C\,e^{-i2k(\sigma-1)}\ , \tag{3.40}$$

$$\tilde{H}(\sigma,z)=\frac{2}{\pi}\cos^{-1}\sqrt{\frac{(1-z)\sigma}{(\sigma-z)}}\ . \tag{3.41}$$

Taking the effects of all the free vortices from the trailing edge $\sigma=1$ to infinity $\sigma\to\infty$, the solution of the prototype complex velocity $\delta\hat{W}(s,z)$ is thus expressed by,

$$\delta\hat{W}(s,z)=-j\,b_0+\delta A\sqrt{\frac{1-z}{z}}-\delta\hat{V}\,\tilde{G}(s,z)-\left(\frac{2k^2}{c}\right)\hat{\Gamma}_C\,\tilde{F}(z)\ , \tag{3.42}$$

where δA is an unknown constant and

$$\tilde{F}(z)=\lim_{\sigma^*\to\infty}\int_1^{\sigma^*}e^{-i2k(\sigma-1)}\,\tilde{H}(\sigma,z)\,d\sigma\ . \tag{3.43}$$

After integration by parts, equation (3.43) can be recast as

$$\tilde{F}(z)=i\left(\frac{c}{\pi k}\right)\left[E_\infty\cos^{-1}\sqrt{1-z}+F^*(z)\right]\ . \tag{3.44}$$

where

$$E_\infty=\lim_{\sigma^*\to\infty}\left[e^{-i2k(\sigma^*-1)}\right], \tag{3.45}$$

and

$$F^*(z)=\lim_{\sigma^*\to\infty}\int_1^{\sigma^*}\frac{\sqrt{(1-z)z}\ e^{-i2k(\sigma-1)}}{2(\sigma-z)\sqrt{(\sigma-1)\sigma}}d\sigma\ . \tag{3.46}$$

Because the perturbation velocity vanishes at infinity, the unknown constant δA can now be determined from the condition $[\delta\hat{W}(s,z)]_{z\to\infty}=0$. From the real part of this condition one obtains $E_\infty=0$ for this indeterminate constant (the same conclusion can also be obtained from the Riemann-Lebesque lemma on Fourier integrals when the theory of distribution is used [62, 137, 195, 200]).

The imaginary part of this condition leads now to the value of the constant

$$\delta A = -b_0 - \delta\hat{V}\, C(s) + i\,\hat{\Gamma}_C \frac{2k}{\pi c} \lim_{\sigma^* \to \infty} \int_1^{\sigma^*} \frac{e^{-i2k(\sigma-1)}}{2\sqrt{(\sigma-1)\sigma}}\, d\sigma \ , \tag{3.47}$$

where $C(s) = (2/\pi)\cos^{-1}\sqrt{s}$. With this value of δA, equation (3.42) can be recast in the form

$$\delta\hat{W}(s,z) = -b_0\left(\sqrt{\frac{1-z}{z}} + j\right) - \delta\hat{V}\left[\tilde{G}(s,z) + \sqrt{\frac{1-z}{z}}\, C(s)\right] + i\,\hat{\Gamma}_C\left(\frac{2k^2}{c}\right) F(z) \ , \tag{3.48}$$

where

$$F(z) = \frac{2}{\pi} \lim_{\sigma^* \to \infty} \int_1^{\sigma^*} \sqrt{\frac{(1-z)\sigma}{(\sigma-1)z}}\, \frac{e^{-i2k(\sigma-1)}}{2\,(\sigma - z)}\, d\sigma \ . \tag{3.49}$$

The reduced circulation around the airfoil,

$$\hat{\Gamma}_C = \mathrm{REAL}_j \left\{ 2 \int_0^1 \delta\hat{W}(s,z)\ c\,dz \right\} , \tag{3.50}$$

becomes now

$$\hat{\Gamma}_C = -\frac{4\,i\,c e^{-ik/2}}{k\ H_1^2(k)} \left[1 + \hat{D}(k)\right] \left\{ b_0 + \delta\hat{V}\left[C(s) + f(s)\right] \right\} , \tag{3.51}$$

where $f(s) = (2/\pi)\sqrt{(1-s)s}$, $H_0^2(k)$ and $H_1^2(k)$ are the Hankel functions of second kind (zero and first order) and the function $\hat{D}(k)$ is given by

$$\hat{D}(k) = \hat{C}(k) - 1 = \frac{-i H_0^2(k)}{H_1^2(k) + i\ H_0^2(k)} \ , \tag{3.52}$$

where $\hat{C}(k)$ is Theodorsen's function [158, 184, 185].

Reduced pressure coefficient

The unsteady pressure coefficient $C_p(x,t)$ on the oscillating airfoil, can be obtained from the Bernoulli-Lagrange equation expressed in terms of the perturbation potential φ,

$$C_p(x,t) = -\frac{2}{U_\infty^2}\frac{\partial\varphi}{\partial t} - 2\frac{u(x,y,t)}{U_\infty} \ , \tag{3.53}$$

which can be recast in terms of the reduced pressure coefficient $\hat{C}_p(x)$ as

$$\hat{C}_p(x) = C_p(x,t)\, e^{-i\omega t} \ , \tag{3.54}$$

$$\hat{C}_p(x) = -\frac{2}{U_\infty}\left[i\,\frac{k}{c}\,\hat{\Gamma}(x) + \hat{u}(x,0)\right] \ , \tag{3.55}$$

$$\hat{\Gamma}(x) = 2\int_0^x \hat{u}(x,0)\; c\; dx \ . \tag{3.56}$$

For the prototype unsteady problem, the reduced pressure coefficient is calculated as

$$\delta\hat{C}_p = -\frac{2}{U_\infty}\left\{ i\frac{k}{c}\delta\hat{\Gamma}(x) + \mathrm{REAL}_j \left[\delta\hat{W}(z)\right]_{z=x}\right\} \ , \tag{3.57}$$

where

$$\delta\hat{\Gamma}(x) = \mathrm{REAL}_j \int_0^x 2\left[\delta\hat{W}(z)\right]_{z=x} c\; dx \ . \tag{3.58}$$

One obtains thus

$$U_\infty\, \delta\hat{C}_p(s,x) = 2A\sqrt{\frac{1-x}{x}} + \delta\hat{V}\;[2 + 2\,ik(x-s)]\,G(s,x) \ , \tag{3.59a}$$

$$A = \left[b_0 + \delta\hat{V}\,C(s)\right]\left[1 + \hat{D}(k) + i\,2\,k\,x\right] + \hat{D}(k)\,\delta\hat{V}\,f(s) \ , \tag{3.59b}$$

where $G(s,x) = \mathrm{REAL}_j\left\{\tilde{G}(s,z)\right\}_{z=x}$ is defined by

$$G(s,x) = \begin{cases} \dfrac{2}{\pi}\cosh^{-1}\sqrt{\dfrac{(1-x)s}{s-x}} & \text{for } x \in (0,s) \\ \dfrac{2}{\pi}\sinh^{-1}\sqrt{\dfrac{(1-x)s}{x-s}} & \text{for } x \in (s,1) \ . \\ 0 & \text{for } x < 0 \text{ and } x > 1 \end{cases} \tag{3.60}$$

3.2.2 Complete solution for oscillating airfoils

The solution of the complete unsteady flow problem of an oscillating airfoil can be obtained considering a continuous distribution of elementary ridges along the chord to model the boundary condition (3.21). Thus, the boundary condition change $\delta\hat{V} = [d\hat{V}(x)/dx]_{x=s}\,ds = \hat{V}'(s)ds$ for such an elementary ridge is introduced in the solution (3.59) of the prototype unsteady problem, which is then integrated with respect to s along the chord,

$$C_p(x) = \int_0^1 \delta C_p(s,x)\, ds \; . \tag{3.61}$$

In the general case of flexible airfoil oscillations, $\hat{V}(x)$, defined by the boundary condition (3.18), is expressed in the general polynomial form

$$\hat{V}(x) = U_\infty \sum_{k=0}^{n} \hat{b}_k\, x^k \; , \qquad \text{where} \qquad \hat{b}_k = b_k + i\, 2k\, a_k \; . \tag{3.62}$$

which leads to the following expression of the reduced pressure difference coefficient across the airfoil, $\Delta\hat{C}_p(x) = -2\,\hat{C}_p(x)$:

$$\Delta\hat{C}_p(x) = -4\sqrt{\frac{1-x}{x}}\sum_{n=0}^{N}\hat{b}_n\left[\sum_{j=0}^{n} g_{n-j}x^j + R_n^V + i2k\,R_n\right], \tag{3.63a}$$

$$R_n^V = \hat{D}(k)\,\frac{2n+1}{n+1}\,g_n \;\; , \;\; R_n = \frac{1}{n+1}\sum_{j=0}^{n} g_{n-j}\,x^{j+1} \;\; , \tag{3.63b}$$

where the coefficients

$$g_j = \frac{(2j)!}{2^{2j}\,(j!)^2} \; , \tag{3.63c}$$

are also defined by the recurrence formula $g_j = g_{j-1}(2j-1)/(2j)$, with $g_0 = 1$ while R_n^V, which are proportional to $\hat{D}(k)$, represent the effect of the free shedding vortices.

To facilitate the aeroelastic applications (especially for the flexural oscillations), expression (3.63a) can be recast in the following form with separate pressure contributions related to the aerodynamic stiffness, $P^S(x)$, aerodynamic damping, $P^D(x)$ and virtual mass, $P^M(x)$, which are useful in the aeroelastic studies:

$$\Delta\hat{C}_p(x) = \sqrt{\frac{1-x}{x}}\,\left[P^S(x) + i\,2k\,P^D(x) - 4\,k^2\,P^M(x)\right], \tag{3.64a}$$

$$P^S(x) = -4\sum_{j=0}^{N} x^j \sum_{n=j}^{N} b_n\,\left(A_{nj}^Q + A_{nj}^V\right), \tag{3.64b}$$

$$P^M(x) = -4\sum_{j=0}^{N} x^j \sum_{n=j}^{N} a_n \tilde{A}_{nj} \; , \tag{3.64c}$$

$$P^D(x) = -4\sum_{j=0}^{N} x^j \sum_{n=j}^{N} \left(a_n\, A_{nj}^Q + a_n\, A_{nj}^V + x b_n\, \widetilde{A}_{nj}\right) \ , \tag{3.64d}$$

$$A_{nj}^V = \delta_{j0} \frac{2n+1}{n+1} \hat{D}(k)\, g_{n-j} \ , \ A_{nj}^Q = g_{n-j} \ , \tag{3.64e}$$

$$\widetilde{A}_{nj} = \frac{g_{n-j}}{n+1} \ . \tag{3.64f}$$

where δ_{ji} is Kronecker's symbol ($\delta_{ji} = 1$ for $j = i$, and $\delta_{ji} = 0$ for $j \neq i$). In these expressions, A_{nj}^V , which are proportional to $\hat{D}(k)$, represent the effect of the free shedding vortices situated in the wake, and are usually much smaller than the quasi-steady terms A_{nj}^Q , especially for small values of the reduced frequency k .

Equations (3.63) and (3.64) represent two simple expressions of the general solution in closed form for the unsteady pressure difference coefficient $\Delta C_p(x,t)$ on the airfoil in the general case of oscillations of flexible (or rigid) airfoils,

$$\Delta C_p(x,t) = \Delta \hat{C}_p(x)\, e^{i\omega t} \ . \tag{3.65}$$

The unsteady lift and pitching moment (with respect to the leading edge, positive nose-down) coefficients,

$$C_L(t) = \hat{C}_L \ e^{i\omega t}, \tag{3.66a}$$

$$C_m(t) = \hat{C}_m\, e^{i\omega t}, \tag{3.66b}$$

can be obtained by integrating the pressure difference coefficient over the chord, thus resulting in

$$\hat{C}_L = -2\pi \sum_{n=0}^{N} \hat{b}_n\, g_n \frac{2n+1}{n+1} \left[1 + \frac{i\,k}{n+2} + \hat{D}(k)\right] \ , \tag{3.67a}$$

$$\hat{C}_m = -\frac{\pi}{2} \sum_{n=0}^{N} \hat{b}_n\, g_n \frac{2n+1}{n+1} \left[\frac{2n+2}{n+2} + \frac{i\,3k}{n+3} + \hat{D}(k)\right] \ . \tag{3.67b}$$

Both unsteady solutions (3.63) and (3.64), as well as the unsteady solutions (3.67) of the lift and pitching moment coefficients, reduce directly to the steady solution in the limit case when k tends to zero (because $\lim_{k\to 0} \hat{D}(k) = 0$).

These equations can also be recast in the following forms, in order to introduce (for the aeroelastic applications) the corresponding aerodynamic stiffness components, $\hat{C}_L^S$ and

$\hat{C}_m^S$, aerodynamic damping terms, $\hat{C}_L^D$ and $\hat{C}_m^D$, and virtual (or added) mass components, $\hat{C}_L^M$ and $\hat{C}_m^M$,

$$\hat{C}_L = \hat{C}_L^S + i\,2k\,\hat{C}_L^D - 4k^2\,\hat{C}_L^M \ , \tag{3.68a}$$

$$\hat{C}_m = \hat{C}_m^S + i\,2k\,\hat{C}_m^D - 4k^2\,\hat{C}_m^M \ , \tag{3.68b}$$

$$\hat{C}_L^S = -2\pi \sum_{n=0}^{N} b_n \left(L_n^Q + L_n^V \right), \tag{3.69a}$$

$$\hat{C}_L^D = -2\pi \sum_{n=0}^{N} \left(a_n L_n^Q + a_n L_n^V + b_n L_n \right), \tag{3.69b}$$

$$\hat{C}_L^M = -2\pi \sum_{n=0}^{N} a_n\, L_n \ , \quad L_n = L_n^Q / (2n+4) \tag{3.69c}$$

$$\hat{C}_m^S = -\frac{\pi}{2} \sum_{n=0}^{N} b_n \left(M_n^Q + M_n^V \right), \tag{3.69d}$$

$$\hat{C}_m^D = -\frac{\pi}{2} \sum_{n=0}^{N} \left(a_n M_n^Q + a_n M_n^V + b_n M_n \right), \tag{3.69e}$$

$$\hat{C}_m^M = -\frac{\pi}{2} \sum_{n=0}^{N} a_n\, M_n \ , \ M_n = 3L_n^Q / (2n+6) \ , \tag{3.69f}$$

where

$$L_n^Q = g_n (2n+1)/(n+1) \ , \ L_n^V = \hat{D}(k)\, L_n^Q \ , \tag{3.69g}$$

$$M_n^Q = 2L_n^Q (n+1)/(n+2) \ , \ M_n^V = L_n^V \ . \tag{3.69h}$$

In these equations, the terms L_n^V and M_n^V represent the effect of the free shedding vortices situated in the wake, which are usually much smaller than the quasi-steady terms L_n^Q and M_n^Q, especially for low frequency oscillations, as shown in the next section.

The unsteady lift and pitching moment coefficients can also be expressed in terms of their amplitude, A_{CL}, A_{Cm}, and phase, Ψ_{CL}, Ψ_{Cm} with respect to the airfoil oscillatory motion, as

$$C_L(t) = A_{CL}\, e^{i\omega t - i\Psi_{CL}} \ , \tag{3.70a}$$

$$C_m(t) = A_{Cm}\, e^{i\omega t - i\Psi_{Cm}} \ , \tag{3.70b}$$

$$A_{CL} = \sqrt{\left(\hat{C}_L^{\mathrm{Re}}\right)^2 + \left(\hat{C}_L^{\mathrm{Im}}\right)^2} \ , \qquad \Psi_{CL} = \tan^{-1}\left(\hat{C}_L^{\mathrm{Im}} / \hat{C}_L^{\mathrm{Re}}\right) , \tag{3.70c}$$

$$A_{Cm} = \sqrt{\left(\hat{C}_m^{\mathrm{Re}}\right)^2 + \left(\hat{C}_m^{\mathrm{Im}}\right)^2}\,, \qquad \Psi_{Cm} = \tan^{-1}\left(\hat{C}_m^{\mathrm{Im}} / \hat{C}_m^{\mathrm{Re}}\right)\,, \tag{3.70d}$$

where the superscripts Re and Im denote the real and imaginary parts, such as $\hat{C}_L^{\mathrm{Re}} = \mathrm{REAL}_i\left\{\hat{C}_L\right\}$ and $\hat{C}_L^{\mathrm{Im}} = \mathrm{IMAG}_i\left\{\hat{C}_L\right\}$. The phase lag of the aerodynamic coefficients with respect to the oscillatory motion of the airfoil is an important parameter in the aeroelastic studies.

3.3 Method validation for oscillating rigid airfoils

The present method of solution has been validated by comparison with the previous results obtained by Theodorsen [184] for the lift and pitching moment coefficients, and by Postel and Leppert [158] for the reduced pressure difference coefficient, in the case of rigid airfoils executing harmonic oscillations in translation $h(t)$

$$h(t) = \hat{h}\, e^{i\omega t}\,, \tag{3.71a}$$

and in rotation $\theta(t)$ with respect to a rotation center situated at $x = a$ on its chord

$$\theta(t) = \hat{\theta}\, e^{i\omega t}\,. \tag{3.71b}$$

In this case, the modal amplitude of oscillations is expressed as

$$\hat{e}(x) = \hat{h} - (x - a)\,\hat{\theta}\,, \tag{3.72}$$

and hence the coefficients b_n and a_n defining the boundary condition (3.18) in the form (3.62), where $N = 1$, become $b_0 = -\hat{\theta}$, $b_1 = 0$, $a_0 = \hat{h} + \hat{\theta} a$, $a_1 = -\hat{\theta}$. The reduced pressure difference coefficient and the reduced lift and pitching moment (with respect to the leading edge) coefficients are expressed in this case by equations (3.64) and (3.68), where the aerodynamic stiffness, damping and virtual mass components are

$$P^S(x) = 4\hat{\theta}\left[1 + \hat{D}(k)\right], \tag{3.73a}$$

$$P^M(x) = \hat{\theta} x\,(1 - 4a + 2x) - 4\hat{h} x\,, \tag{3.73b}$$

$$P^D(x) = \hat{\theta}(2 + 8x - 4a) - 4\hat{h} + \hat{D}(k)\left[\hat{\theta}(3 - 4a) - 4\hat{h}\right], \tag{3.73c}$$

$$\hat{C}_L^S = 2\pi\hat{\theta}\left[1 + \hat{D}(k)\right], \tag{3.74a}$$

$$\hat{C}_L^M = 2\pi\left[\hat{\theta}(1/8 - a/4) - \hat{h}/4\right], \tag{3.74b}$$

$$\hat{C}_L^D = 2\pi \left\{\hat{\theta}\,(1-a) - \hat{h} + \hat{D}(k)\left[\hat{\theta}(3/4-a) - \hat{h}\right]\right\}, \tag{3.74c}$$

$$\hat{C}_m^S = (\pi/2)\hat{\theta}\left[1 + \hat{D}(k)\right], \tag{3.75a}$$

$$\hat{C}_m^M = (\pi/2)\left[\hat{\theta}\,(9/32 - a/2) - \hat{h}/2\right], \tag{3.75b}$$

$$\hat{C}_m^D = (\pi/2)\left\{\hat{\theta}\,(3/2-a) - \hat{h} + \hat{D}(k)\left[\hat{\theta}(3/4-a) - \hat{h}\right]\right\}. \tag{3.75c}$$

The pitching moment with respect to the rotation center ($x = a$) is defined as $\hat{C}_{mR} = \hat{C}_m - a\hat{C}_L$. The aerodynamic stiffness and damping components of these reduced lift and moment coefficients can also be expressed in terms of their quasi-steady and vortex-shedding components (denoted by the superscripts *Q* and *V*, respectively)

$$\hat{C}_L^S = \hat{C}_L^{SQ} + \hat{C}_L^{SV}\ ,\ \hat{C}_L^D = \hat{C}_L^{DQ} + \hat{C}_L^{DV}\ ,$$
$$\hat{C}_m^S = \hat{C}_m^{SQ} + \hat{C}_m^{SV}\ ,\ \hat{C}_m^D = \hat{C}_m^{DQ} + \hat{C}_m^{DV}\ , \tag{3.76}$$

where:

$$\hat{C}_L^{SQ} = 4\,\hat{C}_m^{SQ} = 2\pi\hat{\theta}\ , \qquad \hat{C}_L^{SV} = 4\,\hat{C}_m^{SV} = 2\pi\hat{\theta}\,\hat{D}(k)$$
$$\hat{C}_L^{DQ} = 2\pi\left[\hat{\theta}\,(1-a) - \hat{h}\right], \quad \hat{C}_m^{DQ} = (\pi/2)\left[\hat{\theta}\,(3/2-a) - \hat{h}\right],$$
$$\hat{C}_L^{DV} = 4\hat{C}_m^{DV} = -2\pi\hat{D}(k)\left[\hat{\theta}\,(3/4-a) - \hat{h}\right]. \tag{3.77}$$

The chordwise variations of the real and imaginary parts of the reduced pressure difference coefficient, $\Delta\hat{C}_p(x)$ given by solution (3.73), are compared for validation in Figures 3.6 and 3.7 with the results obtained by Postel and Leppert [158] in the cases of oscillatory rotation around the quarter-chord ($\hat{h} = 0$) and oscillatory translation ($\hat{\theta} = 0$), for two values of the reduced frequency of oscillations, $k = 0.24$ and $k = 0.34$. An excellent agreement can be noticed between the present solutions and Postel and Leppert [158] results in all cases.

The variation with the reduced frequency, k , of the real and imaginary parts of the reduced lift and pitching moment coefficients, $\hat{C}_L$ and $\hat{C}_m$ given by solutions (3.74) and (3.75), in the cases of oscillatory rotation ($\hat{h} = 0$) and oscillatory translation ($\hat{\theta} = 0$) are illustrated in Figures 3.8 and 3.9. The present solutions were found to be in excellent agreement with Theodorsen's results [184].

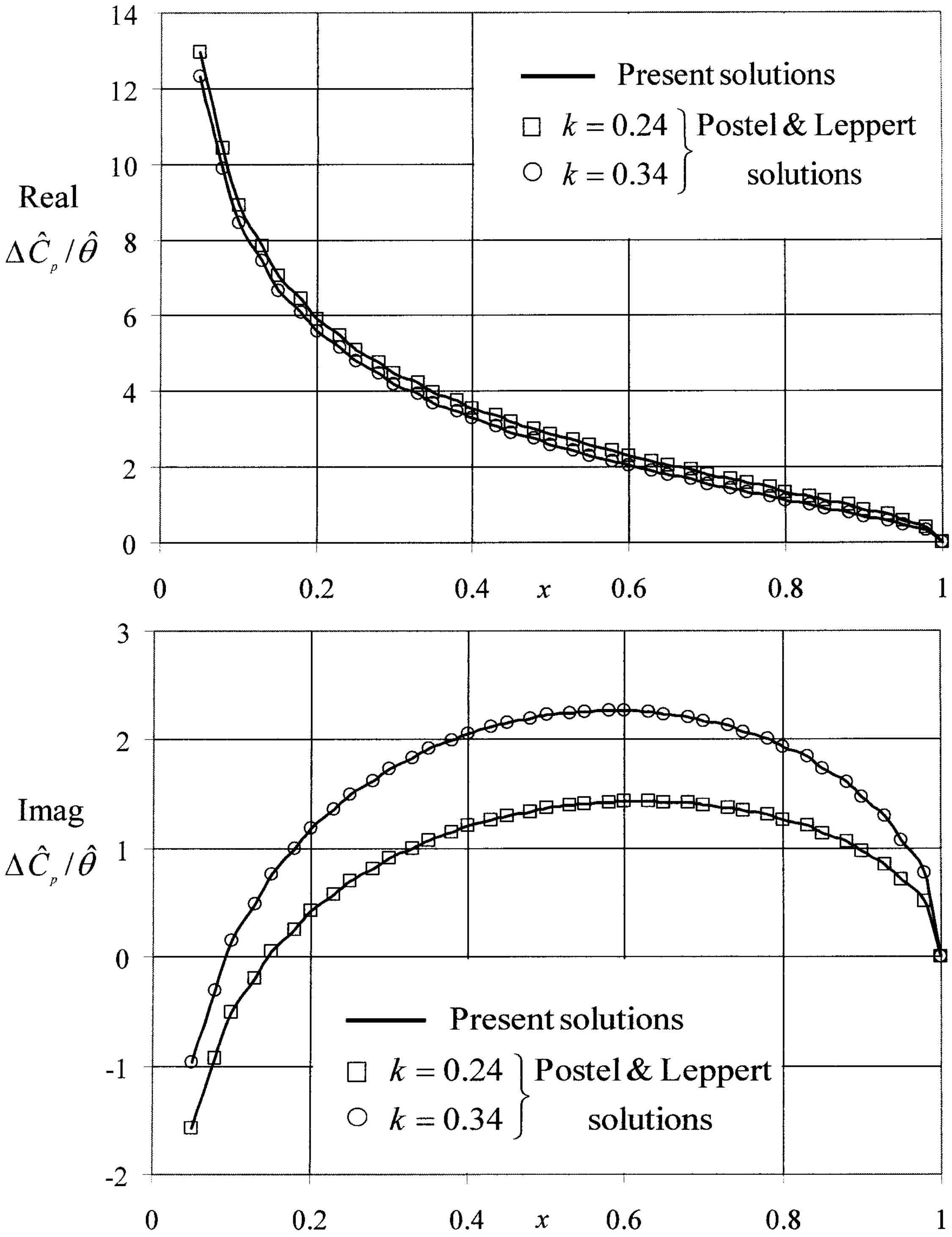

Figure 3.6 Oscillatory rotation of airfoils; real and imaginary parts of the reduced pressure difference coefficient, $\Delta\hat{C}_p(x)$.

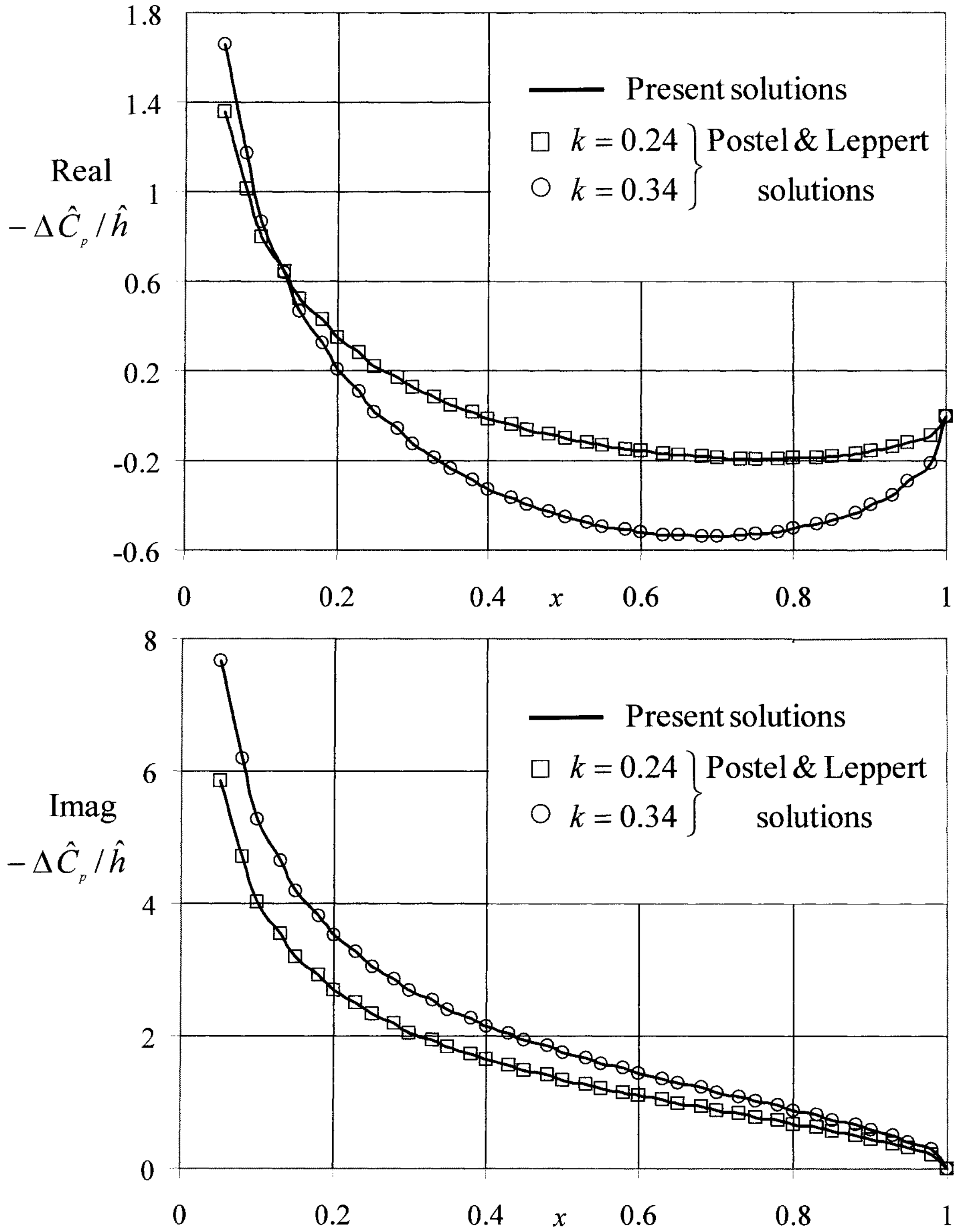

Figure 3.7 Oscillatory translation of airfoils; real and imaginary parts of the reduced pressure difference coefficient, $\Delta\hat{C}_p(x)$.

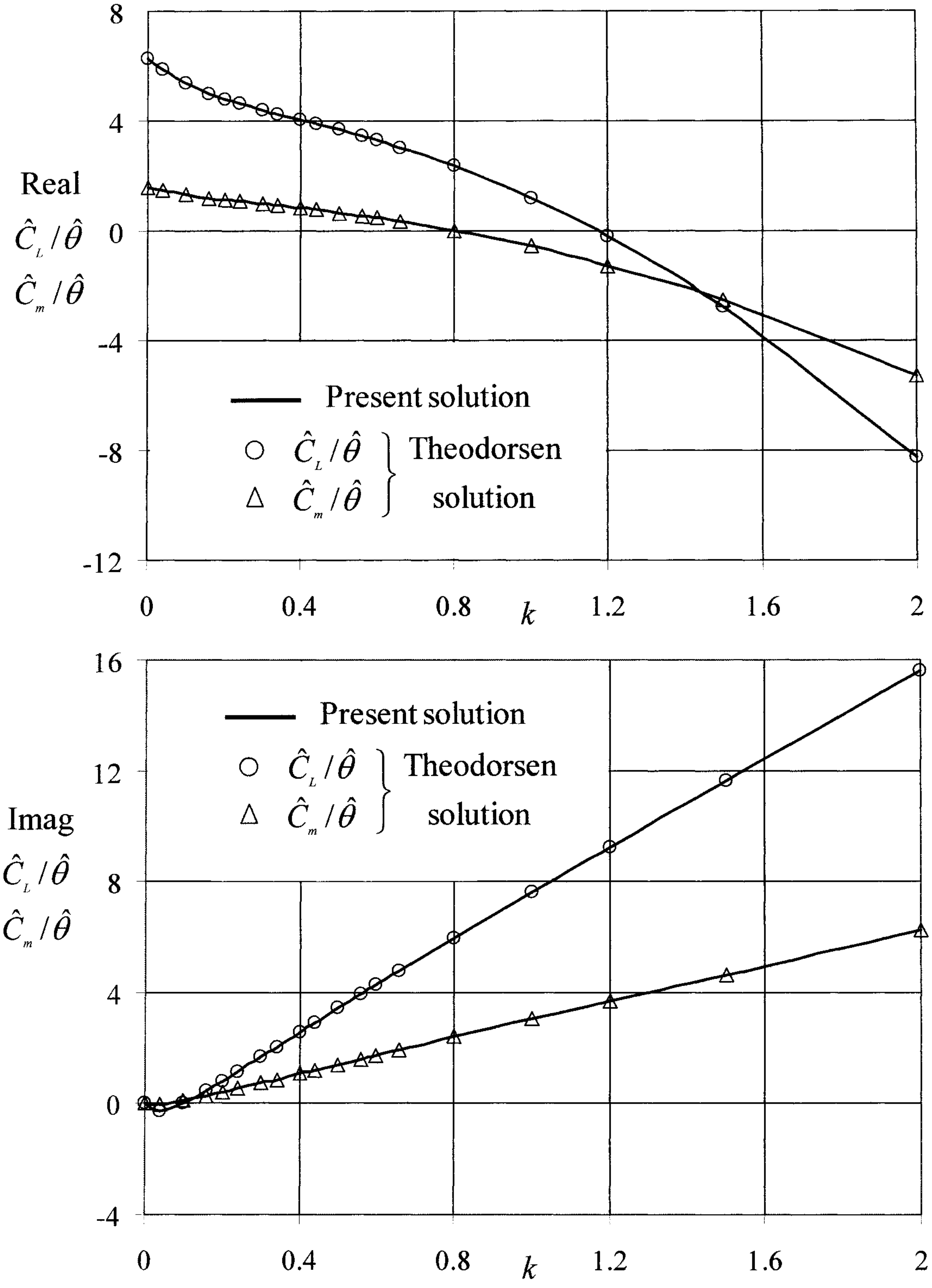

Figure 3.8 Oscillatory rotation of airfoils; real and imaginary parts of the reduced lift and pitching moment coefficients, $\hat{C}_L$ and $\hat{C}_m$.

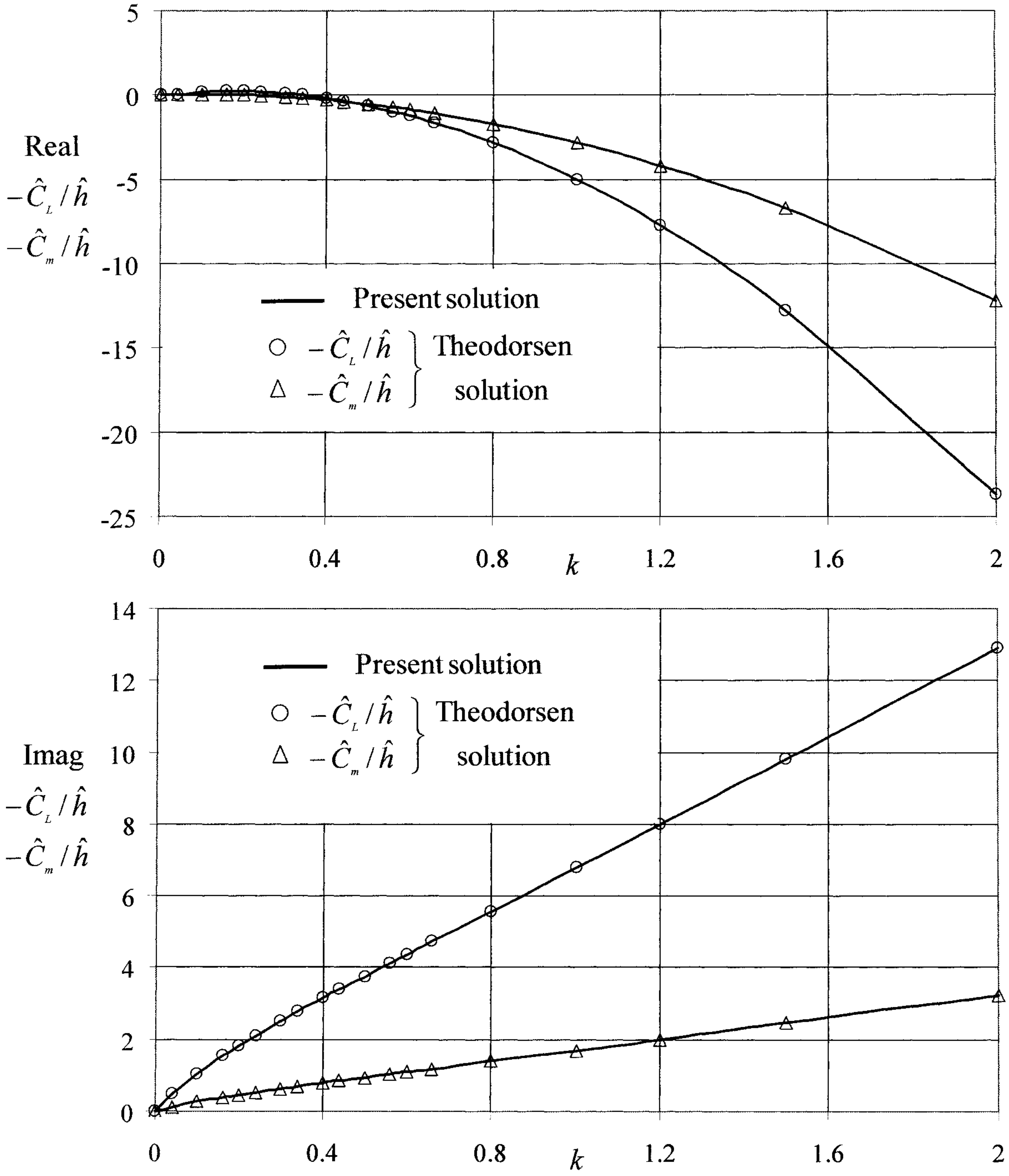

Figure 3.9 Oscillatory translation of airfoils; real and imaginary parts of the reduced lift and pitching moment coefficients, $\hat{C}_L$ and $\hat{C}_m$.

3.3.1 Aerodynamic stiffness, damping and virtual mass

The relative values of the aerodynamic stiffness, damping and virtual mass contributions in the pitching moment coefficient amplitude, A_{Cm}^{S} , $\overline{A}_{Cm}^{D} = (2k)A_{Cm}^{D}$ and $\overline{A}_{Cm}^{M} = (4k^2)A_{Cm}^{M}$, are illustrated for a rigid airfoil in oscillatory rotation in Figure 3.10. Their phases with respect to the airfoil oscillations, Ψ_{Cm}^{S} and Ψ_{Cm}^{D} are also shown (note that an additional 90^{o} and 180^{o} should be added to Ψ_{Cm}^{D} and $\Psi_{Cm}^{M} = 0$, respectively).

3.3.2 Vortex-shedding effect

The variations with k of the amplitudes of the vortex-shedding and quasi-steady terms of the aerodynamic stiffness and damping contributions in the reduced lift coefficient, A_{CL}^{SQ} , A_{CL}^{SV} , $\overline{A}_{CL}^{DQ} = (2k)A_{CL}^{DQ}$, $\overline{A}_{CL}^{DV} = (2k)A_{CL}^{DV}$, are also illustrated in Figure 3.10, together with the phases Ψ_{CL}^{SV} and Ψ_{CL}^{DV} , for a rigid airfoil in oscillatory rotation ($\Psi_{CL}^{SQ} = \Psi_{CL}^{DQ} = 0$). One can notice that the vortex-shedding term amplitudes are much smaller than those of the quasi-steady terms in the case of low frequency oscillations, k .

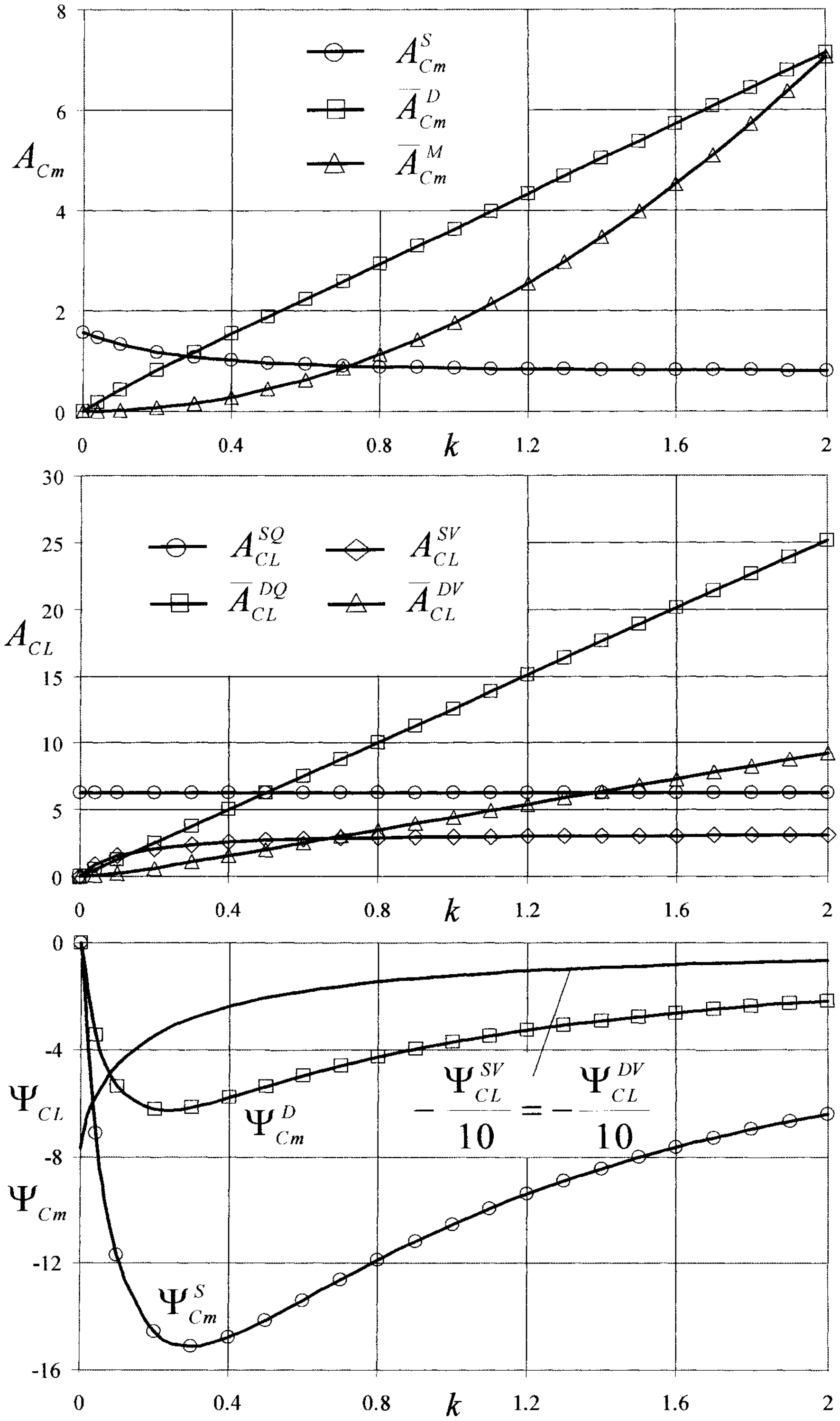

Figure 3.10 Oscillatory rotation of airfoils; aerodynamic stiffness, damping and virtual mass contributions in the reduced pitching moment coefficient amplitude, and the vortex-shedding and quasi-steady components in the reduced lift coefficient amplitude, and their phases.

3.4 Solutions for airfoils executing flexural oscillations

Consider a flexible airfoil executing flexural oscillations,

$$e(x,t) = \hat{e}(x)e^{i\omega t}, \tag{3.78a}$$

where

$$\hat{e}(x) = \sum_{n=1}^{N} e_n x^n . \tag{3.78b}$$

is the modal amplitude of oscillations. In this case, the coefficients b_n and a_n become $b_n = (1-\delta_{nN})(n+1)e_{n+1}$, $a_n = (1-\delta_{n0})e_n$, and the solutions for the reduced pressure, lift and moment coefficients are given by (3.63) - (3.69).

Parabolic flexural oscillations of airfoils

As an example, consider the parabolic flexural oscillations defined as $\hat{e}(x) = e_2 x^2$, in which case $N = 2$, $b_1 = 2e_2$, $a_2 = e_2$ and the rest of the coefficients are zero. The solutions for the reduced pressure difference coefficient $\Delta\hat{C}_p(x)$ is also defined by (3.64a), where

$$P^S(x) = e_2\left[2x + 1 + 3\hat{D}(k)/2\right], \tag{3.79a}$$

$$P^M(x) = e_2\left[x^2/3 + x/6 + 1/8\right], \tag{3.79b}$$

$$P^D(x) = e_2\left[2x^2 + x + 3/8 + 5\hat{D}(k)/8\right]. \tag{3.79c}$$

and the reduced lift and moment coefficients are in this case

$$\hat{C}_L = -(\pi/2)e_2\left[6 + 7ik + \hat{D}(k)(6 + 5ik) - 5k^2/4\right], \tag{3.80a}$$

$$\hat{C}_m = -(\pi/2)e_2\left[2 + 3ik + \hat{D}(k)(3/2 + 5ik/4) - 3k^2/4\right]. \tag{3.80b}$$

For the parabolic flexural oscillations, the chordwise distributions of the real and imaginary parts of $\Delta\hat{C}_p(x)$ are shown in Figure 3.11 for two values of the reduced frequency of oscillations. The variations with k of the real and imaginary parts of $\hat{C}_L$ and $\hat{C}_m$, are shown in Figure 3.12.

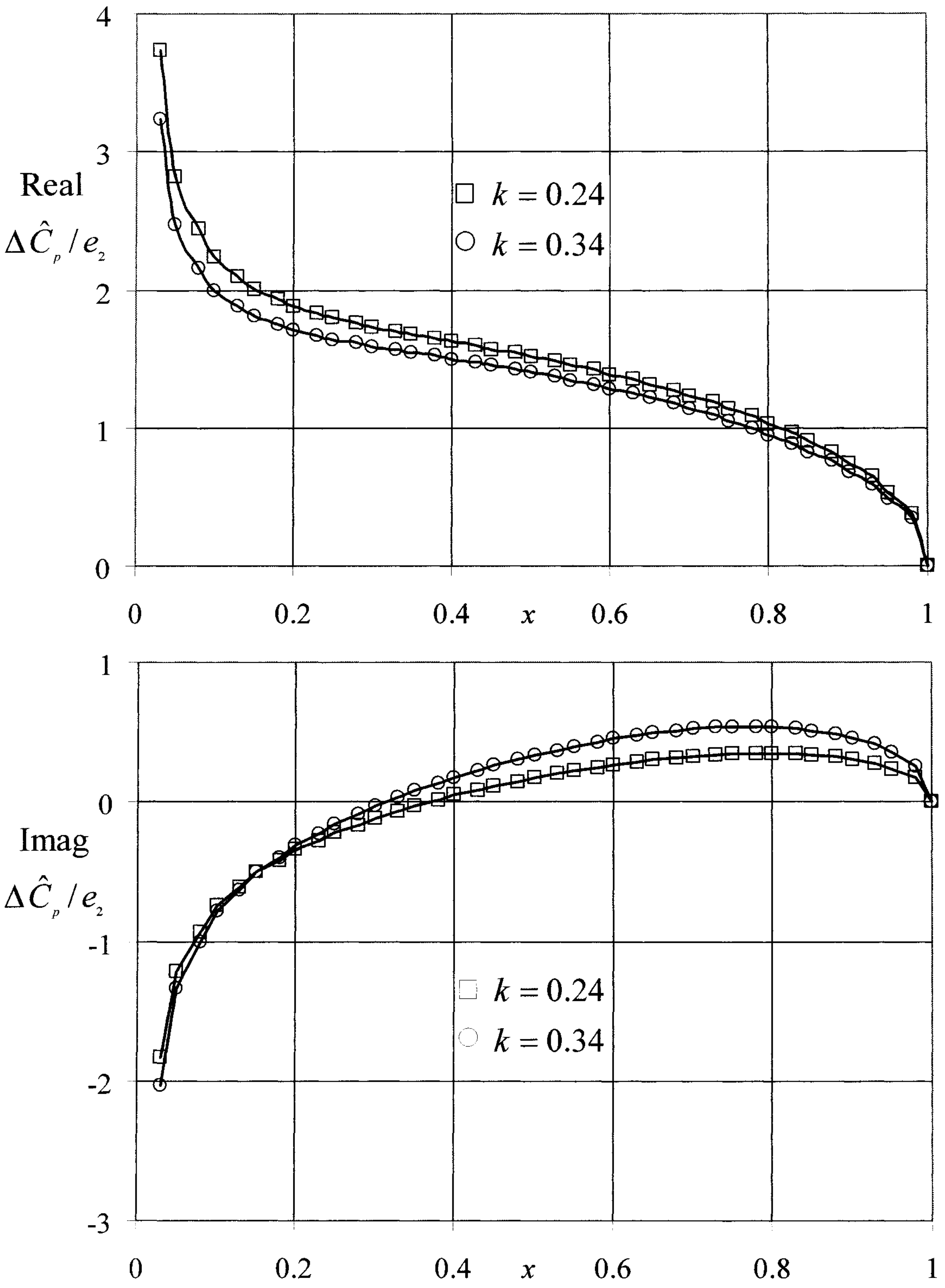

Figure 3.11 Flexural oscillations of airfoils; real and imaginary parts of the reduced pressure difference coefficient, $\Delta\hat{C}_p(x)$.

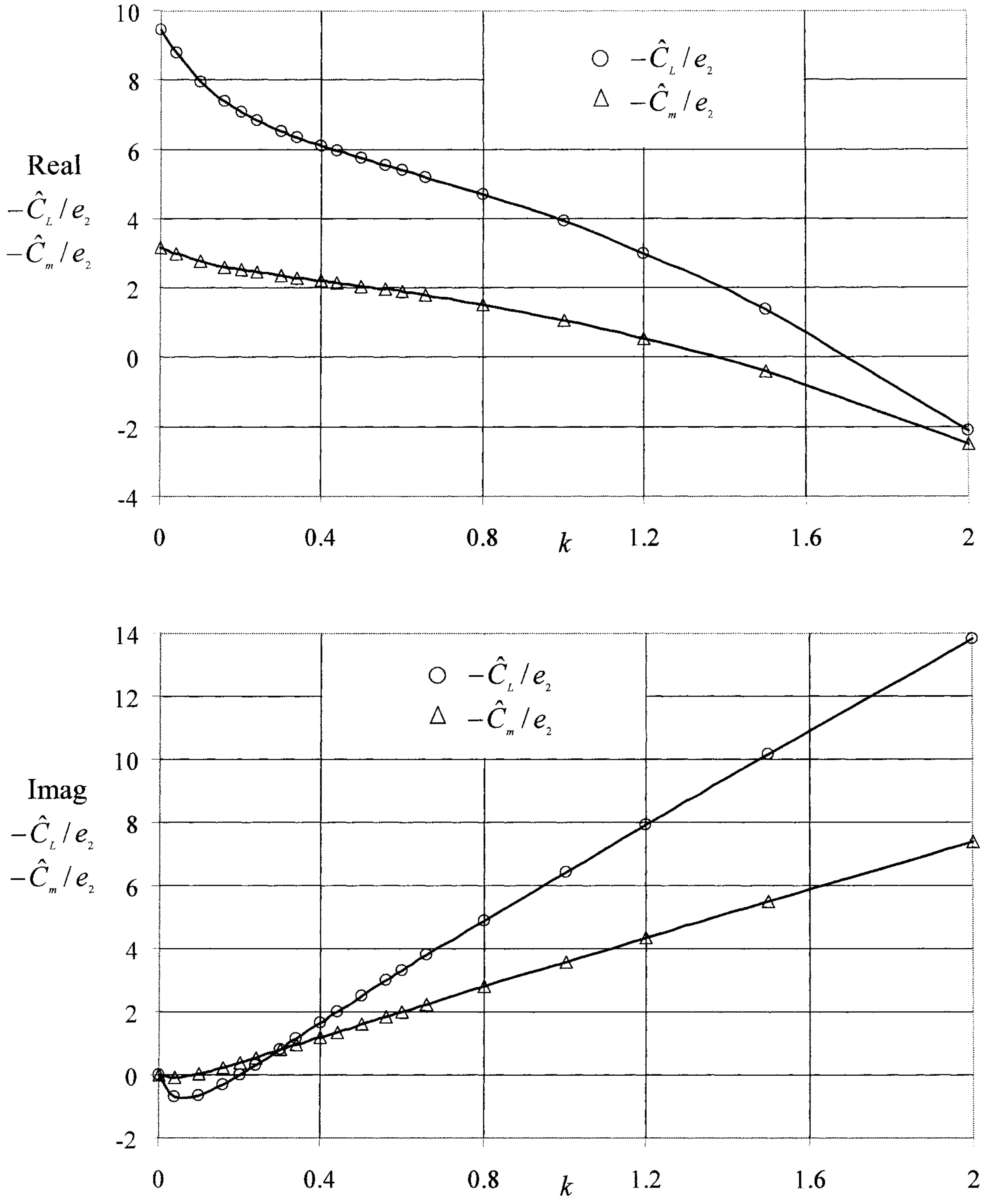

Figure 3.12 Flexural oscillations of airfoils; real and imaginary parts of the reduced lift and pitching moment coefficients, $\hat{C}_L$ and $\hat{C}_m$.

3.5 Solutions for airfoils with oscillating ailerons

To determine the effect of the aileron oscillations, consider a thin airfoil of chord c at zero incidence fitted with an aileron of chord $(1-s)c$, as shown in Figure 3.13, which executes harmonic oscillations defined as

$$y = \varepsilon(x,t) = \hat{\varepsilon}(x)e^{i\omega t} \quad \text{for} \quad s < x < 1 . \tag{3.81}$$

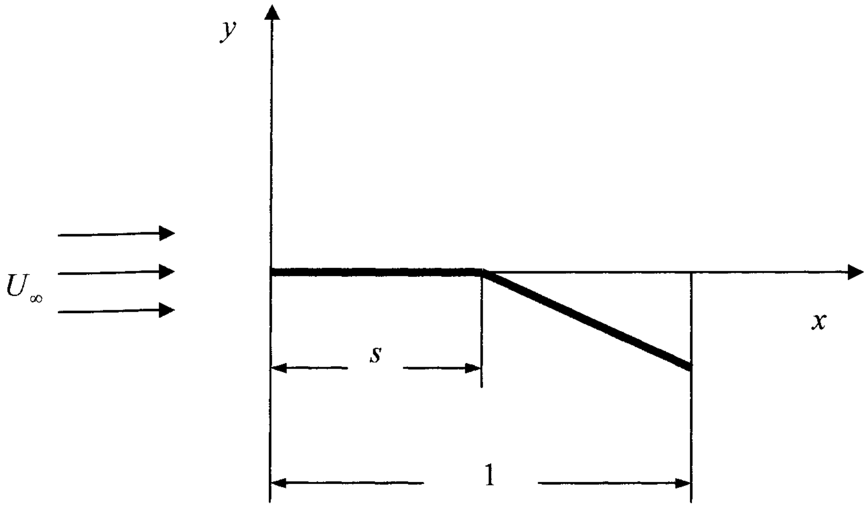

Figure 3.13 Geometry of an airfoil fitted with an oscillating aileron.

The boundary conditions on the airfoil in this case can be obtained in a similar manner as for the entire airfoil executing oscillations, resulting in

$$\text{IMAG}_j\,\{\hat{w}(z)\}_{z=x} = -H(s,x)\,\hat{V}(x) , \tag{3.82a}$$

$$\text{REAL}_j\,\{\hat{w}(z)\}_{z=x} = H_1(x)\,\hat{U}(x) , \tag{3.82b}$$

where

$$\hat{V}(x) = i\omega\,\hat{\varepsilon}(x) + U_\infty \frac{\partial\hat{\varepsilon}}{\partial x} , \tag{3.82c}$$

while $H(s,x)$, $H_1(x)$ and $\hat{U}(x)$ are defined by (3.34a), (3.34b) and (3.30), respectively.

As shown by (3.82), there is a sudden change in the boundary conditions on the airfoil at $x = s$, which is represented by the ridge contribution $\hat{V}(s)\,\tilde{G}(s,z)$ in the complex reduced velocity $\hat{w}(z)$. Similarly to the case of oscillating airfoil, the boundary condition on the oscillating aileron can be modeled by a continuous distribution of elementary ridges, defined by the contributions $\left[\hat{V}'(\sigma)\, d\sigma\right]\widetilde{G}(\sigma,z)$ for $s<\sigma<1$. Considering the solution (3.59) of the prototype unsteady problem for both the ridge at $x=s$ and the distribution of elementary ridges, one obtains for the reduced pressure coefficient in this case

$$U_\infty \hat{C}_p(x) = 2A\sqrt{\frac{1-x}{x}} + [2+i2k(x-s)]\hat{V}(s)G(s,x)$$

$$+\int_0^1 [2+i\,k\,(x-\sigma)]\,\hat{V}'(\sigma)G(\sigma,x)\,d\sigma\ , \tag{3.83a}$$

$$A=\hat{V}(s)\left\{\left[1+\hat{D}(k)+i\,2kx\right]C(s)+\hat{D}(k)f(s)\right\}$$

$$+\int_0^1 \hat{V}'(\sigma)\left\{\left[1+\hat{D}(k)+i\,2kx\right]C(\sigma)+\hat{D}(k)f(\sigma)\right\}d\sigma\ . \tag{3.83b}$$

As in (3.62), the function $\hat{V}(x)$ in (3.83) has the general polynomial representation

$$\hat{V}(x)=U_\infty\sum_{n=0}^{N}\hat{\beta}_n x^n\ ,\quad \hat{\beta}_n=\beta_n+i\,2k\alpha_n\ . \tag{3.84}$$

After inserting this expression in (3.83) and performing the integrals, one obtains the reduced pressure difference coefficient $\Delta\hat{C}_p=-2\hat{C}_p$ for the case of aileron oscillations in the form

$$\Delta\hat{C}_p(x)=-4\sqrt{\frac{1-x}{x}}\sum_{n=0}^{N}\hat{\beta}_n\left\{[1+i\,2k/(n+1)]\hat{P}_n^Q+\hat{P}_n^V\right\}$$

$$-4\,G(s,x)\sum_{n=0}^{N}\hat{\beta}_n\left[x^n+i\,2\,k\left(x^{n+1}-s^{n+1}\right)/(n+1)\right], \tag{3.85}$$

where $G(s,x)$ is defined by (3.60) while

$$\hat{P}_n^Q=\sum_{j=0}^{n}J_{n-j}\,x^{j+1}\ ,\ \hat{P}_n^V=2\,\hat{D}(k)J_{n+1}\ , \tag{3.86a}$$

and the recurrence formula for J_n is given by

$$J_n=\left[s^{n-1}f(s)+(2n-1)J_{n-1}\right]/(2n),$$

$$J_0=C(s)=(2/\pi)\cos^{-1}\sqrt{s}\ ,\qquad f(s)=(2/\pi)\sqrt{(1-s)s}\ . \tag{3.86b}$$

The reduced lift and pitching moment coefficients due to the aileron oscillations are

$$\hat{C}_L = -2\pi \sum_{n=0}^{N} \hat{\beta}_n \left\{ \sum_{j=0}^{n} J_{n-j} \left[\frac{g_j}{j+1} + \frac{i\,2\,k}{n+1} \frac{g_{j+1}}{j+2} \right] \right.$$
$$\left. + \hat{P}_n^V + Q_n + \frac{i\,2\,k}{n+1} \left[Q_{n+1} - s^{n+1} Q_0 \right] \right\} ,$$
$$Q_n = \frac{f(s)}{n+1} \sum_{j=0}^{n} s^{n-j} g_j \ , \tag{3.87a}$$

$$\hat{C}_m = -2\pi \sum_{n=0}^{N} \hat{\beta}_n \left\{ \sum_{j=0}^{n} J_{n-j} \left[\frac{g_{j+1}}{j+2} + \frac{i\,2\,k}{n+1} \frac{g_{j+2}}{j+3} \right] \right.$$
$$\left. + \hat{P}_n^V / 4 + Q_{n+1} + \frac{i\,2\,k}{n+1} \left[Q_{n+2} - s^{n+1} Q_1 \right] \right\} . \tag{3.87b}$$

where g_j is defined by (3.63c).

The unsteady lift coefficient of the aileron and the hinge moment, $C_{La}(t) = \hat{C}_{La} \exp(i\omega t)$ and $C_h(t) = \hat{C}_h \exp(i\omega t)$, are obtained by integrating $\Delta\hat{C}_p(x)$ over the aileron in the form

$$\hat{C}_{La} = -\frac{2\pi}{1-s} \sum_{n=0}^{N} \hat{\beta}_n \left\{ \sum_{j=0}^{n} J_{n-j} \left(\overline{L}_j + \frac{i\,2\,k}{n+1} \overline{L}_{j+1} \right) \right.$$
$$\left. + \hat{P}_n^V L_0 + \overline{Q}_n + \frac{i\,2\,k}{n+1} \left[\overline{Q}_{n+1} - s^{n+1} \overline{Q}_0 \right] \right\} ,$$
$$\overline{Q}_n = \frac{f(s)}{n+1} \sum_{j=0}^{n} s^{n-j} J_j \ , \tag{3.88a}$$

$$\hat{C}_h = -\frac{2\pi}{(1-s)^2} \sum_{n=0}^{N} \hat{\beta}_n \left\{ \sum_{j=0}^{n} J_{n-j} \left(\overline{L}_{j+1} + \frac{i\,2\,k}{n+1} \overline{L}_{j+2} \right) \right.$$
$$\left. + \hat{P}_n^V \overline{L}_1 + \overline{Q}_{n+1} + \frac{i\,2\,k}{n+1} \left[\overline{Q}_{n+2} - s^{n+1} \overline{Q}_1 \right] \right\} ,$$
$$\overline{L}_j = \left[J_j - s^j f(s) \right] / (j+1) \ . \tag{3.88b}$$

3.6 Method validation for a rigid aileron executing oscillatory rotation

In the case of a rigid aileron executing oscillatory rotations about the hinge $x = s$, the modal amplitude of oscillations is $\hat{\varepsilon}(x) = -(x-s)\hat{\beta}$, and hence the coefficients β_n and α_n defining the boundary condition (3.82) in the form (3.84), where $N = 1$, become

$\beta_0 = -\hat{\beta}$, $\beta_1 = 0$, $\alpha_0 = \hat{\beta}\, s$, $\alpha_1 = -\hat{\beta}$, and then $\Delta\hat{C}_p(x)$, $\hat{C}_L$, $\hat{C}_m$, $\hat{C}_{La}$, $\hat{C}_h$ are determined from equations (3.85)-(3.88).

The chordwise variation of the real and imaginary parts of the reduced pressure difference coefficient, $\Delta\hat{C}_p(x)$, are shown in Figure 3.14 for $s = 0.75$ and two values of the reduced frequency of oscillations, $k = 0.24$ and $k = 0.34$.

The variations with k of the real and imaginary parts of the reduced lift and pitching moment coefficients, $\hat{C}_L$ and $\hat{C}_m$, and of the reduced aileron lift and hinge moment coefficients $\hat{C}_{La}$ and $\hat{C}_h$ are shown in Figures 3.15 and 3.16 for $s = 0.7$. The present solutions were found to be in excellent agreement with the results obtained by Theodorsen [184] and by Postel and Leppert [158], also shown in the same figures.

3.7 Solutions for an aileron executing flexural oscillations

Consider an airfoil with a flexible aileron executing flexural oscillations defined by, $\varepsilon(x,t) = \hat{\varepsilon}(x)\exp(i\,\omega t)$, where the modal amplitude of oscillations of the flexible aileron is $\hat{\varepsilon}(x) = \sum_{n=0}^{N} \varepsilon_n (x-s)^n$. This leads to the corresponding values of the coefficients β_n and α_n, and the solutions for the reduced pressure, lift, and moment coefficients are obtained from (3.85)-(3.88).

Parabolic flexural oscillations of ailerons

As an example, consider the parabolic flexural oscillations defined as $\hat{\varepsilon}(x) = \varepsilon_2 (x-s)^2$, in which case $N = 2$, $\beta_0 = -2\varepsilon_2\, s$, $\alpha_0 = \varepsilon_2\, s^2$, $\beta_1 = 2\varepsilon_2$, $\alpha_1 = -2\varepsilon_2\, s$, $\beta_2 = 0$, and $\alpha_2 = \varepsilon_2$. In this case, the variation with k of the real and imaginary parts of the reduced aileron lift and hinge moment coefficients $\hat{C}_{La}$ and $\hat{C}_h$ are shown in Figure 3.17 for $s = 0.6$. The chordwise distributions of the real and imaginary parts of the reduced pressure difference coefficient, $\Delta\hat{C}_p(x)$, are shown in Figure 3.18 for $s = 0.6$ and two values of the reduced frequency of oscillations.

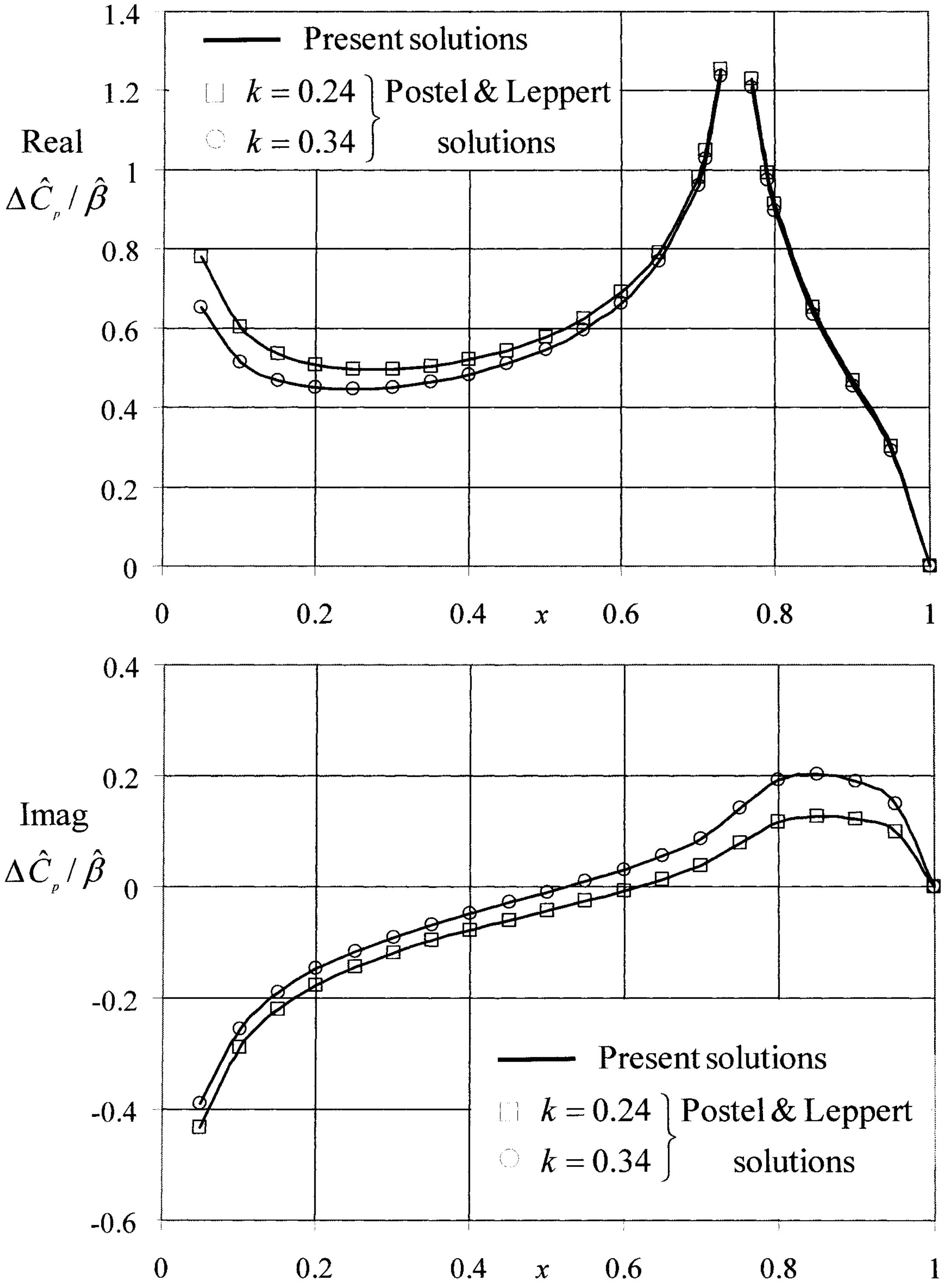

Figure 3.14 Oscillatory rotation of ailerons; real and imaginary parts of the reduced pressure difference coefficient, $\Delta \hat{C}_p(x)$.

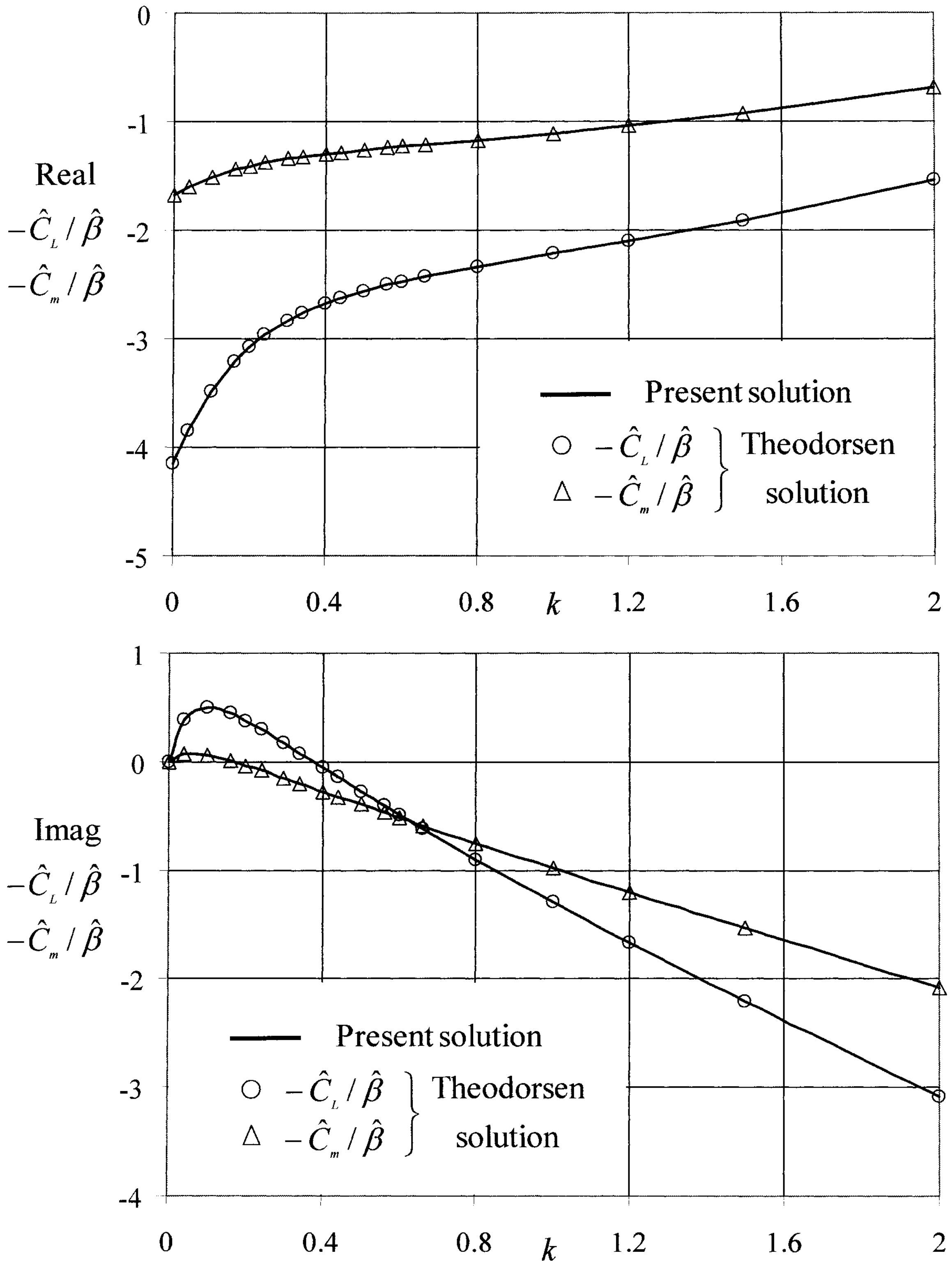

Figure 3.15 Oscillatory rotation of ailerons; real and imaginary parts of the reduced lift and pitching moment coefficients, $\hat{C}_L$ and $\hat{C}_m$.

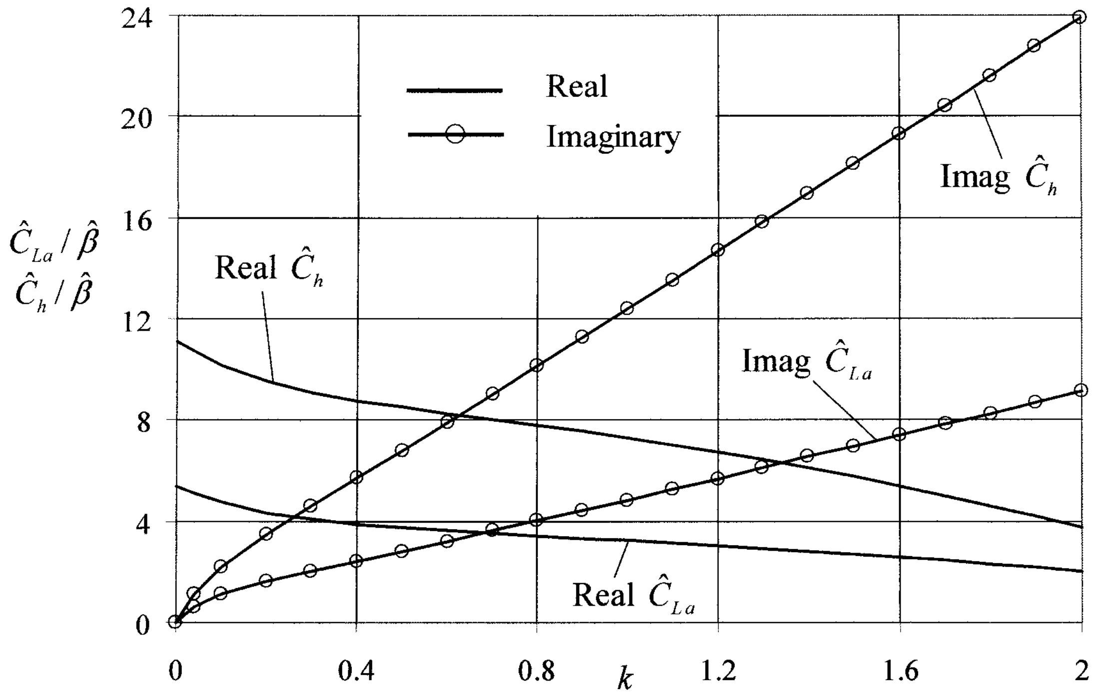

Figure 3.16 Oscillatory rotation of ailerons; real and imaginary parts of the reduced aileron lift and hinge moment coefficients, $\hat{C}_{La}$ and $\hat{C}_h$.

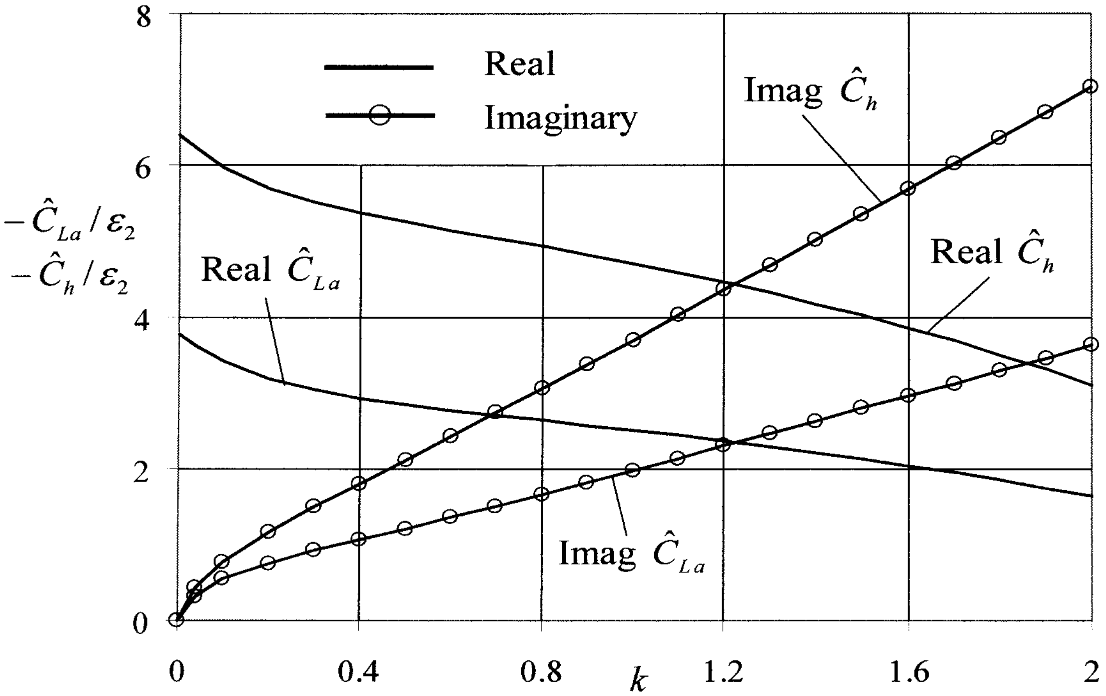

Figure 3.17 Flexural oscillations of ailerons; real and imaginary parts of the reduced aileron lift and hinge moment coefficients, $\hat{C}_{La}$ and $\hat{C}_h$.

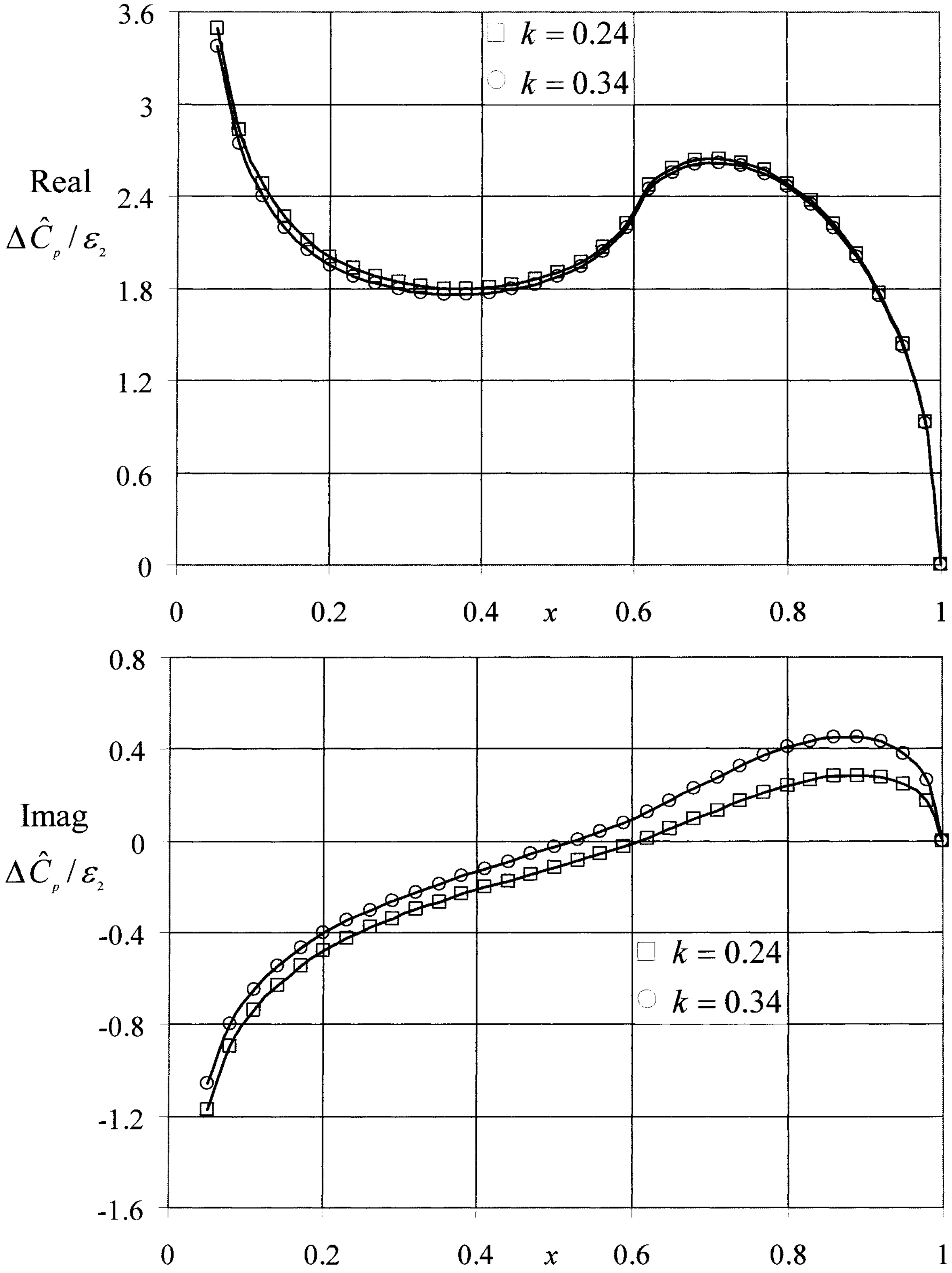

Figure 3.18 Flexural oscillations of ailerons; real and imaginary parts of the reduced pressure difference coefficient, $\Delta\hat{C}_p(x)$.

Chapter 4

Numerical Analysis of Airfoils at Very Low Reynolds Numbers

4.1 Problem formulation and governing flow equations

Consider an airfoil of chord c placed at an incidence α in a uniform stream of velocity U_∞ as shown in Figure 4.1.

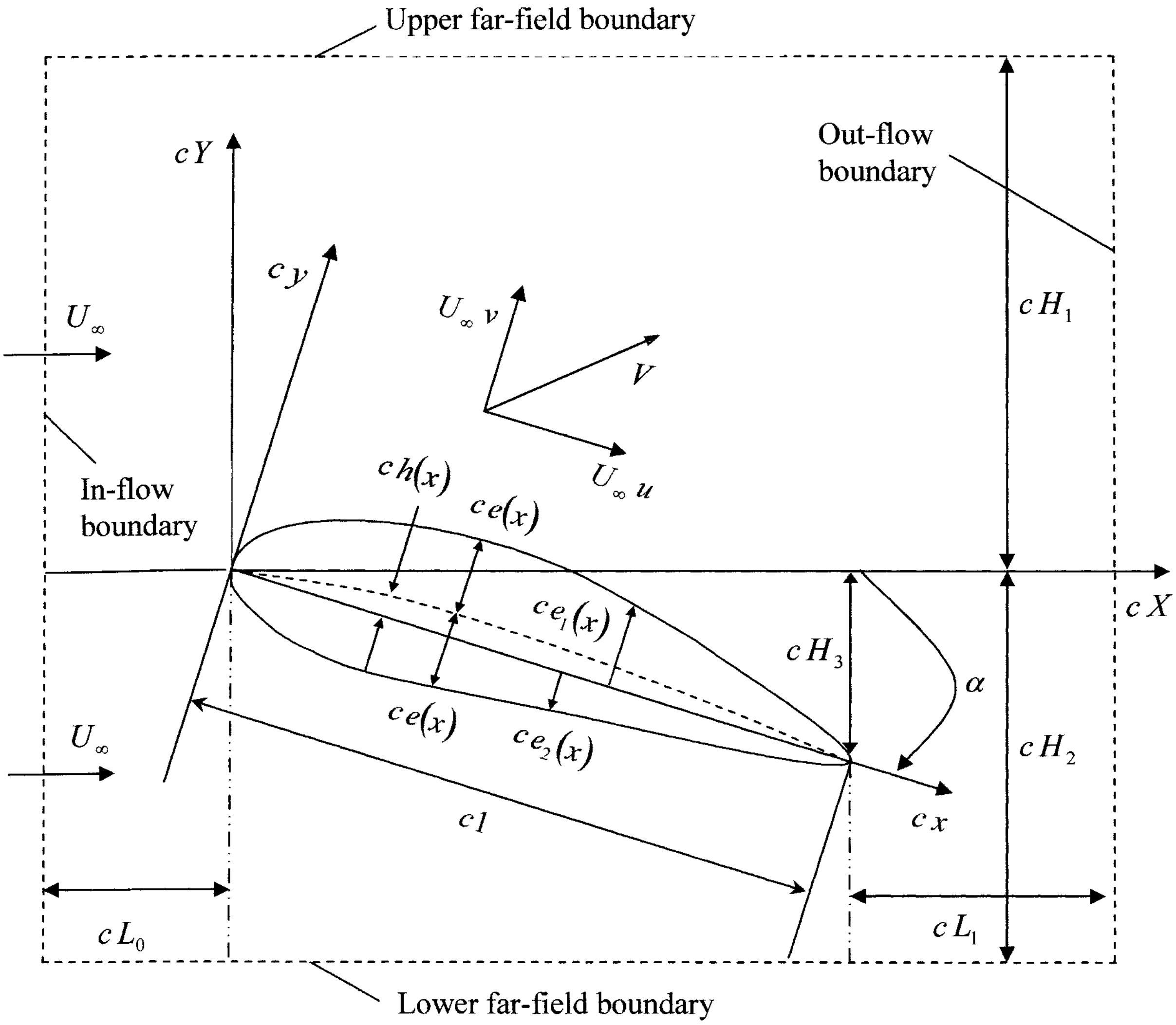

Figure 4.1 Geometric definitions for a general airfoil at incidence in a uniform flow.

The viscous fluid flow past the airfoil is referred to a Cartesian reference system cx, cy, where x and y are nondimensional coordinates, with the x-axis along the airfoil chord and its origin at the airfoil leading edge. Let $U_\infty u$ and $U_\infty v$ denote the fluid velocity components along the x- and y-axes, where u and v are the nondimensional velocity components.

The airfoil upper and lower surfaces are defined by the equations

$$y = \pm\, e_{1,2}(x) \,, \tag{4.1}$$

with

$$e_1(x) = h(x) + e(x) \,, \tag{4.2}$$

$$e_2(x) = -h(x) + e(x) \,. \tag{4.3}$$

where the subscripts 1 and 2 refer to the upper and lower surfaces, and where $h(x)$ and $e(x)$ define, respectively, the camberline and the airfoil thickness variation along the airfoil chord. The special case of symmetric airfoils is characterized by $e_1(x) = e_2(x) = e(x)$ and $h(x) = 0$.

The incompressible steady-state Navier-Stokes and continuity equations for the flow past the airfoil can be expressed in the nondimensional conservation form

$$\mathbf{Q}(\mathbf{V}, p) = \mathbf{0} \,, \tag{4.4}$$

$$\nabla \bullet \mathbf{V} = \frac{\partial u}{\partial x} + \frac{\partial v}{\partial y} = 0 \,, \tag{4.5}$$

where $\mathbf{V} = \{u, v\}^{\mathrm{T}}$ represents the vector of the dimensionless velocity components, and $\mathbf{Q}(\mathbf{V}, p)$, which includes the convective derivative, pressure and viscous terms, can be expressed in two-dimensional Cartesian coordinates in the form

$$\mathbf{Q}(\mathbf{V}, p) = \begin{Bmatrix} Q_u(u, v, p) \\ Q_v(u, v, p) \end{Bmatrix} \,, \tag{4.6}$$

$$Q_u(u, v, p) = \frac{\partial(uu)}{\partial x} + \frac{\partial(vu)}{\partial y} + \frac{\partial p}{\partial x} - \frac{1}{\mathrm{Re}}\left(\frac{\partial^2 u}{\partial x^2} + \frac{\partial^2 u}{\partial y^2}\right), \tag{4.7a}$$

$$Q_v(u, v, p) = \frac{\partial(uv)}{\partial x} + \frac{\partial(vv)}{\partial y} + \frac{\partial p}{\partial y} - \frac{1}{\mathrm{Re}}\left(\frac{\partial^2 v}{\partial x^2} + \frac{\partial^2 v}{\partial y^2}\right), \tag{4.7b}$$

and where p is the dimensionless pressure, nondimensionalized with respect to $\rho U_\infty{}^2$, and $\mathrm{Re} = cU_\infty / \nu$ is the Reynolds number based on the chord length (ρ and ν are the fluid density and kinematic viscosity). In the present computational analysis we focus our attention on flows at very low Reynolds numbers (which represent a measure of the ratio of inertia forces to viscous forces), in which the viscous effects play a very important role.

4.2 Method of solution

4.2.1 Computational domain

Consider the physical and computational spaces shown in Figure 4.2 which are further divided into five sub-domains (or zones). The steady-state incompressible Navier-Stokes and continuity equations are formulated and solved in a computational rectangular domain (refer to Figures 4.1 and 4.2) obtained by the geometrical transformation

$$X = x \cos\alpha + y \sin\alpha \ , \tag{4.8a}$$

$$Y = f(x,y) \ , \tag{4.8b}$$

where

$$f(x,y) = \begin{cases} -x \sin\alpha + y \cos\alpha & x < 0 \text{ and } -H_2 < y < H_1 \\ \dfrac{y - e_1(x)}{H_1 - [-x \sin\alpha + e_1(x)\cos\alpha]} H_1 \cos\alpha & 0 < x < 1 \text{ and } y > e_1(x) \\ \dfrac{y + e_2(x)}{H_2 + [-x \sin\alpha - e_2(x)\cos\alpha]} H_2 \cos\alpha & 0 < x < 1 \text{ and } y < -e_2(x) \\ \dfrac{H_3 + (-x \sin\alpha + y \cos\alpha)}{H_1 + H_3} H_1 & x > 1 \text{ and } y > -H_3 \\ -H_2 \dfrac{H_3 + (-x \sin\alpha + y \cos\alpha)}{-H_2 + H_3} & x > 1 \text{ and } y < -H_3 \end{cases} \ , \tag{4.8c}$$

in which H_1 and H_2 are the physical coordinates of the upper and lower far-field boundaries (see Figure 4.1) of the computational domain, and $H_3 = \sin\alpha$. The upstream inflow and downstream outflow boundaries of the computational domain are defined by the physical coordinates $X = -L_0$ and $X = L_1 \cos\alpha$.

The geometrical transformation $Y = f(x,y)$ is derived and implemented separately for each resulting computational domain. The correlations between the physical and the resulting rectangular computational domains are given below for each sub-domain.

For Domain 0 ($x < 0$ and $-H_2 < y < H_1$)

$$f(x,y) = -x \sin\alpha + y \cos\alpha \ , \tag{4.9a}$$

$$\frac{\partial f}{\partial x} = -\sin\alpha \ , \tag{4.9b}$$

$$\frac{\partial f}{\partial y} = \cos\alpha \ , \tag{4.9c}$$

$$\frac{\partial^2 f}{\partial x^2} = 0 \ , \tag{4.9d}$$

$$\frac{\partial^2 f}{\partial y^2} = 0 \ , \tag{4.9e}$$

At the upper far-field boundary, one obtains

$y \cos\alpha = H_1 + x \sin\alpha$ and $f(x,y) = H_1$,

and similarly at the lower far-field boundary

$y \cos\alpha = -H_2 + x \sin\alpha$ and $f(x,y) = -H_2$,

where along the line passing through the X -axis, one thus obtains

$y \cos\alpha = x \sin\alpha$ and $f(x,y) = 0$.

For Domain 1 ($0 < x < 1$ and $e_1(x) < y < \left[\frac{H_1}{\cos\alpha} + x \tan\alpha\right]$)

$$f(x,y) = \frac{y - e_1(x)}{H_1 - \left[-x \sin\alpha + e_1(x)\cos\alpha\right]} H_1 \cos\alpha \ , \tag{4.10a}$$

$$\frac{\partial f}{\partial x} = \frac{-\left[y - e_1(x)\right]\sin\alpha - e_1'(x)\overline{G}_1(x,y)}{G_1(x)^2} H_1 \cos\alpha \ , \tag{4.10b}$$

$$\frac{\partial f}{\partial y} = \frac{H_1 \cos\alpha}{G_1(x)} \ , \tag{4.10c}$$

$$\frac{\partial^2 f}{\partial x^2} = \frac{F_1(x,y) + F_2(x,y)}{G_1(x)^4} H_1 \cos\alpha \ , \tag{4.10d}$$

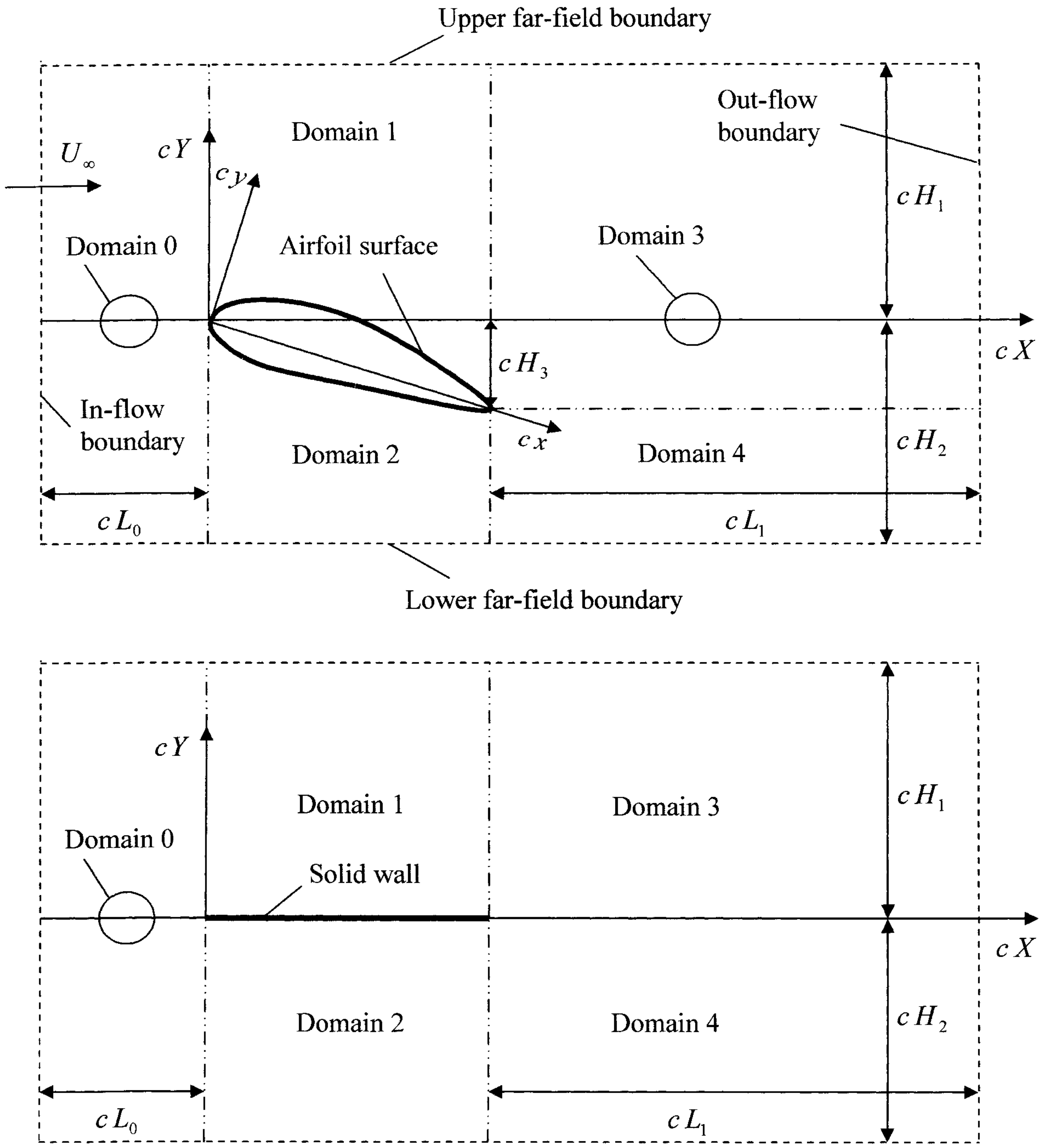

Figure 4.2 Physical and computational domains.

$$\frac{\partial^2 f}{\partial y^2}=0 \ , \tag{4.10e}$$

where

$F_1(x,y) = G_1(x)^2\left[-e_1''(x)\overline{G}_1(x,y)\right]$,

$F_2(x,y) = 2G_1(x)(\sin\alpha - e_1'(x)\cos\alpha)\left\{\left[y - e_1(x)\right]\sin\alpha + e_1'(x)\overline{G}_1(x,y)\right\}$,

$G_1(x) = H_1 + x\ \sin\alpha - e_1(x)\cos\alpha$,

$\overline{G}_1(x,y) = H_1 + x\ \sin\alpha - y\ \cos\alpha$,

At the upper far-field boundary, one obtains

$y\ \cos\alpha = H_1 + x\ \sin\alpha$ and $f(x,y) = H_1$,

and on the airfoil upper surface, the transformation becomes

$y = e_1(x)$ and $f(x,y) = 0$.

For Domain 2 ($0 < x < 1$ and $\left[\dfrac{-H_2}{\cos\alpha} + x\ \tan\alpha\right] < y < -e_2(x)$)

$$f(x,y) = \frac{y + e_2(x)}{H_2 + \left[-x\ \sin\alpha - e_2(x)\cos\alpha\right]} H_2\ \cos\alpha\ , \tag{4.11a}$$

$$\frac{\partial f}{\partial x} = \frac{e_2'(x)\overline{G}_2(x,y) + \left[y + e_2(x)\right]\sin\alpha}{G_2(x)^2} H_2\cos\alpha\ , \tag{4.11b}$$

$$\frac{\partial f}{\partial y} = \frac{H_2\ \cos\alpha}{G_2(x)}\ , \tag{4.11c}$$

$$\frac{\partial^2 f}{\partial x^2} = \frac{\overline{F}_1(x,y) + \overline{F}_2(x,y)}{G_2(x)^4} H_2\cos\alpha\ , \tag{4.11d}$$

$$\frac{\partial^2 f}{\partial y^2} = 0\ , \tag{4.11e}$$

where

$\overline{F}_1(x,y) = G_2(x)^2\left[e_2''(x)\overline{G}_2(x,y)\right]$,

$\overline{F}_2(x,y) = -2G_2(x)(-\sin\alpha - e_2'(x)\cos\alpha)\left\{\left[y + e_2(x)\right]\sin\alpha + e_2'(x)\overline{G}_2(x,y)\right\}$,

$G_2(x) = H_2 - x\ \sin\alpha - e_2(x)\cos\alpha$,

$\overline{G}_2(x,y) = H_2 - x\ \sin\alpha + y\ \cos\alpha$,

At the lower far-field boundary, one obtains

$y\ \cos\alpha = -H_2 + x\ \sin\alpha$ and $f(x,y) = -H_2$,

and on the airfoil lower surface, the transformation becomes

$y = -e_2(x)$ and $f(x,y) = 0$.

For Domain 3 ($x > 1$ and $y > -H_3$)

$$f(x,y) = \frac{H_3 + (-x \sin\alpha + y \cos\alpha)}{H_1 + H_3} H_1 , \tag{4.12a}$$

$$\frac{\partial f}{\partial x} = -\sin\alpha \frac{H_1}{H_1 + H_3} , \tag{4.12b}$$

$$\frac{\partial f}{\partial y} = \cos\alpha \frac{H_1}{H_1 + H_3} , \tag{4.12c}$$

$$\frac{\partial^2 f}{\partial x^2} = 0 , \tag{4.12d}$$

$$\frac{\partial^2 f}{\partial y^2} = 0 , \tag{4.12e}$$

At the upper far-field boundary, one obtains

$y \cos\alpha = H_1 + x \sin\alpha$ and $f(x,y) = H_1$,

and on the common boundary dividing domains 3 and 4, which becomes a line passing through the X -axis , one obtains

$y \cos\alpha = -H_3 + x \sin\alpha$ and $f(x,y) = 0$.

For Domain 4 ($x > 1$ and $y < -H_3$)

$$f(x,y) = -H_2 \frac{H_3 + (-x \sin\alpha + y \cos\alpha)}{-H_2 + H_3} , \tag{4.13a}$$

$$\frac{\partial f}{\partial x} = -\sin\alpha \frac{H_2}{H_2 - H_3} , \tag{4.13b}$$

$$\frac{\partial f}{\partial y} = \cos\alpha \frac{H_2}{H_2 - H_3} , \tag{4.13c}$$

$$\frac{\partial^2 f}{\partial x^2} = 0 , \tag{4.13d}$$

$$\frac{\partial^2 f}{\partial y^2} = 0 , \tag{4.13e}$$

At the lower far-field boundary, one obtains

$y \cos\alpha = -H_2 + x \sin\alpha$ and $f(x,y) = -H_2$, and on the common boundary dividing domains 3 and 4, which becomes a line passing through the X-axis, one obtains

$y \cos\alpha = -H_3 + x \sin\alpha$ and $f(x,y) = 0$.

The coordinate transformation of the form (4.8a) and (4.8b) is used to transform the Navier-Stokes and continuity equations from the physical domain (x,y) to the rectangular computational domain (X,Y). By applying the chain rule of partial differentiation, the derivatives appearing in the governing flow equations become

$$\frac{\partial}{\partial x} = \frac{\partial X}{\partial x}\frac{\partial}{\partial X} + \frac{\partial Y}{\partial x}\frac{\partial}{\partial Y} , \tag{4.14}$$

$$\frac{\partial}{\partial y} = \frac{\partial X}{\partial y}\frac{\partial}{\partial X} + \frac{\partial Y}{\partial y}\frac{\partial}{\partial Y} , \tag{4.15}$$

and upon introducing the derivatives of the transformation equations, one obtains

$$\frac{\partial}{\partial x} = \cos\alpha \ \frac{\partial}{\partial X} + \frac{\partial f}{\partial x}\frac{\partial}{\partial Y} , \tag{4.16a}$$

$$\frac{\partial}{\partial y} = \sin\alpha \ \frac{\partial}{\partial X} + \frac{\partial f}{\partial y}\frac{\partial}{\partial Y} . \tag{4.16b}$$

Similarly, the second-order derivatives are then defined by

$$\frac{\partial^2}{\partial x^2} = (\cos\alpha)^2 \ \frac{\partial^2}{\partial X^2} + 2 \cos\alpha \ \frac{\partial f}{\partial x}\frac{\partial^2}{\partial X \partial Y} + \left(\frac{\partial f}{\partial x}\right)^2 \frac{\partial^2}{\partial Y^2} + \frac{\partial^2 f}{\partial x^2}\frac{\partial}{\partial Y} , \tag{4.17a}$$

$$\frac{\partial^2}{\partial y^2} = (\sin\alpha)^2 \ \frac{\partial^2}{\partial X^2} + 2 \sin\alpha \ \frac{\partial f}{\partial y}\frac{\partial^2}{\partial X \partial Y} + \left(\frac{\partial f}{\partial y}\right)^2 \frac{\partial^2}{\partial Y^2} + \frac{\partial^2 f}{\partial y^2}\frac{\partial}{\partial Y} . \tag{4.17b}$$

In the computational domain obtained by this coordinate transformation, the steady incompressible Navier-Stokes and continuity equations become

$$\mathbf{G}(\mathbf{V},p) = \mathbf{0} , \tag{4.18}$$

$$\mathbf{D}\,\mathbf{V} = 0 , \tag{4.19}$$

where

$$\mathbf{D}\,\mathbf{V} = C_7 \frac{\partial u}{\partial X} + C_2 \frac{\partial u}{\partial Y} + C_8 \frac{\partial v}{\partial X} + C_3 \frac{\partial v}{\partial Y} , \tag{4.20}$$

$$\mathbf{G}(\mathbf{V},p) = \begin{Bmatrix} G_u(u,v,p) \\ G_v(u,v,p) \end{Bmatrix} , \tag{4.21}$$

$$G_u(u,v,p) = C_7\frac{\partial(uu)}{\partial X} + C_2\frac{\partial(uu)}{\partial Y} + C_8\frac{\partial(vu)}{\partial X} + C_3\frac{\partial(vu)}{\partial Y} + C_7\frac{\partial p}{\partial X} + C_2\frac{\partial p}{\partial Y}$$

$$+ C_1\frac{\partial^2 u}{\partial X^2} + C_6\frac{\partial^2 u}{\partial X\partial Y} + C_5\frac{\partial^2 u}{\partial Y^2} + C_4\frac{\partial u}{\partial Y}\ , \tag{4.22a}$$

$$G_v(u,v,p) = C_8\frac{\partial(vv)}{\partial X} + C_3\frac{\partial(vv)}{\partial Y} + C_7\frac{\partial(uv)}{\partial X} + C_2\frac{\partial(uv)}{\partial Y} + C_8\frac{\partial p}{\partial X} + C_3\frac{\partial p}{\partial Y}$$

$$+ C_1\frac{\partial^2 v}{\partial X^2} + C_6\frac{\partial^2 v}{\partial X\partial Y} + C_5\frac{\partial^2 v}{\partial Y^2} + C_4\frac{\partial v}{\partial Y}\ , \tag{4.22b}$$

in which

$$C_1 = -\frac{1}{\mathrm{Re}}\ , \tag{4.23}$$

$$C_2 = \frac{\partial f}{\partial x}\ , \tag{4.24}$$

$$C_3 = \frac{\partial f}{\partial y}\ , \tag{4.25}$$

$$C_4 = -\frac{1}{\mathrm{Re}}\left(\frac{\partial^2 f}{\partial x^2} + \frac{\partial^2 f}{\partial y^2}\right), \tag{4.26}$$

$$C_5 = -\frac{1}{\mathrm{Re}}\left[\left(\frac{\partial f}{\partial x}\right)^2 + \left(\frac{\partial f}{\partial y}\right)^2\right], \tag{4.27}$$

$$C_6 = -\frac{2}{\mathrm{Re}}\left[\cos\alpha\,\frac{\partial f}{\partial x} + \sin\alpha\,\frac{\partial f}{\partial y}\right], \tag{4.28}$$

$$C_7 = \cos\alpha\ , \tag{4.29}$$

$$C_8 = \sin\alpha\ . \tag{4.30}$$

4.2.2 Method of artificial compressibility and pseudo-time relaxation technique

The pseudo (or artificial) compressibility method consists in adding a pseudo-time derivative of the pressure to the continuity equation. At steady state, the divergence-free condition is satisfied and the incompressible viscous flow equations retain its physical meaning. The use of artificial compressibility for the analysis of incompressible flows was first suggested by Chorin [30-32] and frequently used since by other authors (such as Temam [182], Rogers and Kwak [164], Soh [175] and Mateescu *et al.* [125, 126]).

The continuity and incompressible Navier-Stokes equations are augmented by pseudo-time derivative terms involving pressure and velocity in the form

$$\delta\frac{\partial p}{\partial t}+\mathbf{D}\mathbf{V}=0\ , \tag{4.31}$$

$$\frac{\partial \mathbf{V}}{\partial t}+\mathbf{G}(\mathbf{V},p)=\mathbf{0}\ , \tag{4.32}$$

$$\mathbf{V}=\begin{Bmatrix} u \\ v \end{Bmatrix}\ . \tag{4.33}$$

where δ represents an artificially-added compressibility relaxation parameter, $p=\rho/\delta$ is the artificial equation of state and ρ represents the pseudo density. The pseudo-time t in this formulation is not a real physical quantity; however it is similar to the physical time in a compressible flow problem. Although many authors proposed different methods to determine the value of the artificial relaxation parameter (for instance, see Hirsch [79], Chang and Kwak [27], Soh [175] and Mateescu *et al.* [125, 126]), an optimal value of δ is better obtained by numerical experimentation.

The pseudo-continuity and Navier-Stokes equations (4.31) and (4.32) are solved in pseudo-time until a steady state is reached and the physical divergence-free condition is satisfied. An implicit Euler scheme is then used in this respect to discretize these equations in pseudo-time, and the resulting equations are expressed as

$$\frac{\mathbf{V}^{n+1}-\mathbf{V}^{n}}{\Delta t}+\mathbf{G}^{n+1}(\mathbf{V},p)=\mathbf{0}\ , \tag{4.34}$$

$$\frac{p^{n+1}-p^{n}}{\Delta t}+\frac{1}{\delta}\,\mathbf{D}\mathbf{V}^{n+1}=0\ , \tag{4.35}$$

where $\Delta t=t^{n+1}-t^{n}$ is the pseudo-time step and the superscript n indicates the solution at the pseudo-time level $t^{n}=n\,\Delta t$. By introducing the pseudo-time variations

$$\Delta\mathbf{V}=\mathbf{V}^{n+1}-\mathbf{V}^{n}\ , \tag{4.36}$$

$$\Delta\mathbf{G}=\mathbf{G}^{n+1}-\mathbf{G}^{n}\ , \tag{4.37}$$

$$\Delta p=p^{n+1}-p^{n}, \tag{4.38}$$

equations (4.34) and (4.35) can then be expressed in pseudo-delta form

$$\Delta \mathbf{V} + \Delta t \; \Delta \mathbf{G} = -\Delta t \; \mathbf{G}^n \; , \tag{4.39}$$

$$\Delta p + \frac{\Delta t}{\delta} \mathbf{D}(\Delta \mathbf{V}) = -\frac{\Delta t}{\delta} \mathbf{D} \mathbf{V}^n \; . \tag{4.40}$$

The implicit system of equations (4.39) and (4.40) are nonlinearly coupled by the term $\Delta \mathbf{G}$. The initial conditions at time $t^n = t^1$ required to start the pseudo-time relaxation technique are taken to be $\mathbf{V}^n$ and p^n. The corresponding values on the boundaries of the fluid domain are imposed as boundary conditions and kept unchanged. Then equations (4.39) and (4.40) are iterated in pseudo-time until a steady state is reached at $t^n = t^k$, at which point the pseudo-time variations are equal to zero ($\Delta \mathbf{V} = 0$ and $\Delta p = 0$) and hence $\mathbf{V}^{k+1} = \mathbf{V}^k$ and $p^{k+1} = p^k$. This iterative solution procedure in conjunction with the spatial discretization will be discussed in detail in the following sections.

4.2.3 Alternating direction implicit technique

In order to facilitate the pseudo-time relaxation technique, the implicit nonlinear system (4.39) and (4.40) must be appropriately linearized. This is done by lagging the velocity components, which are expressed in pseudo-time delta form as

$$\Delta \mathbf{V} = \begin{bmatrix} \Delta u \\ \Delta v \end{bmatrix} , \tag{4.41}$$

$$\Delta \mathbf{G} = \begin{bmatrix} \Delta G_u(u,v,p) \\ \Delta G_v(u,v,p) \end{bmatrix} , \tag{4.42}$$

where

$$\Delta G_u(u,v,p) = C_7 \frac{\partial (u^n \Delta u)}{\partial X} + C_2 \frac{\partial (u^n \Delta u)}{\partial Y} + C_8 \frac{\partial (v^n \Delta u)}{\partial X} + C_3 \frac{\partial (v^n \Delta u)}{\partial Y}$$

$$+ C_7 \frac{\partial \Delta p}{\partial X} + C_2 \frac{\partial \Delta p}{\partial Y} + C_1 \frac{\partial^2 \Delta u}{\partial X^2} + C_6 \frac{\partial^2 \Delta u}{\partial X \partial Y} + C_5 \frac{\partial^2 \Delta u}{\partial Y^2} + C_4 \frac{\partial \Delta u}{\partial Y} \; , \tag{4.43a}$$

$$\Delta G_v(u,v,p) = C_8 \frac{\partial (v^n \Delta v)}{\partial X} + C_3 \frac{\partial (v^n \Delta v)}{\partial Y} + C_7 \frac{\partial (u^n \Delta v)}{\partial X} + C_2 \frac{\partial (u^n \Delta v)}{\partial Y}$$

$$+ C_8 \frac{\partial \Delta p}{\partial X} + C_3 \frac{\partial \Delta p}{\partial Y} + C_1 \frac{\partial^2 \Delta v}{\partial X^2} + C_6 \frac{\partial^2 \Delta v}{\partial X \partial Y} + C_5 \frac{\partial^2 \Delta v}{\partial Y^2} + C_4 \frac{\partial \Delta v}{\partial Y} \; , \tag{4.43b}$$

and

$$\mathbf{G}^n(\mathbf{V},p)=\begin{Bmatrix} G_u\left(u^n,v^n,p^n\right) \\ G_v\left(u^n,v^n,p^n\right) \end{Bmatrix} . \tag{4.44}$$

This first-order accurate approximation is consistent with the order of accuracy of the implicit Euler pseudo-time discretization. The delta-form implicit system (4.39) and (4.40) is then expressed in the general matrix form

$$\left[\mathbf{I}+\Delta t\left(\mathbf{D}_X+\mathbf{D}_Y\right)\right]\Delta\mathbf{f}=\Delta t\,\mathbf{S} \ , \tag{4.45}$$

where $\mathbf{I}$ is the identity matrix, and

$$\Delta\mathbf{f}=\begin{bmatrix} \Delta u \\ \Delta v \\ \Delta p \end{bmatrix} , \tag{4.46}$$

$$\mathbf{D}_X=\begin{bmatrix} M & 0 & C_7\dfrac{\partial}{\partial X} \\ 0 & M & C_8\dfrac{\partial}{\partial X} \\ \dfrac{C_7}{\delta}\dfrac{\partial}{\partial X} & \dfrac{C_8}{\delta}\dfrac{\partial}{\partial X} & 0 \end{bmatrix} , \tag{4.47a}$$

$$\mathbf{D}_Y=\begin{bmatrix} N & 0 & C_2\dfrac{\partial}{\partial Y} \\ 0 & N & C_3\dfrac{\partial}{\partial Y} \\ \dfrac{C_2}{\delta}\dfrac{\partial}{\partial Y} & \dfrac{C_3}{\delta}\dfrac{\partial}{\partial Y} & 0 \end{bmatrix} , \tag{4.47b}$$

$$\mathbf{S}=\begin{bmatrix} -G_u\left(u^n,v^n,p^n\right) \\ -G_v\left(u^n,v^n,p^n\right) \\ -(1/\delta)\mathbf{D}\mathbf{V}^n \end{bmatrix} , \tag{4.48}$$

in which the differential operators M and N are defined as

$$M\phi=C_7\frac{\partial\left(u^n\phi\right)}{\partial X}+C_8\frac{\partial\left(v^n\phi\right)}{\partial X}+C_1\frac{\partial^2\phi}{\partial X^2} , \tag{4.49a}$$

$$N\phi=C_2\frac{\partial\left(u^n\phi\right)}{\partial Y}+C_3\frac{\partial\left(v^n\phi\right)}{\partial Y}+C_6\frac{\partial^2\phi}{\partial X\partial Y}+C_5\frac{\partial^2\phi}{\partial Y^2}+C_4\frac{\partial\phi}{\partial Y} . \tag{4.49b}$$

By applying an approximate factorization to the left-hand side of the general matrix form (4.45), one thus obtains

$$\left[\mathbf{I} + \Delta t\left(\mathbf{D}_X + \mathbf{D}_Y\right)\right]\Delta\mathbf{f} = \left(\mathbf{I} + \Delta t\, \mathbf{D}_Y\right)\left(\mathbf{I} + \Delta t\, \mathbf{D}_X\right)\Delta\mathbf{f} \ ,$$

Hence, equation (4.45) is rewritten as

$$\left(\mathbf{I} + \Delta t\, \mathbf{D}_Y\right)\left(\mathbf{I} + \Delta t\, \mathbf{D}_X\right)\Delta\mathbf{f} = \Delta t\, \mathbf{S} \ ,$$

A factored alternating direction implicit (ADI) scheme is used to solve this system of equations. The solution proceeds with the alternating sequence of a Y-sweep followed by a X-sweep. Upon introducing the intermediate variable vector

$$\Delta\bar{\mathbf{f}} = \left(\mathbf{I} + \Delta t\, \mathbf{D}_X\right)\Delta\mathbf{f} \ , \tag{4.50}$$

where

$$\Delta\bar{\mathbf{f}} = \begin{bmatrix} \Delta\bar{u} \\ \Delta\bar{v} \\ \Delta\bar{p} \end{bmatrix} , \tag{4.51}$$

the Y-sweep is defined by

$$\left(\mathbf{I} + \Delta t\, \mathbf{D}_Y\right)\Delta\bar{\mathbf{f}} = \Delta t\, \mathbf{S} \ , \tag{4.52}$$

whereas the X-sweep is given by

$$\left(\mathbf{I} + \Delta t\, \mathbf{D}_X\right)\Delta\mathbf{f} = \Delta\bar{\mathbf{f}} \ . \tag{4.53}$$

In scalar form the Y-sweep matrix equation (4.52) is then expressed as

$$\Delta\bar{u} + \Delta t\left[C_2 \frac{\partial(u^n \Delta\bar{u})}{\partial Y} + C_3 \frac{\partial(v^n \Delta\bar{u})}{\partial Y} + C_6 \frac{\partial^2 \Delta\bar{u}}{\partial X \partial Y} + C_5 \frac{\partial^2 \Delta\bar{u}}{\partial Y^2} + C_4 \frac{\partial \Delta\bar{u}}{\partial Y} + C_2 \frac{\partial \Delta\bar{p}}{\partial Y}\right]$$
$$= -\Delta t\, G_u\left(u^n, v^n, p^n\right) , \tag{4.54}$$

$$\Delta\bar{v} + \Delta t\left[C_2 \frac{\partial\left(u^n \Delta\bar{v}\right)}{\partial Y} + C_3 \frac{\partial\left(v^n \Delta\bar{v}\right)}{\partial Y} + C_6 \frac{\partial^2 \Delta\bar{v}}{\partial X \partial Y} + C_5 \frac{\partial^2 \Delta\bar{v}}{\partial Y^2} + C_4 \frac{\partial \Delta\bar{v}}{\partial Y} + C_3 \frac{\partial \Delta\bar{p}}{\partial Y}\right]$$
$$= -\Delta t\, G_v\left(u^n, v^n, p^n\right) , \tag{4.55}$$

$$\Delta\bar{p} + \frac{\Delta t}{\delta}\left[C_2 \frac{\partial \Delta\bar{u}}{\partial Y} + C_3 \frac{\partial \Delta\bar{v}}{\partial Y}\right] = -\frac{\Delta t}{\delta}\mathbf{DV}^n \ , \tag{4.56}$$

whereas Δu, Δv and Δp are solved subsequently in the X-sweep defined by the scalar equations

$$\Delta u+\Delta t\left[C_7\frac{\partial(u^n\Delta u)}{\partial X}+C_8\frac{\partial(v^n\Delta u)}{\partial X}+C_1\frac{\partial^2\Delta u}{\partial X^2}+C_7\frac{\partial\Delta p}{\partial X}\right]=\Delta\bar{u}\ , \qquad (4.57)$$

$$\Delta v+\Delta t\left[C_7\frac{\partial(u^n\Delta v)}{\partial X}+C_8\frac{\partial(v^n\Delta v)}{\partial X}+C_1\frac{\partial^2\Delta v}{\partial X^2}+C_8\frac{\partial\Delta p}{\partial X}\right]=\Delta\bar{v}\ , \qquad (4.58)$$

$$\Delta p+\frac{\Delta t}{\delta}\left[C_7\frac{\partial\Delta u}{\partial X}+C_8\frac{\partial\Delta v}{\partial X}\right]=\Delta\bar{p}\ . \qquad (4.59)$$

By solving the X-sweep and Y-sweep scalar equations (4.54-4.59), the variables $u^{n+1}=u^n+\Delta u$, $v^{n+1}=v^n+\Delta v$ and $p^{n+1}=p^n+\Delta p$ are hence obtained. The solution can then be progressed to the next pseudo-time step until convergence when Δu, Δv and Δp are equal to zero. During this alternating direction implicit technique, Δu and Δv on the boundaries of the computational domain are zero, as the values u^n and v^n are imposed at the beginning of the pseudo-time iteration and kept constant.

4.2.4 Spatial discretization

The Navier-Stokes and continuity scalar equations (4.54-4.59) are further spatially discretized by central differencing on a staggered grid. In order to obtain a good spatial resolution, stretched grids were generated based on hyperbolic sine stretching functions in both the X- and Y- directions. This will cluster more points in regions of higher velocity gradients, for example near the leading and trailing edges of the airfoil. A sketch of points clustering strategy is shown in Figure 4.3.

Consider a domain bounded by two parallel boundaries in the Y- direction with $(J+1)$ points distributed between them, the hyperbolic sine stretching function gives the coordinates Y_j, $j=0,...,J$, of the grid points between the two boundaries by the relation

$$Y_j=Y_0+(Y_J-Y_0)\frac{\sinh\left(\gamma\frac{j}{J}\right)}{\sinh\gamma}\ , \qquad (4.60)$$

where Y_0 and Y_J is the coordinates of the points where the mesh is the finest and coarsest, respectively. The amount of stretching is controlled by the parameter γ and the larger it is, the more the points are clustered near the boundary, in this case Y_0. Similarly, if we want to stretch the grid in the X-direction, we obtain for the locations X_i of the $(I+1)$ points between X_0 and X_I

$$X_i = X_0 + (X_I - X_0)\frac{\sinh\left(\gamma \frac{i}{I}\right)}{\sinh\gamma}, \tag{4.61}$$

Different uses of the hyperbolic sine stretching functions are described by Vinokur [193]. The evaluation of the spatial derivatives that appear in the X-sweep and Y-sweep scalar equations (4.54-4.59) on a stretched grid is described below.

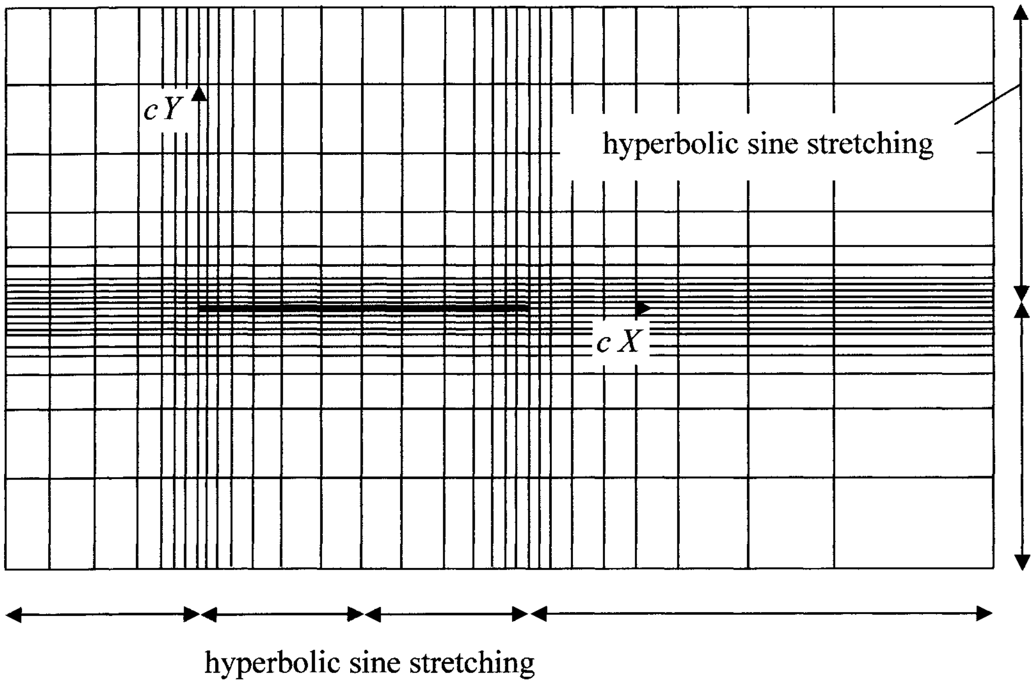

Figure 4.3 A sketch of grid stretching in the rectangular computational domain.

Consider a one-dimensional portion of a typical irregular stretched finite-difference grid, shown in Figure 4.4.

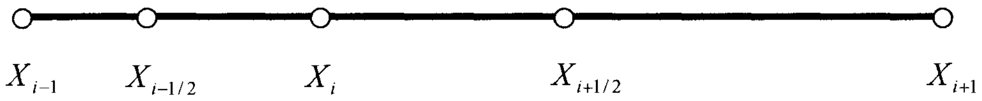

Figure 4.4 Portion of a one-dimensional stretched finite-difference mesh.

Denote by X_i the coordinate of a mesh point and $f_i = f(X_i)$ the function value at that point. The partial derivative of a function $f(X)$ with respect to X is numerically evaluated using central-differencing approximation through the use of Taylor series expansions. Thus, one obtains

$$\left.\frac{\partial f}{\partial X}\right|_{X=X_i} = \frac{f_{i+1} - f_{i-1}}{X_{i+1} - X_{i-1}} , \tag{4.62a}$$

or in the alternative form

$$\left.\frac{\partial f}{\partial X}\right|_{X=X_i} = \frac{f_{i+1/2} - f_{i-1/2}}{X_{i+1/2} - X_{i-1/2}} , \tag{4.62b}$$

Similarly, the numerical evaluation of the second partial derivative of the function $f(X)$ is done as

$$\begin{aligned}\left.\frac{\partial^2 f}{\partial X^2}\right|_{X=X_i} = \left[\frac{\partial}{\partial X}\left(\frac{\partial f}{\partial X}\right)\right]_{X=X_i} &= \frac{1}{X_{i+1/2} - X_{i-1/2}}\left[\left(\frac{\partial f}{\partial X}\right)_{X_{i+1/2}} - \left(\frac{\partial f}{\partial X}\right)_{X_{i-1/2}}\right] \\ &= \frac{1}{X_{i+1/2} - X_{i-1/2}}\left[\frac{f_{i+1} - f_i}{X_{i+1} - X_i} - \frac{f_i - f_{i-1}}{X_i - X_{i-1}}\right] . \end{aligned} \tag{4.63}$$

The Navier-Stokes and continuity flow equations (4.54-4.59) is centrally differenced on a stretched staggered grid [76] in the computational space, as shown schematically in Figure 4.5. In a staggered grid, the velocity components u and v are defined at different grid points, namely at (X_i^u, Y_j^u) and (X_i^v, Y_j^v) for $u_{i,j}$ and $v_{i,j}$, respectively, which are also different from the grid point where the pressure $p_{i,j}$ is defined, which is (X_i^v, Y_j^u). For a cell (i, j) centered at the point (X_i^v, Y_j^u) where the pressure is defined, the four sides correspond to grid points where $u_{i-1,j}$, $u_{i,j}$, $v_{i,j-1}$ and $v_{i,j}$ are defined. Moreover, the X- and Y- momentum and the continuity equations (4.54-4.59) are centrally differenced about the points where $u_{i,j}$, $v_{i,j}$ and $p_{i,j}$ are defined, respectively.

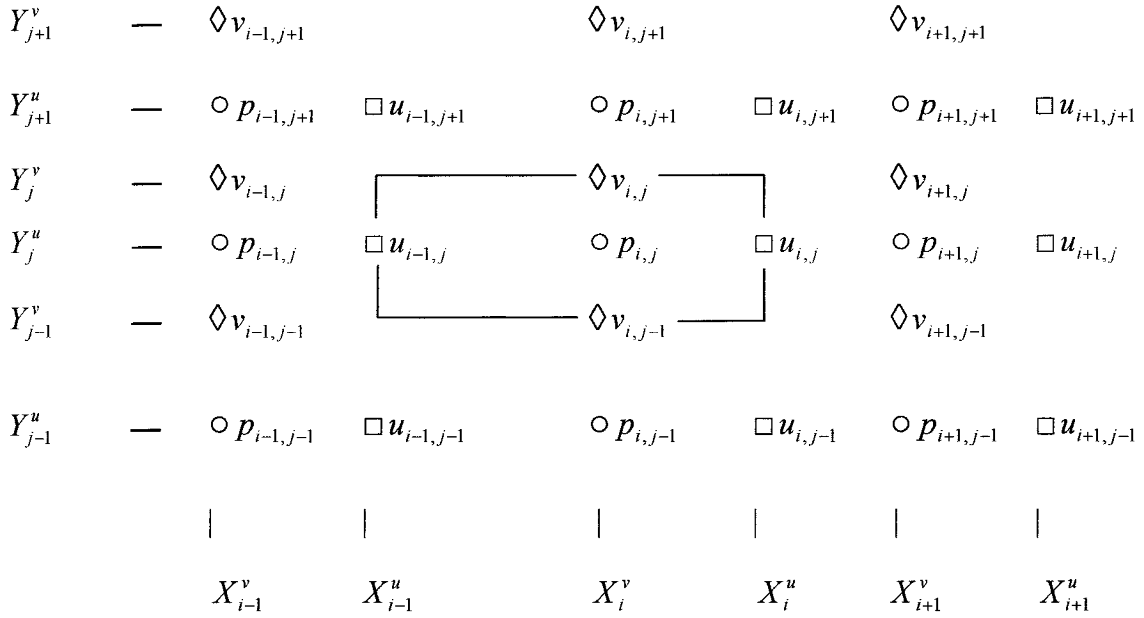

Figure 4.5 Schematic representation of the staggered grid used in the spatial differentiation.

In order to perform the spatial discretization of the equations, we first introduce the linear interpolates of the velocity and pressure components on the staggered mesh, which are given by

$$u_u^{X+} = \frac{\nabla X_{i+1}^u\, u_{i,j} + \nabla X_{i+1}^v\, u_{i+1,j}}{\Delta X_{i+1}^v}, \qquad u_u^{X-} = \frac{\nabla X_i^u\, u_{i-1,j} + \nabla X_i^v\, u_{i,j}}{\Delta X_i^v}, \tag{4.64a}$$

$$u_u^{Y+} = \frac{\nabla Y_{j+1}^u\, u_{i,j} + \nabla Y_j^v\, u_{i,j+1}}{\Delta Y_j^v}, \qquad u_u^{Y-} = \frac{\nabla Y_j^u\, u_{i,j-1} + \nabla Y_{j-1}^v\, u_{i,j}}{\Delta Y_{j-1}^v}, \tag{4.64b}$$

$$v_u^{Y+} = \frac{\nabla X_{i+1}^v\, v_{i,j} + \nabla X_i^u\, v_{i+1,j}}{\Delta X_i^u}, \qquad v_u^{Y-} = \frac{\nabla X_{i+1}^v\, v_{i,j-1} + \nabla X_i^u\, v_{i+1,j-1}}{\Delta X_i^u}, \tag{4.64c}$$

$$v_v^{X+} = \frac{\nabla X_{i+1}^v\, v_{i,j} + \nabla X_i^u\, v_{i+1,j}}{\Delta X_i^u}, \qquad v_v^{X-} = \frac{\nabla X_i^v\, v_{i-1,j} + \nabla X_{i-1}^u\, v_{i,j}}{\Delta X_{i-1}^u}, \tag{4.64d}$$

$$v_v^{Y+} = \frac{\nabla Y_{j+1}^v\, v_{i,j} + \nabla Y_{j+1}^u\, v_{i,j+1}}{\Delta Y_{j+1}^u}, \qquad v_v^{Y-} = \frac{\nabla Y_j^v\, v_{i,j-1} + \nabla Y_j^u\, v_{i,j}}{\Delta Y_j^u}, \tag{4.64e}$$

$$(u_v)^{--}_{i,j} = \frac{\nabla Y^u_j\, U_1 + \nabla Y^v_{j-1}\, U_2}{\Delta Y^v_{j-1}} , \qquad (u_v)^{++}_{i-1,j-1} = (u_v)^{--}_{i,j} , \tag{4.65a}$$

$$(u_v)^{-+}_{i,j-1} = (u_v)^{--}_{i,j} , \quad (u_v)^{+-}_{i-1,j} = (u_v)^{--}_{i,j} , \tag{4.65b}$$

where

$$U_1 = \frac{\nabla X^v_i\, u_{i,j-1} + \nabla X^u_i\, u_{i-1,j-1}}{\Delta X^v_i}, \qquad U_2 = \frac{\nabla X^v_i\, u_{i,j} + \nabla X^u_i\, u_{i-1,j}}{\Delta X^v_i} , \tag{4.65c}$$

$$(v_u)^{--}_{i,j} = \frac{\nabla Y^v_j\, V_1 + \nabla Y^u_j\, V_2}{\Delta Y^u_j} , \qquad (v_u)^{++}_{i-1,j-1} = (v_u)^{--}_{i,j} , \tag{4.66a}$$

$$(v_u)^{-+}_{i,j-1} = (v_u)^{--}_{i,j} , \quad (v_u)^{+-}_{i-1,j} = (v_u)^{--}_{i,j} , \tag{4.66b}$$

where

$$V_1 = \frac{\nabla X^v_i\, v_{i-1,j-1} + \nabla X^u_{i-1}\, v_{i,j-1}}{\Delta X^u_{i-1}}, \qquad V_2 = \frac{\nabla X^v_i\, v_{i-1,j} + \nabla X^u_{i-1}\, v_{i,j}}{\Delta X^u_{i-1}} , \tag{4.66c}$$

$$(p_v)^{X+}_{i,j} = (p_u)^{Y+}_{i,j} = \frac{\nabla Y^u_{j+1}\, P_1 + \nabla Y^v_j\, P_2}{\Delta Y^v_j} , \tag{4.67a}$$

$$(p_v)^{X-}_{i+1,j} = (p_v)^{X+}_{i,j} , \quad (p_u)^{Y-}_{i,j+1} = (p_u)^{Y+}_{i,j} , \tag{4.67b}$$

where

$$P_1 = \frac{\nabla X^v_{i+1}\, p_{i,j} + \nabla X^u_i\, p_{i+1,j}}{\Delta X^u_i} , \qquad P_2 = \frac{\nabla X^v_{i+1}\, p_{i,j+1} + \nabla X^u_i\, p_{i+1,j+1}}{\Delta X^u_i} . \tag{4.67c}$$

where, in these relations, Δ and ∇, which we will sometimes refer to as the delta's and nabla's of the grid point coordinates, denote the central and backward difference operators applied to these grid point coordinates. These are defined as

$$\Delta X^u_i = X^v_{i+1} - X^v_i , \qquad \Delta X^v_i = X^u_i - X^u_{i-1} , \tag{4.68a}$$

$$\Delta Y^u_j = Y^v_j - Y^v_{j-1} , \qquad \Delta Y^v_j = Y^u_{j+1} - Y^u_j , \tag{4.68b}$$

$$\nabla X^u_i = X^u_i - X^v_i , \qquad \nabla X^v_i = X^v_i - X^u_{i-1} , \tag{4.68c}$$

$$\nabla Y^u_j = Y^u_j - Y^v_{j-1} , \qquad \nabla Y^v_j = Y^v_j - Y^u_j . \tag{4.68d}$$

The spatial discretization of the partial derivatives that appear in the X- momentum equation (4.22a) denoted by $G_u(u,v,p)$ is performed using central differencing about the point where $u_{i,j}$ is defined. Thus, one obtains

$$G_u(u,v,p) = C_7\frac{\partial(uu)}{\partial X} + C_2\frac{\partial(uu)}{\partial Y} + C_8\frac{\partial(vu)}{\partial X} + C_3\frac{\partial(vu)}{\partial Y} + C_7\frac{\partial p}{\partial X} + C_2\frac{\partial p}{\partial Y}$$

$$+ C_1\frac{\partial^2 u}{\partial X^2} + C_6\frac{\partial^2 u}{\partial X\partial Y} + C_5\frac{\partial^2 u}{\partial Y^2} + C_4\frac{\partial u}{\partial Y}\ , \tag{4.69}$$

where

$$\frac{\partial(uu)}{\partial X} = \frac{u_u^{X+}\,u_u^{X+} - u_u^{X-}\,u_u^{X-}}{\Delta X_i^u}\ , \tag{4.70}$$

$$\frac{\partial(uu)}{\partial Y} = \frac{u_u^{Y+}\,u_u^{Y+} - u_u^{Y-}\,u_u^{Y-}}{\Delta Y_j^u}\ , \tag{4.71}$$

$$\frac{\partial(vu)}{\partial X} = \frac{\left(v_v^{Y-}\right)_{i+1,j}u_u^{X+} - \left(v_v^{Y-}\right)_{i,j}u_u^{X-}}{\Delta X_i^u}\ , \tag{4.72}$$

$$\frac{\partial(vu)}{\partial Y} = \frac{v_u^{Y+}\,u_u^{Y+} - v_u^{Y-}\,u_u^{Y-}}{\Delta Y_j^u}\ , \tag{4.73}$$

$$\frac{\partial p}{\partial X} = \frac{p_{i+1,j} - p_{i,j}}{\Delta X_i^u}\ , \tag{4.74}$$

$$\frac{\partial p}{\partial Y} = \frac{(p_u)_{i,j}^{Y+} - (p_u)_{i,j}^{Y-}}{\Delta Y_j^u}\ , \tag{4.75}$$

$$\frac{\partial^2 u}{\partial X^2} = \frac{1}{\Delta X_i^u}\left[\left(\frac{u_{i+1,j} - u_{i,j}}{\Delta X_{i+1}^v}\right) - \left(\frac{u_{i,j} - u_{i-1,j}}{\Delta X_i^v}\right)\right], \tag{4.76}$$

$$\frac{\partial^2 u}{\partial X\partial Y} = \frac{1}{\Delta Y_j^u}\left[\left(\frac{(u_v)_{i,j}^{++} - (u_v)_{i,j}^{-+}}{\Delta X_i^u}\right) - \left(\frac{(u_v)_{i,j}^{+-} - (u_v)_{i,j}^{--}}{\Delta X_i^u}\right)\right], \tag{4.77}$$

$$\frac{\partial^2 u}{\partial Y^2} = \frac{1}{\Delta Y_j^u}\left[\left(\frac{u_{i,j+1} - u_{i,j}}{\Delta Y_j^v}\right) - \left(\frac{u_{i,j} - u_{i,j-1}}{\Delta Y_{j-1}^v}\right)\right], \tag{4.78}$$

$$\frac{\partial u}{\partial Y} = \frac{u_u^{Y+} - u_u^{Y-}}{\Delta Y_j^u}\ . \tag{4.79}$$

Similarly, the spatial discretization of the partial derivatives that appear in the Y-momentum equation (4.22b) denoted by $G_v(u,v,p)$ is performed using central differencing about the point where $v_{i,j}$ is defined. Thus, one obtains

$$G_v(u,v,p) = C_8 \frac{\partial(vv)}{\partial X} + C_3 \frac{\partial(vv)}{\partial Y} + C_7 \frac{\partial(uv)}{\partial X} + C_2 \frac{\partial(uv)}{\partial Y} + C_8 \frac{\partial p}{\partial X} + C_3 \frac{\partial p}{\partial Y}$$

$$+ C_1 \frac{\partial^2 v}{\partial X^2} + C_6 \frac{\partial^2 v}{\partial X \partial Y} + C_5 \frac{\partial^2 v}{\partial Y^2} + C_4 \frac{\partial v}{\partial Y} \ , \tag{4.80}$$

where

$$\frac{\partial(vv)}{\partial X} = \frac{v_v^{X+} v_v^{X+} - v_v^{X-} v_v^{X-}}{\Delta X_i^v} \ , \tag{4.81}$$

$$\frac{\partial(vv)}{\partial Y} = \frac{v_v^{Y+} v_v^{Y+} - v_v^{Y-} v_v^{Y-}}{\Delta Y_j^v} \ , \tag{4.82}$$

$$\frac{\partial(uv)}{\partial X} = \frac{u_v^{X+} v_v^{X+} - u_v^{X-} v_v^{X-}}{\Delta X_i^v} \ , \tag{4.83}$$

$$\frac{\partial(uv)}{\partial Y} = \frac{u_v^{Y+} v_v^{Y+} - u_v^{Y-} v_v^{Y-}}{\Delta Y_j^v} \ , \tag{4.84}$$

$$\frac{\partial p}{\partial X} = \frac{(p_v)_{i,j}^{X+} - (p_v)_{i,j}^{X-}}{\Delta X_i^v} \ , \tag{4.85}$$

$$\frac{\partial p}{\partial Y} = \frac{p_{i,j+1} - p_{i,j}}{\Delta Y_j^v} \ , \tag{4.86}$$

$$\frac{\partial^2 v}{\partial X^2} = \frac{1}{\Delta X_i^v} \left[\left(\frac{v_{i+1,j} - v_{i,j}}{\Delta X_i^u} \right) - \left(\frac{v_{i,j} - v_{i-1,j}}{\Delta X_{i-1}^u} \right) \right] \ , \tag{4.87}$$

$$\frac{\partial^2 v}{\partial X \partial Y} = \frac{1}{\Delta Y_j^v} \left[\left(\frac{(v_u)_{i,j}^{++} - (v_u)_{i,j}^{-+}}{\Delta X_i^v} \right) - \left(\frac{(v_u)_{i,j}^{+-} - (v_u)_{i,j}^{--}}{\Delta X_i^v} \right) \right] , \tag{4.88}$$

$$\frac{\partial^2 v}{\partial Y^2} = \frac{1}{\Delta Y_j^v} \left[\left(\frac{v_{i,j+1} - v_{i,j}}{\Delta Y_{j+1}^u} \right) - \left(\frac{v_{i,j} - v_{i,j-1}}{\Delta Y_j^u} \right) \right] \ , \tag{4.89}$$

$$\frac{\partial v}{\partial Y} = \frac{v_v^{Y+} - v_v^{Y-}}{\Delta Y_j^v} \ . \tag{4.90}$$

The spatial discretization of the partial derivatives that appear in the continuity equation (4.20) denoted by $\mathbf{DV}$ is performed using central differencing about the point where $p_{i,j}$ is defined. Thus, one obtains

$$\mathbf{DV} = C_7 \frac{\partial u}{\partial X} + C_2 \frac{\partial u}{\partial Y} + C_8 \frac{\partial v}{\partial X} + C_3 \frac{\partial v}{\partial Y} , \tag{4.91}$$

where

$$\frac{\partial u}{\partial X} = \frac{u_{i,j} - u_{i-1,j}}{\Delta X_i^v} , \tag{4.92}$$

$$\frac{\partial u}{\partial Y} = \frac{(u_v)_{i,j}^{-+} - (u_v)_{i,j}^{--}}{\Delta Y_j^u} , \tag{4.93}$$

$$\frac{\partial v}{\partial X} = \frac{(v_u)_{i,j}^{+-} - (v_u)_{i,j}^{--}}{\Delta X_i^v} , \tag{4.94}$$

$$\frac{\partial v}{\partial Y} = \frac{v_{i,j} - v_{i,j-1}}{\Delta Y_j^u} . \tag{4.95}$$

The evaluation of the viscous derivatives near a boundary (such as a solid wall) requires special treatment. In fact, in the staggered grid a boundary parallel with the *X*-axis passes through the points where for example, $v_{i,1}$ are defined, and similarly a boundary parallel with the *Y*-axis passes through the points where $u_{1,j}$ are defined, see Figure 4.6. Hence the numerical evaluation of $\partial^2 u / \partial Y^2$ in the former case and of $\partial^2 v / \partial X^2$ in the latter case would require points defined outside the physical domain. To overcome this difficulty, we use non-central differencing (second-order accurate three-points forward or backward differencing obtained from Taylor series expansion) to compute the derivative of the term in (4.63) which would otherwise require points outside the domain. Thus, the viscous derivatives near a boundary are numerically evaluated as

$$\left.\frac{\partial^2 u}{\partial Y^2}\right|_{Y=Y_2^u} = \frac{1}{\Delta Y_2^u}\left[\left(\frac{u_{i,3} - u_{i,2}}{\Delta Y_2^v}\right) - \left(\frac{\frac{8}{3}u_{i,b} - 3u_{i,2} + \frac{1}{3}u_{i,3}}{\frac{8}{3}Y_1^v - 3Y_2^u + \frac{1}{3}Y_3^u}\right)\right] , \tag{4.96}$$

$$\left.\frac{\partial^2 v}{\partial X^2}\right|_{X=X_2^v} = \frac{1}{\Delta X_2^v}\left[\left(\frac{v_{3,j} - v_{2,j}}{\Delta X_2^u}\right) - \left(\frac{\frac{8}{3}v_{b,j} - 3v_{2,j} + \frac{1}{3}v_{3,j}}{\frac{8}{3}X_1^u - 3X_2^v + \frac{1}{3}X_3^v}\right)\right] . \tag{4.97}$$

The second term in the square brackets in these last two expressions represents the one-sided evaluation of the first derivative at the boundary, $u_{i,b}$ and $v_{b,j}$ are the velocity components at the boundary (such as a solid wall) which are specified as boundary conditions.

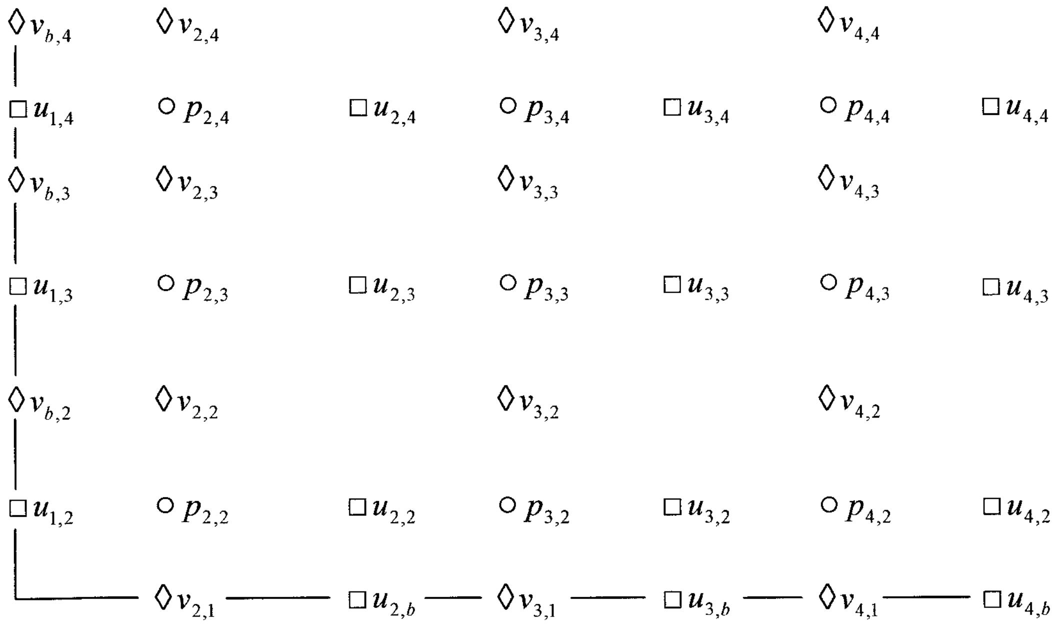

Figure 4.6 Numerical evaluation of viscous derivatives near boundaries.

4.2.5 Efficient decoupling procedure and the solution of scalar tridiagonal system

It is seen in the *Y*-sweep, equations (4.54-4.56), that the continuity and Navier-Stokes equations couple $\Delta\bar{u}$ and $\Delta\bar{v}$ to $\Delta\bar{p}$. Hence (4.54) and (4.55) can not be solved independently of (4.56). However, it is possible to uncouple $\Delta\bar{u}$ and $\Delta\bar{v}$ from $\Delta\bar{p}$ by elimination of $\Delta\bar{p}$ from the equations after performing the differencing on the staggered grid.

The *X*-momentum equation (4.54) is written in differenced form utilizing the expressions for the partial derivatives similar to equations (4.70-4.79) and the interpolates of overbarred quantities similar to those found in Section 4.2.4. Thus, the discretized *X*-momentum equation after regrouping the terms becomes

$$\Delta\bar{u}_{i,\,j-1}\left[\frac{\Delta t\,\left(C_5-\nabla Y_j^u\left\{C_2\left(u^n\right)_u^{Y-}+C_3\left(v^n\right)_u^{Y-}+C_4\right\}\right)}{\Delta Y_j^u\,\Delta Y_{j-1}^v}\right]$$

$$+\Delta\bar{u}_{i,\,j}\left[1+\frac{\Delta t}{\Delta Y_j^u}\left\{C_2\left(\frac{\left(u^n\right)_u^{Y+}\nabla Y_{j+1}^u}{\Delta Y_j^v}-\frac{\left(u^n\right)_u^{Y-}\nabla Y_{j-1}^v}{\Delta Y_{j-1}^v}\right)+C_3\left(\frac{\left(v^n\right)_u^{Y+}\nabla Y_{j+1}^u}{\Delta Y_j^v}-\frac{\left(v^n\right)_u^{Y-}\nabla Y_{j-1}^v}{\Delta Y_{j-1}^v}\right)\right.\right.$$

$$\left.\left.-C_5\left(\frac{1}{\Delta Y_j^v}+\frac{1}{\Delta Y_{j-1}^v}\right)+C_4\left(\frac{\nabla Y_{j+1}^u}{\Delta Y_j^v}-\frac{\nabla Y_{j-1}^v}{\Delta Y_{j-1}^v}\right)\right\}\right]$$

$$+\Delta\bar{u}_{i,\,j+1}\left[\frac{\Delta t\,\left(C_5+\nabla Y_j^v\left\{C_2\left(u^n\right)_u^{Y+}+C_3\left(v^n\right)_u^{Y+}+C_4\right\}\right)}{\Delta Y_j^u\,\Delta Y_j^v}\right]$$

$$=-\Delta t\left[G_u\left(u^n,v^n,p^n\right)+C_2\frac{\partial\Delta\bar{p}}{\partial Y}+C_6\frac{\partial^2\Delta\bar{u}}{\partial X\partial Y}\right], \tag{4.98}$$

where $G_u\left(u^n,v^n,p^n\right)$ is obtained from (4.69) and (4.70-4.79) and the coordinate transformation coefficients (such as C_2 and C_5) are numerically evaluated at the point where $u_{i,j}$ is defined, as shown in Figure 4.5.

The partial derivatives $\partial\Delta\bar{p}/\partial Y$ and $\partial^2\Delta\bar{u}/\partial X\partial Y$ that appear in the right-hand side of (4.98) are either assumed zero because at convergence the delta quantities $\Delta\bar{p}$ and $\Delta\bar{u}$ become zero or they are numerically evaluated at the previous pseudo-time step $n-1$ from (4.75) and (4.77), respectively.

For a given *X*-coordinate location, X_i, the setting up of (4.98) for each j, $2 \le j \le J-1$, where J is the number of grid points in the *Y*-direction, gives a tridiagonal system of equations which has to be solved for $\Delta\bar{u}_{i,j}$. This is done at each X_i, $2 \le i \le I-1$, where I is the number of grid points in the *X*-direction, in order to obtain $\Delta\bar{u}_{i,j}$, for all i, j.

The flow quantities at X_i, $i=1$ and $i=I$, are specified as boundary conditions and this is why the tridiagonal systems are set up only for X_i, $2 \le i \le I-1$. Near a boundary (such as a far-field or a solid wall), the implementation of non-central differencing as shown in Section 4.2.4 will result in a slightly modified equation.

In addition, on a far-field or a solid wall boundaries $\Delta\bar{u}$ is zero because the velocity $u_{i,b}^{n}$, of the boundary at t^{n} is imposed as a boundary condition and remains unchanged during the pseudo-time relaxation.

Similarly, as with the *X*-momentum equation, we can express the *Y*-momentum and continuity equations (4.55-4.56) in differenced form, after utilizing expressions for the partial derivatives similar to equations (4.81-4.90) and for the interpolates presented in Section 4.2.4. Thus, in *Y*-sweep the discretized *Y*-momentum equation becomes

$$\Delta\bar{v}_{i,j-1}\left[\frac{\Delta t\left(C_5-\nabla Y_j^v\left\{C_2\left(u^n\right)_v^{Y-}+C_3\left(v^n\right)_v^{Y-}+C_4\right\}\right)}{\Delta Y_j^u\,\Delta Y_j^v}\right]$$

$$+\Delta\bar{v}_{i,j}\left[1+\frac{\Delta t}{\Delta Y_j^v}\left\{C_2\left(\frac{\left(u^n\right)_v^{Y+}\nabla Y_{j+1}^v}{\Delta Y_{j+1}^u}-\frac{\left(u^n\right)_v^{Y-}\nabla Y_j^u}{\Delta Y_j^u}\right)+C_3\left(\frac{\left(v^n\right)_v^{Y+}\nabla Y_{j+1}^v}{\Delta Y_{j+1}^u}-\frac{\left(v^n\right)_v^{Y-}\nabla Y_j^u}{\Delta Y_j^u}\right)\right.\right.$$

$$\left.\left.-C_5\left(\frac{1}{\Delta Y_{j+1}^u}+\frac{1}{\Delta Y_j^u}\right)+C_4\left(\frac{\nabla Y_{j+1}^v}{\Delta Y_{j+1}^u}-\frac{\nabla Y_j^u}{\Delta Y_j^u}\right)\right\}\right]$$

$$+\Delta\bar{v}_{i,j+1}\left[\frac{\Delta t\left(C_5+\nabla Y_{j+1}^u\left\{C_2\left(u^n\right)_v^{Y+}+C_3\left(v^n\right)_v^{Y+}+C_4\right\}\right)}{\Delta Y_j^v\,\Delta Y_{j+1}^u}\right]+\Delta t\,C_3\frac{\partial\Delta\bar{p}}{\partial Y}$$

$$=-\Delta t\left[G_v\left(u^n,v^n,p^n\right)+C_6\frac{\partial^2\Delta\bar{v}}{\partial X\partial Y}\right], \tag{4.99}$$

$$\Delta\bar{p}_{i,j}=-\frac{\Delta t}{\delta}\mathbf{DV}_{i,j}^n-\frac{\Delta t}{\delta}\left[C_2^p\frac{\left(\Delta\bar{u}_v\right)_{i,j}^{-+}-\left(\Delta\bar{u}_v\right)_{i,j}^{--}}{\Delta Y_j^u}+C_3^p\frac{\Delta\bar{v}_{i,j}-\Delta\bar{v}_{i,j-1}}{\Delta Y_j^u}\right], \tag{4.100}$$

where $G_v\left(u^n,v^n,p^n\right)$ is obtained from (4.80) and (4.81-4.90) and the coordinate transformation coefficients (such as C_2 and C_5) are numerically evaluated at the point where $v_{i,j}$ is defined while C_2^p and C_3^p are evaluated at the point where $p_{i,j}$ is defined, as shown in Figure 4.5. The partial derivative $\partial^2\Delta\bar{v}/\partial X\partial Y$ that appear in the right-hand side of (4.99) is either assumed zero because it is very small and at convergence the delta quantity $\Delta\bar{v}$ becomes zero or it is numerically evaluated at the previous pseudo-time step

$n-1$ from (4.88) utilizing the barred variable. It is seen that (4.99) requires the derivative $\partial \Delta \bar{p} / \partial Y$, which is given by

$$\frac{\partial \Delta \bar{p}}{\partial Y} = \frac{\Delta \bar{p}_{i,j+1} - \Delta \bar{p}_{i,j}}{\Delta Y_j^v} , \tag{4.101}$$

where the expression $\Delta \bar{p}_{i,j+1} - \Delta \bar{p}_{i,j}$ is evaluated from the continuity equation (4.100), hence

$$\begin{aligned} \frac{\partial \Delta \bar{p}}{\partial Y} = \frac{1}{\Delta Y_j^v} \Bigg[& -\frac{\Delta t}{\delta} \mathbf{DV}_{i,j+1}^n + \frac{\Delta t}{\delta} \mathbf{DV}_{i,j}^n - \frac{\Delta t}{\delta} C_2^p \frac{(\Delta \bar{u}_v)_{i,j+1}^{-+} - (\Delta \bar{u}_v)_{i,j+1}^{--}}{\Delta Y_{j+1}^u} \\ & + \frac{\Delta t}{\delta} C_2^p \frac{(\Delta \bar{u}_v)_{i,j}^{-+} - (\Delta \bar{u}_v)_{i,j}^{--}}{\Delta Y_j^u} - \frac{\Delta t}{\delta} C_3^p \frac{\Delta \bar{v}_{i,j+1} - \Delta \bar{v}_{i,j}}{\Delta Y_{j+1}^u} + \frac{\Delta t}{\delta} C_3^p \frac{\Delta \bar{v}_{i,j} - \Delta \bar{v}_{i,j-1}}{\Delta Y_j^u} \Bigg], \end{aligned} \tag{4.102}$$

where the interpolates that appear in this last expression are evaluated in a similar manner as shown in Section 4.2.4. Upon substituting (4.102) in (4.99), we thus obtain for the latter

$$\begin{aligned} & \Delta \bar{v}_{i,j-1} \left[\frac{\Delta t \left(C_5 - \nabla Y_j^v \left\{ C_2 (u^n)_v^{Y-} + C_3 (v^n)_v^{Y-} + C_4 \right\} - \Delta t\, C_3\, C_3^p / \delta \right)}{\Delta Y_j^u\, \Delta Y_j^v} \right] \\ & + \Delta \bar{v}_{i,j} \Bigg[1 + \frac{\Delta t}{\Delta Y_j^v} \Bigg\{ C_2 \left(\frac{(u^n)_v^{Y+} \nabla Y_{j+1}^v}{\Delta Y_{j+1}^u} - \frac{(u^n)_v^{Y-} \nabla Y_j^u}{\Delta Y_j^u} \right) + C_3 \left(\frac{(v^n)_v^{Y+} \nabla Y_{j+1}^v}{\Delta Y_{j+1}^u} - \frac{(v^n)_v^{Y-} \nabla Y_j^u}{\Delta Y_j^u} \right) \\ & - C_5 \left(\frac{1}{\Delta Y_{j+1}^u} + \frac{1}{\Delta Y_j^u} \right) + C_4 \left(\frac{\nabla Y_{j+1}^v}{\Delta Y_{j+1}^u} - \frac{\nabla Y_j^u}{\Delta Y_j^u} \right) + C_3 \left(\frac{\Delta t\, C_3^p}{\delta} \right) \left(\frac{1}{\Delta Y_{j+1}^u} + \frac{1}{\Delta Y_j^u} \right) \Bigg\} \Bigg] \\ & + \Delta \bar{v}_{i,j+1} \left[\frac{\Delta t \left(C_5 + \nabla Y_{j+1}^u \left\{ C_2 (u^n)_v^{Y+} + C_3 (v^n)_v^{Y+} + C_4 \right\} - \Delta t\, C_3\, C_3^p / \delta \right)}{\Delta Y_j^v\, \Delta Y_{j+1}^u} \right] \\ & = -\Delta t \left[G_v (u^n, v^n, p^n) + C_6 \frac{\partial^2 \Delta \bar{v}}{\partial X \partial Y} \right] - \frac{\Delta t\, C_3}{\Delta Y_j^v} \Bigg[-\frac{\Delta t}{\delta} \mathbf{DV}_{i,j+1}^n + \frac{\Delta t}{\delta} \mathbf{DV}_{i,j}^n \\ & \qquad - \frac{\Delta t}{\delta} C_2^p \frac{(\Delta \bar{u}_v)_{i,j+1}^{-+} - (\Delta \bar{u}_v)_{i,j+1}^{--}}{\Delta Y_{j+1}^u} + \frac{\Delta t}{\delta} C_2^p \frac{(\Delta \bar{u}_v)_{i,j}^{-+} - (\Delta \bar{u}_v)_{i,j}^{--}}{\Delta Y_j^u} \Bigg], \end{aligned} \tag{4.103}$$

This is the tridiagonal system of equations which has to be solved to obtain $\Delta \bar{v}_{i,j}$ that has been uncoupled from $\Delta \bar{p}_{i,j}$. A procedure similar to that for the Y-sweep for $\Delta \bar{u}_{i,j}$ is then used, specifically equation (4.103) is set up for each j, $2 \le j \le J-2$ ($j = J-1$ corresponds, for example, to a far-field boundary or a solid wall), to obtain tridiagonal systems of equations which are solved for $\Delta \bar{v}_{i,j}$, where $2 \le i \le I-1$. $\Delta \bar{p}_{i,j}$ is thus obtained from (4.100) after evaluating $\Delta \bar{u}_{i,j}$ and $\Delta \bar{v}_{i,j}$. This special decoupling procedure which remarkably reduced the problem to the solution of tridiagonal systems of equation is computationally efficient.

The solution of the X-sweep proceeds in a similar manner as in the Y-sweep. Δp is eliminated from (4.57) with the aid of (4.59) to obtain Δu. Here we will thus only give the scalar tridiagonal systems of equations that one sets up from the differenced forms of equations (4.57-4.59). The equation for Δu is given by

$$
\begin{aligned}
&\Delta u_{i-1,j}\left[\frac{\Delta t\left(C_1 - \nabla X_i^u\left\{C_7\left(u^n\right)_u^{X-} + C_8\left(v^n\right)_v^{Y-}\right\} - \Delta t\, C_7\, C_7^p/\delta\right)}{\Delta X_i^u\, \Delta X_i^v}\right] \\
&+ \Delta u_{i,j}\left[1 + \frac{\Delta t}{\Delta X_i^u}\left\{C_7\left(\frac{\left(u^n\right)_u^{X+}\nabla X_{i+1}^u}{\Delta X_{i+1}^v} - \frac{\left(u^n\right)_u^{X-}\nabla X_i^v}{\Delta X_i^v}\right) + C_8\left(\frac{\left(v_v^n\right)_{i+1,j}^{Y-}\nabla X_{i+1}^u}{\Delta X_{i+1}^v} - \frac{\left(v_v^n\right)_{i,j}^{Y-}\nabla X_i^v}{\Delta X_i^v}\right)\right.\right. \\
&\qquad\qquad\qquad\qquad\qquad\qquad\left.\left. + \left(\frac{\Delta t\, C_7 C_7^p}{\delta} - C_1\right)\left(\frac{1}{\Delta X_{i+1}^v} + \frac{1}{\Delta X_i^v}\right)\right\}\right] \\
&+ \Delta u_{i+1,j}\left[\frac{\Delta t\left(C_1 + \nabla X_{i+1}^v\left\{C_7\left(u^n\right)_u^{X+} + C_8\left(v_v^n\right)_{i+1,j}^{Y-}\right\} - \Delta t\, C_7\, C_7^p/\delta\right)}{\Delta X_i^u\, \Delta X_{i+1}^v}\right] \\
&= \Delta \bar{u}_{i,j} - \frac{\Delta t\, C_7}{\Delta X_i^u}\left[\Delta \bar{p}_{i+1,j} - \Delta \bar{p}_{i,j}\right. \\
&\qquad\qquad \left. - \frac{\Delta t}{\delta} C_8^p\, \frac{\left(\Delta v_u\right)_{i+1,j}^{+-} - \left(\Delta v_u\right)_{i+1,j}^{--}}{\Delta X_{i+1}^v} + \frac{\Delta t}{\delta} C_8^p\, \frac{\left(\Delta v_u\right)_{i,j}^{+-} - \left(\Delta v_u\right)_{i,j}^{--}}{\Delta X_i^v}\right], \qquad (4.104)
\end{aligned}
$$

and then the equation for Δv

$$
\begin{aligned}
&\Delta v_{i-1,\,j}\left[\frac{\Delta t\left(C_1-\nabla X_i^v\left\{C_7\left(u^n\right)_v^{X-}+C_8\left(v^n\right)_v^{X-}\right\}\right)}{\Delta X_{i-1}^u\,\Delta X_i^v}\right] \\
&+\Delta v_{i,\,j}\left[1+\frac{\Delta t}{\Delta X_i^v}\left\{C_7\left(\frac{\left(u^n\right)_v^{X+}\nabla X_{i+1}^v}{\Delta X_i^u}-\frac{\left(u^n\right)_v^{X-}\nabla X_{i-1}^u}{\Delta X_{i-1}^u}\right)+C_8\left(\frac{\left(v^n\right)_v^{X+}\nabla X_{i+1}^v}{\Delta X_i^u}-\frac{\left(v^n\right)_v^{X-}\nabla X_{i-1}^u}{\Delta X_{i-1}^u}\right)\right.\right. \\
&\qquad\qquad\left.\left.-C_1\left(\frac{1}{\Delta X_i^u}+\frac{1}{\Delta X_{i-1}^u}\right)\right\}\right] \\
&+\Delta v_{i+1,\,j}\left[\frac{\Delta t\left(C_1+\nabla X_i^u\left\{C_7\left(u^n\right)_v^{X+}+C_8\left(v^n\right)_v^{X+}\right\}\right)}{\Delta X_i^u\,\Delta X_i^v}\right] \\
&=\Delta\bar{v}_{i,j}-C_8\,\Delta t\frac{\partial\Delta p}{\partial X}\ ,
\end{aligned}
\tag{4.105}
$$

while the pressure variation Δp is recovered by the relation

$$
\Delta p_{i,j}+\frac{\Delta t}{\delta}\left[C_7^p\left(\frac{\Delta u_{i,j}-\Delta u_{i-1,j}}{\Delta X_i^v}\right)+C_8^p\left(\frac{\left(\Delta v_u^{+-}\right)_{i,j}-\left(\Delta v_u^{--}\right)_{i,j}}{\Delta X_i^v}\right)\right]=\Delta\bar{p}_{i,j}\ . \tag{4.106}
$$

The partial derivative $\partial\Delta p/\partial X$ that appear in the right-hand side of (4.105) is either assumed zero because it is very small and at convergence the delta quantity Δp becomes zero or it is numerically evaluated at the previous pseudo-time step $n-1$ from (4.85) utilizing the delta variable and (4.106).

The setting up of (4.104) or (4.105) for each i, $2 \le i \le I-1$, gives a tridiagonal system of equations which is solved for $\Delta u_{i,j}$ at each Y_j, $2 \le j \le J-1$, and $2 \le j \le J-2$ for $\Delta v_{i,j}$.

The inflow and outflow boundary conditions are assumed to be at X_i, $i=1$ and $i=I$, respectively. Fluid is entering the domain at the inlet, such that we impose the velocity profile there; the velocity components u and v will thus be set to known values at X_1, for example $u=\cos\alpha$ and $v=\sin\alpha$. Since the velocity components u and v are imposed at the inflow, we thus have that $\Delta u_{1,j}$ and $\Delta v_{1,j}$ are equal to zero there. Also there is no need to impose boundary conditions for the pressure at the inflow because we are using a staggered grid, as shown in Figure 4.6. Now, at the outlet, $X_i = X_I$, the fluid leaves the domain and the velocity components are thus extrapolated from inside the fluid domain, using the following second-order accurate relations

$$u_{I,j} = \left(1 + \frac{\Delta X_I^v}{\Delta X_{I-1}^v}\right) u_{I-1,j} - \frac{\Delta X_I^v}{\Delta X_{I-1}^v} u_{I-2,j} \, , \tag{4.107}$$

$$v_{I,j} = \left(1 + \frac{\Delta X_{I-1}^u}{\Delta X_{I-2}^u}\right) v_{I-1,j} - \frac{\Delta X_{I-1}^u}{\Delta X_{I-2}^u} v_{I-2,j} \, . \tag{4.108}$$

The viscous boundary conditions are imposed on the airfoil upper and lower surfaces which are transformed in the computational domain to a solid wall, that is $u = 0$ and $v = 0$. The upper and lower far-field boundaries can be either treated as solid walls ($u = 0$ and $v = 0$) or the velocities can be imposed as those of the uniform stream at incidence ($u = \cos\alpha$ and $v = \sin\alpha$), we thus have that Δu and Δv are equal to zero there. As far as the pressure at the outlet is concerned, it can be either extrapolated from inside the fluid domain, computed from the momentum equation normal to an upper or lower far-field boundary at the outlet, or set equal to zero in order to fix the pressure level in the domain.

4.2.6 Comparison with experiments

The present numerical method has been first validated by comparison with experimental and previous numerical results for the two-dimensional flows over a downstream-facing step before using it for the analysis of the flows past airfoils at very low Reynolds numbers, for which there are no experimental results available. The details of the numerical validations are given in Appendix D.

4.3 Solutions for airfoils at various low Reynolds numbers

4.3.1 Pressure distribution for symmetric airfoils at zero incidence

The method presented in Section 4.2 has been first used to analyze the flow at zero incidence past symmetric airfoils at very low Reynolds numbers. Four symmetric NACA airfoils ranging in relative thickness from 2% to 8% were investigated. These airfoils are shown in Figure 4.7.

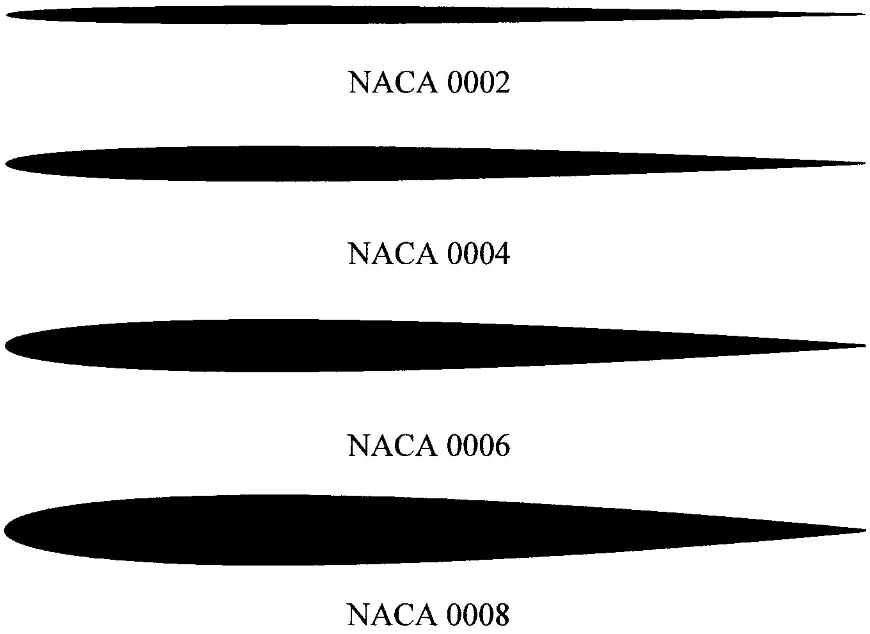

NACA 0002

NACA 0004

NACA 0006

NACA 0008

Figure 4.7 Geometry of four symmetric NACA airfoils with 2%-8% relative thicknesses.

The pressure distributions obtained with the present numerical method for NACA 0002 and NACA 0008 airfoils at zero incidence, for the Reynolds numbers Re=400, 600, 800, 1000, 2000 and 6000 are shown in Figures 4.8 and 4.9.

The present solutions for the pressure coefficient distribution on the NACA 0002 and NACA 0008 airfoils are compared in Figures 4.8 and 4.9 with the results obtained by Kunz and Kroo [99] using the INS2D code from NASA Ames (developed by Rogers and Kwak [164] and based on an upwind differencing scheme, instead of the central differencing scheme on a stretched staggered mesh used by the present method). The comparison shown for the Reynolds numbers Re=1000, 2000 and 6000 (no results were available for Reynolds numbers smaller than 1000) indicates a very good agreement between the present solutions and the results obtained by Kunz and Kroo [99]. For a better illustration of the low Reynolds number effects, the inviscid solutions obtained using the analytical method developed in Chapter 2 are also shown in Figures 4.8 and 4.9. One can notice a dramatic change in the pressure coefficient distribution at Re=6000 in comparison with the inviscid solution.

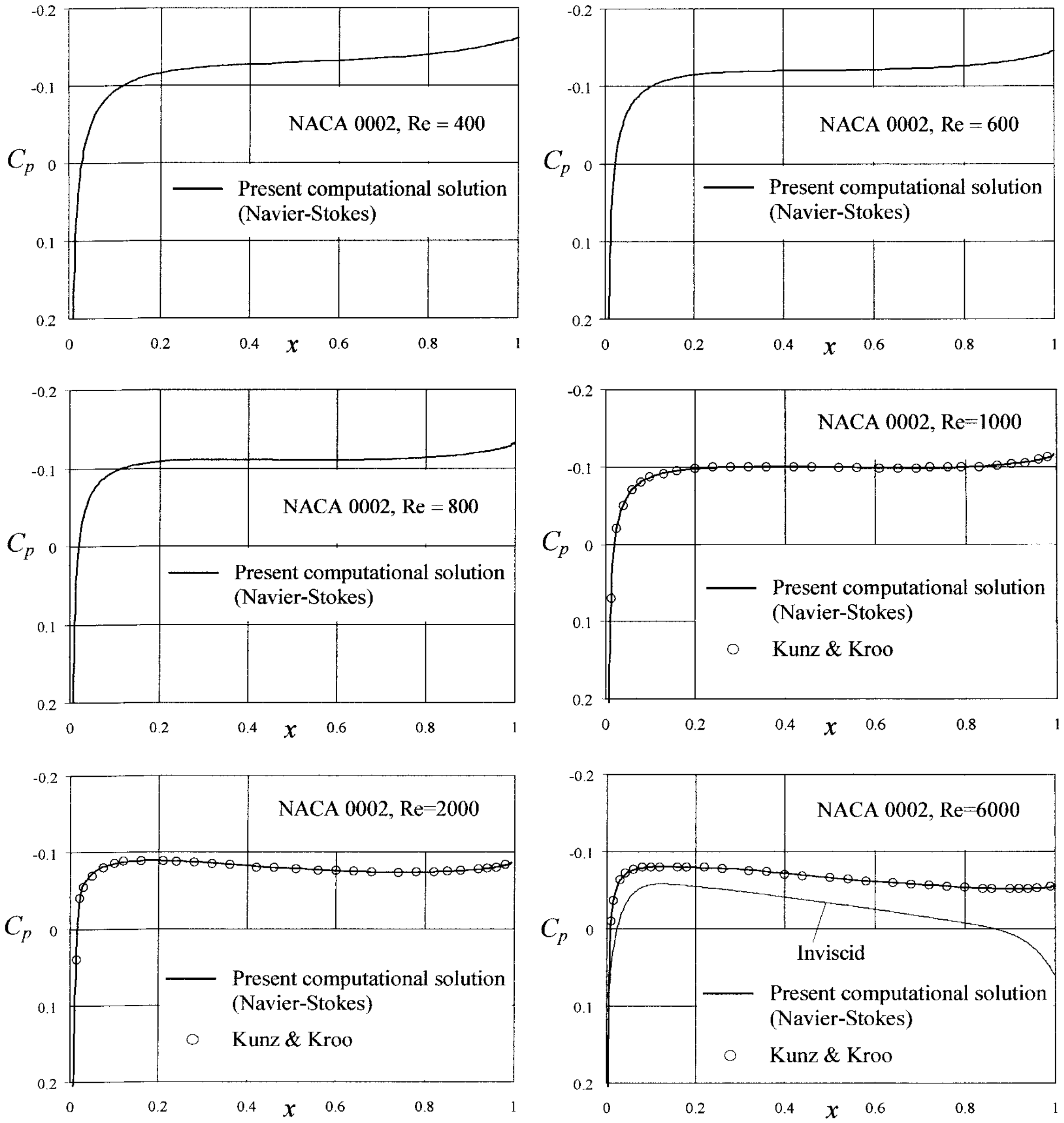

Figure 4.8 Pressure coefficient distribution on a NACA 0002 airfoil at zero incidence and Reynolds numbers Re =400, 600, 800, 1000, 2000 and 6000.

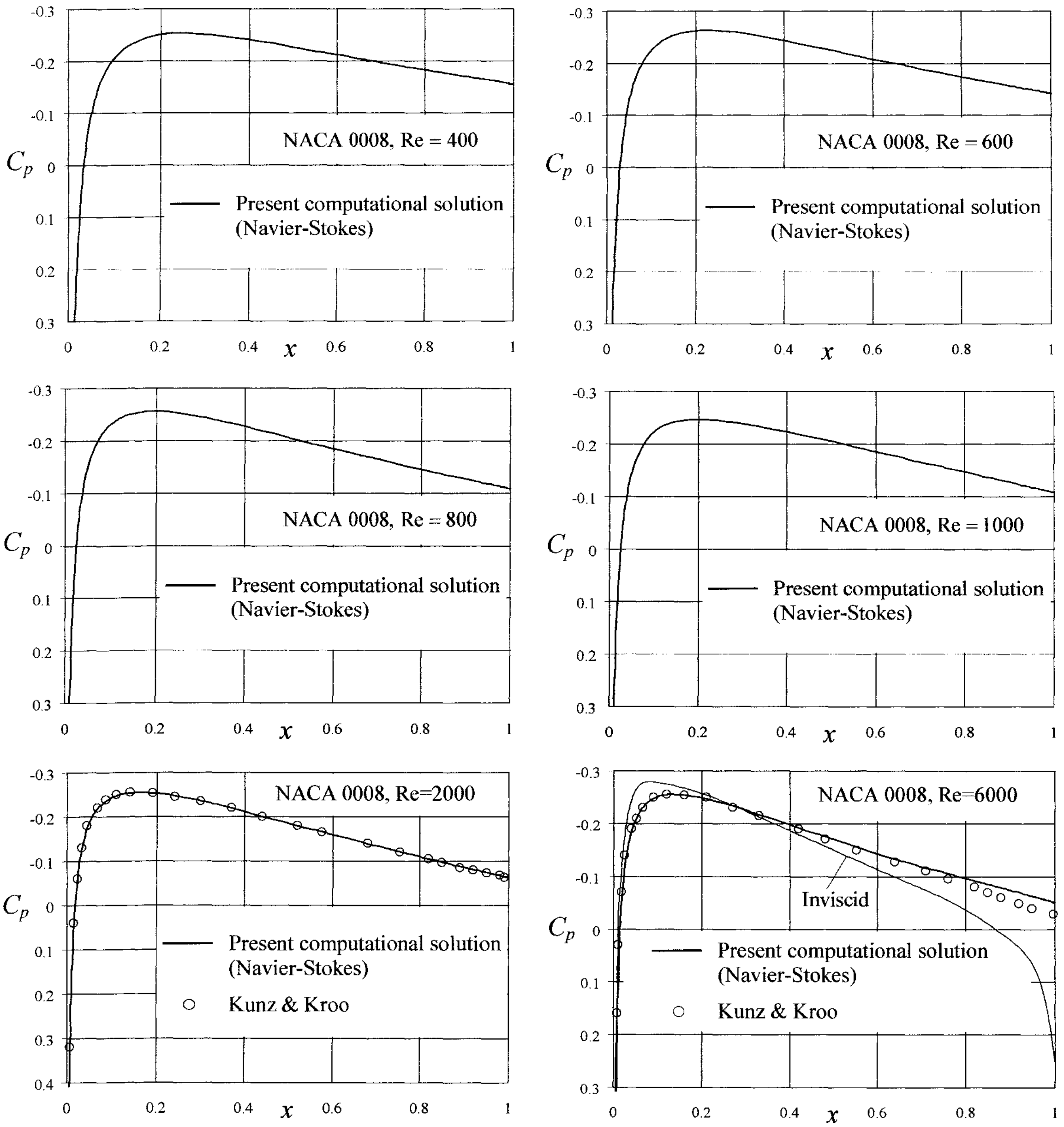

Figure 4.9 Pressure coefficient distribution on a NACA 0008 airfoil at zero incidence and Reynolds numbers Re =400, 600, 800, 1000, 2000 and 6000.

4.3.2 Pressure distribution for airfoils at incidence

The present method has also been used to analyze the flow at incidence past symmetric and cambered airfoils at very low Reynolds numbers. Several cambered NACA airfoils were analyzed. Figure 4.10 shows the geometries of various NACA four-digits airfoils with different relative thickness, camber and maximum camber location along the airfoil chord.

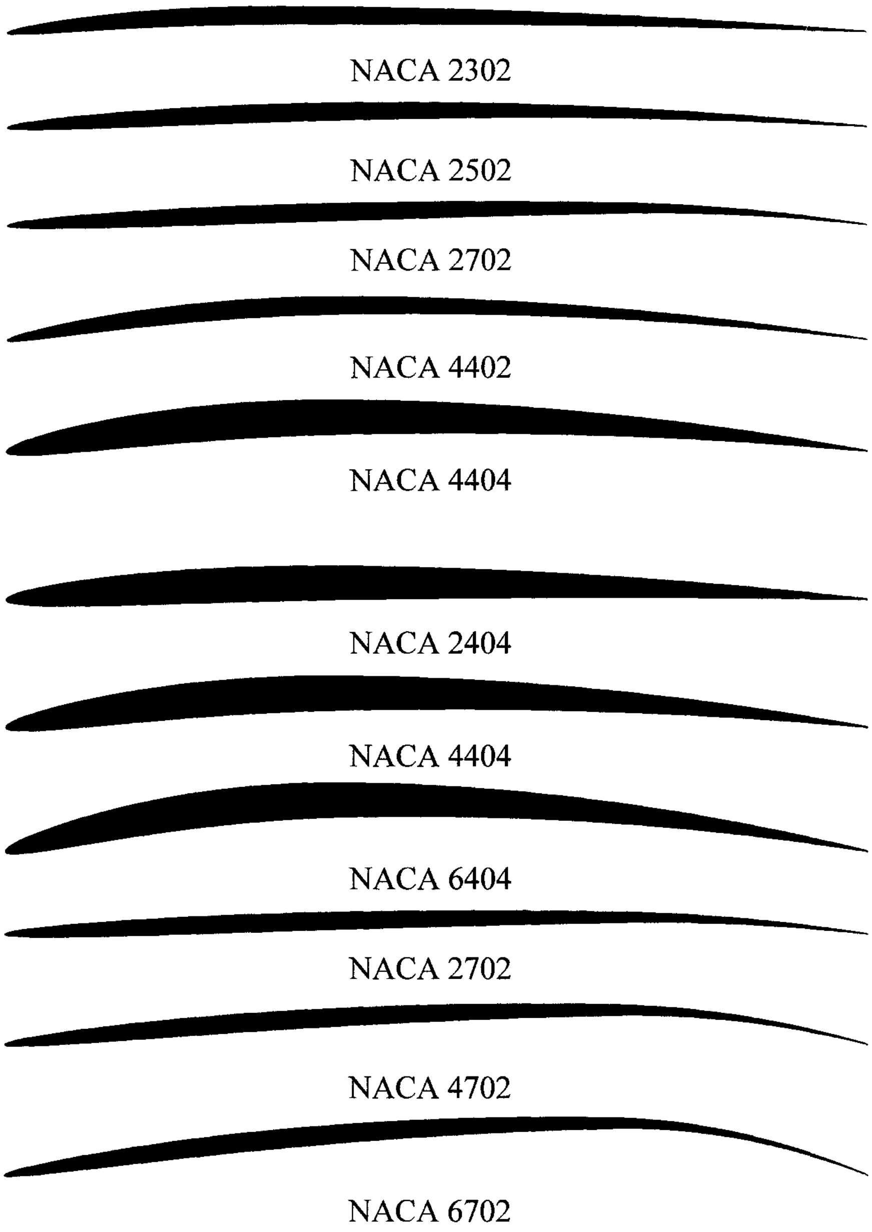

Figure 4.10 Geometry comparison of various cambered NACA airfoils.

The numbering system of NACA four-digits airfoils is very simple, NACA 4702 for example, has a 2% relative thickness and 4% maximum camber positioned at 70% of the chord from the airfoil leading edge. The pressure distributions on a NACA 0002 airfoil at various Reynolds numbers and angles of attack are shown in Figures 4.11-4.13.

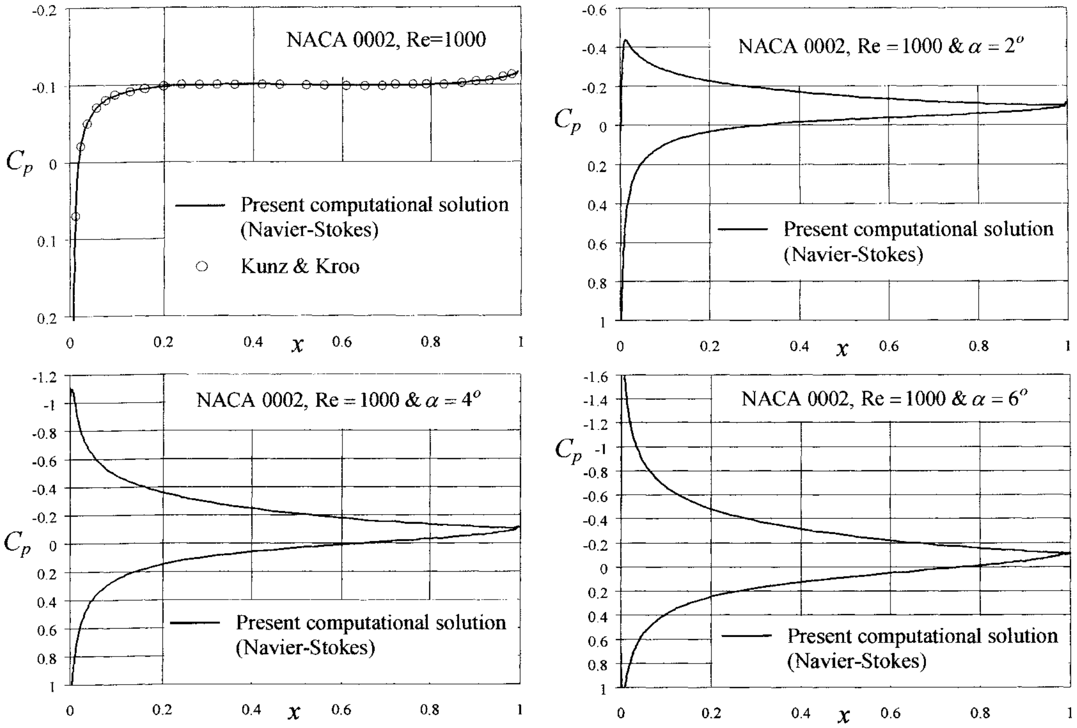

Figure 4.11 Pressure coefficient distribution on a NACA 0002 airfoil at Reynolds number Re =1000 and angles of attack $\alpha = 0$, 2^o, 4^o and 6^o.

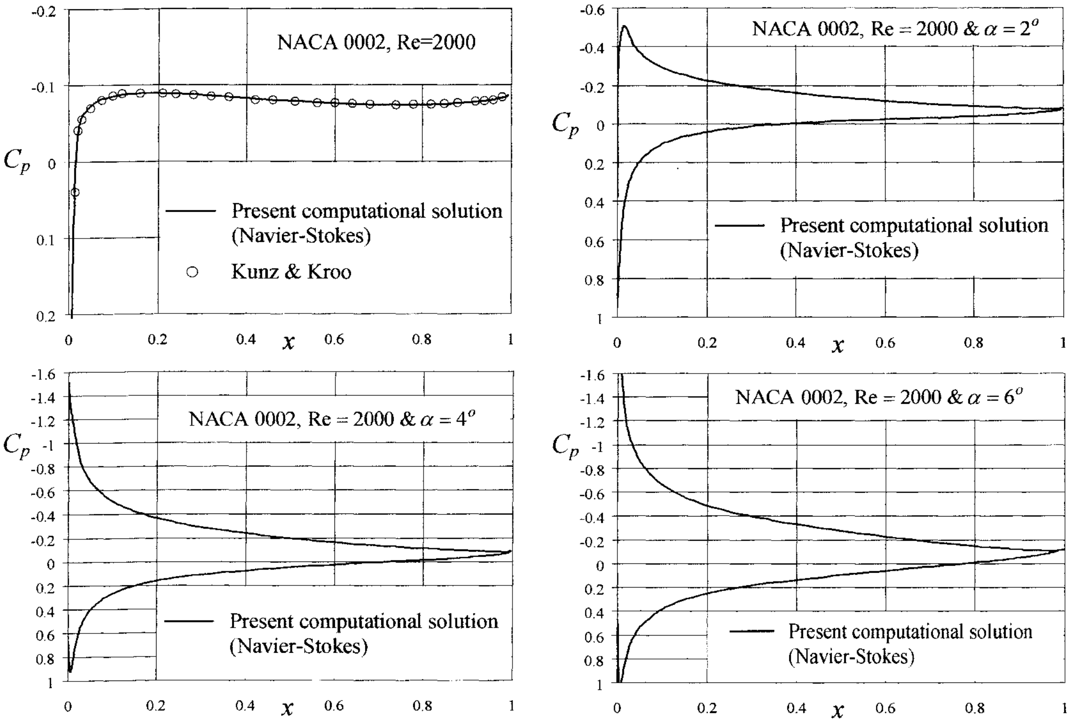

Figure 4.12 Pressure coefficient distribution on a NACA 0002 airfoil at Reynolds number Re =2000 and angles of attack $\alpha = 0$, 2^o, 4^o and 6^o.

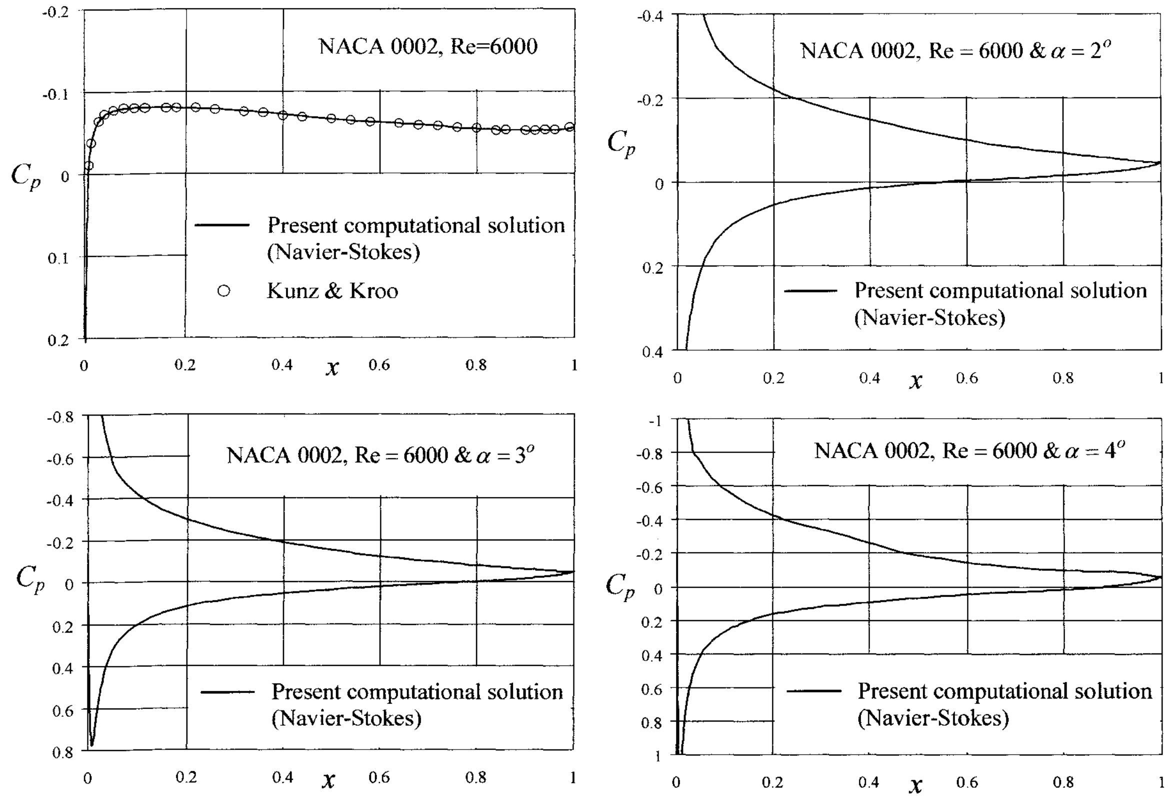

Figure 4.13 Pressure coefficient distribution on a NACA 0002 airfoil at Reynolds number Re =6000 and angles of attack $\alpha = 0$, 2^o, 3^o and 4^o.

The pressure distributions on a NACA 0004 and NACA 0006 airfoils at Reynolds number Re=2000 and angles of attack $\alpha = 0$, 2^o, 4^o and 6^o are shown in Figures 4.14 and 4.15. Figures 4.16 and 4.17 present the results obtained for NACA 0008 airfoil at Reynolds numbers Re=2000 and 6000 at $\alpha = 0$, 1^o, 2^o, 3^o, 4^o and 6^o.

Solutions were also obtained for NACA 4402 airfoil (2% relative thickness, 4% maximum camber positioned at 40% chord from the leading edge of the airfoil) at Reynolds numbers Re=1000 and 2000 and incidences $\alpha = 0$, 2^o, 4^o and 6^o, as shown in Figures 4.18 and 4.19. It is shown in these figures the effect of the relative camber on the pressure distribution as compared to the symmetric NACA 0002 airfoil (with a 2% thickness) at Reynolds numbers Re=1000 and 2000. The comparison is indicative of the large variations in performance (larger pressure difference between the upper and lower airfoil surfaces) due to the introduction of camber, even at low incidences.

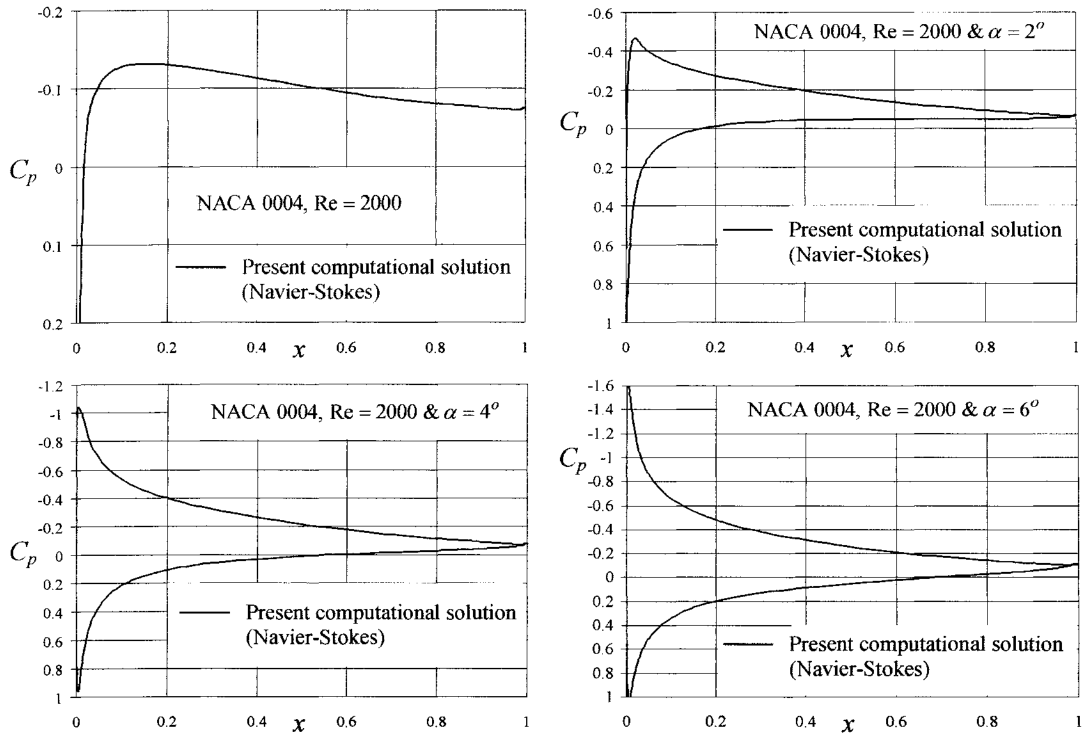

Figure 4.14 Pressure coefficient distribution on a NACA 0004 airfoil at Reynolds number Re =2000 and angles of attack $\alpha = 0,\ 2^o,\ 4^o$ and 6^o.

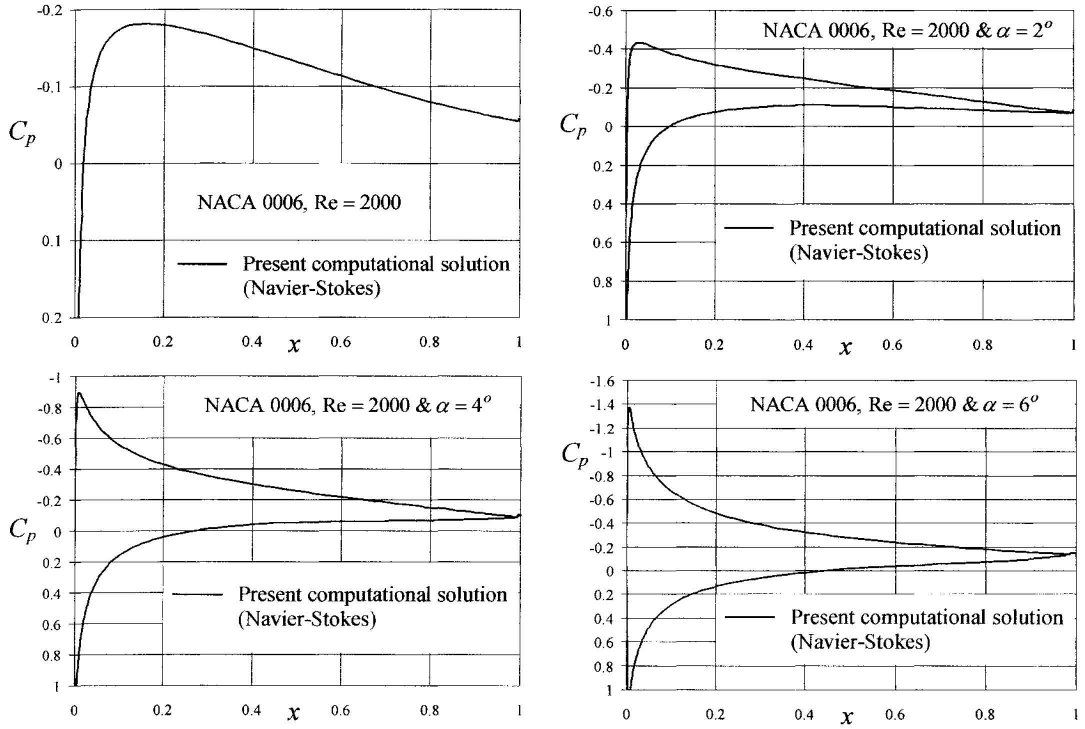

Figure 4.15 Pressure coefficient distribution on a NACA 0006 airfoil at Reynolds number Re =2000 and angles of attack $\alpha = 0,\ 2^o,\ 4^o$ and 6^o.

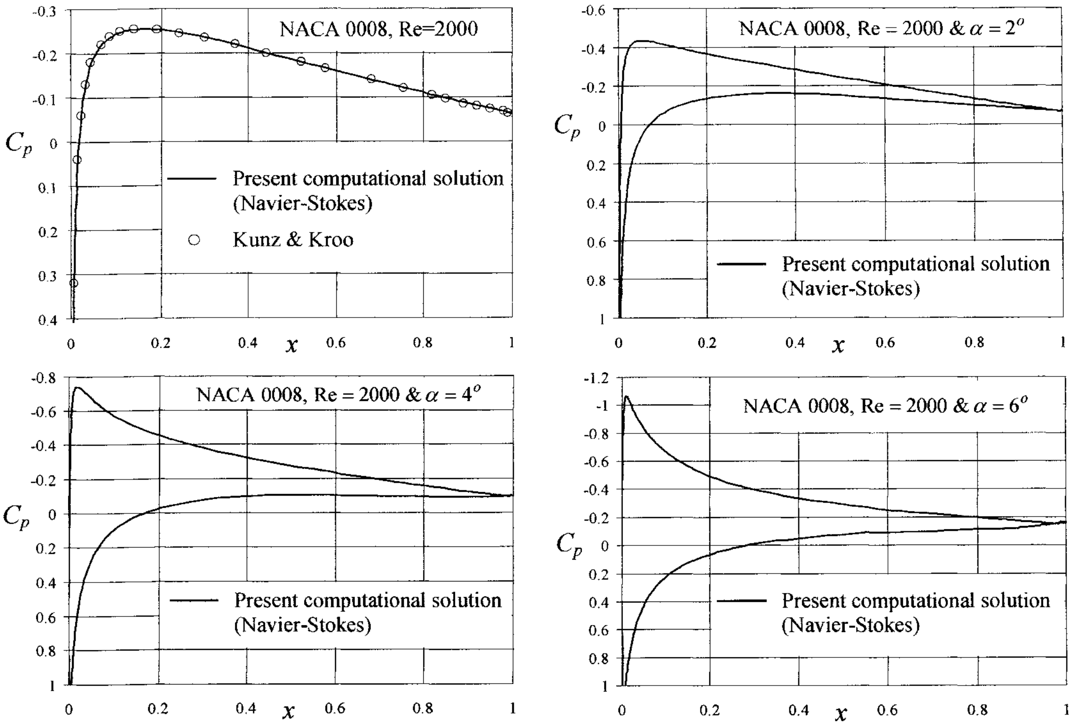

Figure 4.16 Pressure coefficient distribution on a NACA 0008 airfoil at Reynolds number Re =2000 and angles of attack $\alpha = 0$, 2^o, 4^o and 6^o.

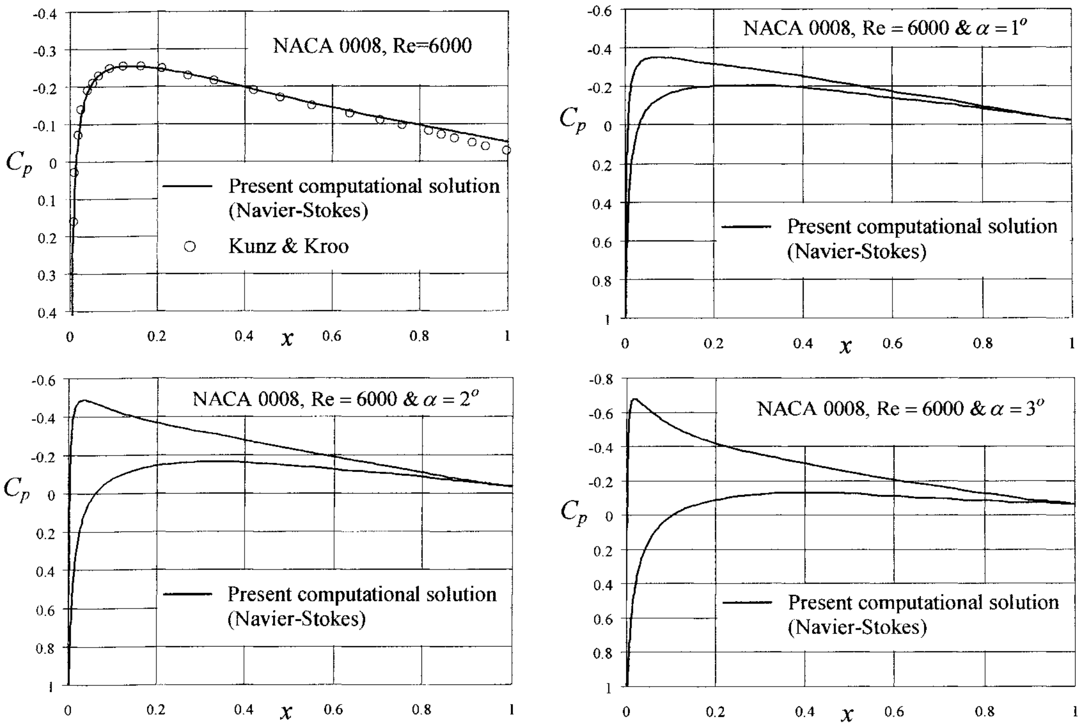

Figure 4.17 Pressure coefficient distribution on a NACA 0008 airfoil at Reynolds number Re =6000 and angles of attack $\alpha = 0$, 1^o, 2^o and 3^o.

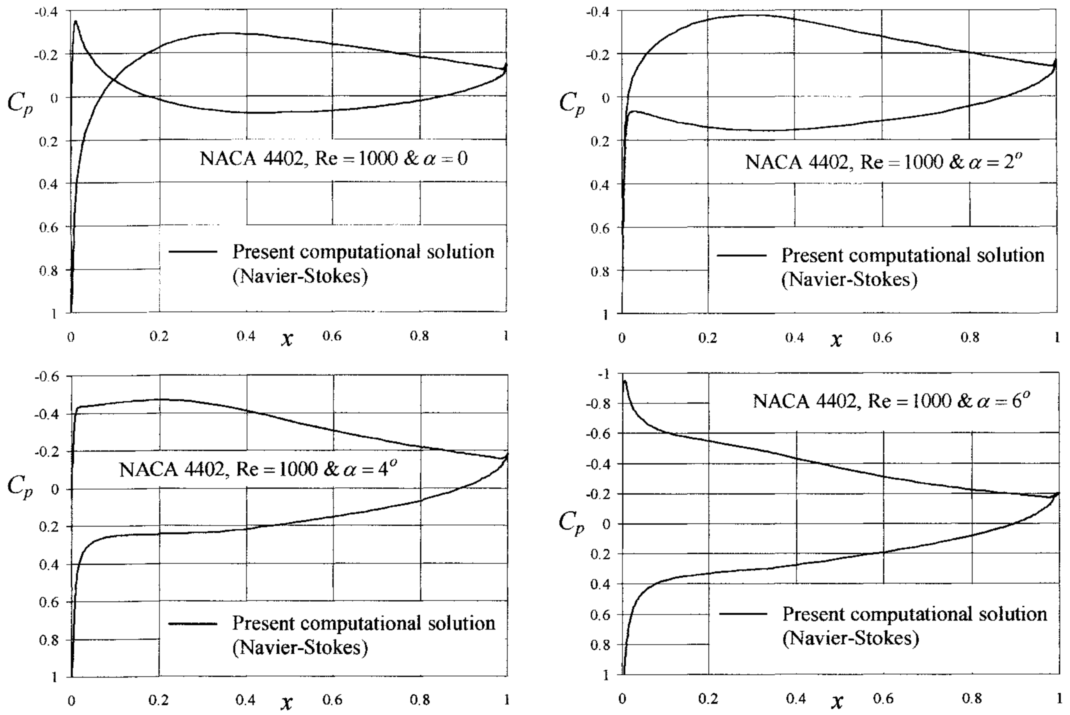

Figure 4.18 Pressure coefficient distribution on a NACA 4402 airfoil at Reynolds number Re =1000 and angles of attack $\alpha = 0$, 2^o, 4^o and 6^o.

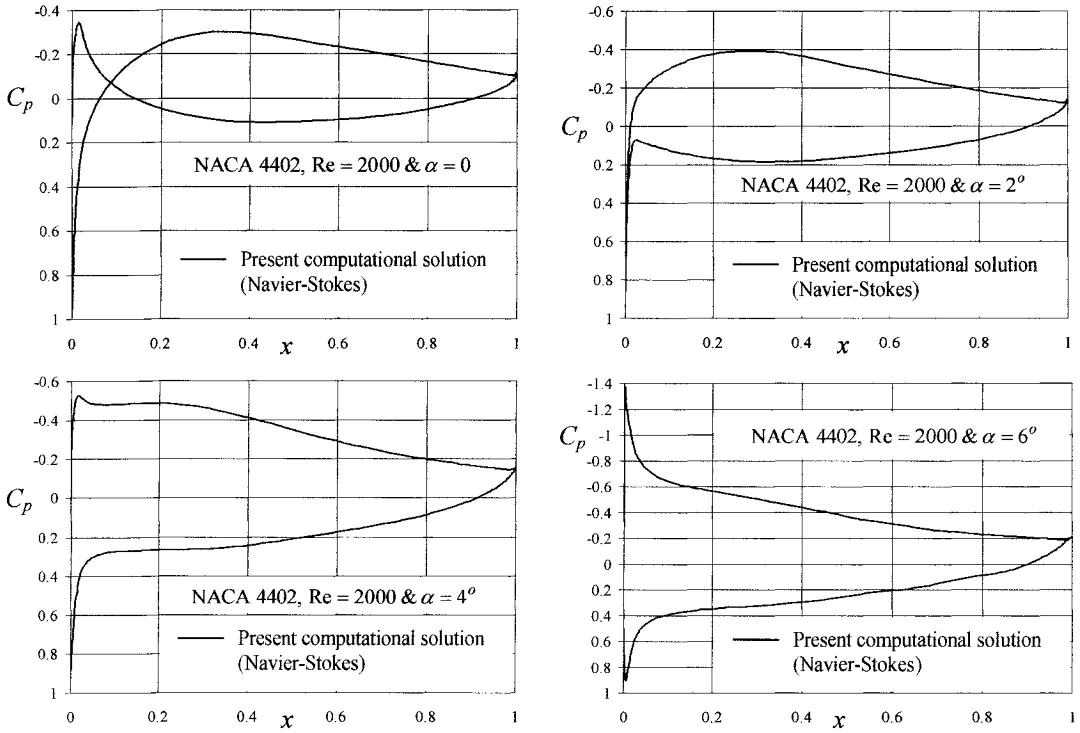

Figure 4.19 Pressure coefficient distribution on a NACA 4402 airfoil at Reynolds number Re =2000 and angles of attack $\alpha = 0$, 2^o, 4^o and 6^o.

The effects of varying the location of the maximum camber along the chord were investigated by computing the pressure coefficient distribution on NACA 2302, 2502 and 2702 airfoils. For these profiles, the relative thickness and camber are 2%, while the locations of the maximum camber are 30%, 50% and 70% chord from the leading edge. The present computational solutions for these airfoils at Reynolds number Re=1000 and angles of attack $\alpha = 0$, 2^o, 4^o and 6^o are shown in Figures 4.20-4.22.

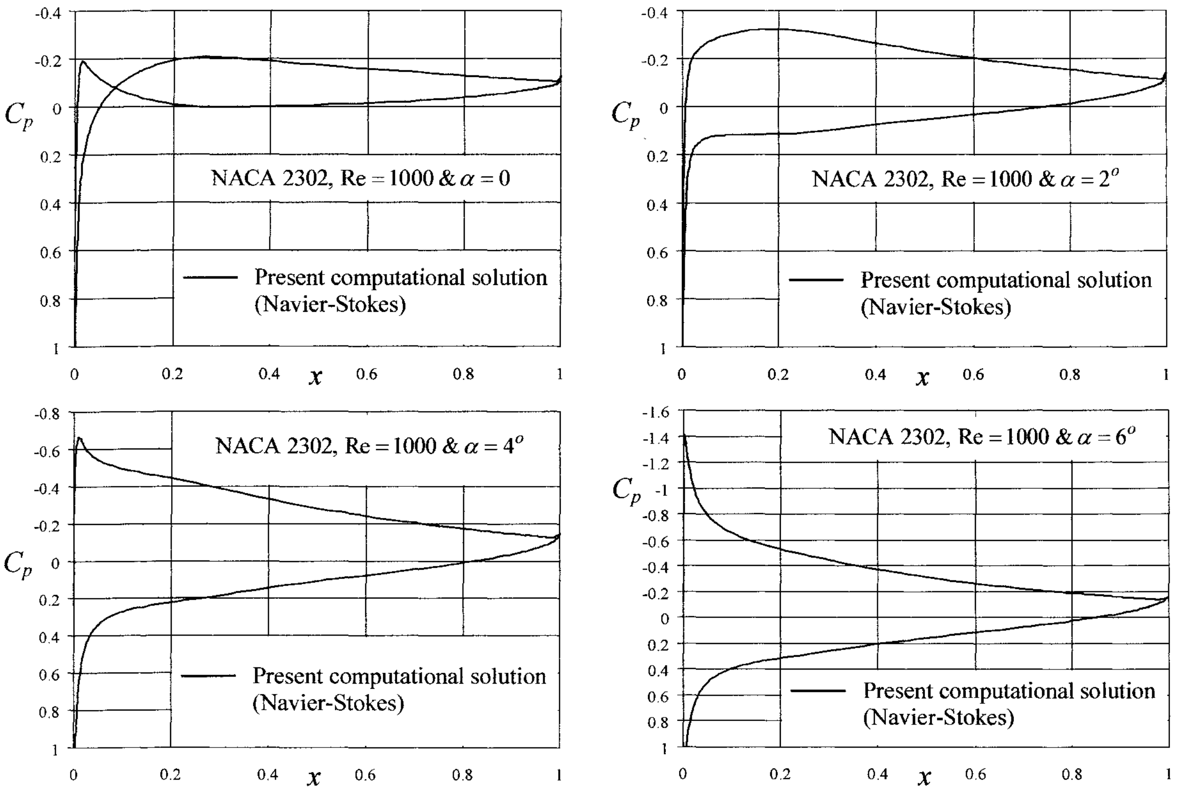

Figure 4.20 Pressure coefficient distribution on a NACA 2302 airfoil at Reynolds number Re =1000 and angles of attack $\alpha = 0$, 2^o, 4^o and 6^o.

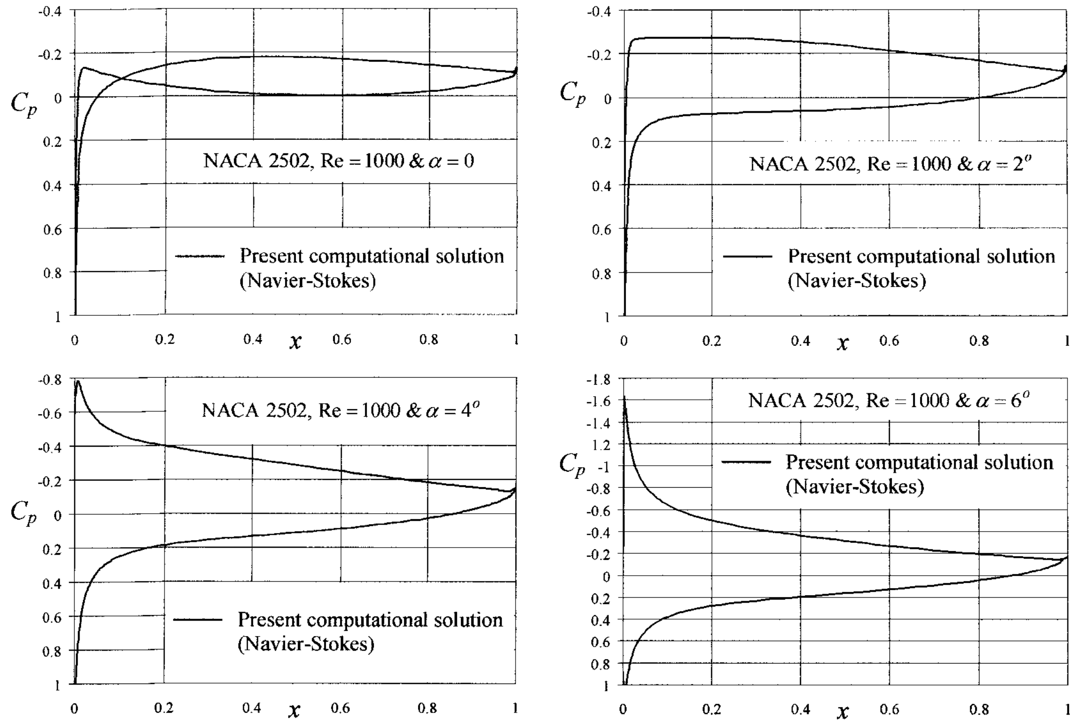

Figure 4.21 Pressure coefficient distribution on a NACA 2502 airfoil at Reynolds number Re =1000 and angles of attack $\alpha = 0$, 2^o, 4^o and 6^o.

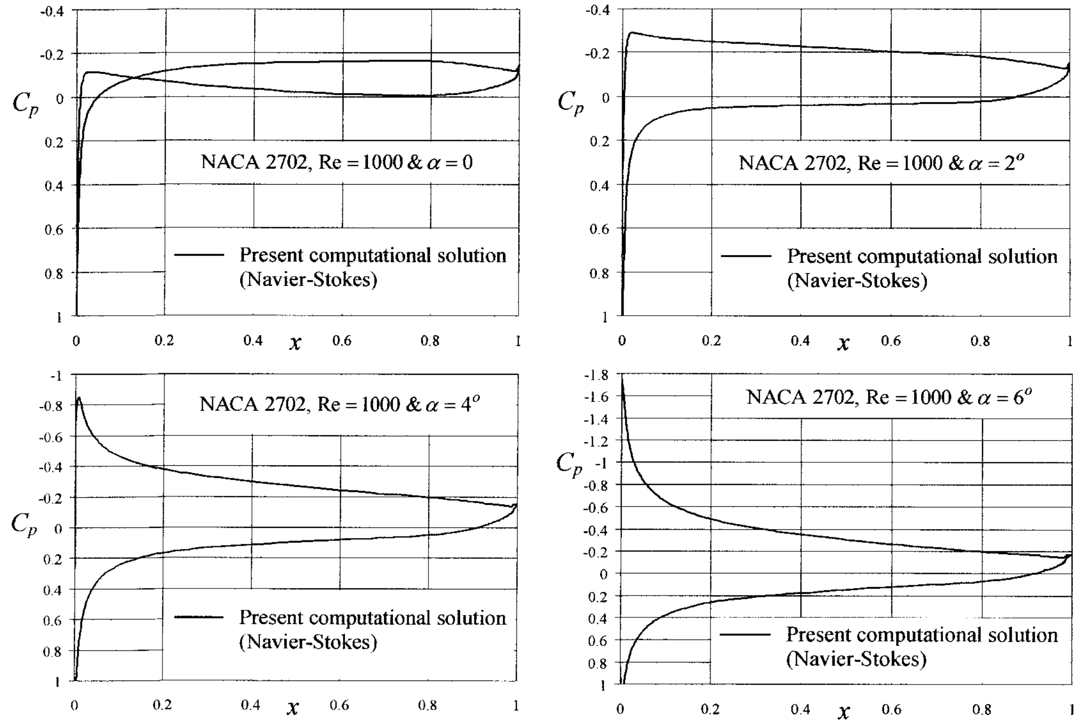

Figure 4.22 Pressure coefficient distribution on a NACA 2702 airfoil at Reynolds number Re =1000 and angles of attack $\alpha = 0$, 2^o, 4^o and 6^o.

The pressure coefficient distributions on a NACA 4404 airfoil (4% relative thickness and 4% maximum camber positioned at 40% chord) at Reynolds numbers Re=400, 600, 800 and 1000 and angles of attack $\alpha = 0$, 2^o, 4^o and 6^o are shown in Figures 4.23-4.26. Figures 4.27 and 4.28 present additional results obtained for NACA 2404 and NACA 6404 airfoils at Reynolds number Re=800 at $\alpha = 0$, 2^o, 4^o and 6^o. NACA 2404 and NACA 6404 airfoils have the same relative thickness and camber location as those of NACA 4404 airfoil and are characterized by a 2% and 6% relative camber, respectively. These figures illustrate the dramatic effects of Reynolds number and maximum camber on the negative pressure peaks and the slopes of the adverse gradients in the pressure recovery region. As the Reynolds number is reduced, these pressure gradients and peaks are reduced.

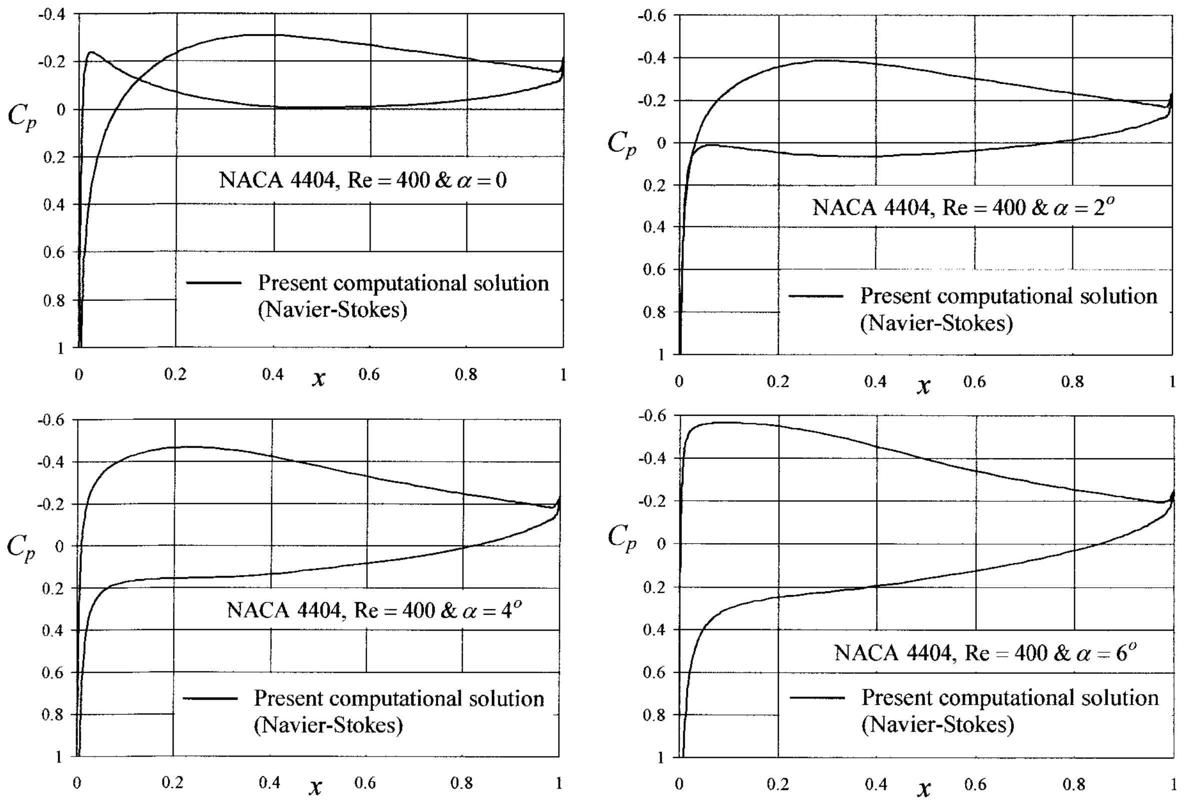

Figure 4.23 Pressure coefficient distribution on a NACA 4404 airfoil at Reynolds number Re =400 and angles of attack $\alpha = 0$, 2^o, 4^o and 6^o.

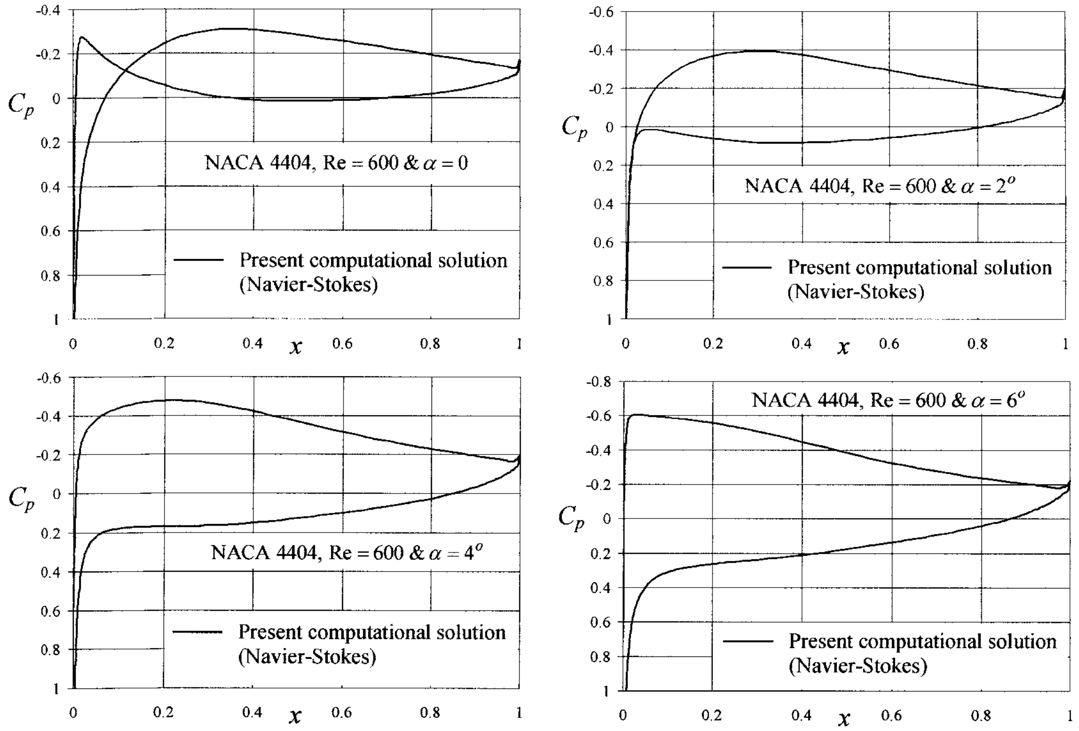

Figure 4.24 Pressure coefficient distribution on a NACA 4404 airfoil at Reynolds number Re =600 and angles of attack $\alpha = 0$, 2^o, 4^o and 6^o.

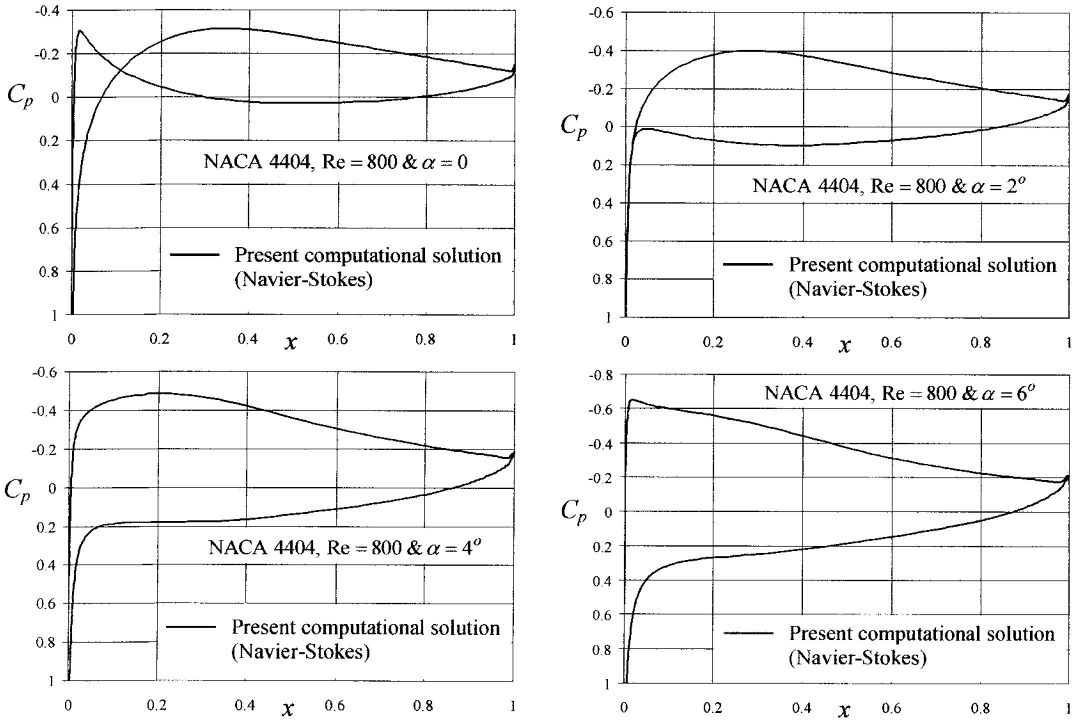

Figure 4.25 Pressure coefficient distribution on a NACA 4404 airfoil at Reynolds number Re =800 and angles of attack $\alpha = 0$, 2^o, 4^o and 6^o.

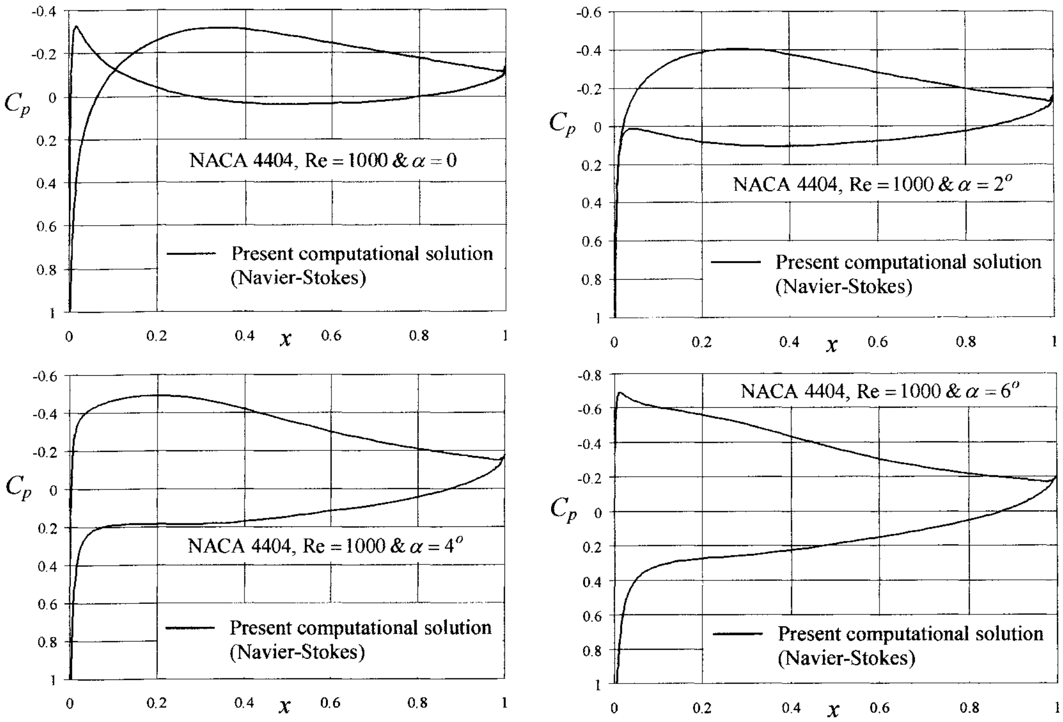

Figure 4.26 Pressure coefficient distribution on a NACA 4404 airfoil at Reynolds number Re =1000 and angles of attack $\alpha = 0$, 2^o, 4^o and 6^o.

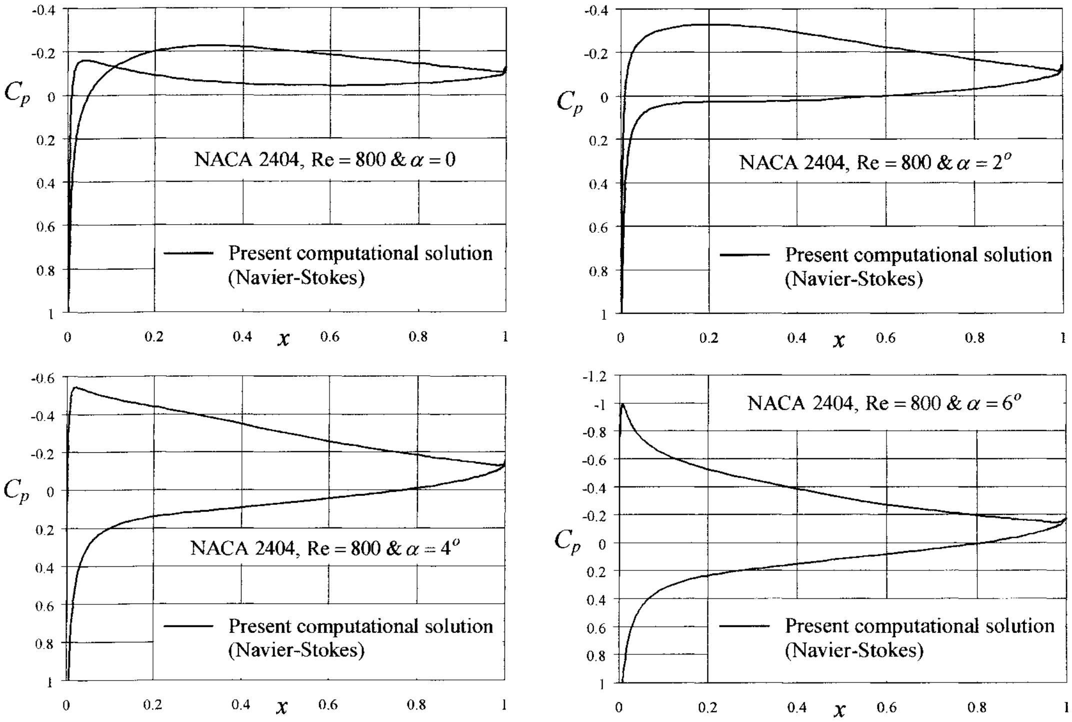

Figure 4.27 Pressure coefficient distribution on a NACA 2404 airfoil at Reynolds number Re =800 and angles of attack $\alpha = 0$, 2^o, 4^o and 6^o.

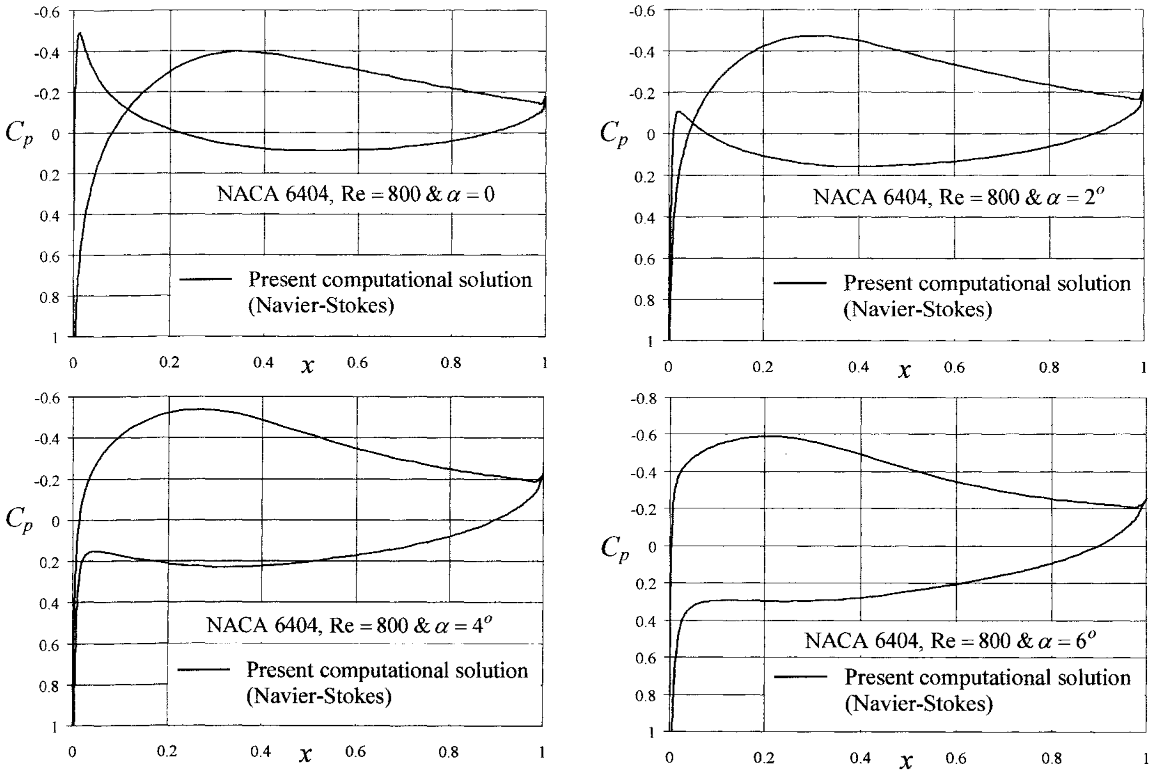

Figure 4.28 Pressure coefficient distribution on a NACA 6404 airfoil at Reynolds number Re =800 and angles of attack $\alpha = 0$, 2^o, 4^o and 6^o.

The pressure distributions at Reynolds numbers Re=400, 600, 800 and 1000 on a NACA 4702 airfoil (2% relative thickness and 4% camber located at 70% chord) and angles of attack $\alpha = 0$, 2^o, 4^o and 6^o are shown in Figures 4.29-4.32. For NACA 2702 airfoil which is less cambered than NACA 4702 airfoil by 2%, the solutions were also obtained at Re=600 and $\alpha = 0$, 2^o, 4^o and 6^o, as shown in Figure 4.33. Figure 4.34 presents the solutions obtained for NACA 6702 airfoil (with a 6% relative camber) at Reynolds number Re=600 at $\alpha = 0$, 2^o, 4^o and 6^o. Figures 4.29-4.34 demonstrate the effect of Reynolds number, angle of attack and airfoil relative camber (the airfoil thickness is fixed at 2% and the maximum camber location is kept unchanged at 70% of the chord while the relative camber is varied) on the pressure coefficient distribution.

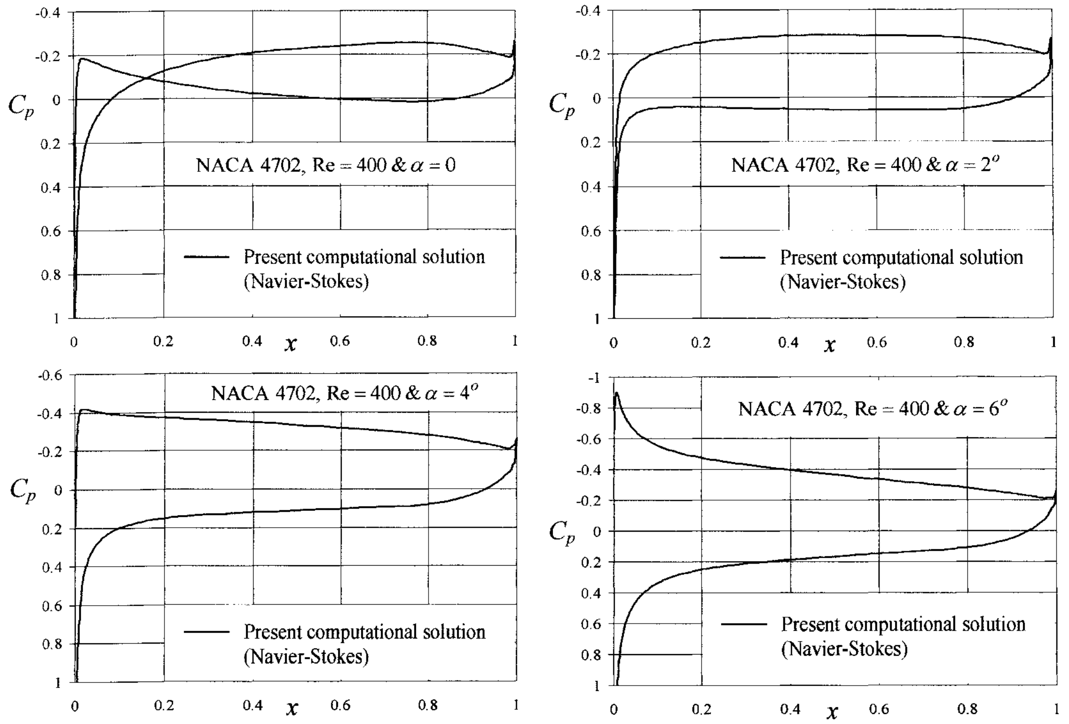

Figure 4.29 Pressure coefficient distribution on a NACA 4702 airfoil at Reynolds number Re =400 and angles of attack $\alpha = 0$, 2^o, 4^o and 6^o.

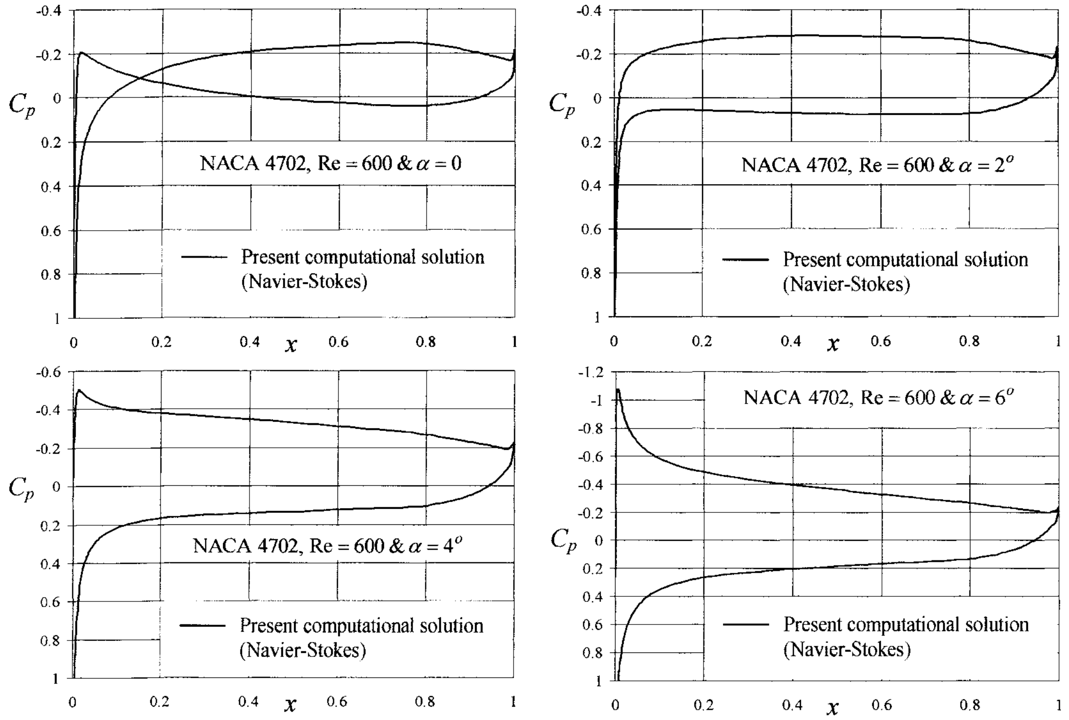

Figure 4.30 Pressure coefficient distribution on a NACA 4702 airfoil at Reynolds number Re =600 and angles of attack $\alpha = 0$, 2^o, 4^o and 6^o.

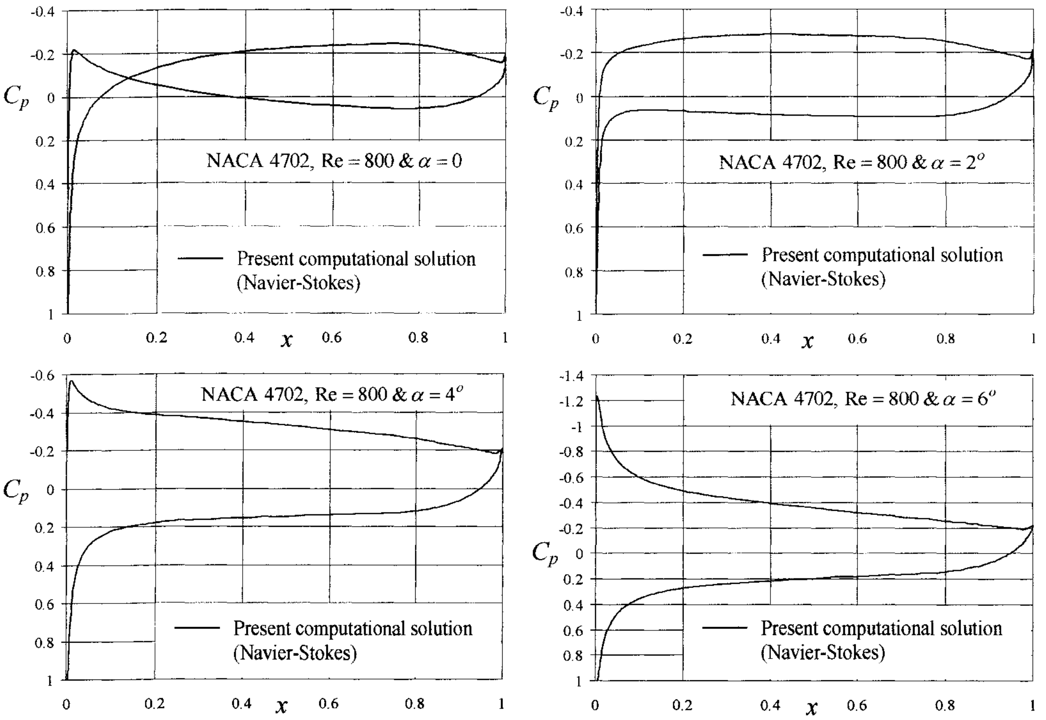

Figure 4.31 Pressure coefficient distribution on a NACA 4702 airfoil at Reynolds number Re =800 and angles of attack $\alpha = 0$, 2^o, 4^o and 6^o.

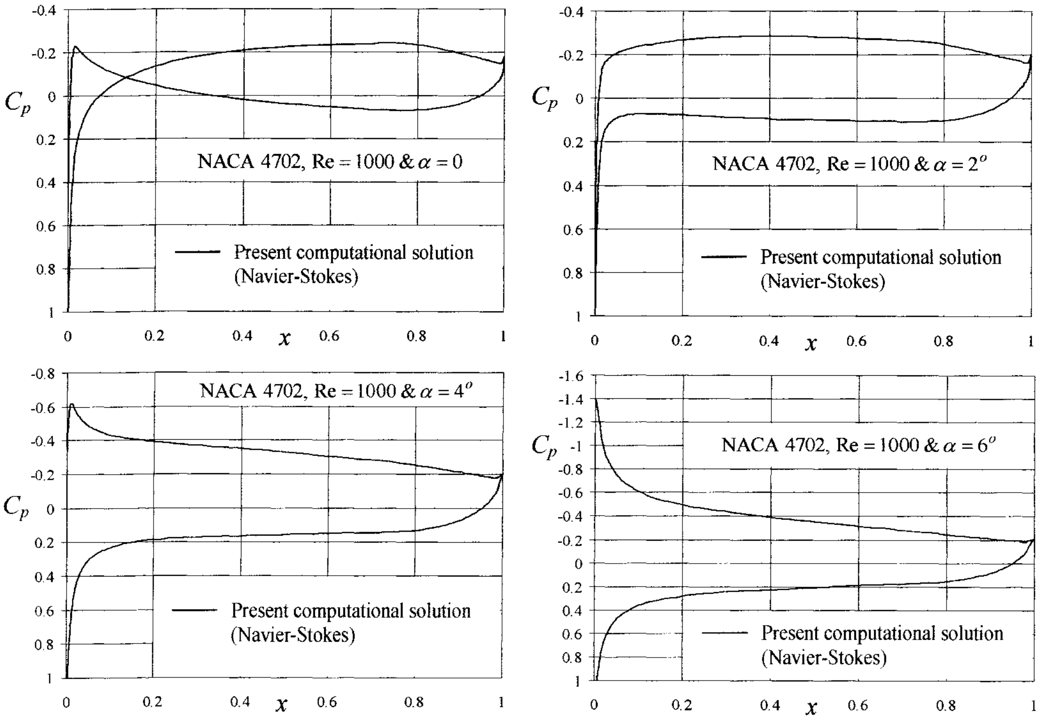

Figure 4.32 Pressure coefficient distribution on a NACA 4702 airfoil at Reynolds number Re =1000 and angles of attack $\alpha = 0$, 2^o, 4^o and 6^o.

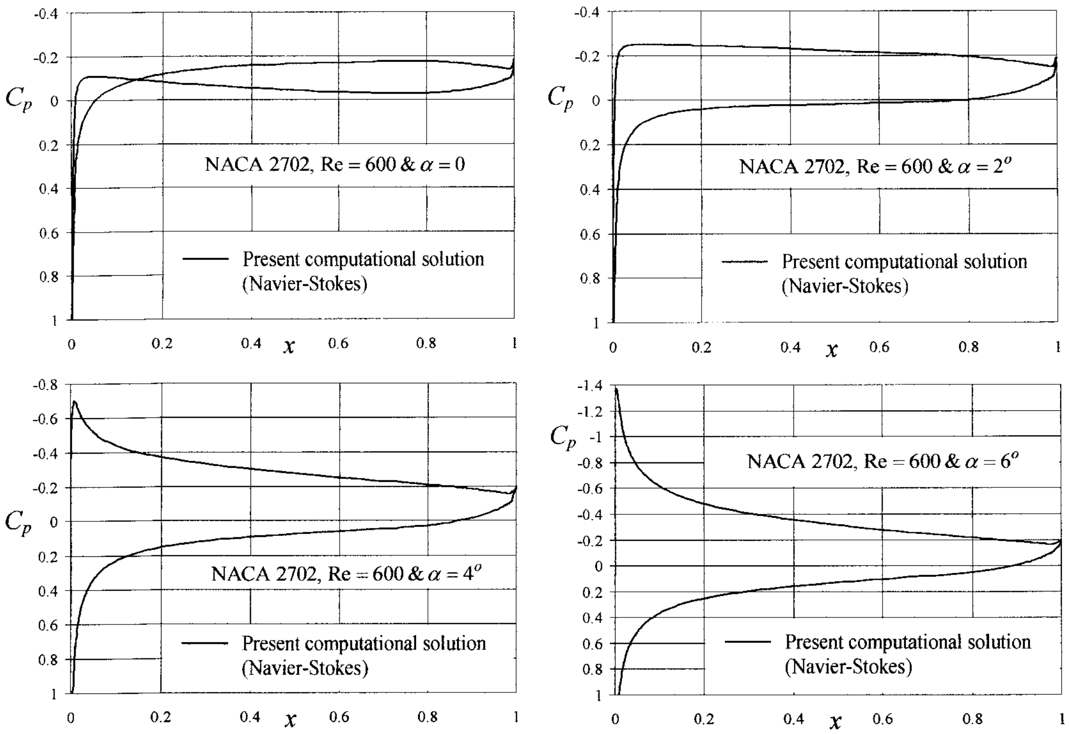

Figure 4.33 Pressure coefficient distribution on a NACA 2702 airfoil at Reynolds number Re =600 and angles of attack $\alpha = 0$, 2^o, 4^o and 6^o.

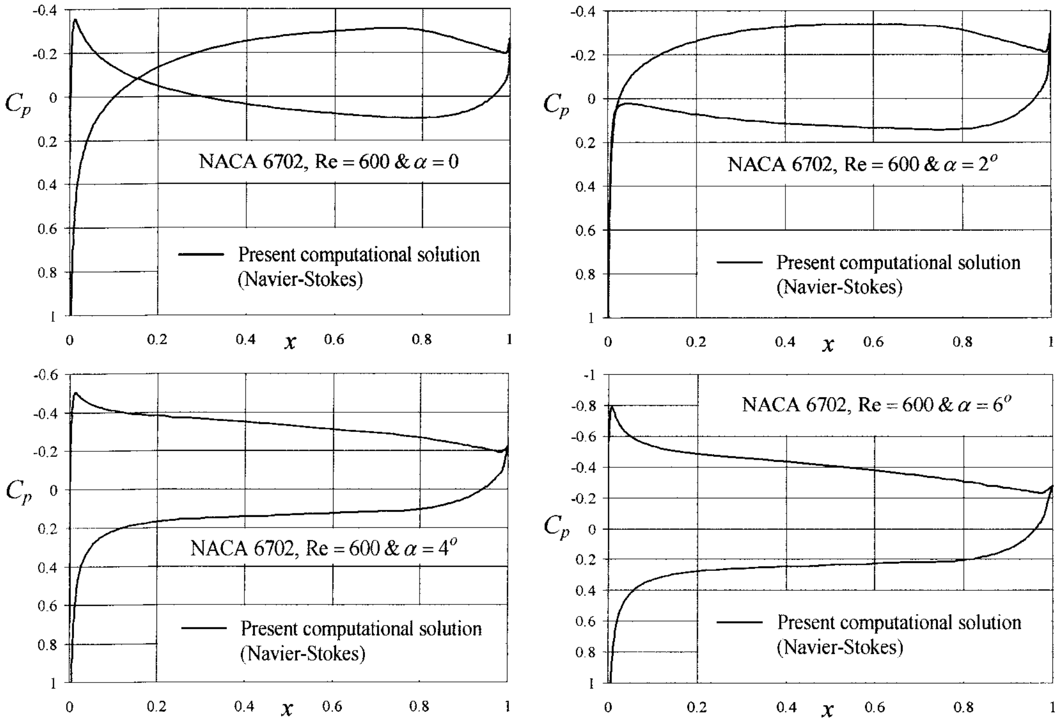

Figure 4.34 Pressure coefficient distribution on a NACA 6702 airfoil at Reynolds number Re =600 and angles of attack $\alpha = 0$, 2^o, 4^o and 6^o.

4.3.3 Lift and drag coefficients at very low Reynolds numbers

No matter how complex the airfoil (or body shape) may be, the aerodynamic lift and drag forces are entirely due to the pressure and shear stress distribution over the airfoil surface [7]. The pressure p obtained by solving the incompressible Navier-Stokes and continuity equations acts normal to the surface and the shear stress τ acts tangential to the airfoil surface. The shear stress is due to the friction between the airfoil surface and the air. To calculate the lift and drag coefficients, consider an airfoil of chord c placed at an incidence α in a uniform flow of velocity U_∞ as shown in Figure 4.35.

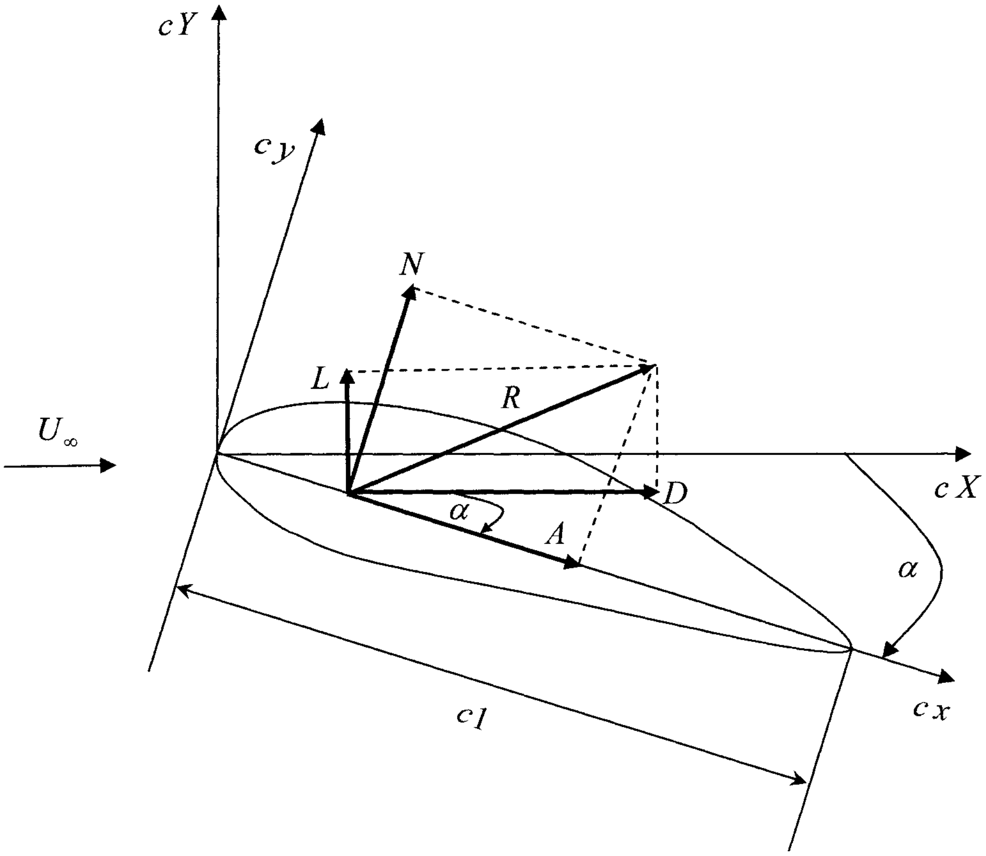

Figure 4.35 Illustration of the components of the resultant aerodynamic force.

The resultant aerodynamic force R is due to the net effect of the p and τ distributions integrated over the complete airfoil. The aerodynamic lift L per unit span is the component of R perpendicular to U_∞ while the drag force D is the component of R parallel to it. The normal force N is defined as the component of R perpendicular to the chord of the airfoil while the chordwise force A is the component that is parallel to it. From Figure 4.35, one deduces

$$L = N\cos\alpha - A\sin\alpha \ , \tag{4.109}$$

$$D = N\sin\alpha + A\cos\alpha \ . \tag{4.110}$$

The pressure and shear stress on the upper surface of the airfoil are denoted by p_u and τ_u, with p_l and τ_l for the lower surface, as shown in Figure 4.36. At a given point, the pressure is normal to the surface and is oriented at an angle θ relative to the perpendicular; shear stress is tangential to the surface and is oriented at the same angle relative to the horizontal. In Figure 4.36, the sign convention for θ is positive when measured clockwise from the vertical line to the direction of p and from the horizontal line in the direction of τ.

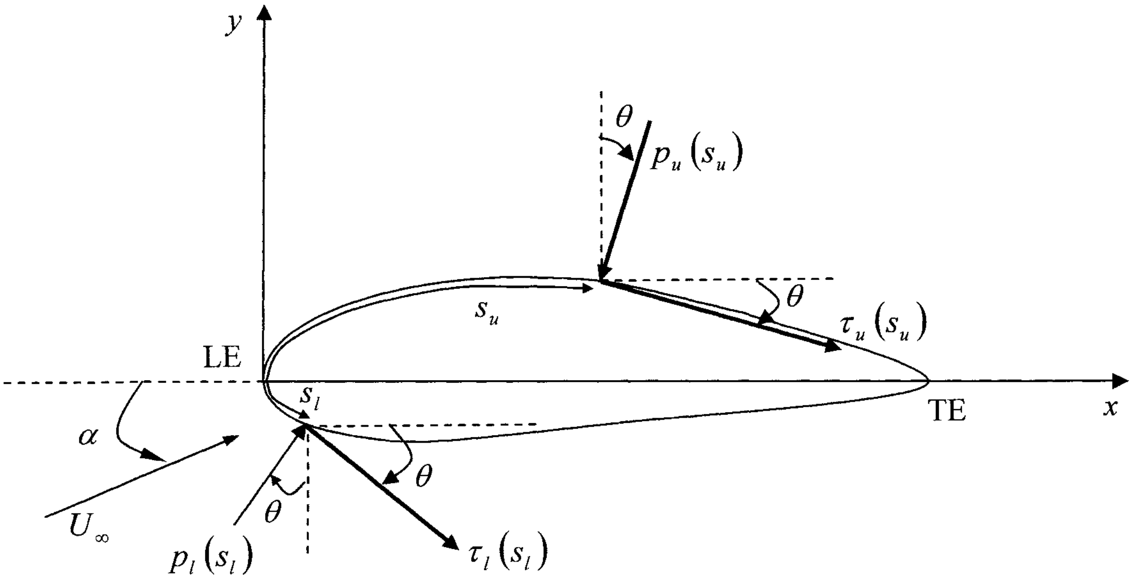

Figure 4.36 The integration of the pressure and shear stress distributions over an airfoil.

By considering an elemental surface unit area on the airfoil $dS = ds.1$ and integrating the normal and tangential pressure and shear distributions along the airfoil arc s from the leading edge (LE) to the trailing edge (TE), one obtains the total normal and chordwise forces per unit span

$$N = -\int_{LE}^{TE}(p_u\cos\theta + \tau_u\sin\theta)\,ds_u + \int_{LE}^{TE}(p_l\cos\theta - \tau_l\sin\theta)\,ds_l \ , \tag{4.111}$$

$$A = \int_{LE}^{TE} \left(-p_u \sin\theta + \tau_u \cos\theta \right) ds_u + \int_{LE}^{TE} \left(p_l \sin\theta + \tau_l \cos\theta \right) ds_l \ , \qquad (4.112)$$

The lift and drag forces per unit span are then evaluated using (4.109) and (4.110), respectively. The normal and chordwise coefficients are then expressed in terms of the pressure and skin friction coefficients by noting that

$$dx = ds \cos\theta \ , \qquad (4.113)$$

$$dy = -\left(ds \sin\theta \right) , \qquad (4.114)$$

and hence

$$C_N = \int_0^1 \left(C_{pl} - C_{pu} \right) dx + \int_0^1 \left(C_{fu} \frac{dy_u}{dx} + C_{fl} \frac{dy_l}{dx} \right) dx \ , \qquad (4.115)$$

$$C_A = \int_0^1 \left(C_{pu} \frac{dy_u}{dx} - C_{pl} \frac{dy_l}{dx} \right) dx + \int_0^1 \left(C_{fu} + C_{fl} \right) dx \ , \qquad (4.116)$$

with $C_N = N / \left(c \frac{1}{2} \rho_\infty U_\infty \right)$ and $C_A = A / \left(c \frac{1}{2} \rho_\infty U_\infty \right)$, where $C_p = 2\left(p - p_\infty \right)$ is the nondimensional pressure coefficient (p is nondimensionalized with respect to $\rho_\infty U_\infty$) and $C_f = \tau / \left(\frac{1}{2} \rho_\infty U_\infty \right)$ is the skin friction coefficient, while dy/dx is the slope of the surface. The shear stress on the airfoil surface is evaluated numerically from

$$\tau = \mu \left(\frac{\partial V(n)}{\partial n} \right)_{\text{airfoil surface}} , \qquad (4.117)$$

where $V(n)$ is the velocity in the direction tangent to the surface and n is the direction normal to the airfoil surface, and μ is the viscosity.

The two-dimensional lift and drag coefficients can then be expressed as

$$C_L = C_N \cos\alpha - C_A \sin\alpha \ , \qquad (4.118)$$

$$C_D = C_N \sin\alpha + C_A \cos\alpha \ , \qquad (4.119)$$

where $C_L = L / \left(c \frac{1}{2} \rho_\infty U_\infty \right)$ and $C_D = D / \left(c \frac{1}{2} \rho_\infty U_\infty \right)$.

The present method has been further validated by comparison with the results obtained by Kunz and Kroo [99] using the INS2D code from NASA Ames (developed by Rogers and Kwak [164]) for the lift and drag coefficients. The drag polar ($C_L - C_D$ plot) for NACA 4404 airfoil at Re=1000 is shown in Figure 4.37. Figures 4.38-4.41 present the variation of the lift coefficient with incidence ($C_L - \alpha$ plots) at Re=2000 for NACA 0002, 0004, 0006 and 0008 airfoils, the solutions of Kunz and Kroo [99] are also shown in the same figures for comparison. Figure 4.42 presents a comparison for two NACA airfoils (NACA 0002 and NACA 4402) at Re=1000 with the previous results obtained by the INS2D code from NASA Ames. The gains in airfoil performance due to the introduction of camber at such low Reynolds number are well pronounced in Figure 4.42.

At a Reynolds number Re=6000, the present lift coefficient solutions compared favorably with the previous results [99] obtained by the INS2D code [164] for NACA 0002 and NACA 0008 airfoils, as shown in Figure 4.43. The $C_L - C_D$ plots obtained with the present method for NACA 4402 airfoil were also compared with the numerical data of Kunz and Kroo [99] for two Reynolds numbers Re=1000 and 2000, as shown in Figure 4.44. In all these comparisons, the results obtained with the present computational method were in excellent agreement with the results obtained by Kunz and Kroo [99] using the INS2D code from NASA Ames [164].

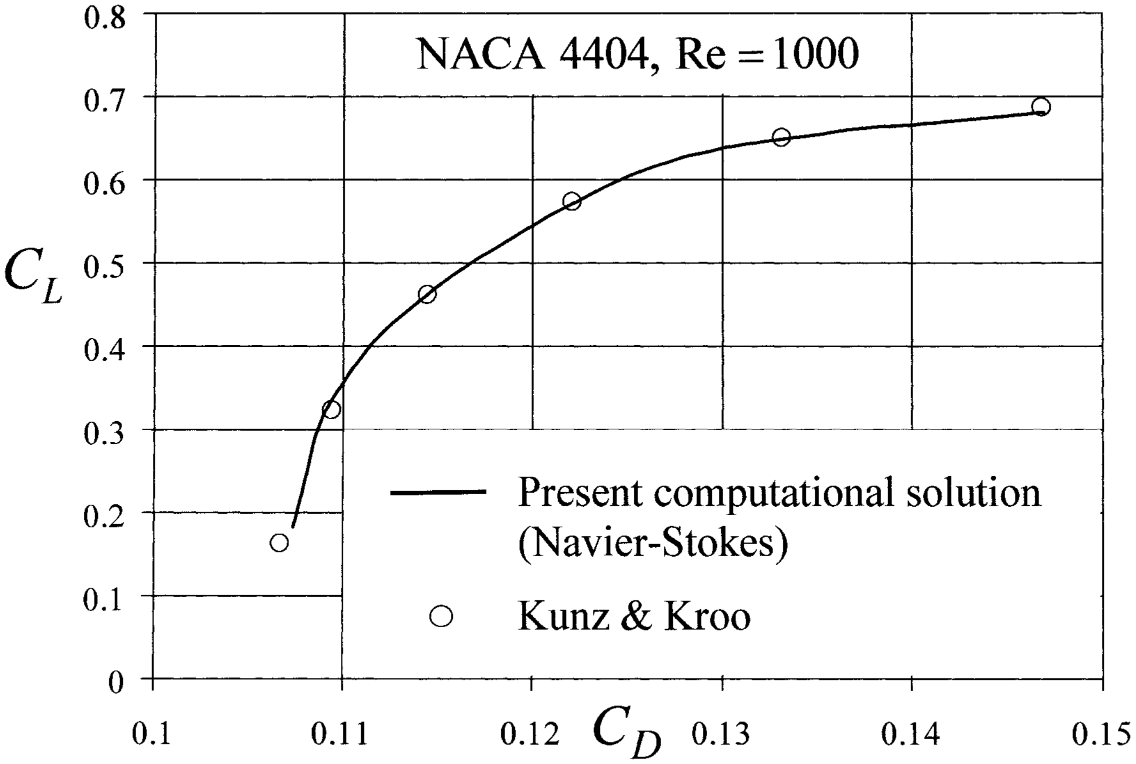

Figure 4.37 Drag polar for NACA 4404 airfoil at Re=1000.

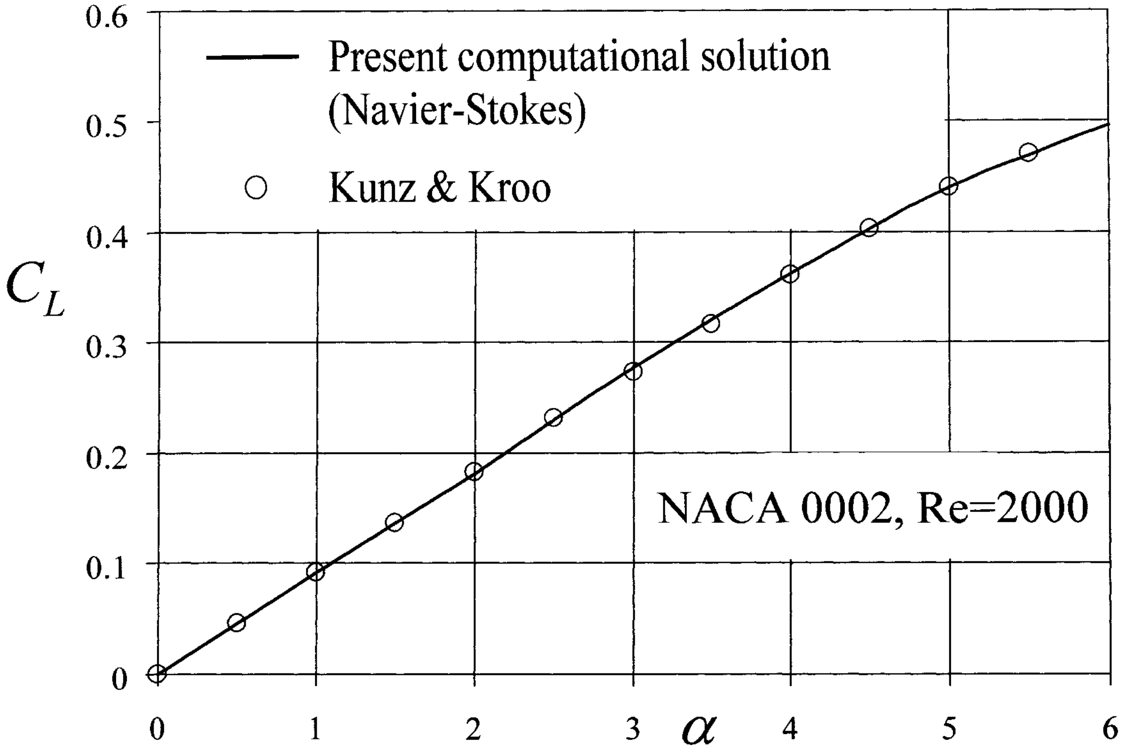

Figure 4.38 Lift coefficient variation for NACA 0002 airfoil at Re=2000.

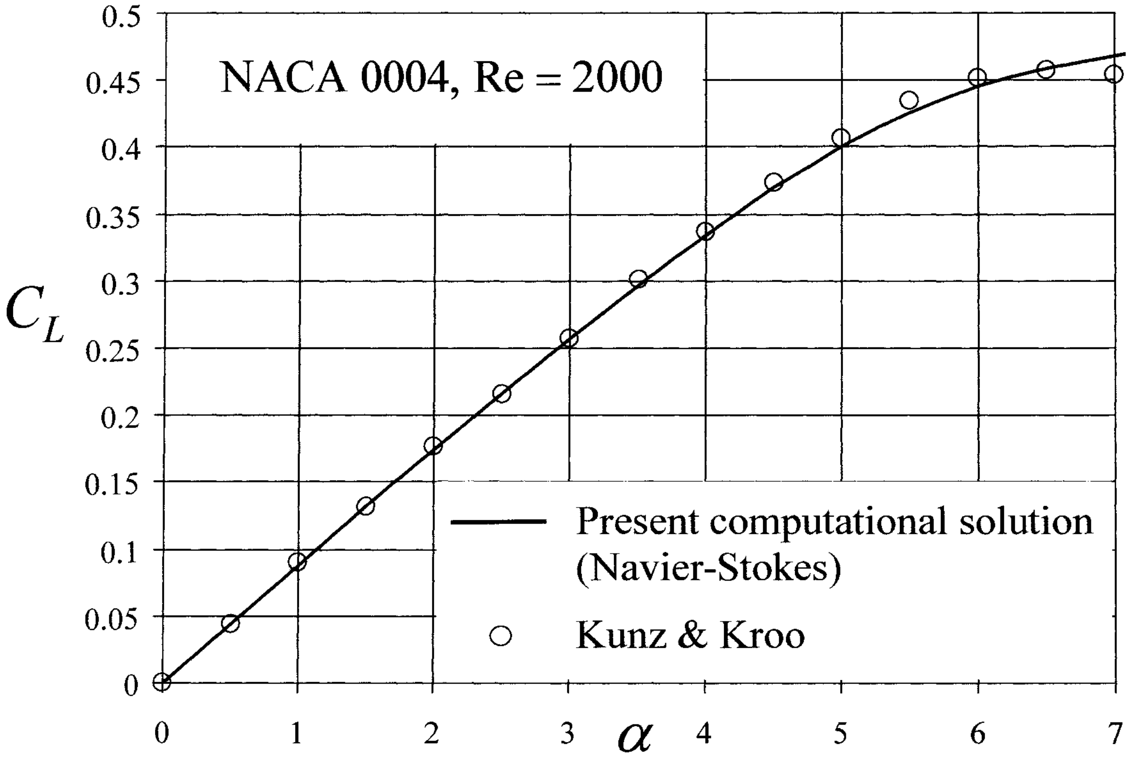

Figure 4.39 Lift coefficient variation for NACA 0004 airfoil at Re=2000.

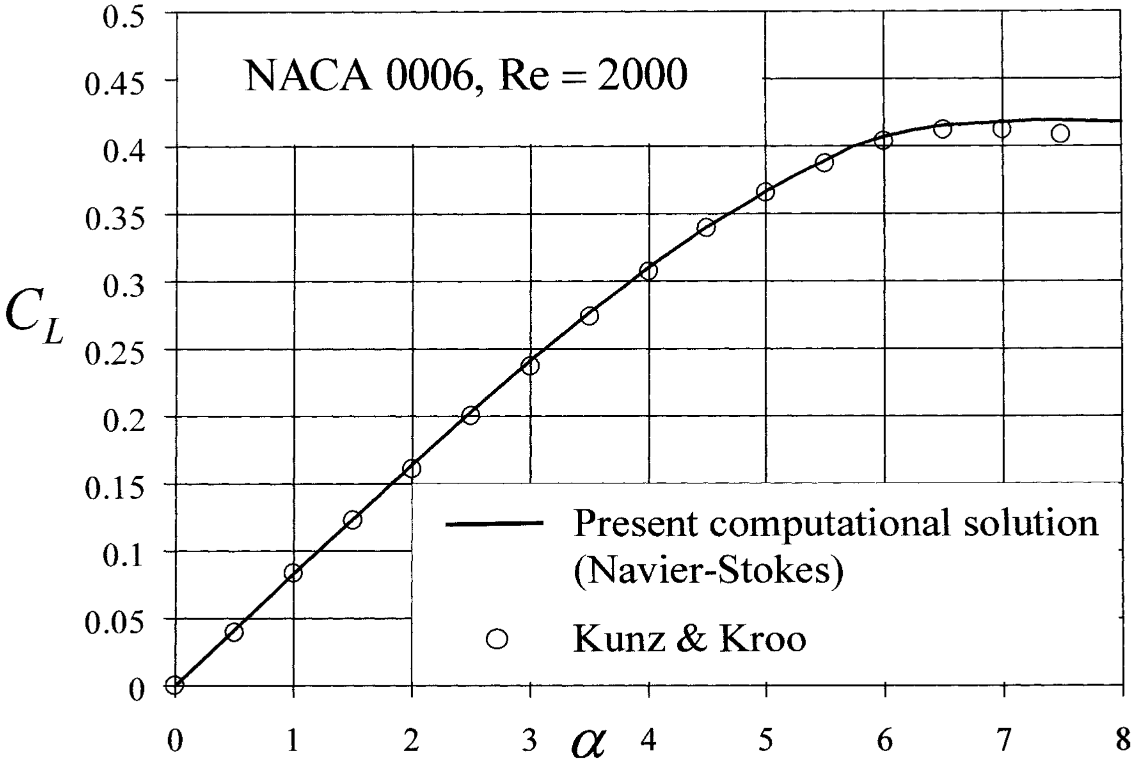

Figure 4.40 Lift coefficient variation for NACA 0006 airfoil at Re=2000.

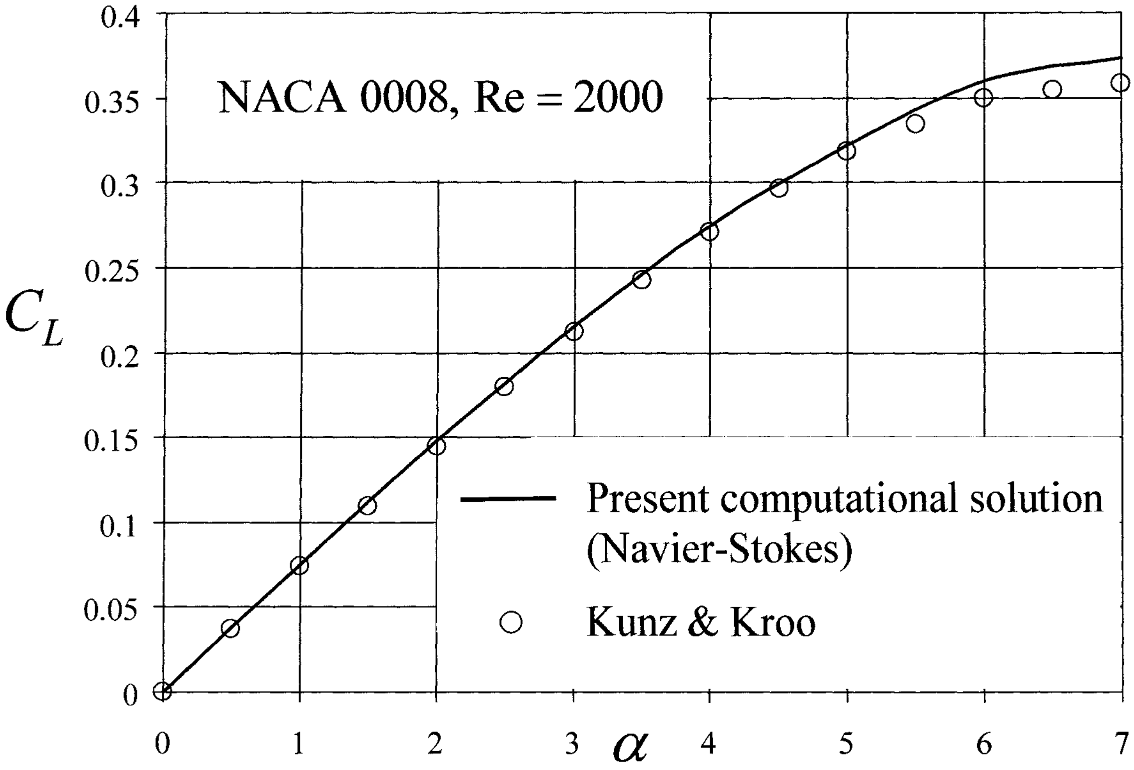

Figure 4.41 Lift coefficient variation for NACA 0008 airfoil at Re=2000.

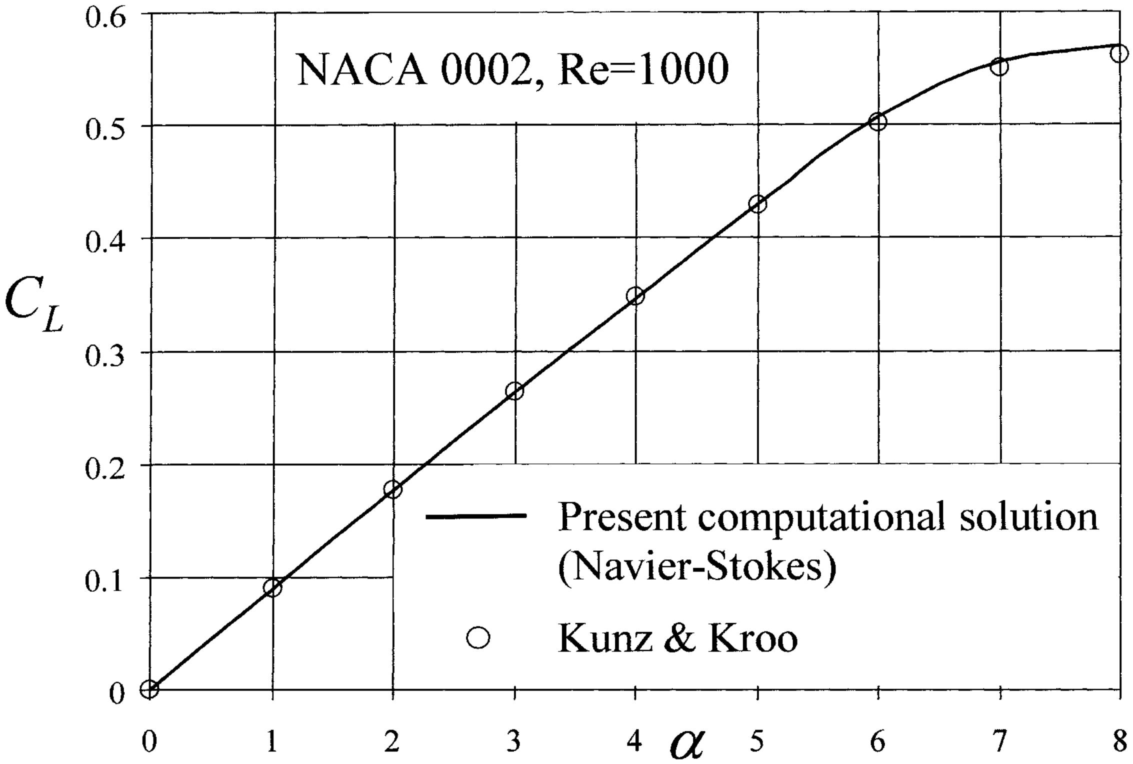

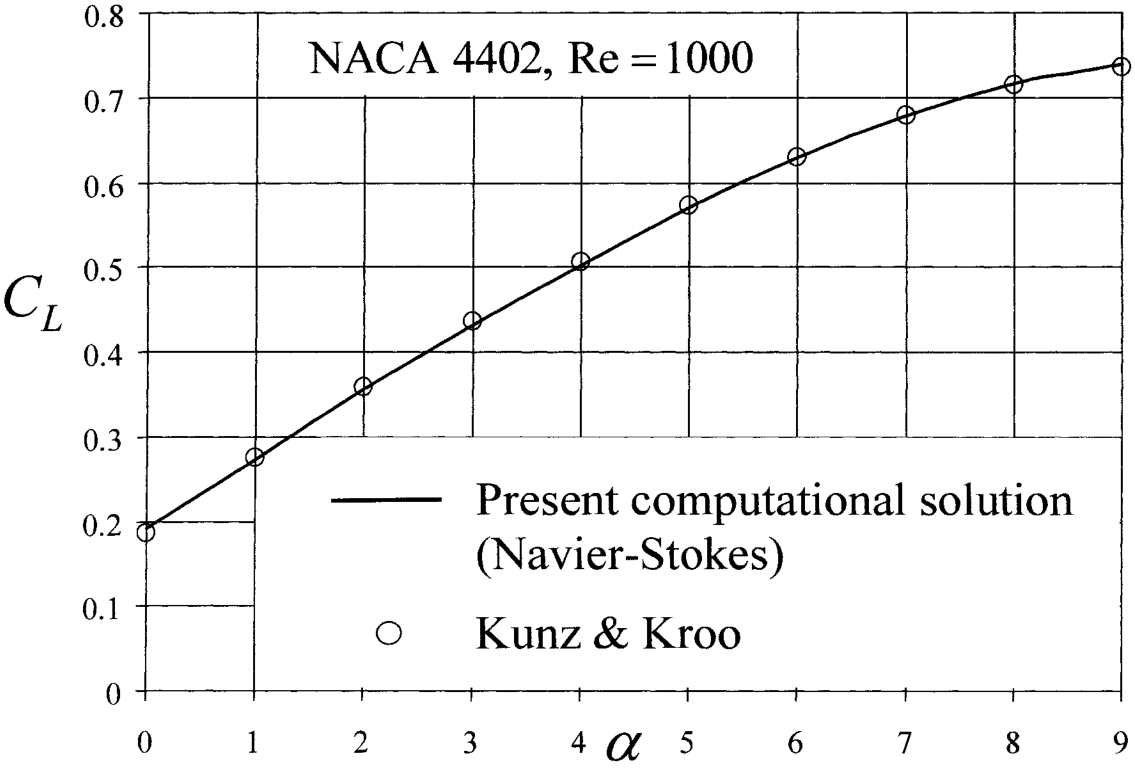

Figure 4.42 Lift coefficient variation for NACA 0002 and 4402 airfoils at Re=1000.

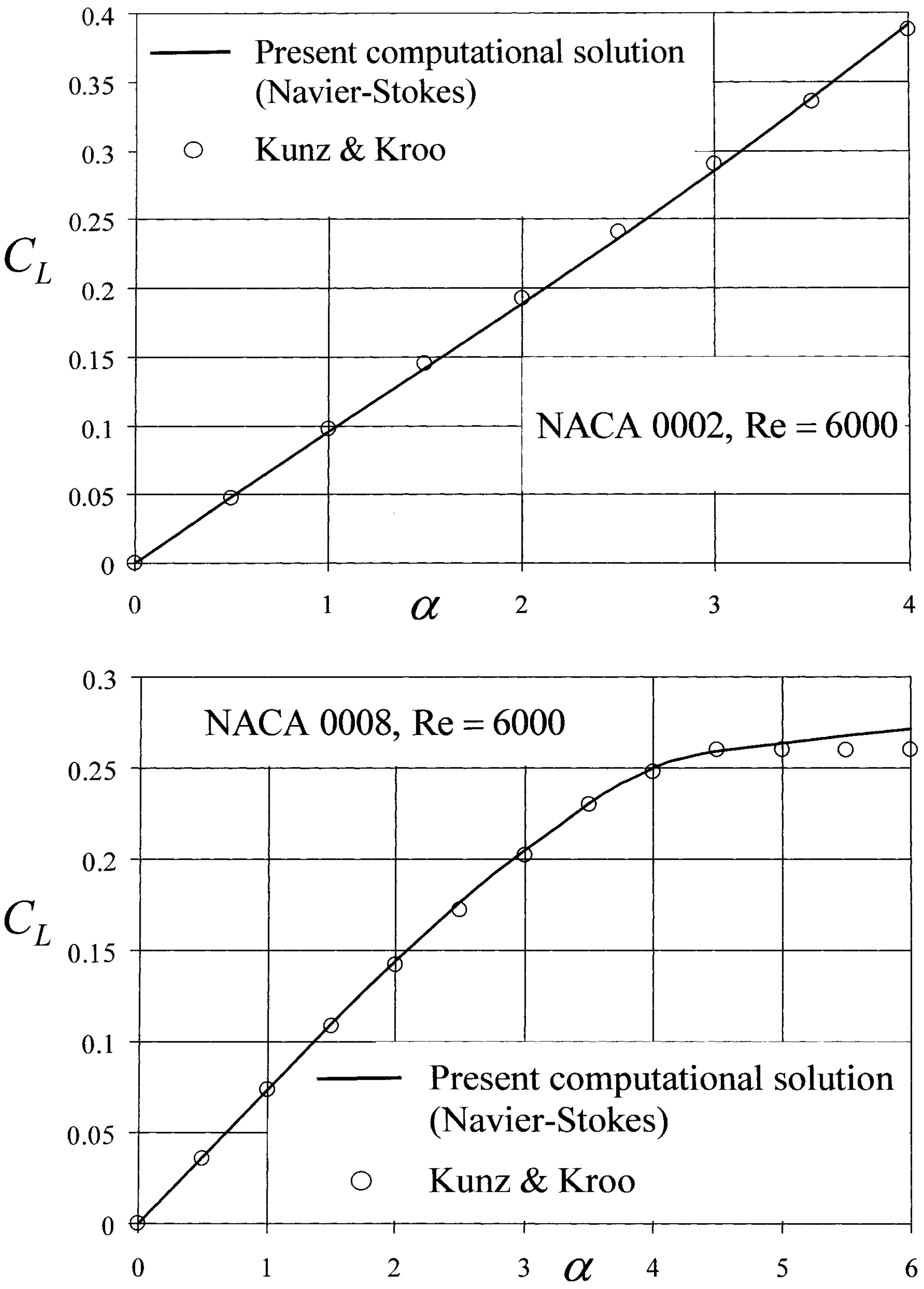

Figure 4.43 Lift coefficient variation for NACA 0002 and 0008 airfoils at Re=6000.

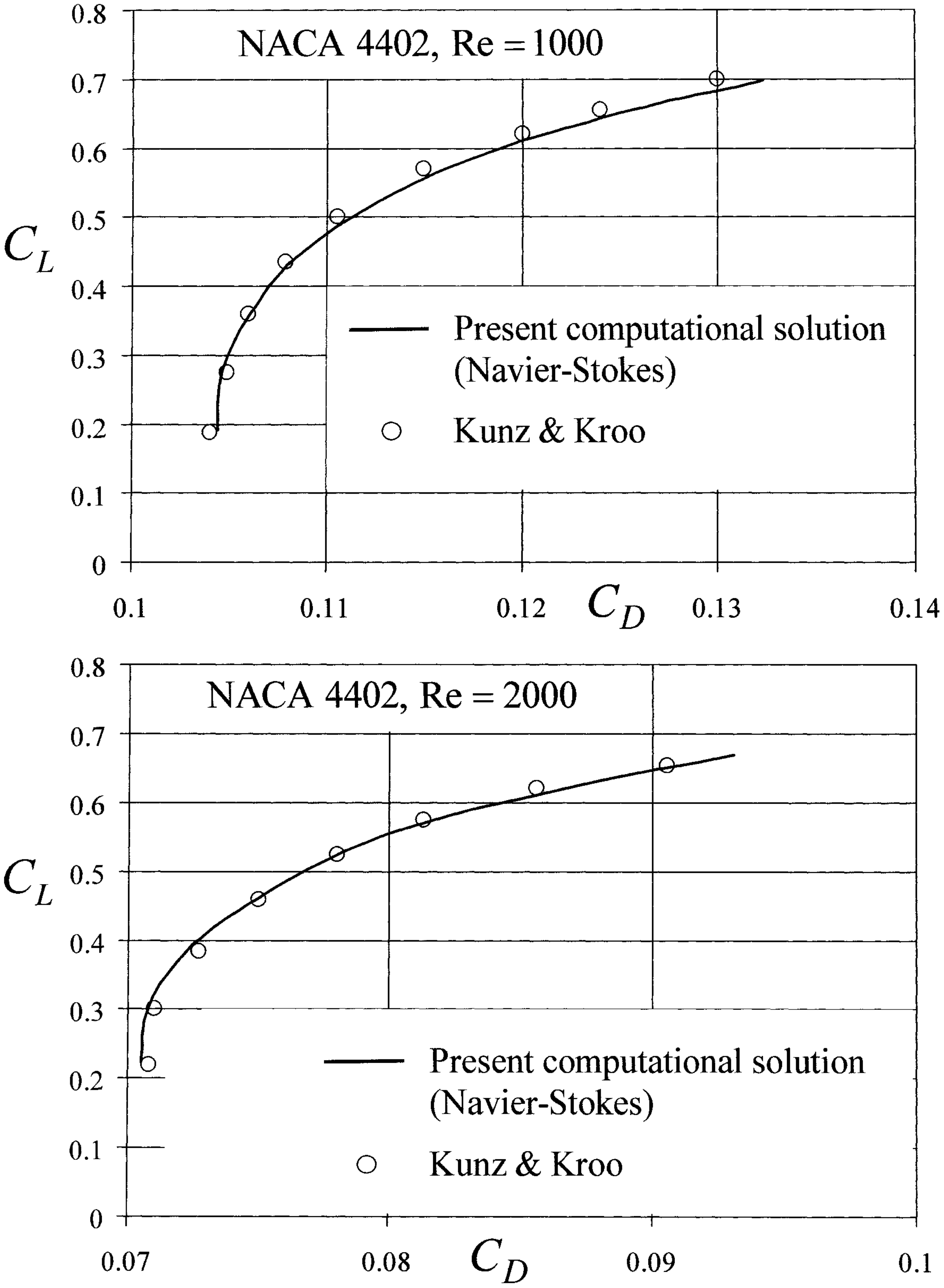

Figure 4.44 Drag polar for NACA 4402 airfoil at Re=1000 and 2000.

Since no previous results were available for Reynolds numbers smaller than 1000, after validation, the present method has been used to obtain solutions for different airfoils at various low Reynolds numbers. This will help us better understand the complex nature of the viscous flows at very low Reynolds numbers, the effect of geometric variations on airfoil performance and establish benchmark solutions for viscous flows with separation.

The drag coefficient variation with angle of attack ($C_D - \alpha$ plots) as well as the drag polars ($C_L - C_D$ plots) were obtained for NACA 4404 airfoil at Reynolds numbers Re=400, 600, 800 and 1000, as shown in Figure 4.45. At Reynolds number Re=800, the lift and drag coefficients as well as the drag polars were obtained for NACA 2404, NACA 4404 and NACA 6404 airfoils (maximum camber is increased in increments of 2%), as shown in Figure 4.46.

For NACA 2302, NACA 2502 and NACA 2702 airfoils (with the maximum camber located at 30%, 50% and 70% chord, respectively), $C_L - \alpha$, $C_D - \alpha$ and $C_L - C_D$ plots at a constant Reynolds number Re=1000 were generated and presented in Figure 4.47.

For profiles with 2% relative thickness, 70% camber position along the chord and 2%, 4% and 6% maximum camber (NACA 2702, NACA 4702 and NACA 6702 airfoils), the lift, drag and drag polar plots at Reynolds number Re=600 are shown in Figure 4.48.

For NACA 4702 airfoil, the drag variation with incidence and the drag polars are shown in Figure 4.49 for Reynolds numbers Re=400, 600, 800 and 1000.

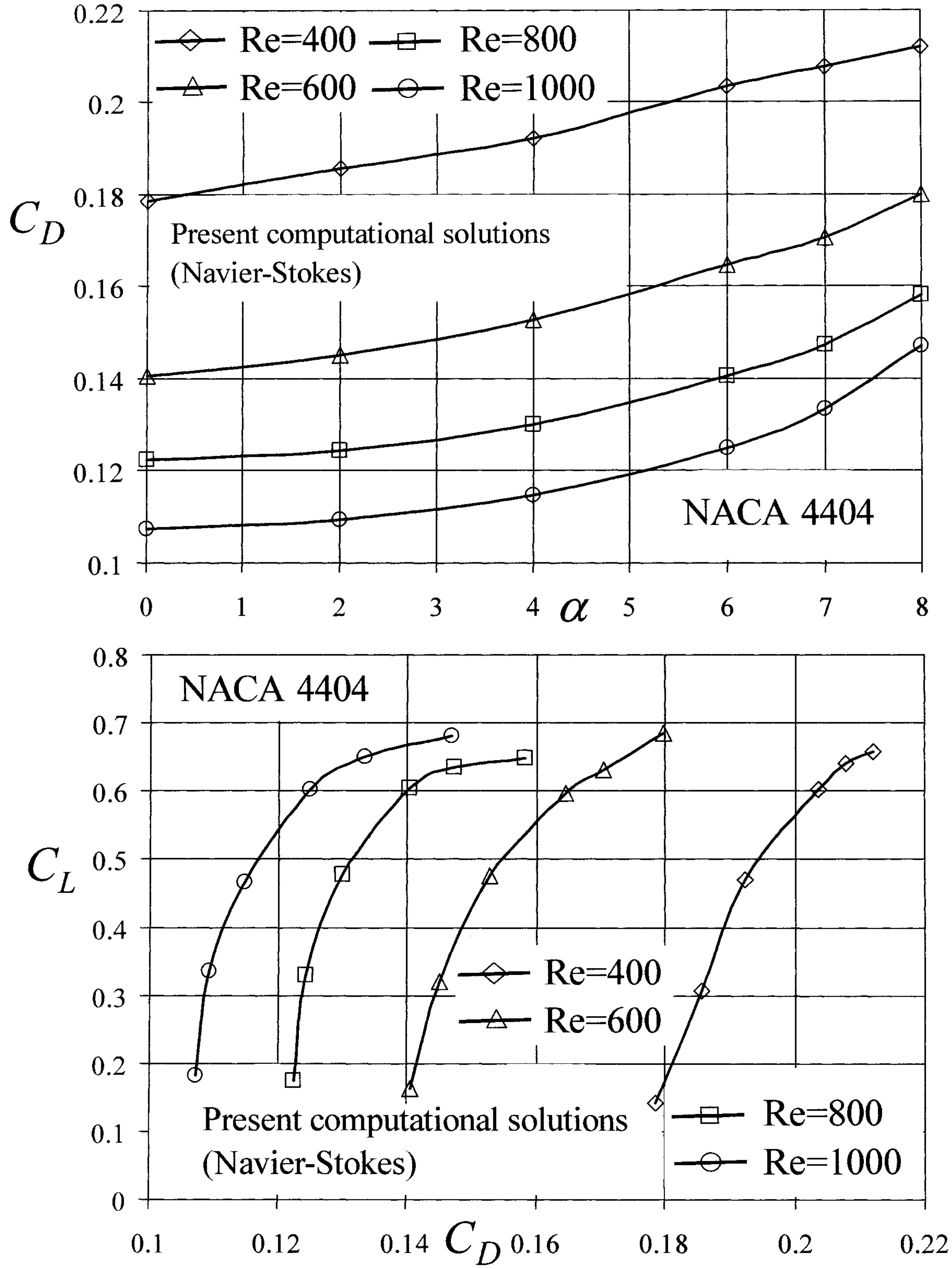

Figure 4.45 Drag variation and drag polars for NACA 4404 airfoil at Reynolds numbers, Re=400, 600, 800 and 1000.

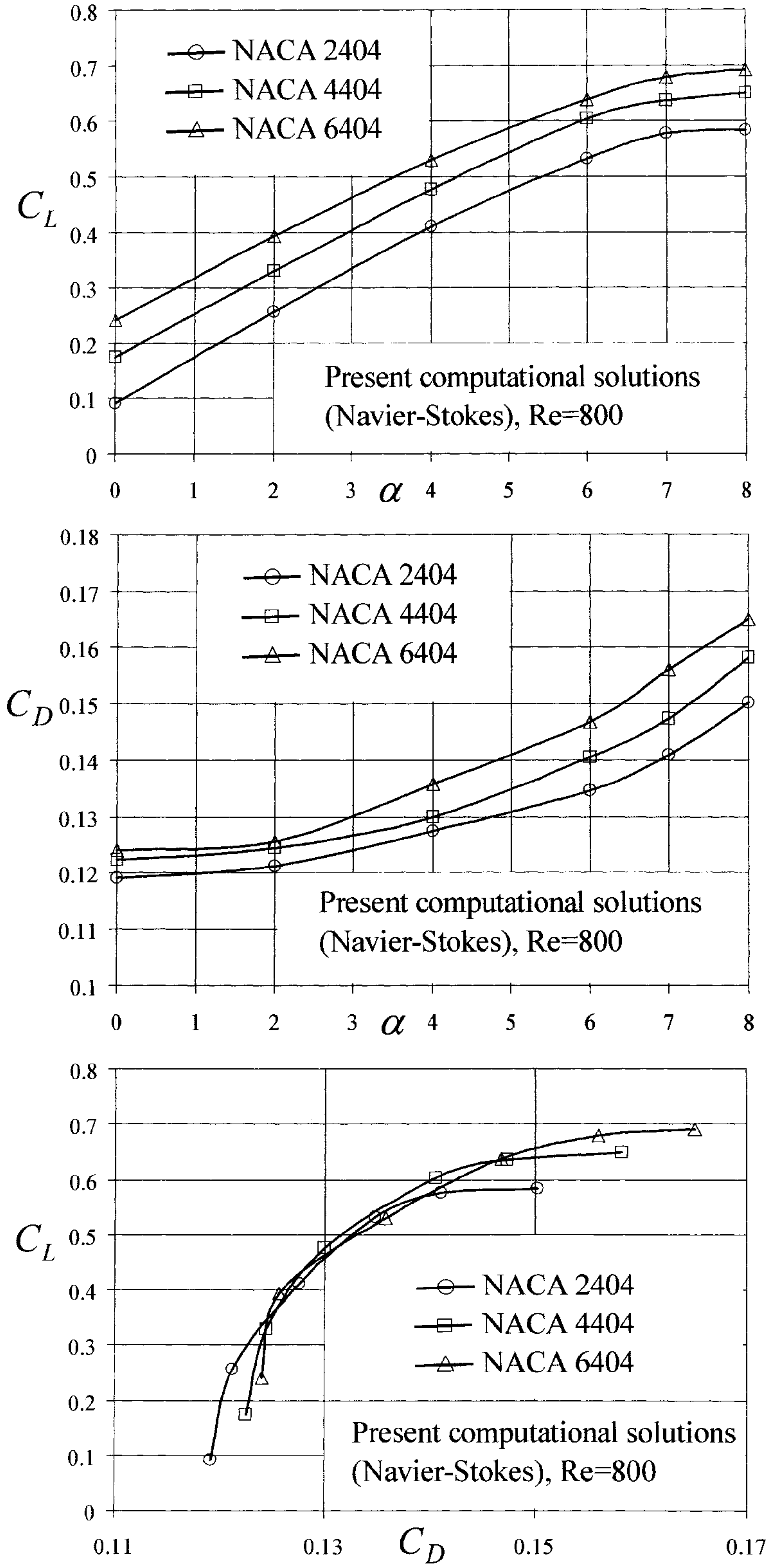

Figure 4.46 Lift, drag and drag polar curves for NACA 2404, NACA 4404 and NACA 6404 airfoils at Re=800.

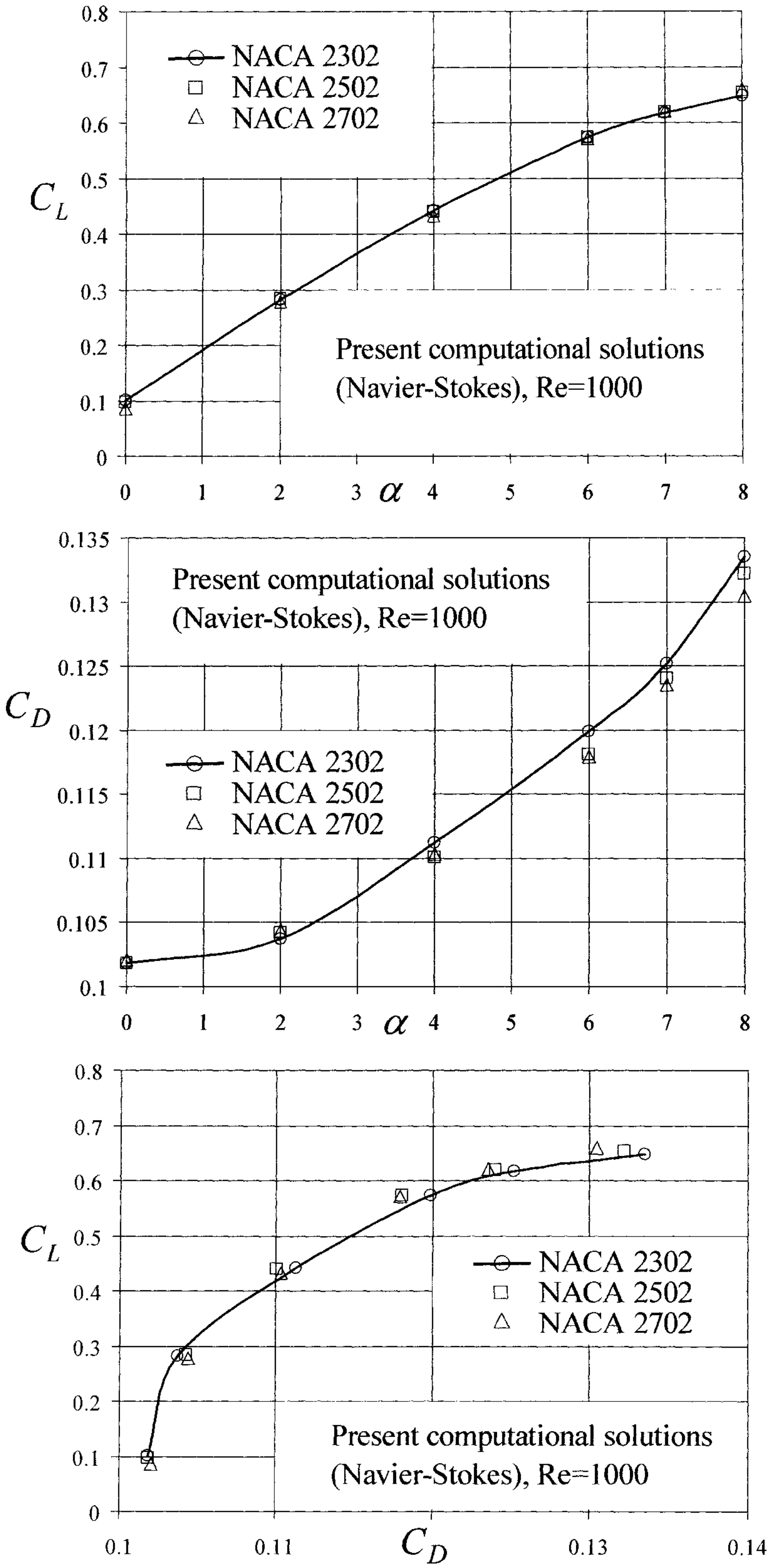

Figure 4.47 Lift, drag and drag polar curves for NACA 2302, NACA 2502 and NACA 2702 airfoils at Re=1000.

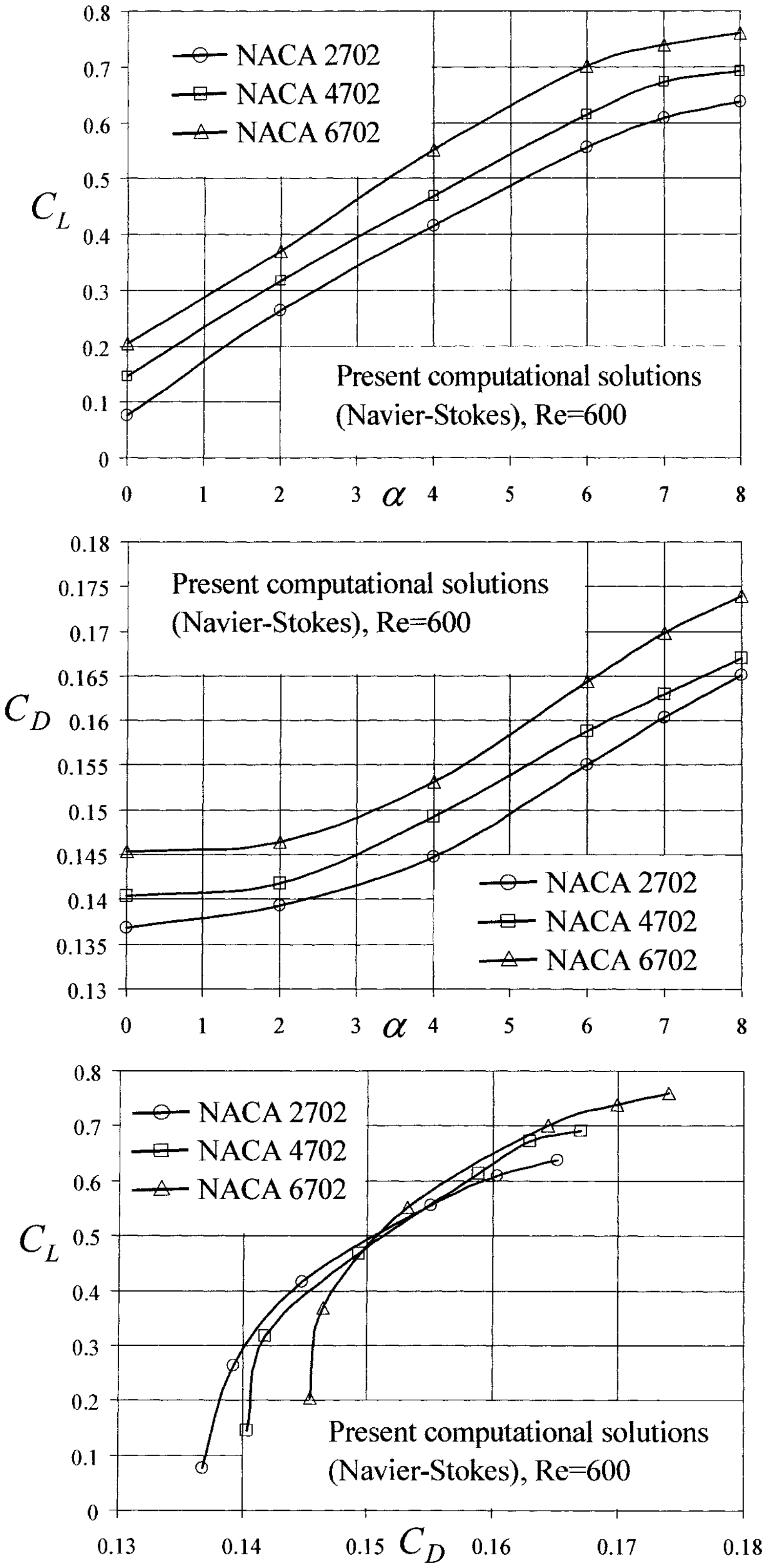

Figure 4.48 Lift, drag and drag polar curves for NACA 2702, NACA 4702 and NACA 6702 airfoils at Re=600.

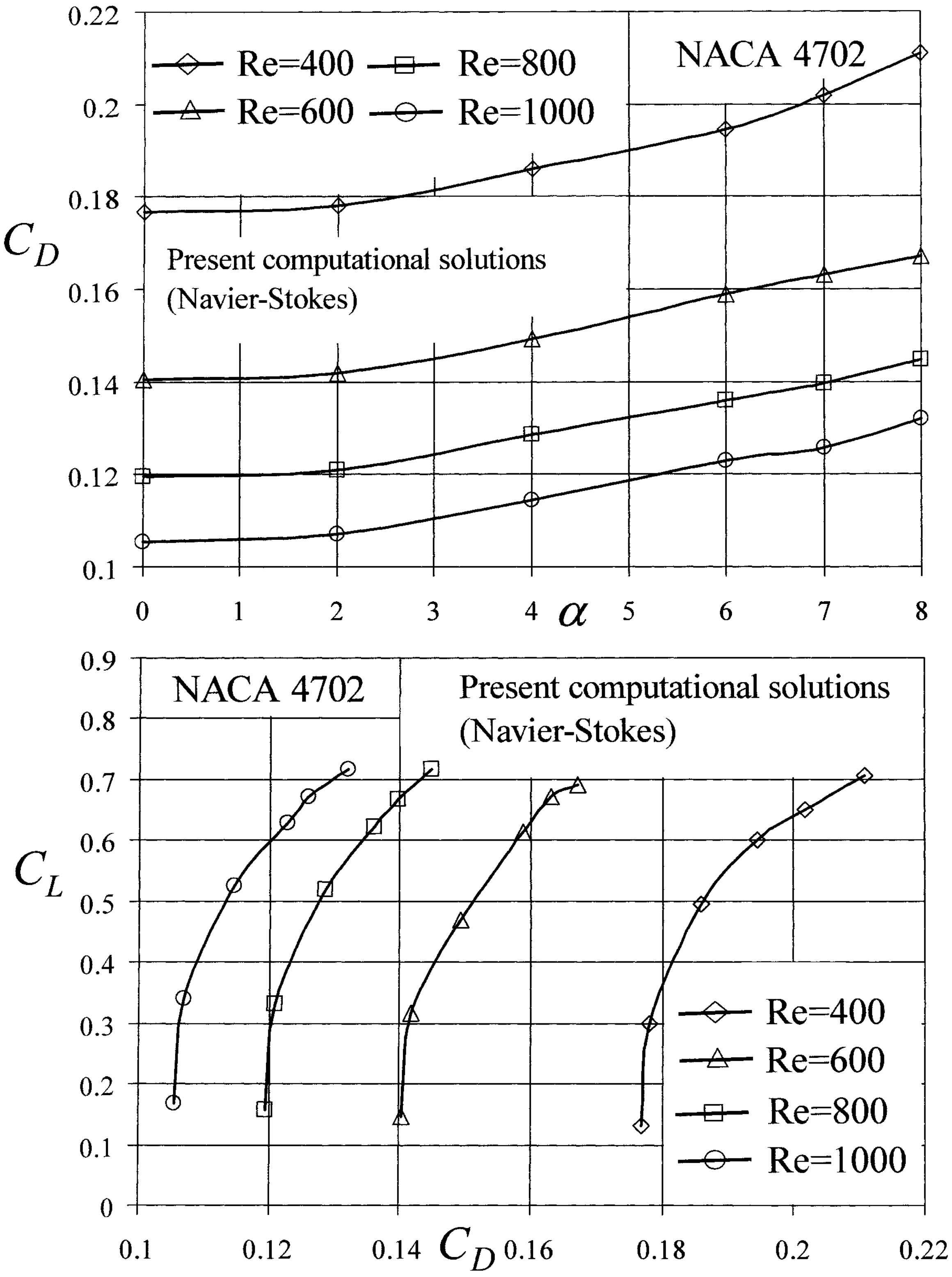

Figure 4.49 Drag variation and drag polars for NACA 4702 airfoil at Reynolds numbers, Re=400, 600, 800 and 1000.

4.4 Discussion of the numerical results

4.4.1 Reynolds number effects

The effects of Reynolds number on the pressure distribution and the aerodynamic performance of a series of airfoil sections have been investigated based on solving the two-dimensional, incompressible, Navier-Stokes equations. The effect of the change in the Reynolds number on the pressure coefficient distributions on NACA 0002 airfoil can be seen by comparing the results shown in Figure 4.8. One can notice a marked increase in the pressure coefficient on the airfoil with the decrease in the Reynolds number. The increase in the pressure coefficient, which is due to a thicker boundary layer, is more pronounced towards the trailing edge. At the same time, the variation of the pressure coefficient near the leading edge is smoother due to stronger viscous effects at smaller Reynolds numbers.

Similar effects, although less pronounced, can also be seen for the pressure coefficient distributions on the NACA 0008 airfoil by comparing the results shown in Figure 4.9. However, the low Reynolds number effects are somewhat less pronounced than for NACA 0002 airfoil, because in this case the boundary layer thickness is relatively smaller with respect to the airfoil thickness. For a better illustration of the low Reynolds number effects, the inviscid solution obtained in Chapter 2 is also shown in Figures 4.8 and 4.9. One can notice a dramatic change in the pressure coefficient distribution at Re=6000 in comparison with the inviscid solution.

It is also seen in Figures 4.11-4.13 that reducing the Reynolds number from Re=6000 to Re=1000 results in a reduction in both the slope of the adverse gradient in the pressure recovery region and the minimum pressure close to the leading edge of the airfoil. The Re=1000 case for NACA 4402 airfoil results in a reduction of the leading edge suction peak more than that for Re=2000 case. The reduction of Reynolds number alters the effective camber of the airfoil and hence results in smoother pressure distribution near the leading edge of the airfoil. As shown in Figures 4.23-4.26, for NACA 4404 airfoil the effect of reducing the Reynolds number on the pressure distribution is more pronounced at the trailing edge of the airfoil and at high angles of attack, for example at $\alpha = 6^o$. A similar behavior is also observed for NACA 4702 airfoil when the Reynolds number is reduced from Re=1000 to Re=400, as depicted in Figures 4.29-4.32. It is seen that the effect of reducing the Reynolds number plays a more important role in improving the performance of thin airfoils compared to thicker ones.

The most obvious effect of flight at very low Reynolds numbers is the increase in the drag coefficient of the airfoil due to viscous effects. At the same lift coefficient, flows at lower Reynolds numbers have more drag than those at higher ones. This is observed in the drag polar plots shown in Figure 4.44 for NACA 4402 airfoil when the Reynolds number is decreased from Re=2000 to Re=1000. An interesting physical aspect to observe is the fact that the increase in drag due to the reduction of Reynolds number is not reciprocated in lift, as shown in Figure 4.45 for NACA 4404 airfoil. For the same lift coefficient, the drag is much higher, nearly double, for Re=400 case than Re=1000 one. This is explained by the changed airfoil geometry due to the more dominant viscous effects at lower Reynolds numbers (that is physically related to the increase in boundary layer thickness) which in turn reduces the effective camber of the airfoil. This phenomena can also be observed for NACA 4702 airfoil when the Reynolds number is reduced from Re=1000 to Re=400, as shown in Figure 4.49.

4.4.2 Flow separation on airfoils at incidence

The viscous effects in flows at very low Reynolds numbers dominate the fluid inertia forces. The velocity changes from zero at the airfoil surface to that of the free stream at some distance far from it; this change takes place in the boundary layer. An important question to answer is to determine the conditions when separation of the flow from the airfoil surface may occur. The point of separation is defined as the point where the velocity gradient at the airfoil surface becomes zero, which is the limit between regions of forward and reverse flow. Numerically,

$$\text{point of separation: } \left(\frac{\partial V(n)}{\partial n}\right)_{\text{airfoil surface}} = 0 . \tag{4.120}$$

In order to better understand the flow separation phenomena in highly viscous flows and answer the question of whether and where separation occurs, the streamline contours for different airfoil sections at various low Reynolds numbers and angles of attack have been generated.

A comparison of the separation and reattachment positions (denoted by x_s and x_r, respectively) as well as the separation length l_s is given in Table 4.1 for NACA 0002, NACA 0004, NACA 0006 and NACA 0008 airfoils at Reynolds number Re=2000 and $\alpha = 6^o$. The corresponding streamline contours are shown in Figure 4.50. Streamlines near the trailing edge of the airfoil are displayed at an enlarged scale in the same Figure.

Table 4.1 Flow separation comparison for NACA 0002, NACA 0004, NACA 0006 and NACA 0008 airfoils at Reynolds number Re=2000 and $\alpha = 6^o$.

Airfoil type	separation position, x_s	reattachment position, x_r	separation length, l_s
NACA 0002	0.009448	0.983755	0.974307
NACA 0004	0.345298	0.985038	0.639739
NACA 0006	0.493517	0.987267	0.493749
NACA 0008	0.501505	0.986959	0.485453

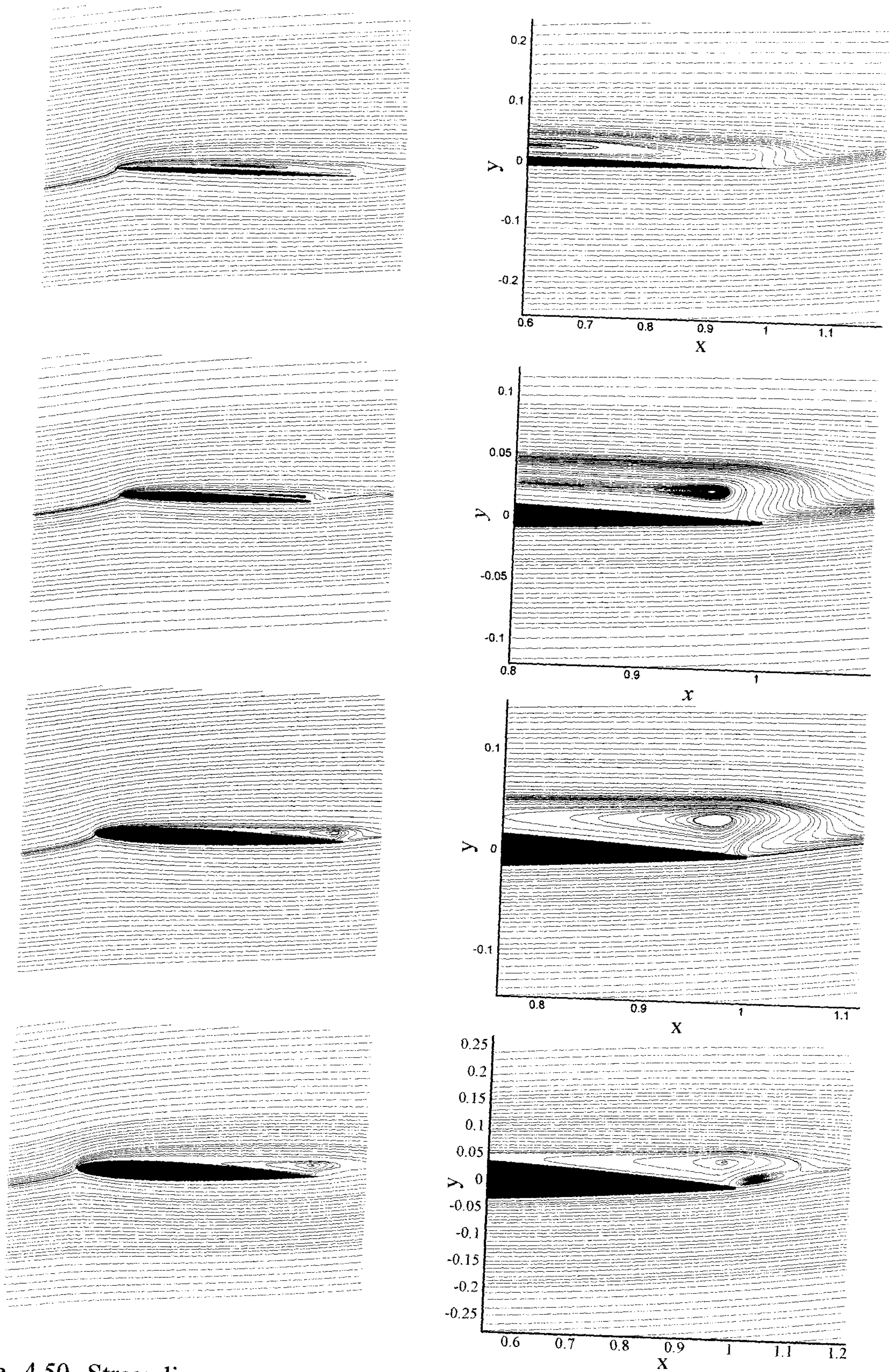

Figure 4.50 Streamline contours at Reynolds number Re=2000 and $\alpha = 6^o$ for NACA 0002, NACA 0004, NACA 0006 and NACA 0008 airfoils, respectively.

As shown in Table 4.1 and Figure 4.50, increasing the airfoil thickness from 2% to 8% (NACA 0002 to NACA 0008 airfoils) at Reynolds number Re=2000 and $\alpha = 6^o$ has the effect of shifting the onset of separation from the leading edge to almost mid-chord while reducing the separation length and maintaining the reattachment position at nearly 98% of the chord. It is seen that a region of recirculation extends behind the trailing edge of the NACA 0008 airfoil as compared to the other thinner profiles.

The streamline contours for NACA 0004 airfoil at Reynolds number Re=2000 and $\alpha = 4^o$, 6^o and 7^o are shown in Figure 4.51. It is seen that at $\alpha = 4^o$ the flow is completely attached and separation only appears at higher angles of attack. At $\alpha = 7^o$, separation is initiated at $x_s = 0.07848$ from the leading edge of the airfoil with a separation length of $l_s = 0.90638$ compared to $x_s = 0.34529$ and $l_s = 0.639739$ at $\alpha = 6^o$. In this case, increasing the incidence by 1^o results in a severe separation extending almost along the entire airfoil chord with a more pronounced circulation region.

A comparison of the separation and reattachment positions as well as the separation length is given in Table 4.2 for NACA 4402 airfoil at Reynolds numbers Re=1000 and 2000 and angles of attack ranging from $\alpha = 3^o$ to $\alpha = 8^o$. The streamline contours for NACA 4402 airfoil at Re=2000 are shown in Figure 4.52. A notable physical aspect of the flow at these conditions is the development of a recirculation region at a relatively low incidence $\alpha = 6^o$ behind the trailing edge of the airfoil. The onset of trailing edge separation is pushed from $\alpha = 3^o$ at Re=2000 to $\alpha = 5^o$ at Re=1000. For the same amounts of trailing edge separation, the lower Reynolds number case achieves more than 1.5^o higher angle of attack as the incidence is increased.

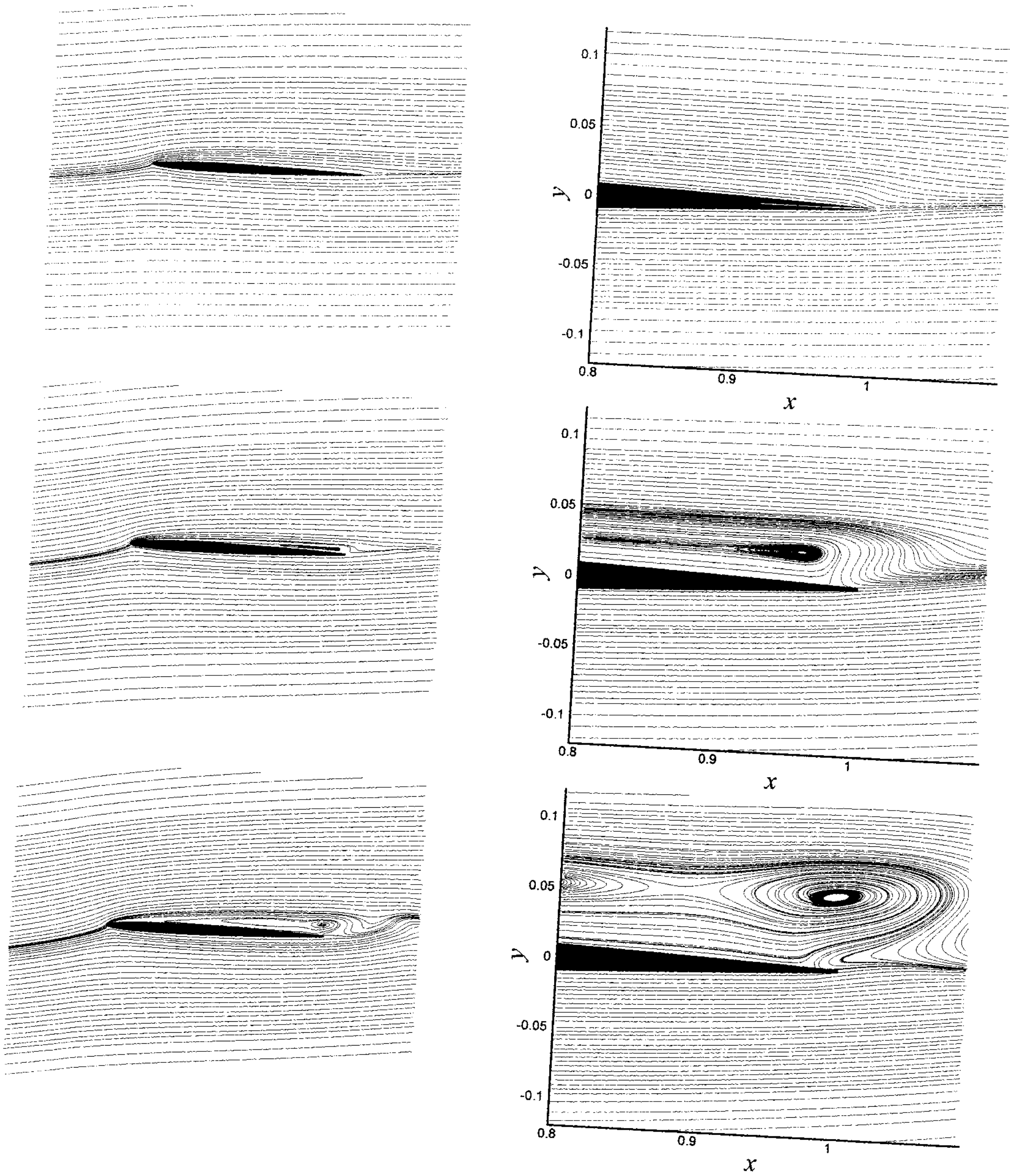

Figure 4.51 Streamline contours for NACA 0004 airfoil at Reynolds number Re=2000 and $\alpha = 4^o$, 6^o and 7^o, respectively.

Table 4.2 Flow separation comparison for NACA 4402 airfoil at Reynolds numbers Re=1000 and 2000 at different incidences.

Reynolds number, Re		1000	2000
$\alpha = 3^o$	x_s	No separation	0.935308
	x_r		0.984812
	l_s		0.049504
$\alpha = 4^o$	x_s	No separation	0.836689
	x_r		0.986345
	l_s		0.149655
$\alpha = 5^o$	x_s	0.904969	0.734218
	x_r	0.975679	0.985281
	l_s	0.070710	0.251063
$\alpha = 6^o$	x_s	0.795799	0.639649
	x_r	0.978205	0.983608
	l_s	0.182406	0.343958
$\alpha = 7^o$	x_s	0.683689	0.553424
	x_r	0.977878	0.984331
	l_s	0.294189	0.430906
$\alpha = 8^o$	x_s	0.571705	0.450262
	x_r	0.975285	0.961226
	l_s	0.403579	0.510963

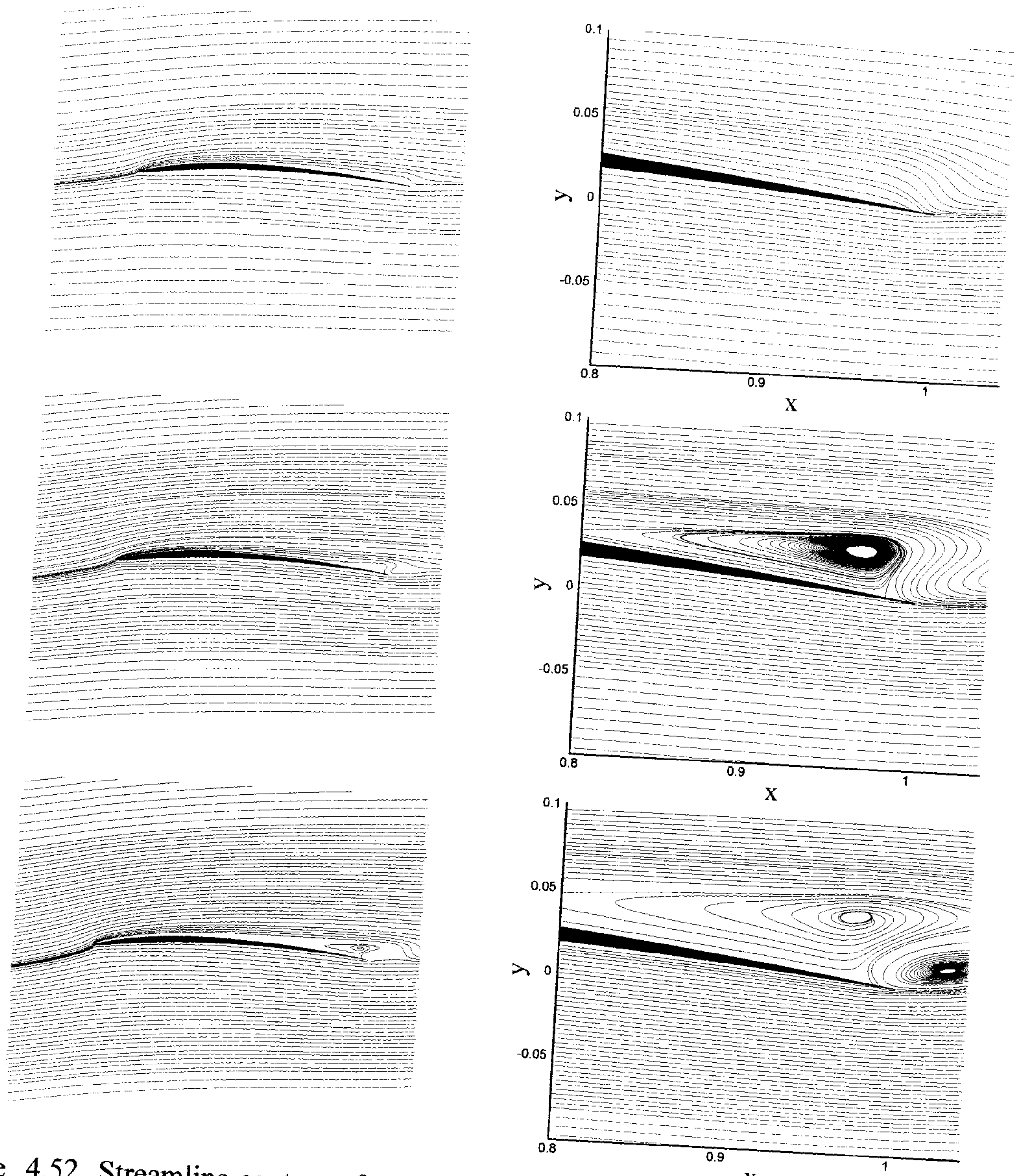

Figure 4.52 Streamline contours for NACA 4402 airfoil at Reynolds number Re=2000 and $\alpha = 4^o$, 5^o and 6^o, respectively.

At Reynolds number Re=800, the separation and reattachment positions are given in Table 4.3 for NACA 2404, NACA 4404 and NACA 6404 airfoils (characterized by 4% relative thickness while the camber is fixed at 40% chord and 2%, 4% and 6% maximum camber, respectively) at $\alpha = 2^o$, 4^o, 6^o, 7^o and 8^o. It is seen that the separation at the trailing edge is initiated at lower incidences for NACA 6404, while the flow is fully attached for the lower cambered sections (NACA 2404 and NACA 4404 airfoils).

Table 4.3 Onset of separation comparison for NACA 2404, NACA 4404 and NACA 6404 airfoils at Reynolds number Re=800 at different angles of attack.

Airfoil type		NACA 2404	NACA 4404	NACA 6404
$\alpha = 2^o$	x_s	No separation	No separation	0.930617
	x_r			0.975605
	l_s			0.044988
$\alpha = 4^o$	x_s	No separation	No separation	0.812921
	x_r			0.979555
	l_s			0.166634
$\alpha = 6^o$	x_s	0.929389	0.777701	0.689317
	x_r	0.965549	0.976729	0.976999
	l_s	0.036160	0.199027	0.287681
$\alpha = 7^o$	x_s	0.749063	0.682713	0.632371
	x_r	0.974572	0.975893	0.974353
	l_s	0.225509	0.293180	0.341982
$\alpha = 8^o$	x_s	0.573599	0.592716	0.579414
	x_r	0.973947	0.972774	0.969257
	l_s	0.400348	0.380058	0.389843

For the same angle of attack, augmenting the airfoil camber from 2% to 6% causes an increase in the separation length while the separation position is pushed towards the leading edge. However, it is seen that the reattachment position is maintained at nearly 97% chord as indicated in Table 4.3. The onset of trailing edge separation is displayed for NACA 2404 airfoil at Re=800 and $\alpha = 6^o$, 7^o and 8^o in Figure 4.53.

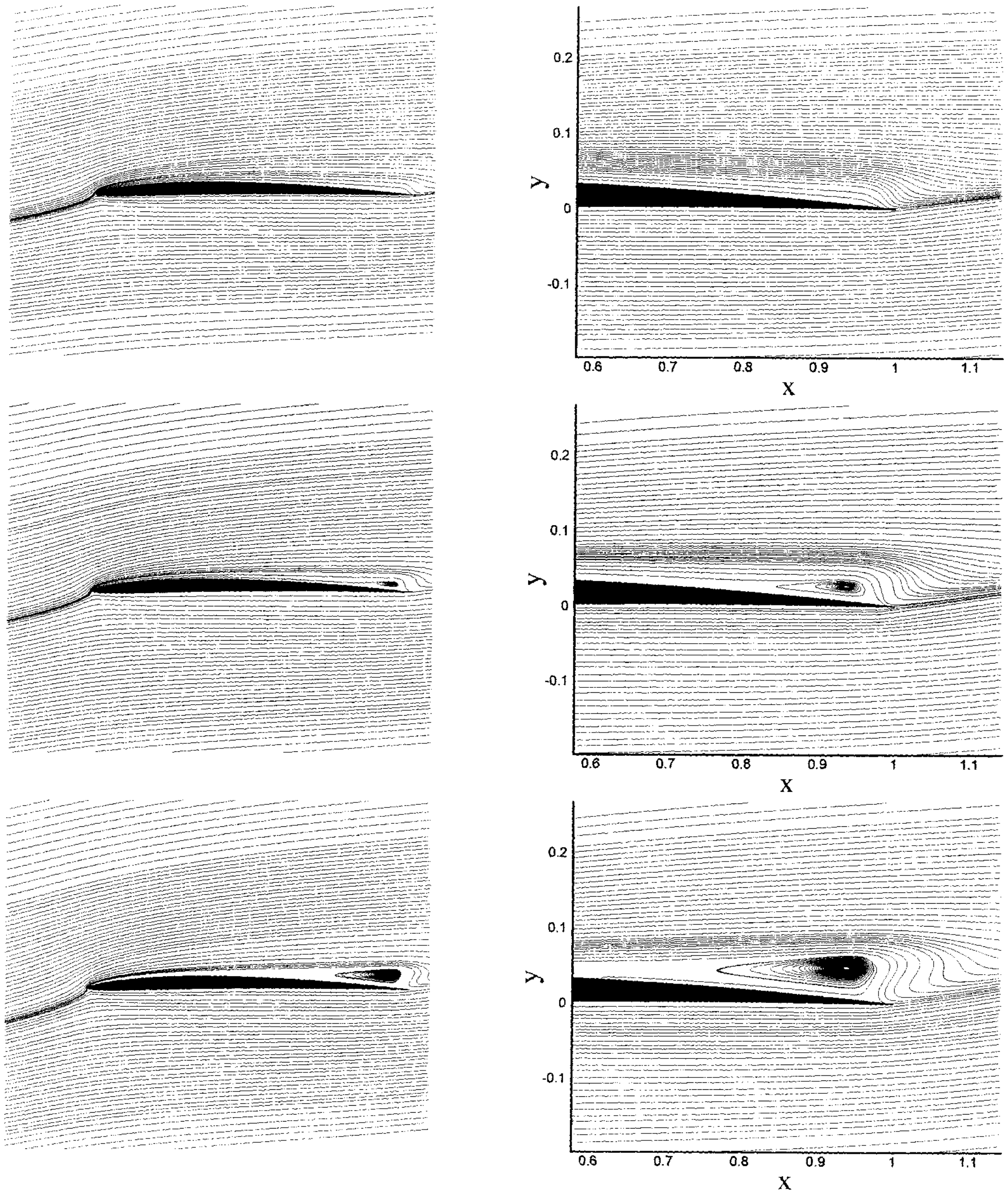

Figure 4.53 Streamline contours for NACA 2404 airfoil at Reynolds number Re=800 and $\alpha = 6^o$, 7^o and 8^o, respectively.

A comparison of the streamline contours and the onset of trailing edge separation is shown in Figure 4.54 for NACA 2404, NACA 4404 and NACA 6404 airfoils at Re=800 and $\alpha = 7^o$. As a result of increasing the airfoil camber, a region of flow recirculation behind the trailing edge (in the wake of the airfoil) develops for NACA 6404 airfoil at this angle of attack while flow continues without recirculation for NACA 2404 and NACA 4404 airfoils.

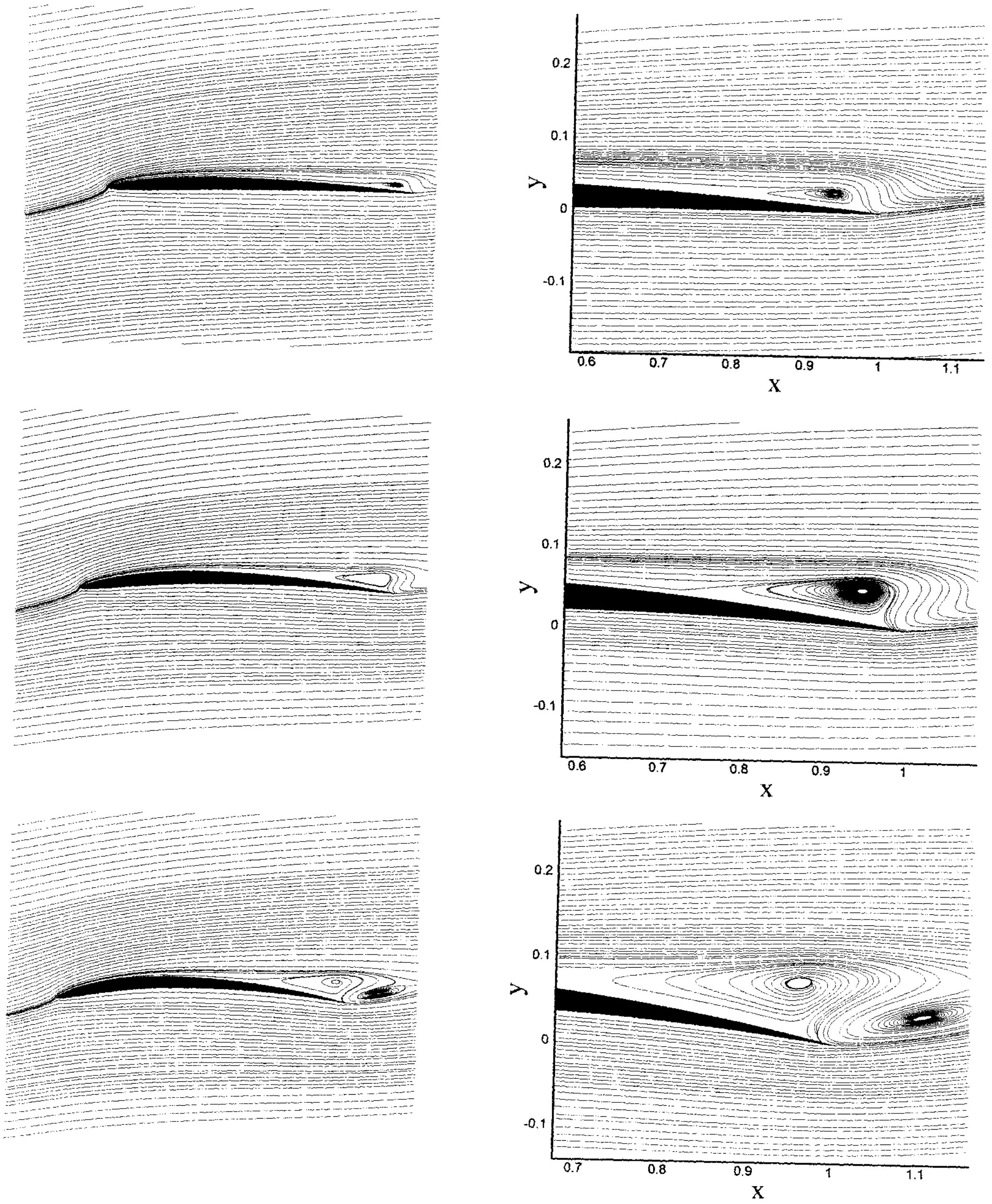

Figure 4.54 Streamline contours for NACA 2404, NACA 4404 and NACA 6404 airfoils at Reynolds number Re=800 and $\alpha = 7^o$, respectively.

For NACA 4404 airfoil at angles of attack $\alpha = 4^o$, 6^o, 7^o and 8^o, the onset of trailing edge separation is compared for Reynolds numbers Re=400, 600, 800 and 1000 in Table 4.4. As the Reynolds number is reduced, the effects of the increased boundary layer thickness become more pronounced and the onset of trailing edge separation is pushed from $\alpha = 4^o$ at Re=1000 to $\alpha = 7^o$ at Re=400. For the same amounts of trailing edge separation, the lower Reynolds number case achieves more than 2.5^o higher angle of attack as the incidence is increased. The reattachment position slightly moves towards the trailing edge for higher Reynolds numbers. It is seen that the effective airfoil geometry is altered by the increased boundary layer thickness at lower Reynolds numbers which has the effect of decambering the airfoil and hence delaying the onset of trailing edge separation. The streamline contours for NACA 4404 airfoil at a fixed angle of attack $\alpha = 8^o$ and Reynolds numbers Re=400, 600, 800 and 1000 are shown in Figure 4.55.

Table 4.4 Comparison of trailing edge separation for NACA 4404 airfoil at Reynolds numbers Re=400, 600, 800 and 1000 at different angles of attack.

Reynolds number, Re		Re=400	Re=600	Re=800	Re=1000
$\alpha = 4^o$	x_s	No separation	No separation	No separation	0.901651
	x_r				0.978418
	l_s				0.076766
$\alpha = 6^o$	x_s	No separation	0.860459	0.777701	0.717352
	x_r		0.970041	0.976729	0.979368
	l_s		0.109581	0.199027	0.262016
$\alpha = 7^o$	x_s	0.894895	0.765829	0.682713	0.625532
	x_r	0.953618	0.971379	0.975893	0.977933
	l_s	0.058723	0.205550	0.293180	0.352401
$\alpha = 8^o$	x_s	0.800136	0.670082	0.592716	0.550572
	x_r	0.960186	0.969762	0.972774	0.975735
	l_s	0.160050	0.299680	0.380058	0.425163

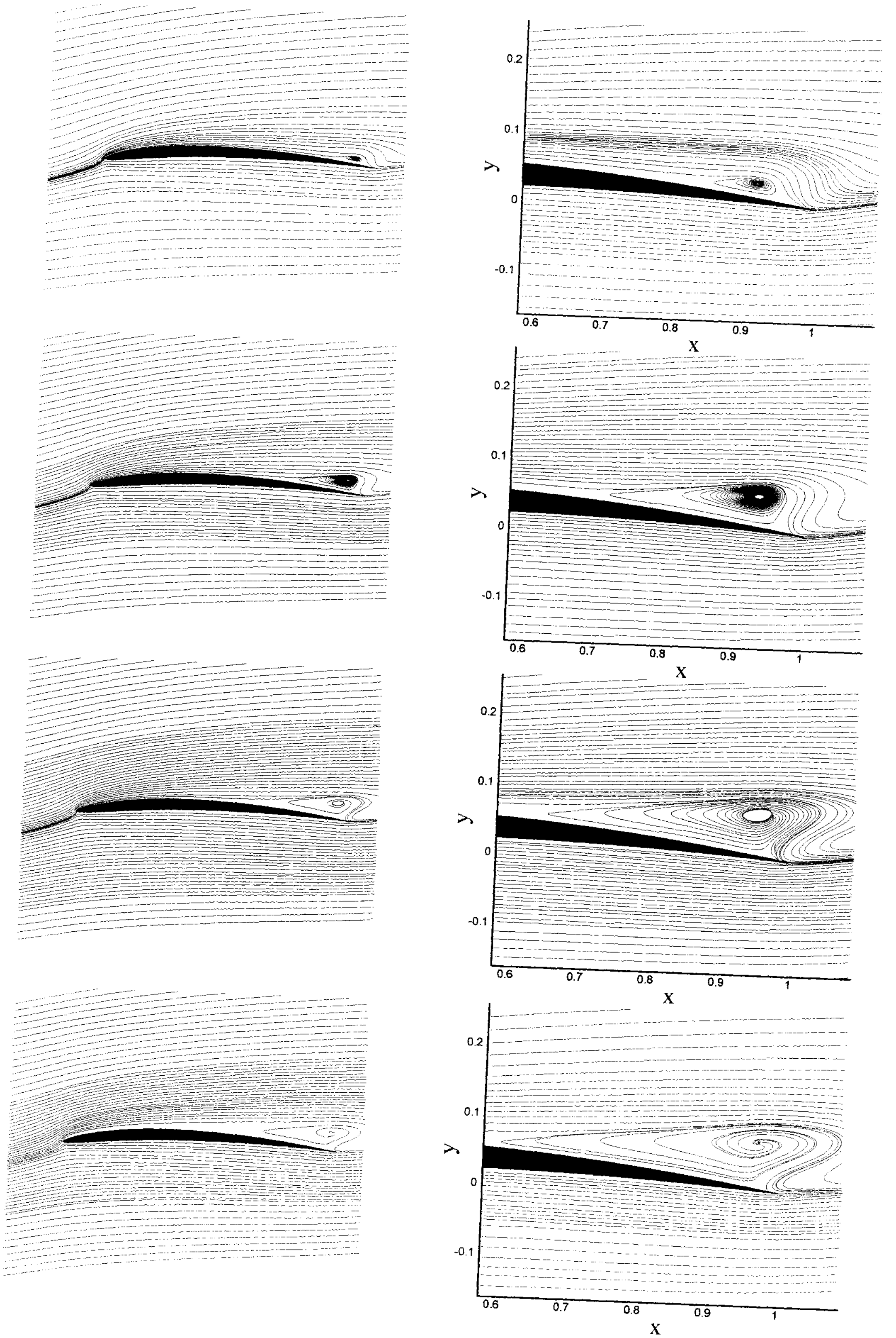

Figure 4.55 Streamline contours for NACA 4404 airfoil at $\alpha = 8^o$ and Reynolds numbers Re=400, 600, 800 and 1000, respectively.

At Reynolds number Re=1000, the separation and reattachment positions are given in Table 4.5 for NACA 2302, NACA 2502 and NACA 2702 airfoils (characterized by 2% relative thickness and 2% maximum camber positioned at 30%, 50% and 70% chord, respectively) at $\alpha = 7^o$ and 8^o. The flow is fully attached at incidences below $\alpha = 7^o$.

Table 4.5 Onset of separation comparison for NACA 2302, NACA 2502 and NACA 2702 airfoils at Reynolds number Re=1000 and $\alpha = 7^o$ and 8^o.

Airfoil type		NACA 2302	NACA 2502	NACA 2702
$\alpha = 7^o$	x_s	0.661726	0.790039	0.890950
	x_r	0.977018	0.975401	0.972803
	l_s	0.315292	0.185362	0.081853
$\alpha = 8^o$	x_s	0.433419	0.503408	0.456976
	x_r	0.976692	0.975639	0.974173
	l_s	0.543272	0.472231	0.517197

Although these airfoils are characterized by very similar performance, it is seen that NACA 2702 airfoil is slightly better than the other two airfoils in terms of drag reduction and separation. Also, at $\alpha = 7^o$, shifting the maximum camber position from 30% to 70% chord results in a reduction of the length of separation.

A comparison of the streamline contours and the onset of trailing edge separation at $\alpha = 7^o$ and Reynolds number Re=1000 for NACA 2302, NACA 2502 and NACA 2702 airfoils is shown in Figure 4.56. The reduction of the circulation region at the trailing edge due to moving the camber position is indicated in this Figure.

As shown in Table 4.5, the reattachment position for these airfoils is similar and is located at nearly 97% chord.

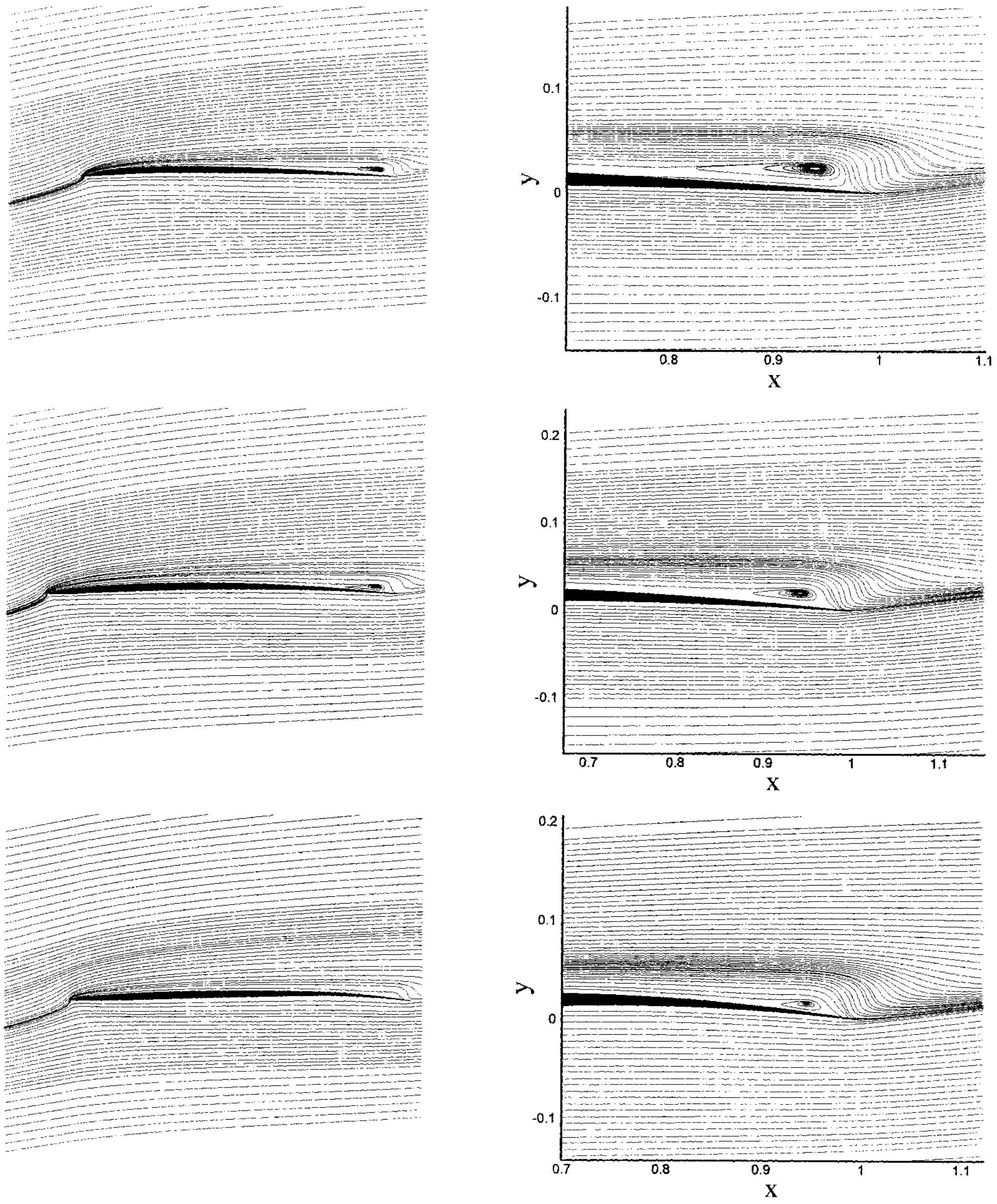

Figure 4.56 Streamline contours at Reynolds number Re=1000 and $\alpha = 7^o$ for NACA 2302, NACA 2502 and NACA 2702 airfoils, respectively.

Similarly for Reynolds number Re=600, the separation and reattachment positions are given in Table 4.6 for NACA 2702, NACA 4702 and NACA 6702 airfoils (characterized by 2% relative thickness while the camber is fixed at 70% chord and 2%, 4% and 6% maximum camber, respectively) at $\alpha = 6^o$, 7^o and 8^o.

Table 4.6 Onset of separation comparison for NACA 2702, NACA 4702 and NACA 6702 airfoils at Reynolds number Re=600 and $\alpha = 6^o$, 7^o and 8^o.

Airfoil type		NACA 2702	NACA 4702	NACA 6702
$\alpha = 6^o$	x_s	No separation	No separation	0.909446
	x_r			0.971874
	l_s			0.062428
$\alpha = 7^o$	x_s	No separation	0.934453	0.890378
	x_r		0.961508	0.969632
	l_s		0.027055	0.079254
$\alpha = 8^o$	x_s	0.906227	0.888767	0.864333
	x_r	0.959092	0.964874	0.967086
	l_s	0.052864	0.076106	0.102753

As the maximum camber is reduced, the onset of trailing edge separation at Re=600 is pushed from $\alpha = 4^o$ for NACA 6702 airfoil to $\alpha = 8^o$ for NACA 2702 airfoil. The flow remains fully attached for NACA 2702 and 4702 airfoils at $\alpha = 6^o$ compared to NACA 6702 airfoil. For the same amounts of trailing edge separation, the lower camber airfoil achieves more than 2^o higher angle of attack as the incidence is increased at Re=600. Also, the separation length is linearly proportional to the angle of attack, that is, separation severity is more pronounced at high incidences for NACA 6702 airfoil than NACA 2702 one.

For NACA 4702 airfoil, the onset of trailing edge separation at angles of attack $\alpha = 6^o$, 7^o and 8^o is analyzed in Table 4.7 for Reynolds numbers Re=400, 600, 800 and 1000. It is seen that the flow is fully attached at Reynolds number Re=400 due to the dominant viscous effects which modify the effective geometry of the airfoil and hence decamber it.

However, for higher angles of attack the onset of separation at the trailing edge is shifted towards the leading edge and characterized by an increase in separation length. The separation position at $\alpha = 8^o$ is shifted from $x_s = 0.89$ at Re=600 to $x_s = 0.80$ at Re=1000.

Table 4.7 Comparison of trailing edge separation for NACA 4702 airfoil at Reynolds numbers Re=400, 600, 800 and 1000 at angles of attack $\alpha = 6^o$, 7^o and 8^o.

Reynolds number, Re		Re=400	Re=600	Re=800	Re=1000
$\alpha = 6^o$	x_s	No separation	No separation	0.935611	0.913614
	x_r			0.971238	0.976174
	l_s			0.035627	0.062559
$\alpha = 7^o$	x_s	No separation	0.934453	0.899760	0.871858
	x_r		0.961508	0.971579	0.975112
	l_s		0.027055	0.071818	0.103254
$\alpha = 8^o$	x_s	No separation	0.888767	0.842411	0.799521
	x_r		0.964874	0.970268	0.972652
	l_s		0.076106	0.127856	0.173131

A comparison of the streamline contours and the onset of trailing edge separation at a fixed angle of attack $\alpha = 8^o$ and Reynolds numbers Re=600, 800 and 1000 is shown in Figure 4.57 for NACA 4702. The growth of trailing edge separation is proportional to Reynolds number, as shown in this Figure.

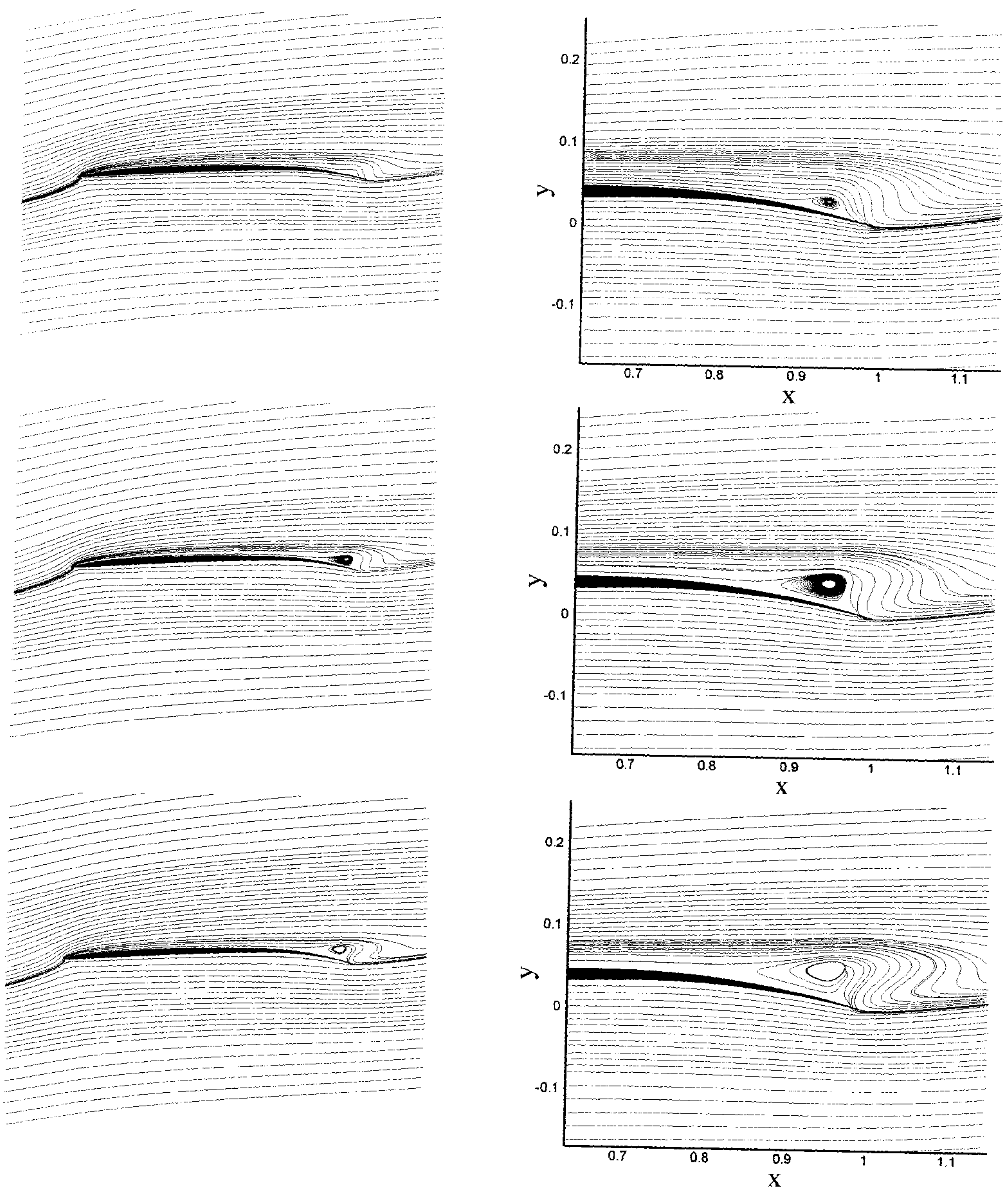

Figure 4.57 Streamline contours for NACA 4702 airfoil at $\alpha = 8^o$ and Reynolds numbers Re=600, 800 and 1000, respectively.

4.4.3 Effect of maximum thickness on airfoil performance

Four uncambered airfoils ranging from 2% to 8% thick in 2% increments have been tested to better understand the effect of maximum thickness on airfoil performance.

At a constant Reynolds number Re=2000, the pressure distribution for NACA 0002, NACA 0004, NACA 0006 and NACA 0008 are presented in Figures 4.12 and 4.14-4.16. The most obvious effect of reducing the maximum airfoil thickness is an increase in the pressure difference between the upper and lower surfaces of the airfoil. The growth of the boundary layer dominates the flow at very low Reynolds numbers which in turn alters the effective geometry of the airfoil; hence increasing the maximum thickness of the airfoil results in a reduction in the lift curve slope in the linear region, as shown in Figures 4.38-4.41. It is seen that the lift coefficient for the 8% thick section (NACA 0008 airfoil) is lower than that for the 2% thick airfoil. Another effect of increasing the airfoil thickness is a reduction of the slope of the lift curve beyond the linear range due to the severity of the trailing edge separation which degrades the performance of the airfoil, as shown in Section 4.4.2 and Figure 4.50.

The effect of increasing the airfoil maximum thickness on the pressure distribution can also be seen in Figures 4.18 and 4.26 for NACA 4402 and NACA 4404 airfoils at Reynolds number Re=1000 and angles of attack $\alpha = 0$, 2^o, 4^o and 6^o. The variations in drag with section thickness are illustrated for NACA 4404 and NACA 4402 airfoils by the drag polars in Figures 4.37 and 4.44. It is noted from this comparison that for the same lift coefficient the thinner NACA 4402 airfoil generated less drag than NACA 4404 airfoil which is thicker by 2%. Also notable is the large increase in the drag coefficient between the Re=2000 and Re=1000 results for NACA 4402 airfoil, as indicated in Figure 4.44. The drag penalty, which is due to the pressure recovery associated with increasing thickness, grows as the Reynolds number is reduced.

4.4.4 Camber effect on airfoil performance

One of the effective geometric parameters that play an important role in improving the performance of the airfoil is the camber. The gain in performance is notable when comparing the pressure distributions on NACA 0002 and NACA 4402 airfoils, as shown in Figures 4.11 and 4.18 for Reynolds number Re=1000 and Figures 4.12 and 4.19 for

Re=2000. The introduction of 4% camber positioned at 40% chord results in smoother pressure distributions as compared to the uncambered NACA 0002 airfoil; this effect is clearly seen at incidences $\alpha = 2^o$ and 4^o. Also, the cambered airfoil produces a larger pressure difference between the upper and lower surfaces for the most part of the section.

A comparison of the NACA 2404, NACA 4404 and NACA 6404 airfoils indicate the overall effects of camber on the pressure distribution. For these airfoils, the maximum thickness is 4% while the camber position is fixed at 40% chord and the maximum camber is increased from 2% to 6% in increments of 2%. The differences in pressure distributions at Re=800 are shown in Figures 4.25, 4.27 and 4.28; increasing the camber results in shifting the minimum pressure from the leading edge area in the case of NACA 2404 airfoil to around the quarter-chord for NACA 6404. Lift and drag curves as well as drag polars are provided for these airfoils in Figure 4.46. An important behavior to observe is the increase in both the lift and drag coefficients as the maximum camber is increased. Although the drag is increased, the ability to attain higher lift coefficients generally results in a net gain in airfoil performance. In flows at very low Reynolds numbers, the addition of camber results in earlier trailing edge separation while still maintaining higher lift coefficients, as indicated in Table 4.3 and Figure 4.46.

The design space is further investigated by exploring the possible benefits of varying the location of maximum camber along the chord. Three NACA airfoils were investigated using 2% maximum thickness and camber; located at 30%, 50% and 70% chord; that is NACA 2302, NACA 2502 and NACA 2702 airfoils, respectively. The aerodynamic characteristics for these airfoils at Re=1000 are given in Figure 4.47. An interesting behavior to observe is the negligible reduction in the lift coefficient in the linear range due to shifting the camber from 30% to 70% chord while producing less drag. This behavior is associated with the fact that the NACA 2702 airfoil displays a reduced or equivalent trailing edge separation as compared with NACA 2302 and NACA 2502 airfoils at the same angle of attack, as shown in Table 4.5. Also, shifting the location of maximum camber toward the trailing edge results in less adverse pressure gradients than sections with forward camber. This concentration of camber acts like a separation ramp in the pressure distribution [99, 130]. Thus, by maintaining less adverse pressure gradients ahead of the maximum camber location, the onset of trailing edge separation is contained after the maximum camber, as displayed in Figure 4.56. This physical behavior is clearly captured in Figures 4.20-4.22 which present the pressure coefficient distribution for these airfoils.

By fixing the location of maximum camber at 70% chord, the effects of varying the amount of camber are further investigated. Three NACA airfoils characterized by 2% maximum thickness and 2%, 4% and 6% maximum camber are examined; they are NACA 2702, NACA 4702 and NACA 6702 airfoils, respectively. By comparing the pressure coefficient distribution for these airfoils one can observe that the adverse pressure gradients ahead of the maximum camber become more pronounced as the camber is increased from 2% to 6%, this is depicted in Figures 4.33 and 4.34 for Reynolds number Re=600 and angles of attack $\alpha = 0$, 2^o, 4^o and 6^o. For a given angle of attack, increasing the camber is translated into lift gains and drag penalties, as shown in Figure 4.48. However, it is seen that the NACA 4702 airfoil maintains an equivalent performance in terms of the lift-to-drag ratio and the levels of trailing edge separation as compared to the more cambered NACA 6702 airfoil.

Chapter 5

Conclusions and Future Work

The main conclusions which can be drawn from this work are presented below in categories corresponding to chapters 2 through 4.

5.1 Airfoils of arbitrary shapes in steady flows

An efficient and accurate method was presented for the steady aerodynamic analysis of airfoils of arbitrary shape. This theoretical method is first developed for the second-order analysis of inviscid incompressible flows past airfoils, by using velocity singularities [115, 116, 119, 124]. Efficient analytical expressions in closed form are determined for the velocity and, hence, the pressure distributions on airfoils of arbitrary shapes by solving simultaneously the anti-symmetric and symmetric flow components, which are defined by coupled boundary conditions. In the present analysis, the physical behavior of the velocity at the leading and trailing edges of the symmetric airfoils at zero angle of attack is respected (they are stagnation points), in contrast to the linear methods in which the fluid velocity tends unphysically to infinity at both edges. The accurate analytical solutions derived in this work have been successfully validated by comparison with the exact solutions obtained for special airfoils defined by conformal transformation, with panel method results [98] and with numerical results obtained by an Euler code (inviscid MSES code [43, 44]). In all cases studied, for both symmetric and cambered airfoils at incidence, the present nonlinear solutions were found to be in very good agreement with the exact solutions and with the numerical results.

The second-order method developed for the inviscid flows was then modified in order to take into account the main viscous effects on the pressure distribution for attached flows past airfoils at moderate angles of attack. This modified method includes the viscous effects by taking into account the real physical behavior of the velocity at the airfoil trailing edge (which is different than that in the inviscid flows where the trailing edge is a stagnation point), and by considering the displacement thickness of the boundary layer developed along the airfoil contour and the airfoil wake. Simple analytical solutions in closed form have also been derived for the viscous case, by using velocity singularities. The present analytical solutions including viscous effects have been successfully validated by comparison with experimental results [186] and with numerical results obtained using the viscous MSES code [43, 44].

The present inviscid and viscous solutions derived for incompressible flows have then been extended to compressible flows by using the compressibility correction developed by Karman-Tsien [7, 22, 142]. The present compressible viscous solutions have been found to be in good agreement with numerical results obtained with the viscous MSES code [43, 44] and with experimental results for various Mach and Reynolds numbers and angles of attack.

The accurate analytical solutions derived in this work for inviscid incompressible, viscous and compressible attached flows are applicable to airfoils of any arbitrary shape, including airfoils with rounded or pointed leading edges, double-wedge airfoils, symmetric and cambered thin or thick airfoils at incidence. The present solutions were found to be very efficient and accurate in all cases studied.

5.2 Unsteady flows past oscillating flexible airfoils

A new method of solution has been presented in this thesis for the analysis of unsteady incompressible flows past oscillating airfoils. The method is based on the determination of the singular contributions of the leading edge, ridges (points where the airfoil boundary conditions change) and the unsteady shedding free vortices in the expression for the reduced velocity and pressure coefficient [117, 118]. This has led to very efficient and simple theoretical solutions in closed form for the pressure difference coefficient, lift and pitching moment coefficients and aileron lift and hinge moment coefficients. These unsteady flow solutions lead directly to the steady flow solutions in the limit case when the frequency of oscillations tends to zero.

The method has been validated for the case of rigid airfoil and aileron oscillations in translation and rotation, by comparison with the results obtained by Theodorsen [184] for the lift and moment coefficients and by Postel and Leppert [158] for the reduced pressure difference coefficient. An excellent agreement was found between the present solutions and these previous results.

The present method was used further to derive efficient theoretical solutions, also in closed form, for the case of flexural oscillations of flexible airfoils, fitted or not with oscillating flexible ailerons, which are of interest for the aeroelastic studies in the aeronautical applications.

The aerodynamic stiffness, damping and virtual (or added) mass contributions in the solutions of the unsteady pressure distribution, lift, and moment coefficients (which are needed in the aeroelastic studies) are specifically determined. An analysis of the relative magnitude of the quasi-steady and vortex shedding contributions in the aerodynamic coefficients is also presented.

5.3 Airfoil flow analysis at very low Reynolds numbers

An efficient numerical method for the analysis of the steady flows past airfoils at very low Reynolds numbers has been presented. This is of interest for the micro aerial vehicles (MAV), as well as the biologically inspired systems (such as small insects), for which there are few computational and experimental aerodynamic results available. The flow at very low Reynolds numbers is dominated by viscous effects, flow separations and the growth of the boundary layer modifies significantly the effective shape of the airfoil.

The present analysis of airfoils in incompressible laminar flows at very low Reynolds numbers is based on a pseudo-time integration method using artificial compressibility to accurately solve the Navier-Stokes equations. This is done in a rectangular computational domain obtained by a coordinate transformation from the physical flow domain around the airfoil. The method uses a central differencing approach on a stretched staggered grid in the computational domain.

In the present method, the governing equations are recast in delta form after the introduction of the pseudo-time relaxation procedure (not before, as adopted by Soh and Goodrich [176]) and a factored alternating direction implicit (ADI) scheme is used, which simplifies the approach considerably and increases the implicit coupling in the solution. A special decoupling procedure in each sweep using the continuity equation is used finally to reduce the problem to the computationally efficient solution of scalar tridiagonal systems of equations.

The method is first used to obtain the pressure coefficient distributions, lift and drag coefficients for several airfoils at very low Reynolds numbers between 400 and 6000. The present airfoil solutions were validated by comparison with the numerical results obtained by Kunz and Kroo [99] for Reynolds numbers between 1000 and 6000 (no results were available for Reynolds numbers smaller than 1000). A very good agreement has been found between the two sets of results.

The present method has then been used to study the effects of varying the Reynolds number, angle of attack and airfoil maximum relative thickness and camber as well as the maximum camber position along the chord on the pressure distribution, lift and drag coefficients and the onset of flow separation. The variation of lift and drag coefficients with angle of attack as well as the drag polars have been determined for several flow conditions and airfoils.

In order to physically understand the complex flow separation phenomena in viscous laminar flows past airfoils at very low Reynolds numbers, the onset of separation and reattachment positions as well as the separation length have also been calculated, analyzing the effect of various parameters (such as the Reynolds number, incidence, relative maximum thickness and camber, and the relative position along the chord) affecting the flow separation. The streamline contours for several airfoils at various Reynolds numbers and angles of attack have been also generated and compared.

The most obvious effect on the flight at very low Reynolds numbers is the increase in the drag coefficient of the airfoil due to viscous effects, which are also reducing the effective camber. At the same lift coefficient, the drag coefficients at lower Reynolds numbers are much larger than those at higher ones. In addition to the decambering effect, flow separation occurs at lower angles of attack which results in reduced airfoil performance.

A decrease in the low Reynolds number leads to an increase in the negative pressure coefficient on the airfoil, due to a thicker boundary layer, which is more pronounced towards the trailing edge. This effect was found to be more important for thinner airfoils due to the relative thickness of the boundary layer in comparison with the airfoil thickness. At the same time, the variation of the pressure coefficient near the leading edge is smoother due to stronger viscous effects at smaller Reynolds numbers.

Reducing the Reynolds number results in a reduction in both the slope of the adverse gradient in the pressure recovery region and the leading edge suction peak of the airfoil.

An important behavior to be observed is the increase in both the lift and drag coefficients as the maximum camber of the airfoil is increased. Although the drag is increased, the ability to attain higher lift coefficients generally results in a net gain in the airfoil performance. In flows at very low Reynolds numbers, the addition of camber results in earlier trailing edge separation, while still maintaining higher lift coefficients.

It was found that shifting the location of maximum camber toward the trailing edge results in less adverse pressure gradients than sections with forward camber. This change acts like a separation ramp in the pressure distribution. Thus, by maintaining less adverse pressure gradients ahead of the maximum camber location, the onset of the flow separation is moved downstream towards the trailing edge after the maximum camber.

5.4 Future work

As a suggestion for future work, the numerical method developed for solving the steady incompressible Navier-Stokes equations can be extended for solving the unsteady flows past oscillating airfoils at low Reynolds numbers.

Originality and Research Contributions

The main contributions of this thesis consist in the development of three methods of solution for the theoretical and numerical analysis of steady and unsteady flows past fixed or oscillating airfoils. New computational solutions have been obtained for flows past airfoils at low Reynolds numbers, which are presently of topical interest for micro aerial vehicles (MAV).

Accurate theoretical solutions for airfoils in steady flows

An accurate method of solution was developed for the steady aerodynamic analysis of airfoils. Efficient analytical expressions in closed form are determined for the velocity and the pressure distributions on airfoils of arbitrary shapes, which are based on the correct implementation of the boundary conditions (without resorting to the small perturbation assumption). These solutions are obtained by a method based on specific singular contributions in the expression of the fluid velocity (in contrast to distributed singularities in the expression of the potential that is used in the boundary element methods). These singular contributions are associated to special points on the airfoil (leading edge and ridges) and satisfy all boundary conditions on the airfoil and outside it, including Kutta condition at the trailing edge; hence there is no need in this method to specifically impose the Kutta condition in the final solution. This second-order accurate method (as opposed to the linear methods based on the small perturbation assumption), simultaneously solves the symmetric and anti-symmetric flow components which are defined by *coupled boundary conditions*. The treatment of the coupled nonlinear boundary conditions using velocity singularities represents one of the contributions of the present analytical method.

Accurate analytical solutions are first derived for inviscid incompressible steady flows and then modified to take into account the viscous effects on the pressure distribution for airfoils in attached flows. The derivation of closed form analytical solutions including the viscous effects for the velocity and the pressure distributions also represents a contribution of this thesis.

The accurate analytical solutions derived in this work for inviscid incompressible, viscous and compressible attached flows are applicable to airfoils of any arbitrary shape, including airfoils with rounded or pointed leading edges, double-wedge airfoils, symmetric and cambered thin or thick airfoils at moderate angles of attack. This unified approach for the solution of the velocity and pressure distributions on various airfoils at different flow conditions permits a better understanding of steady airfoil aerodynamics.

Theoretical solutions for oscillating flexible airfoils in unsteady flows

A new method of solution was developed for the analysis of unsteady incompressible flows past oscillating thin airfoils. This method is based on the derivation of specific contributions in the solutions of the fluid velocity and unsteady pressure coefficient associated to the singular points on the oscillating airfoil and to the unsteady shedding free vortices in the airfoil wake.

This method is used to obtain simple and efficient aerodynamic solutions in closed form for oscillating rigid or flexible airfoils fitted or not with oscillating rigid or flexible ailerons. This method, which avoids the difficulties encountered in the classical theories, provides an effective approach for the general case of oscillations, including the flexural oscillations (previous results were mainly obtained for the case of rigid airfoil oscillations in translation and rotation). The derivation of a special class of velocity singularities for unsteady flows, the treatment of the unsteady shedding free vortices in the airfoil wake and the development of unified closed form solutions for oscillating rigid and flexible airfoils (which are needed in the aeroelastic studies) represent the main contributions of the present method.

The aerodynamic stiffness, damping, and virtual (or added) mass contributions in the solutions of the unsteady pressure distribution, lift coefficient, and moment coefficient are specifically determined, which provide a better understanding of the complex nature of the unsteady flows past oscillating flexible airfoils.

Numerical analysis of airfoil flows at low Reynolds numbers

In this thesis, an implicit pseudo-time integration method using artificial compressibility has also been developed to accurately solve the Navier-Stokes equations for airfoil flows at very low Reynolds numbers. This method of solution is based on a central differencing approach on a stretched staggered grid. The problem is solved in a rectangular computational domain defined by a general coordinate transformation from the fluid flow domain around the airfoil.

A special decoupling procedure based on the continuity equation and on a factored alternating direction implicit scheme reduced the problem to the computationally efficient solution of scalar tridiagonal systems.

A detailed study of the effects of varying the Reynolds number, angle of attack and airfoil relative thickness and camber (along with the maximum camber position along the chord) on the pressure distribution, lift and drag coefficients has been performed. This study has broadened our understanding of the flows past airfoils at very low Reynolds numbers.

A thorough analysis of the flow separation on the airfoils at very low Reynolds numbers has been performed by determining the onset of the separation and the reattachment positions and by studying the streamline contours generated for four symmetric and nine cambered airfoils at various angles of incidence and a large range of Reynolds numbers between 400 and 6000. This represents a very useful database for airfoils at low Reynolds numbers (not available previously) which permits the analysis of the influence on the flow separation of various parameters, such as Reynolds number, angle of incidence, relative thickness and camber, and maximum camber position along the airfoil chord. This database can also be used for comparison by future experimental and computational results.

Bibliography

[1] Abdo, M., and Mateescu, D., "Low-Reynolds number aerodynamics of airfoils at incidence," 43rd Aerospace Sciences Meeting and Exhibit, Reno, Nevada, *AIAA Paper* 2005-1038, January 2005 (submitted for publication).

Other publications by Abdo, M. listed in:

[Ref. 117] Mateescu, D., and Abdo, M., "Theoretical solutions for unsteady flows past oscillating flexible airfoils using velocity singularities," *Journal of Aircraft*, Vol. 40, No. 1, January-February, 2003, pp. 153-163.

[Ref. 118] Mateescu, D., and Abdo, M., "Unsteady aerodynamic solutions for oscillating airfoils," *AIAA Paper* 2003-227, Reno, January 2003.

[Ref. 119] Mateescu, D., and Abdo, M., "Nonlinear theoretical solutions for airfoil aerodynamics," *AIAA Paper* 2003-4296, Orlando, June 2003.

[Ref. 120] Mateescu, D., and Abdo, M., "Aerodynamic analysis of airfoils at very low Reynolds numbers," *AIAA Paper* 2004-1053, Reno, January 2004.

[Ref. 121] Mateescu, D., and Abdo, M., "Airfoil flow analysis at low-Reynolds numbers," *AIAA Journal* (submitted for publication), 2004.

[2] Abbott, I. H., and Von Doenhoff, A., *Theory of Wing Sections*, Dover, New York, 1959.

[3] Acharya, M., and Metwally, M., "Evolution of the unsteady pressure field and vorticity production at the surface of a pitching airfoil," *AIAA Paper* 90-1472, 1990.

[4] Amiet, R. K., "High frequency thin-airfoil theory for subsonic flow," *AIAA Journal*, Vol. 14, No. 8, August, 1976, pp. 1076-1082.

[5] Anderson, D. A., Tannehill, J. C., and Pletcher, R. H., *Computational Fluid Mechanics and Heat Transfer*, New York, McGraw-Hill, 1984.

[6] Anderson, E., *Computational Fluid Dynamics*, McGraw-Hill, New York, 1985.

[7] Anderson, J. D., *Fundamentals of Aerodynamics*, 2nd ed., McGraw-Hill, New York, 1991.

[8] Anderson, Jr. J. D., *A History of Aerodynamics*, Cambridge University Press, Cambridge, 1998.

[9] Anderson, J. M., Streitlien, K., Barrett, D. S., and Triantafyllou, M. S., "Oscillating foils of high propulsive efficiency," *Journal of Fluid Mechanics*, 360, 1998, pp. 41-72.

[10] Azevedo, J. F., and Oliveira, L. C., "Unsteady airfoil flow simulations using the Euler equations," *AIAA Paper* 94-1892, 1994, pp. 650-660.

[11] Azuma, A., *Biokinetics of Flying and Swimming*, Springer-Verlag, 1992.

[12] Basu, B. C., and Hancock, G. J., "The unsteady motion of a two-dimensional airfoil in incompressible inviscid flow," *Journal of Fluid Mechanics*, Vol. 87, 1978, pp. 159-178.

[13] Batina, J. T., "Unsteady Euler airfoil solutions using unstructured dynamic meshes," *AIAA Journal*, Vol. 28, No. 8, August 1990, pp. 1381-1388.

[14] Bauer, F., Garabedian, P., and Korn, D., *Supercritical Wing Sections*, Springer, Berlin, 1972.

[15] Beam, R., and Warming, R. F., "An implicit finite-difference algorithm for hyperbolic systems in conservation law form," *Journal of Computational Physics*, Vol. 74, 1977.

[16] Bisplinghoff, R. I., and Ashley, H., *Principles of Aeroelasticity*, Dover, New York, 1962, Ch. 4.

[17] Brackenbury, J., *Insects in Flight*, Blandford, London, 1992.

[18] Bragg, M. B., Heinrich, D. C., Balow, F. A., and Zaman, K. Q., "Flow oscillation over an airfoil near stall," *AIAA Journal*, Vol. 34, No. 1, 1996, pp. 199-201.

[19] Brodsky, A. K., *The Evolution of Insect Flight*, Oxford Science Publications, Oxford, 1996.

[20] Broeren, A. P., and Bragg, M. B., "Spanwise variation in the unsteady stalling flowfields of two-dimensional airfoil models," *AIAA Journal*, Vol. 39, No. 9, September, 2001, pp. 1641-1651.

[21] Carafoli, E., Mateescu, D., and Nastase, A., *Wing Theory in Supersonic Flow*, Pergamon Press, Oxford, London and New York, 1969.

[22] Carafoli, E., *Tragflügeltheorie*, VebVerlag, Berlin, 1954.

[23] Cebeci, T., *An Engineering Approach to the Calculation of Aerodynamic Flows*, Springer-Verlag, Berlin, 1999, Ch. 1-3, 6.

[24] Cebeci, T., and Smith, A.M.O., *Analysis of Turbulent Boundary Layers*, Academic Press, New York, 1974, Ch. 3-5, 7-9.

[25] Cebeci, T., Platzer, M. F., Jang, H. M., and Chen, H. H., "An inviscid-viscous interaction approach to the calculation of dynamic stall initiation on airfoil," *Journal of Turbomachinery*, Vol. 115, No. 4, 1993, pp. 714-723.

[26] Chandrashekhara, M., and Carr, L., "Flow visualization of the Mach number effects on the dynamic stall of an oscillating airfoil," *AIAA Paper* 89-0023, 1989.

[27] Chang, J. L., and Kwak, D., "On the method of pseudo compressibility for numerically solving incompressible flows," *AIAA Paper* 84-0252, 1984.

[28] Cheng, H. K., and Rott, N., "Generalization of the inversion formula of thin airfoil theory," *Journal of Rational Mechanics and Analysis*, Vol.3, No. 3, 1954, pp. 357-382.

[29] Choi, D., and Merkle, C. L., "Application of time iterative schemes to incompressible flow," *AIAA Journal*, Vol. 23, 1985, pp. 1518-1524.

[30] Chorin, A., "A numerical method for solving incompressible viscous flow problems," *Journal of Computational Physics*, Vol. 2, 1967, pp. 12-26.

[31] Chorin, A., "A numerical method for solving incompressible viscous flow problems," *Journal of Computational Physics*, Vol. 135, 1997, pp. 118-125.

[32] Chorin, A., "Numerical solution of the Navier-Stokes equations," *Mathematics of Computation*, Vol. 22, 1968, pp. 745-762.

[33] Choudhuri, P. G., Knight, D. D., and Visbal, M. R., "Two-dimensional unsteady leading-edge separation on a pitching airfoil," *AIAA Journal*, Vol. 32, No. 4, April 1994, pp. 673-681.

[34] Chyu, W. J., Davis, S. S., and Chang, K. S., "Calculation of unsteady transonic flow over an airfoil," *AIAA Journal*, Vol. 19, No. 6, June 1981, pp. 684-690.

[35] Coiro, D.P., and Pagano, A., "Unsteady airloads prediction for oscillating airfoils at separated flow conditions," 20th ICAS congress, *ICAS Paper* 96-2.8.3, 8-13 September 1996, pp. 1800-1809.

[36] Davis, W. R., Kosicki, B. B., Boroson, D. M., and Kostishack, "Micro air vehicles for optical surveillance," *The Lincoln Laboratory Journal*, Vol. 9, No. 2, 1996, pp. 197-213.

[37] Deiwert, G. S., and Bailey, H. E., "Prospects for computing airfoil aerodynamics with Reynolds averaged Navier-Stokes codes," Proceedings of the Advanced Technology Airfoil Research Conference, Vol. 1, *NASA Conference Publications* 2045, Virginia, 1978, pp. 119-131.

[38] Dickinson, M. H., "The effects of wing rotation on unsteady aerodynamic performance at low Reynolds numbers," *Journal of Experimental Biology*, Vol. 192, 1994, pp. 179-206.

[39] Dickinson, M. H., and Götz, K., "Unsteady aerodynamic performance of model wings at low Reynolds numbers," *Journal of Experimental Biology*, Vol. 174, 1993, pp. 45-64.

[40] Dowell, E. H., Bland, S. R., and Williams, M. H., "Linear/nonlinear behavior in unsteady transonic aerodynamics," *AIAA Paper* 81-0643 CP, 1981.

[41] Dowell, E. H., Crawley, E. F., Curtiss, H. C., Peters, D. A., Scanlan, R. H., and Sisto, F., *A Modern Course in Aeroelasticity*, 3rd edition, Kluwer Publication, Netherlands, 1995, Ch. 1 and 4.

[42] Dowell, E. H., Hall, K. C., and Romanowski, M. C., "Eigenmode analysis in unsteady aerodynamics: Reduced order models," *Applied Mechanics Review*, Vol. 50, No. 6, 1997, pp. 371-386.

[43] Drela, M., and Giles, M. B., "ISES- A two-dimensional viscous aerodynamic design and analysis code," *AIAA Paper* 87-0424, January, 1987.

[44] Drela, M., and Giles, M. B., "Viscous-inviscid analysis of transonic and low Reynolds number airfoils," *AIAA Journal*, Vol. 25, No. 10, pp. 1347-1355, 1987.

[45] Du, X., and Lee, T., "Flow past an airfoil with a leading-edge rotating cylinder," *Journal of Aircraft*, Vol. 39, No. 6, 2002, pp. 1079-1084.

[46] Dutto, L. C. and Habashi, W. G., "Parallelization of the ILU(0) preconditioner for CFD problems on shared memory computers," *International Journal for Numerical Methods in Fluids*, Vol. 30, No. 8, 1999, pp. 995-1008.

[47] Dutto, L. C., Habashi, W. G., and Fortin, M., "An algebraic multilevel parallelizable preconditioner for large-scale CFD problems," *Journal of Computer Methods in Applied Mechanics and Engineering*, Vol. 149, 1997, pp. 303-318.

[48] Dutto, L. C., Habashi, W. G., Robichaud, M. P., and Fortin, M., "A method for finite element parallel viscous compressible flow calculations," *International Journal for Numerical Methods in Fluids*, Vol. 19, 1994, pp. 275-294.

[49] Dvorak, F. A., and Kind, R. J., "An analysis method for the viscous flow over circulation-controlled airfoils," *Journal of Aircraft*, Vol. 16, 1979.

[50] Edwards, J. W., and Thomas, J. L., "Computational methods for unsteady transonic flows," *AIAA Paper* 87-0107, January 1987.

[51] Ellington, C. P., "Aerodynamics and the origin of flight," *Advances in Insect Physiology*, Vol. 23, 1991, pp. 171-210.

[52] Ellington, C. P., "The aerodynamics of hovering insect flight part I: The quasi-steady analysis," *Philosophical Transactions of the Royal Society*, serie B, London, Vol. 305, 1984, pp. 1-15.

[53] Elrefaee, M. M., Wu, J. C., and Lekoudis, S. G. "Solutions of the compressible Navier-Stokes equations using the integral method," *AIAA Journal*, Vol. 20, No. 3, pp. 356-362, March, 1982.

[54] Ennos, A. R., "The kinematics and aerodynamics of the free flight of some Diptera," *Journal of Experimental Biology*, Vol. 142, 1989, pp. 49-85.

[55] Ericsson, L. E., and Reding, J. P., "Unsteady flow concepts for dynamic stall analysis," *Journal of Aircraft*, Vol. 21, No. 8, August 1984, pp. 601-606.

[56] Fidders, S. P., Kirby, D. A., Woodward, D. S., and Peckham, D. H., "Investigation into the effects of scale and compressibility on lift and drag in the RAE 5m pressurized low-speed wind tunnel," *Aeronautical Journal*, Vol. 89, No. 883, 1985, pp. 93-108.

[57] Fletcher, C. A., *Computational Techniques for Fluid Dynamics*, Vol. II, Springer Verlag, Berlin, 1988.

[58] Florea, R., and Hall, K. C., “Eigenmode analysis of unsteady flows about airfoils,” *Journal of Computational Physics*, Vol. 147, December 1998, pp. 568-593.

[59] Freuler, R. J. and Gregorek, G. M., “An evaluation of four single element airfoil analytic methods,” Proceedings of the Advanced Technology Airfoil Research Conference, Vol. 1, *NASA Conference Publications* 2045, Virginia, 1978, pp. 133-162.

[60] Freymyth, P. et al., “Visualization and computation of hovering mode vortex dynamics, in vortex method and vortex motion,” Editors, Gustafson, K., and Sethian, J., *SIAM*, Philadelphia, 1991.

[61] Freymyth, P., “Propulsive vertical signatures of plunging and pitching airfoils,” *AIAA Paper* 88-0323, Reno, 1988.

[62] Fung, Y. C., *An Introduction to the Theory of Aeroelasticity*, Dover, New York, 1993, pp. 381-462.

[63] Geissler, W., “Methods for inviscid subsonic flows about aircraft configurations,” Special Course on Unsteady Aerodynamics, *AGARD Report* No. 679, 1980, pp. 5.1-5.21.

[64] Ghia, K. N., Hankey, W. L., and Hodge, J. K., “Use of primitive variables in the solution of incompressible Navier-Stokes equations,” *AIAA Journal*, Vol. 17, 1979, pp. 298-301.

[65] Glauert, H., *The Elements of Aerofoil and Airscrew Theory*, Cambridge University Press, UK, 1959.

[66] Grasmeyer, J. M., and Keennon, M. T., “Development of the Black Widow micro air vehicle,” *AIAA Paper* 2001-0127, 2001.

[67] Guruswamy, P., and Goorjian, P. M., “Effects of viscosity on transonic-aerodynamic and aeroelastic characteristics of oscillating airfoils,” *Journal of Aircraft*, Vol. 21, No. 9, September 1984, pp. 700-707.

[68] Habashi, W. G., “A finite-element approach to subsonic aerodynamics,” *International Journal for Numerical Methods in Engineering*, Vol. 14, No. 5, 1979, pp. 665-680.

[69] Habashi, W. G., Dompierre, J., Bourgault, Y., Ait-Ali-Yahia, D., Fortin, M., and Vallet, M., "Anisotropic mesh adaptation: towards user-independent, mesh-independent and solver-independent CFD solutions: Part I: general principles," *International Journal for Numerical Methods in Fluids*, Vol. 32, No. 6, 2000, pp.725-744.

[70] Habashi, W. G., Nguyen, V., and Bhat, M. V., "Efficient direct solvers for large-scale computational fluid dynamics problems," *Journal of Computer Methods in Applied Mechanics and Engineering*, Vol. 87, 1991, pp. 253-265.

[71] Hafez, M. M., Habashi, W. G., and Przybytkowski, S. M., "Transonic viscous-inviscid interaction by a finite element method," *International Journal for Numerical Methods in Fluids*, Vol.13, No. 3, 1991, pp. 309-319.

[72] Hall, K. C., Thomas, J. P., and Dowell, E. H., "Proper orthogonal decomposition technique for transonic unsteady aerodynamic flows," *AIAA Journal*, Vol. 38, No. 10, October 2000, pp. 1853-1862.

[73] Halsey, N. D., "Potential flow analysis of multielement airfoils using conformal mapping," *AIAA Journal*, 17, 1979, pp. 1281-1288.

[74] Han, C., Ahn, J., Cho, J., and Moon, Y., "Unsteady aerodynamic analysis of oscillating flat plates," 21st Applied Aerodynamics Conference, *AIAA Paper* 2003-3674, Orlando, Florida, 23-26 June, 2003.

[75] Hancock, G. J., and Doe, R., "Methods for inviscid subsonic flows about unsteady aerofoils," Special Course on Unsteady Aerodynamics, *AGARD Report* No. 679, 1980, pp. 12.1-12.10.

[76] Harlow, F. H., and Welch, J. E., "Numerical computation of time-dependent viscous incompressible flow of fluid with free surface," *The Physics of Fluids*, Vol. 8, 1965, pp. 2182-2189.

[77] Harris, C. D., "NASA supercritical airfoils, a matrix of family-related airfoils," *NASA TP*- 2969, 1990.

[78] Hess, J. L., and Smith, A.M.O., "Calculation of potential flow about arbitrary bodies," *Progress in Aerospace Sciences*, Vol. 8, Pergamon Press, New York, 1966.

[79] Hirsch, C., *Numerical Computation of Internal and External Flow*, Vol. 1 and 2, New York, John Wiley & Sons, 1990, Ch. 23.

[80] Hunt, B., *Numerical Methods in Applied Fluid Dynamics*, Academic Press, London, 1980.

[81] Ives, D. C., "A modern look at conformal mapping including multiple connected regions," *AIAA Journal*, 1976, pp. 1006-1011.

[82] Jameson, A., "Solution of the Euler equations for two-dimensional transonic flow by a multigrid method," *Applied Mathematics and Computation*, Vol. 13, 1983, pp. 327-356.

[83] Jameson, A., "The role of CFD in preliminary aerospace design," 4th ASME-JSME Joint Fluids Engineering Conference, *ASME Paper* FEDSM2003-45812, Honolulu, Hawaii, July 6-11, 2003.

[84] Jameson, A., "Time integration methods in computational aerodynamics," *2003 AFOSR Work Shop on Advances and Challenges in Time-Integration of PDEs*, Providence, RI, August 18, 2003.

[85] Jameson, A., Schmidt, W., and Turkel, E., "Numerical solution of the Euler equations by finite volume methods using Runge-Kutta time stepping schemes," *AIAA paper* 81-1259, June 1981.

[86] Jameson, A., and Yoon, S., "Lower-upper implicit schemes with multiple grids for the Euler equations," *AIAA Journal*, Vol. 25, No. 7, 1987, pp. 929-935.

[87] Jenkins, D. A., Shyy, W., Sloan, J., Klevebring, F., and Nilsson, M., "Airfoil performance at low Reynolds numbers for micro air vehicles applications," *13th Bristol International RPV/UAV Conference*, University of Bristol, 1998.

[88] Jiang, Y. T., Damodaran, M., and Lee, K. H., "High-resolution finite volume computation of turbulent transonic flows past airfoils," *AIAA Journal*, Vol. 35, No. 7, 1997, pp. 1134-1142.

[89] Jones, K. D., and Platzer, M. F., "Numerical computation of flapping-wing propulsion and power extraction," *AIAA Paper* 97-0826, Reno, 1997.

[90] Kandil, O. A., and Chuang, H. A., "Unsteady transonic airfoil computation using implicit Euler scheme on body-fixed grid," *AIAA Journal*, Vol. 27, No. 8, August 1989, pp. 1031-1037.

[91] Katz, J., and Plotkin, A., *Low Speed Aerodynamics*, McGraw-Hill, New York, 1991.

[92] Katz, J., and Weihs, D., "Large amplitude unsteady motion of a flexible slender propulsor," *Journal of Fluid Mechanics*, Vol. 90, 1979, pp. 713-723.

[93] Katz, J., and Weihs, D., "Wake rollup and the Kutta condition for airfoils oscillating at high frequency," *AIAA Journal*, Vol. 19, 1981, pp. 1604-1606.

[94] Kemp, N. H., and Homicz, G., "Approximate unsteady thin airfoil theory for subsonic flow," *AIAA Journal*, Vol. 14, 1976, pp. 1083-1089.

[95] Kerho, M. F., "Effect of large distributed roughness near an airfoil leading edge on boundary-layer development and transition," *Ph.D. Dissertation*, Department of Aeronautical and Astronautical Engineering, University of Illinois at Urbana-Champain, Urbana, IL, 1995.

[96] Kerho, M. F., and Bragg, M. B., "Airfoil boundary-layer development and transition with large leading-edge roughness," *AIAA Journal*, Vol. 35, No. 1, January, 1997, pp. 75-84.

[97] Kinsey, D. W., and Barth, T. J., "Description of a hyperbolic grid generation procedure for arbitrary two-dimensional bodies," *Air Force Wright Aeronautical Lab.*, AFWAL-TM-84-191-FIMM, July 1984.

[98] Kuethe, A. M., and Chow, C. Y., *Foundations of Aerodynamics*, Wiley, New York, 1986.

[99] Kunz, P., and Kroo, I., "Analysis and design of airfoils for use at ultra-low Reynolds numbers," *Proceedings of the AIAA Fixed, Flapping and Rotating Wing Aerodynamics at Very Low Reynolds Numbers Conference*, Notre Dame, June 5-7, 2000, pp. 35-60.

[100] Küssner, H. G., "Nonstationary theory of airfoils of finite thickness in incompressible flow," *AGARD Manual on Aeroelasticity*, Part 2, 1960, Ch. 5.

[101] Küssner, H. G., "Zusammenfassender Bericht über den instationären Auftrieb von Flügeln," *Luftfahrtforschung*, Vol. 13, 1936, pp. 410.

[102] Kwak, D., Chang, J. L., Shanks, S. P., and Chakravarthy, S., "A three-dimensional incompressible Navier-Stokes flow solver using primitive variables," *AIAA Journal*, Vol. 24, 1986, pp. 390-396.

[103] Laitone, E. V., "Aerodynamic lift at Reynolds numbers below 70,000," *AIAA Paper* 95-0434, Reno, 1995.

[104] Landahl, M., *Unsteady Transonic Flow*, Pergamon Press, New York, 1961, pp. 27-30.

[105] Lee, T., and Basu, S., "Investigation of unsteady boundary layer developing on an oscillating airfoil," *Experiments in Fluids*, Vol. 25, 1998, pp. 108-117.

[106] Lentink, D., and Gerritsma, M., "Influence of airfoil shape on performance in insect flight," *AIAA Paper* 2003-3447, June 23-26, 2003.

[107] Liebeck, R. H., "Design of subsonic airfoils for high lift," *Journal of Aircraft*, Vol. 15, No. 9, 1978, pp. 547-561.

[108] Liebeck, R. H., "Subsonic airfoil design," *Applied Computational Aerodynamics*, edited by Henne, P. A., Vol. 125 of Progress in Astronautics and Aeronautics, AIAA, Washington, D.C., 1990.

[109] Lin, J. C., and Dominik, C. J., "Parametric investigation of a high-lift airfoil at high Reynolds numbers," *Journal of Aircraft*, Vol. 34, No. 4, July-August, 1997, pp. 485-491.

[110] Liu, H., Ellington, C. P., Kawachi, K., Van den Berg, C., and Willmott, A. P., "A computational fluid dynamics study of hawkmoth hovering," *Journal of Experimental Biology*, Vol. 201, 1998, pp. 461-477.

[111] Lyon, C. A., Broeren, A. P., Giguere, P., Gopalarathnam, A., and Selig, M. S., *Summary of low-Speed Airfoil Data*, Vol. 3, SoarTech Publications, Virginia Beach, VA, 1998.

[112] MacCormack, R. W., "The effect of viscosity on hypervelocity impact cratering," *AIAA Paper* 69-0354, 1969.

[113] Martinelli, L., Jameson, A., and Grasso, F., "A multigrid method for the Navier-Stokes equations," *AIAA paper* 86-0208, January, 1986.

[114] Mateescu, D., "A hybrid panel method for aerofoil aerodynamics," *Boundary Element XII*, Springer-Verlag, Berlin and New York, Vol. 2, 1990, pp.3-14.

[115] Mateescu, D., "Steady and unsteady flow solutions using velocity singularities for fixed and oscillating airfoils and wings," *Computational Methods and Experimental Measurements X*, Comp. Mech. Pub., Boston, 2001, pp.3-12.

[116] Mateescu, D., "Wing and conical body of arbitrary cross-section in supersonic flow," *Journal of Aircraft*, Vol. 24, No. 4, 1987, pp. 239-247.

[117] Mateescu, D., and Abdo, M., "Theoretical solutions for unsteady flows past oscillating flexible airfoils using velocity singularities," *Journal of Aircraft*, Vol. 40, No. 1, January-February, 2003, pp. 153-163.

[118] Mateescu, D., and Abdo, M., "Unsteady aerodynamic solutions for oscillating airfoils," *AIAA Paper* 2003-227, Reno, January 2003.

[119] Mateescu, D., and Abdo, M., "Nonlinear theoretical solutions for airfoil aerodynamics," *AIAA Paper* 2003-4296, Orlando, June 2003.

[120] Mateescu, D., and Abdo, M., "Aerodynamic analysis of airfoils at very low Reynolds numbers," *AIAA Paper* 2004-1053, Reno, January 2004.

[121] Mateescu, D., and Abdo, M., "Airfoil flow analysis at low-Reynolds numbers," *AIAA Journal* (submitted for publication), 2004.

[122] Mateescu, D., and Abdo, M., "Efficient second-order analytical solutions for airfoils in subsonic flows," *Aerospace Science and Technology Journal*, AST No. 1236, 2004 (accepted for publication).

[123] Mateescu, D., and Nadeau, Y., "A nonlinear analytical solution for airfoils in irrotational flows," *Proceedings of the 3rd International Congress of Fluid Mechanics*, Cairo, Vol. 4, 1990, pp. 1421-1423.

[124] Mateescu, D., and Newman, B. G., "Analysis of flexible-membrane and jet-flapped airfoils using velocity singularities," *Journal of Aircraft*, Vol. 28, No. 11, 1991, pp. 789-795.

[125] Mateescu, D., Païdoussis, M. P., and Bélanger, F., "A time-integration method using artificial compressibility for unsteady viscous flows," *Journal of Sound and Vibration*, Vol. 177, 1994a, pp. 197-205.

[126] Mateescu, D., Païdoussis, M. P., and Bélanger, F., "Unsteady annular viscous flows between oscillating cylinders. Part I: Computational solutions based on a time integration method. & Part II: A hybrid time-integration solution based on azimuthal Fourier expansions for configurations with annular steps," *Journal of Fluids and Structures*, Vol. 8, 1994b, pp. 489-507 and pp. 509-527.

[127] Mateescu, D., Seytre, J. F., and Berhe, A. M., "Aerodynamic solutions for finite-span wings of arbitrary shapes," *Journal of Aircraft*, Vol. 40, No. 4, May-June 2003.

[128] Mateescu, D., and Stanescu, D., "A biased flux method for solving the Euler equations in subsonic, transonic and supersonic flows," *Computational Methods and Experimental Measurements VII*, Computational Mechanics Publications, Southampton & Boston, 1995, pp. 327-335.

[129] Mateescu, D., and Venditti, D., "Unsteady confined viscous flows with oscillating walls and multiple separation regions over a downstream-facing step," *Journal of Fluids and Structures* , Vol. 15, 2001, pp. 1187-1205.

[130] Maughmer, M. D., and Somers, D. M., "Design and experimental results for a high altitude long endurance airfoil," *Journal of Aircraft*, Vol. 26, No. 2, 1989, pp. 148-153.

[131] Mavriplis, F. "Comparison of surface-vorticity method with surface-source method and with exact solution for two dimensional potential flow around two adjacent lifting airfoils," *CAS Journal*, Vol. 19, 1973, pp. 411-413.

[132] Maxworthy, T., "Experiments on the Weis-Fogh mechanism of lift generation by insects in hovering flight part I: dynamics of fling," *Journal of Fluid Mechanics*, Vol. 93, 1979, pp. 47-63.

[133] McAlister, K. W., Carr, L. W., and McCroskey, W. J., "Dynamic stall experiments on the NACA 0012 airfoil," *NASA TP* 1100, January 1978.

[134] McCroskey, W. J., "Inviscid flow field of an unsteady airfoil," *AIAA Journal*, Vol. 11, 1973, pp. 1130-1137.

[135] McCroskey, W. J., "Unsteady airfoils," *Ann. Rev. Fluid Mech.*, Vol. 14, 1982, pp. 285-311.

[136] McGowan, A. R., "AVST morphing project research summaries in fiscal year 2001," *NASA TM* 2002-211769, August 2002.

[137] McLachlan, N.W., *Bessel Functions For Engineers*, Oxford at the Clarendon Press, 1934, pp. 61-70.

[138] McMullen, M. S., "The application of non-linear frequency domain methods to the Euler and Navier-Stokes Equations," *Ph.D. Dissertation*, Department of Aeronautics and Astronautics, Stanford University, 2003.

[139] Mehta, U. B., "Dynamic stall of an oscillating airfoil," Unsteady Aerodynamics, *AGARD CP*-227, 1977, pp. 23.1-23.32.

[140] Mehta, U. B., "Starting vortex, separation bubbles and stall –A numerical study of laminar unsteady flow around an airfoil," *Ph.D. Dissertation*, Illinois Institute of Technology, Chicago, 1972.

[141] Merriam, M., "UNSTRUCT-An unstructured grid generator for the iris workstation," *NASA Ames Research Center*, 1991.

[142] Milne-Thomson, L. M., *Theoretical Aerodynamics*, Dover, New York, 1966.

[143] Morris, S., and Holden, M., "Design of micro air vehicles and flight test validation," *Proceedings of the AIAA Fixed, Flapping and Rotating Wing Aerodynamics at Very Low Reynolds Numbers Conference*, Notre Dame, June 5-7, 2000, pp. 153-176.

[144] Mueller, T. J., (editor), *Conference on fixed, flapping and rotary wing vehicles at low Reynolds numbers*, Notre Dame University, Indiana, June 5-7, 2000.

[145] Mueller, T. J., "Aerodynamic measurements at low Reynolds numbers for fixed wing micro-air vehicles," *Development and Operation of UAVs for Military and Civil Applications*, VKI, Belgium, September 13-17, 1999.

[146] Mueller, T. J., and Balill, S. M., "Experimental studies of separation and a two-dimensional airfoil at low Reynolds numbers," *AIAA Journal*, Vol. 20, 1982.

[147] Munk, M., "Elements of the wing section theory and of the wing theory," *NACA Report* No. 191, 1924.

[148] Nadarajah, S., McMullen, M., and Jameson, A., "Optimal control of unsteady flows using time accurate and non-linear frequency domain methods," *AIAA Paper* 2003-3875, Orlando, Florida, June 23-26, 2003.

[149] Nelson, T.E., Zingg, D. W., and Johnston, G. W. "Compressible Navier-Stokes computations of multielement airfoils flows using multiblock grids," *AIAA Journal*, Vol. 32, No. 3, pp. 506-511, March, 1994.

[150] Nemec, M., "Optimal shape design of aerodynamic configurations: A Newton-Krylov approach," *Ph.D. Dissertation*, Graduate Department of Aerospace Science and Engineering, University of Toronto, 2003.

[151] Ni, R. H., "A multiple grid scheme for solving the Euler equations," *Proceedings of the 5th AIAA Computational Fluid Dynamics Conference*, 1981, pp. 257-264.

[152] Oshima, H., and Ramaprian, B. R., "Velocity measurement over a pitching airfoil," *AIAA Journal*, Vol. 35, No. 1, January 1997, pp. 119-126.

[153] Panda, J., and Zaman, K. Q., "Experimental investigation of the flowfield of an oscillating airfoil," *AIAA Paper* 92-2622-CP, 1992, pp. 201-218.

[154] Patankar, S. V., and Spalding, D. B., "A calculation procedure for heat, mass and momentum transfer in three-dimensional parabolic flows," *International Journal of Heat and Mass Transfer*, Vol. 15, 1972, pp. 1787-1806.

[155] Patankar, S. V., *Numerical Heat Transfer and Fluid Flow*, Hemishpere, Washington, D.C., 1980.

[156] Perić, M., Kessler, R., and Scheurer, G., "Comparison of finite volume numerical methods with staggered and colocated grids," *Computers and Fluids*, Vol. 16, 1988, pp. 389-403.

[157] Peyret, R., and Taylor, T. D., *Computational Methods for Fluid Flow*, New York, Springer Verlag, 1983.

[158] Postel, E. E., and Leppert, E. L., "Theoretical pressure distributions for a thin airfoil oscillating in incompressible flow," *Journal of Aeronautical Sciences*, Vol. 15, 1948, pp. 486-492.

[159] Pueyo, A., "An efficient Newton-Krylov method for the Euler and Navier-Stokes equations," *Ph.D. Dissertation*, Graduate Department of Aerospace Science and Engineering, University of Toronto, 1998.

[160] Pueyo, A., and Zingg, D. W., "Efficient Newton-Krylov solver for aerodynamic computations," *AIAA Journal*, Vol. 36, 1998, pp. 1991-1997.

[161] Ramamurti, R., and Sandberg, W. C., "A three dimensional computational study of the aerodynamic mechanism of insect flight," *Journal of Experimental Biology*, Vol. 205, 2002, pp. 1507-1518.

[162] Raney, D. L., and Waszak, M. R., "Biologically inspired micro-flight research," *AIAA Paper* 2003-01-3042, 2003.

[163] Rizzi, A., and Eriksson, L. E., "Computation of inviscid incompressible flow with rotation," *Journal of Fluid Mechanics*, Vol. 153, 1985, pp. 275-312.

[164] Rogers, S., and Kwak, D. "An upwind differencing scheme for the time-accurate incompressible Navier-Stokes equations," *AIAA Journal* 28, 253-262, 1990.

[165] Romanowski, M. C., and Dowell, E. H., "Reduced order Euler equations for unsteady aerodynamic flows: numerical techniques," *AIAA Paper* 96-0528, January 1996.

[166] Schlichting, H., *Boundary Layer Theory*, 7th ed, McGraw-Hill, New York, 1979, Ch. 2, 7, 18, 19, 21-23.

[167] Schlichting, H., and Gersten, K., *Boundary Layer Theory*, 8th ed, Springer-Verlag, Berlin, 2000, Ch. 2, 6, 16-18, 23.

[168] Segal, G., Zijlema, M., Nooyen, R. V., and Moulinec, C., "User Manual of the Delft Incompressible Flow Solver," *Delft University of Technology*, version 1.1, 2001.

[169] Selig, M. S., and Guglielmo, J. J., "High-lift low Reynolds number airfoil design," *Journal of Aircraft*, Vol. 34, No. 1, January-February, 1997, pp. 72-79.

[170] Selig, M. S., Lyon, C. A., Giguere, P., Ninham, C. N., and Guglielmo, J. J., *Summary of Low-Speed Airfoil Data*, Vol. 2, SoarTech Publications, Virginia Beach, VA, 1996.

[171] Sells, C.C.L. "Plane subcritical flow past a lifting aerofoil," *Proc. Royal Soc*, London, ser A, Vol. 308, 1968, pp. 377-401.

[172] Shyy, W., Berg, M., and Ljungqvist, D., "Flapping and flexible wings for biological and micro vehicles," *Progress in Aerospace Sciences*, Vol. 35, No. 5, 1999, pp. 455-506.

[173] Simons, M., *Model Aircraft Aerodynamics*, Argus Books, Herts, 1994.

[174] Singh, J., and Wu, J. C., "Unsteady aerodynamics of nonrigid bodies undergoing time-dependant motions/deformations- A simplified zonal approach," *AIAA Paper* 94-1889-CP, 1994, pp. 621-632.

[175] Soh, W., "Time-marching solution of incompressible Navier-Stokes equations for internal flows," *Journal of Computational Physics*, Vol. 70, 1987, pp. 232-252.

[176] Soh, W., and Goodrich, J. "Unsteady solution of incompressible Navier-Stokes equations," *Journal of Computational Physics*, Vol. 79, 1988, pp. 113-134.

[177] Sorenson, R. L., "A computer program to generate two-dimensional grids about airfoils and other shapes by the use of Poisson's equation," *NASA Ames Research Center, NASA TM* 81198, Moffett field, CA, May 1980.

[178] Steger, J. L., and Kutler, P., "Implicit finite-difference procedures for the computation of vortex wakes," *AIAA Journal*, Vol. 15, 1977, pp. 581-590.

[179] Summa, J., Strash, D., and Yoo, S., "Zonal flow analysis method for two-dimensional airfoils," *AIAA Journal*, Vol. 30, No. 2, 1992, pp. 548-549.

[180] Sun, M., and Tang, J., "Unsteady aerodynamic force generation by a model fruit-fly wing in flapping motion," *Journal of Experimental Biology*, Vol. 205, 2002, pp. 55-70.

[181] Sunada, S., and Ellington, C. P., "Approximate added-mass method for estimating induced power for flapping flight," *AIAA Journal*, Vol. 38, No. 8, August 2000, pp. 1313-1321.

[182] Temam, R., *Navier-Stokes Equations*, Amsterdam, North Holland Publishing Co., 1977.

[183] Temperton, C., "Algorithms for the solution of cyclic tridiagonal systems," *Journal of Computational Physics*, Vol. 19, 1975, pp. 317-323.

[184] Theodorsen, T., "General theory of aerodynamic instability and the mechanism of flutter," *NACA TR* 496, 1935.

[185] Theodorsen, T., and Garrick, I. E., "Nonstationary flow about a wing-aileron-tab combination including aerodynamic balance," *NACA TR* 736, 1942.

[186] Thibert, J., Grandjacques, M., and Ohman, L. "Experimental data base for computer program assessment- *NACA 0012 Airfoil*," *Report of Fluid Dynamics Panel, Working group 4, AGARD*-AR-138, pp. A1. 1-36, May, 1979.

[187] Thompson, J. F., Warsi, Z. U. A., and Mastin, C. W., *Numerical Grid Generation: Foundations and Applications*, New York, North-Holland Elsevier, 1985.

[188] Thwaites, B., *Incompressible Aerodynamics*, Oxford University Press, Oxford, UK, 1960.

[189] Tuncer, I. H., Ekaterinaris, A., and Platzer, M. F., "Viscous-inviscid interaction method for unsteady low-speed airfoil flows," *AIAA Journal*, Vol. 33, No. 1, January 1995, pp. 151-154.

[190] Valarezo, W. O., Dominik, C. J., McGhee, R. J., Goodman, W. L., and Pascchal, K. B., "Multi-element airfoil optimization at high Reynolds numbers," *AIAA Paper* 91-3332, September, 1991.

[191] Venkatakrishnan, V., and Jameson, A., "Computation of unsteady transonic flows by the solution of the Euler equations," *AIAA Journal*, Vol. 26, No. 8, August, 1988, pp. 974-981.

[192] Vidal, R. J., Catlin, P. A., and Chudyk, D. W., "Two-dimensional subsonic experiments with an NACA 0012 airfoil," *Calspan Report* No. RK-5070-A-3, Calspan corporation, New York, December, 1973.

[193] Vinokur, M., "On one-dimensional stretching functions for finite-difference calculations," *Journal of Computational Physics*, Vol. 50, 1983, pp. 216-234.

[194] Visbal, M. R., "On the formation and control of the dynamic stall vortex on a pitching airfoil," *AIAA Paper* 91-0006, 1991.

[195] Von Karman, T., and Sears, W. R., "Airfoil theory for nonuniform motion," *Journal of Aeronautical Sciences*, Vol. 5, 1938, pp. 370-390.

[196] Wagner, H., "Dynamischer auftrieb von tragflügeln," *Zeitschr. f. Angew. Math. U. Mech.*, Vol. 5, 1925, pp. 17.

[197] Walsh, P., and Zingg, D. "A solution-adaptive solver for aerodynamic applications using unstructured grids," *4th Annual Conference of the CFD society of Canada*, Ottawa, Ontario, June 2-6, 1996, pp. 161-168.

[198] Wang, J. Z., "Two-dimensional mechanism for insect hovering," *Physical Review Letters*, 85(10), 2000, pp. 2216-2219.

[199] Wang, J. Z., "Vortex shedding and frequency selection in flapping flight," *Journal of Fluid Mechanics*, Vol. 410, 2000, pp. 323-341.

[200] Watson, G.N., *Theory of Bessel Functions*, Cambridge University Press, Second edition, 1966, pp. 160-183.

[201] Weber, J., "The calculation of the pressure distribution on the surface of thick cambered wings and the design of wings with given pressure distribution," *British ARC* R&M 3026, 1955.

[202] Weber, J., "The calculation of the pressure distribution over the surface of two-dimensional and swept wings with symmetrical aerofoil sections," *British ARC* R&M 2918, 1953.

[203] Weis-Fogh, T., "Quick estimates of flight fitness in hovering animals, including mechanisms for lift production," *Journal of Experimental Biology*, Vol. 59, 1973, pp. 169-230.

[204] White, F. M., *Viscous Fluid Flow*, McGraw-Hill , New York, 1974, Ch. 2, 6, 7.

[205] Willcox, K., and Megretski, A., "Fourier series for accurate, stable, reduced-order models for linear CFD applications," *15th Computational Fluid Dynamics Conference, AIAA Paper* 2003-4235, Orlando, Florida, June 2003.

[206] Zanker, J. M., "The wing beat of Drosophila melanogaster: Part I kinematics," *Philosophical Transactions of the Royal Society*, serie B, London, Vol. 327, 1990, pp. 1-8.

[207] Zanker, J. M., and Götz, K., "The wing beat of Drosophila melanogaster: Part II dynamics," *Philosophical Transactions of the Royal Society*, serie B, London, Vol. 327, 1990, pp. 19-44.

[208] Zdanski, P., Ortega, M., and Fico, N., "A novel algorithm for the incompressible Navier-Stokes equations," *AIAA Paper* 2003-434, 2003.

[209] Zingg, D. W., "Grid studies for thin-layer Navier-Stokes computations of airfoil flowfields," *AIAA Journal*, Vol. 30, 1992, pp. 2561-2564.

Appendix A: General Integrals

A.1 Recurrence formulas for the integral L_j

Consider the recurrence integral defined by,

$$L_j = \int_0^1 \frac{s^j}{2\sqrt{1-s}} ds \ , \tag{A1.1}$$

When $j = 0$, equation (A1.1) becomes

$$L_0 = \int_0^1 \frac{1}{2\sqrt{1-s}} ds = -\sqrt{1-s}\,\bigg|_{s=0}^{s=1} = \sqrt{1} = 1 \ , \tag{A1.2}$$

By integrating equation (A1.1) by parts one thus obtains,

$$L_j = \int_0^1 \frac{s^j}{2\sqrt{1-s}} ds = s^j\left[-\sqrt{1-s}\,\right]\bigg|_{s=0}^{s=1} - \int_0^1 j\, s^{j-1}\left[-\sqrt{1-s}\,\right] ds \ , \tag{A1.3}$$

By noting that

$$-\sqrt{1-s} = 2\frac{-(1-s)}{2\sqrt{1-s}} \ ,$$

one obtains

$$L_j = s^j\left[-\sqrt{1-s}\,\right]\bigg|_{s=0}^{s=1} + 2j\left[L_{j-1} - L_j\right]. \tag{A1.4}$$

After rearranging the common terms, one obtains the following equation

$$L_j = -\frac{s^j}{2j+1}\left[\sqrt{1-s}\,\right]\bigg|_{s=0}^{s=1} + \frac{2j}{2j+1} L_{j-1} \qquad \text{for } j \geq 1 \ , \tag{A1.5}$$

This equation finally leads to the recurrence formula for the integral L_j

$$L_j = \frac{2j}{2j+1} L_{j-1} \qquad \text{for } j \geq 1 \quad \text{and} \quad L_0 = 1. \tag{A1.6}$$

A.2 Recurrence formulas for the integral g_k

Consider the recurrence integral defined by,

$$g_k = \frac{1}{\pi}\int_0^1 \frac{s^k}{\sqrt{(1-s)s}}\,ds \ , \tag{A2.1}$$

Note that s^k can be written by,

$$s^k = -\frac{1}{2}\left[(1-2s)s^{k-1} - s^{k-1}\right], \tag{A2.2}$$

By substituting the value of s^k into the recurrence integral, one obtains,

$$g_k = -\frac{1}{\pi}\left[\int_0^1 \frac{s^{k-1}(1-2s)}{2\sqrt{s(1-s)}}\,ds - \int_0^1 \frac{s^{k-1}}{2\sqrt{s(1-s)}}\,ds\right] \ ,$$

Note that $\int_0^1 \frac{s^{k-1}(1-2s)}{2\sqrt{s(1-s)}}\,ds = s^{k-1}\sqrt{s(1-s)} - (k-1)\int_0^1 s^{k-2}\sqrt{s(1-s)}\,ds$

The second integral can then be given by,

$$\int_0^1 s^{k-2}\sqrt{s(1-s)}\,ds = \int_0^1 \frac{s^{k-2}s(1-s)}{\sqrt{(1-s)s}}\,ds = \int_0^1 \frac{s^{k-1}}{\sqrt{s(1-s)}}\,ds - \int_0^1 \frac{s^k}{\sqrt{s(1-s)}}\,ds \ , \tag{A2.3}$$

By arranging the terms, one concludes,

$$g_k = \left(\frac{2k-1}{2k}\right) g_{k-1} \ , \quad k \geq 1 \ . \tag{A2.4}$$

The value of the integral at $k = 0$ (g_0) is given by,

$$g_0 = \frac{1}{\pi}\int_0^1 \frac{1}{\sqrt{s(1-s)}}\,ds = -2\cos^{-1}\sqrt{s}\,\Big|_{s=0}^{s=1} = 1 \ , \tag{A2.5}$$

A.3 Recurrence formula for the integral H_q

Consider the recurrence integral defined by,

$$H_q = \frac{1}{\pi}\int_0^1 s^q\sqrt{s(1-s)}\,ds \ , \tag{A3.1}$$

By noting that this integral is related to the recurrence formula for the integral g_k derived in section A.2, one obtains

$$H_q = \frac{1}{\pi}\int_0^1 s^q \sqrt{s(1-s)}\, ds = \frac{1}{\pi}\int_0^1 s^q \frac{s(1-s)}{\sqrt{s(1-s)}}\, ds = g_{q+1} - g_{q+2} , \tag{A3.2}$$

By noting that

$$g_{q+2} = \frac{2(q+2)-1}{2(q+2)}\, g_{q+1} , \tag{A3.3}$$

one obtains the following recurrence formula for the integral H_q

$$H_q = \frac{1}{2(q+2)} g_{q+1} . \tag{A3.4}$$

where g_k is derived in section A.2.

A.4 The integral ξ_1

Consider the integral defined by,

$$\xi_1 = \int_0^1 \frac{ds}{2(s-x)\sqrt{1-s}} , \tag{A4.1}$$

This integral can be easily determined by noticing the derivative of the following special function

$$\widetilde{H}_1(x,s) = \cosh^{-1} \widetilde{R}_1 , \tag{A4.2}$$

where,

$$\widetilde{R}_1 = \sqrt{\frac{1-x}{s-x}} . \tag{A4.3}$$

The derivative of this function is given by the following relation,

$$\frac{d\widetilde{H}_1}{ds} = \frac{1}{\sqrt{\left(\widetilde{R}_1\right)^2 - 1}} \frac{d\widetilde{R}_1}{ds} . \tag{A4.4}$$

After performing the derivation and arranging the terms, one thus obtains

$$\frac{d\widetilde{H}_1}{ds} = \frac{d}{ds}\left[\cosh^{-1} \sqrt{\frac{1-x}{s-x}} \right] = \frac{-\sqrt{1-x}}{2(s-x)\sqrt{1-s}} . \tag{A4.5}$$

The integral ξ_1 is then given by

$$\xi_1 = \int_0^1 \frac{ds}{2(s-x)\sqrt{1-s}} = \frac{-1}{\sqrt{1-x}} \cosh^{-1} \sqrt{\frac{1-x}{s-x}} \Bigg|_{s=0}^{s=1} = \frac{1}{\sqrt{1-x}} \left(\frac{i\pi}{2} + \sinh^{-1} \sqrt{\frac{1-x}{x}} \right) ,$$

By taking the real part of the equation, the integral is then reduced to

$$\xi_1 = \frac{1}{\sqrt{1-x}} \sinh^{-1} \sqrt{\frac{1-x}{x}} \ . \tag{A4.6}$$

A.5 The integral ξ_2

Consider the integral defined by,

$$\xi_2 = \frac{1}{\pi} \int_0^1 \frac{\sqrt{s(1-s)}}{s-x} \, ds \ , \tag{A5.1}$$

This integral can be rewritten in the following form

$$\xi_2 = \frac{1}{\pi} \int_0^1 \frac{\sqrt{s(1-s)}}{s-x} \, ds = \frac{1}{\pi} \int_0^1 \frac{s(1-s)}{(s-x)\sqrt{s(1-s)}} \, ds \ . \tag{A5.2}$$

By noting that $s(1-s) = (s-x+x)(1-s) = x(1-s) + (s-x)(1-s)$ which can be also rewritten in the form $s(1-s) = x(1-x) - x(s-x) + (s-x)(1-s)$, the integral becomes

$$\xi_2 = (1-x)g_0 - g_1 + \frac{1}{\pi} \sqrt{x(1-x)} \int_0^1 \frac{\sqrt{x(1-x)}}{(s-x)\sqrt{s(1-s)}} \, ds \ . \tag{A5.3}$$

The integral within ξ_2 is determined by noticing the derivative of the following special function

$$\widetilde{H}_1(x,s) = \cosh^{-1} \widetilde{R}_1 \ , \tag{A5.4}$$

where,

$$\widetilde{R}_1 = \sqrt{\frac{(1-x)s}{(s-x)}} \ . \tag{A5.5}$$

The derivative of this function is given by the following relation,

$$\frac{d\widetilde{H}_1}{ds} = \frac{1}{\sqrt{\left(\widetilde{R}_1\right)^2 - 1}} \frac{d\widetilde{R}_1}{ds} \ . \tag{A5.6}$$

After performing the derivation and arranging the terms, one thus obtains

$$\frac{d\widetilde{H}_1}{ds} = \frac{d}{ds}\left[\cosh^{-1} \sqrt{\frac{(1-x)s}{(s-x)}} \right] = \frac{-\sqrt{x(1-x)}}{2(s-x)\sqrt{s(1-s)}} \ . \tag{A5.7}$$

Thus equation (A5.3) becomes

$$\xi_2 = (1-x)g_0 - g_1 + \frac{1}{\pi}\sqrt{x(1-x)}\left(-2\cosh^{-1}\sqrt{\frac{(1-x)s}{(s-x)}}\right)\Bigg|_{s=0}^{s=1}$$

$$= (1-x)g_0 - g_1 + i\sqrt{x(1-x)} \ . \tag{A5.8}$$

where $i = \sqrt{-1}$.

By taking the real part of equation (A5.8) and introducing $g_0 = 1$ and $g_1 = 1/2$, one obtains

$$\xi_2 = \frac{1}{2} - x \ . \tag{A5.9}$$

A.6 The integrals I_k

Consider the recurrence integral defined by,

$$I_k = \int \frac{s^k}{\sqrt{(1-s)s}} ds \ , \tag{A6.1}$$

Note that s^k can be written by,

$$s^k = -\frac{1}{2}\left[(1-2s)s^{k-1} - s^{k-1}\right], \tag{A6.2}$$

By substituting the value of s^k into the recurrence integral, one concludes,

$$I_k = -\left[\int \frac{s^{k-1}(1-2s)}{2\sqrt{s(1-s)}} ds - \int \frac{s^{k-1}}{2\sqrt{s(1-s)}} ds\right], \tag{A6.3}$$

Note that $\int \frac{s^{k-1}(1-2s)}{2\sqrt{s(1-s)}} ds = s^{k-1}\sqrt{s(1-s)} - (k-1)\int s^{k-2}\sqrt{s(1-s)}\, ds$

The second integral can be then given by,

$$\int s^{k-2}\sqrt{s(1-s)}\, ds = \int \frac{s^{k-2}s(1-s)}{\sqrt{(1-s)s}} ds = \int \frac{s^{k-1}}{\sqrt{s(1-s)}} ds - \int \frac{s^k}{\sqrt{s(1-s)}} ds \ , \tag{A6.4}$$

Substituting the above integral into the definition of the recurrence integral, one obtains,

$$I_k = -\left[s^{k-1}\sqrt{s(1-s)} - (k-1)(I_{k-1} - I_k) - \frac{1}{2}I_{k-1}\right], \tag{A6.5}$$

By arranging the terms, one concludes,

$$I_k = -\frac{s^{k-1}}{k}\sqrt{s(1-s)} + \left(\frac{2k-1}{2k}\right) I_{k-1} , \qquad k \geq 1 . \tag{A6.6}$$

The value of the integral at $k = 0$ (I_0) is given by,

$$I_0 = \int \frac{1}{\sqrt{s(1-s)}} ds = -2 \cos^{-1} \sqrt{s} , \tag{A6.7}$$

The value of the integral at $k = 1$ (I_1) is given by,

$$I_1 = \int \frac{s}{\sqrt{s(1-s)}} ds = -\sqrt{s(1-s)} - \cos^{-1} \sqrt{s} . \tag{A6.8}$$

A.7 The integrals J_k and $\bar{J}_k$

Consider the integral defined by

$$J_k = \int_0^s \frac{s^k}{\sqrt{s(1-s)}} ds , \tag{A7.1}$$

This recurrence integral is a special case of the integral I_k defined in Section A.6, by introducing the limits of integration, one hence obtains

$$J_k = I_k \Big|_{s=0}^{s} = -\frac{s^{k-1}}{k}\sqrt{s(1-s)} \Big|_{s=0}^{s} + \left(\frac{2k-1}{2k}\right) I_{k-1} , \tag{A7.2}$$

The value of the integral at $k = 0$ (J_0) is given by,

$$J_0 = \int_{s=0}^{s} \frac{1}{\sqrt{s(1-s)}} ds = -2 \cos^{-1} \sqrt{s} \Big|_{s=0}^{s} = \pi - 2 \cos^{-1} \sqrt{s} , \tag{A7.3}$$

The value of the integral at any k is thus given by,

$$J_k = -\frac{s^{k-1}}{k}\sqrt{(1-s)s} + \frac{2k-1}{2k} J_{k-1} . \tag{A7.4}$$

Similarly for $\bar{J}_k$ which is also a special case of the integral defined in Section A.6, one obtains

$$\bar{J}_k = \frac{s^{k-1}}{k}\sqrt{(1-s)s} + \frac{2k-1}{2k} \bar{J}_{k-1} , \quad \bar{J}_0 = 2 \cos^{-1} \sqrt{s} . \tag{A7.5}$$

A.8 The integrals $Q(x)$, $\overline{Q}(x)$

Consider the integral $Q(x)$ defined by

$$Q(x)=\int_0^s \frac{\sqrt{s(1-s)}}{s-x}\,ds\ , \tag{A8.1}$$

This integral can be rearranged in the following equivalent form

$$Q(x)=\int_0^s \frac{(1-s)s}{(s-x)\sqrt{s(1-s)}}\,ds\ , \tag{A8.2}$$

By noting that $s(1-s)=(s-x)(1-s-x)+(1-x)x$, the integral thus becomes

$$Q(x)=\int_0^s \frac{\sqrt{s(1-s)}}{s-x}\,ds=\int_0^s \frac{(1-x)-s}{\sqrt{s(1-s)}}\,ds+\sqrt{(1-x)x}\int_0^s \frac{\sqrt{(1-x)x}}{(s-x)\sqrt{(1-s)s}}\,ds\ , \tag{A8.3}$$

By noting the derivative of the following special function

$$\frac{d}{ds}\left[\cosh^{-1}\sqrt{\frac{(1-x)s}{(s-x)}}\right]=\frac{-\sqrt{x(1-x)}}{2(s-x)\sqrt{s(1-s)}}\ , \tag{A8.4}$$

and the recurrence integrals J_k, the recurrence integral $Q(x)$ is then given by

$$Q(x)=(1-x)J_0-J_1+\sqrt{(1-x)x}\left[\cosh^{-1}\sqrt{\frac{(1-x)s}{(s-x)}}\right]_{s=0}^{1}\ , \tag{A8.5}$$

which is then given in the final form

$$Q(x)=(1-x)J_0-J_1-2\sqrt{(1-x)x}\ G(s,x)\ , \tag{A8.6}$$

By following the same procedure given above, one obtains for $\overline{Q}(x)$

$$\overline{Q}(x)=(1-x)\overline{J}_0-\overline{J}_1+2\sqrt{(1-x)x}\ G(s,x)\ , \tag{A8.7}$$

where

$$G(s,x)=\begin{cases}\dfrac{2}{\pi}\cosh^{-1}\sqrt{\dfrac{(1-x)s}{s-x}} & \text{for } x\in(0,s)\\[2ex] \dfrac{2}{\pi}\sinh^{-1}\sqrt{\dfrac{(1-x)s}{x-s}} & \text{for } x\in(s,1).\\[2ex] 0 & \text{for } x<0 \text{ and } x>1\end{cases}$$

A.9 The integral $\int\limits_0^1 \frac{1}{2(s-x)\sqrt{s}}ds$

Consider the special function

$$\hat{H}_1(x,s) = \cosh^{-1}\hat{R}_1 \ , \tag{A9.1}$$

where,

$$\hat{R}_1 = \sqrt{\frac{s}{(s-x)}} \ . \tag{A9.2}$$

The derivative of this function is given by the following relation,

$$\frac{d\hat{H}_1}{ds} = \frac{1}{\sqrt{\left(\hat{R}_1\right)^2 - 1}}\frac{d\hat{R}_1}{ds} \ . \tag{A9.3}$$

By noting that

$$\frac{d\hat{R}_1}{ds} = \frac{1}{2}\sqrt{\frac{s-x}{s}}\left(\frac{-x}{(s-x)^2}\right),$$

$$\sqrt{\left(\hat{R}_1\right)^2 - 1} = \sqrt{\frac{x}{s-x}} \ .$$

After rearranging the terms, one thus obtains

$$\frac{d\hat{H}_1}{ds} = \frac{d}{ds}\left[\cosh^{-1}\sqrt{\frac{s}{(s-x)}}\right] = \frac{-\sqrt{x}}{2(s-x)\sqrt{s}} \ . \tag{A9.4}$$

Thus one obtains for the special integral

$$\int\limits_0^1 \frac{1}{2(s-x)\sqrt{s}}ds = \frac{-1}{\sqrt{x}}\cosh^{-1}\sqrt{\frac{s}{(s-x)}}\Bigg|_{s=0}^{s=1} = \frac{-1}{\sqrt{x}}\cosh^{-1}\sqrt{\frac{1}{(1-x)}} \ . \tag{A9.5}$$

Appendix B: Theodorsen's Formulas

B.1 Formulas related to Theodorsen's results

$$P_\omega = 1 - 2i\frac{V}{b\omega}(F + iG) , \tag{B1.1}$$

$$P_\varphi = \frac{1}{2} - i\frac{V}{b\omega}[1 + 2(F + iG)] - 2\left(\frac{V}{b\omega}\right)^2 (F + iG) , \tag{B1.2}$$

$$P_\beta = -\frac{T_1}{\pi} + i\left(\frac{V}{b\omega}\right)\frac{T_4}{\pi} - i\frac{V}{b\omega}\frac{T_{11}}{\pi}(F + iG) - 2\left(\frac{V}{b\omega}\right)^2 \frac{T_{10}}{\pi}(F + iG) , \tag{B1.3}$$

$$M_\omega = \frac{1}{2}, \quad M_\varphi = \frac{3}{8} - i\frac{V}{b\omega} , \tag{B1.4}$$

$$M_\beta = -\frac{T_1}{\pi} - \left(c_1 + \frac{1}{2}\right)\frac{T_1}{\pi} + i\frac{V}{b\omega}\frac{T_4 - \frac{2}{3}\left(\sqrt{1 - c_1^2}\right)^3}{\pi} - \left(\frac{V}{b\omega}\right)^2 \frac{T_1 + T_{10}}{\pi} , \tag{B1.5}$$

$$T_\omega = -\frac{T_1}{\pi} - i\frac{V}{b\omega}\frac{T_{12}}{\pi}(F + iG) , \tag{B1.6}$$

$$\begin{aligned} T_\varphi = &-\frac{1}{\pi}\left[T_7 + \left(c_1 + \frac{1}{2}\right)T_1\right] + i\frac{V}{b\omega}\frac{\frac{2}{3}\left(\sqrt{1 - c_1^2}\right)^3 + 2T_1 + T_4}{2\pi} - i\frac{V}{b\omega}\frac{T_{12}}{\pi}(F + iG) \\ &-\left(\frac{V}{b\omega}\right)^2 \frac{T_{12}}{\pi}(F + iG) \end{aligned} , \tag{B1.7}$$

$$\begin{aligned} T_\beta = &-\frac{T_3}{\pi^2} + i\frac{V}{b\omega}\frac{T_4 T_{11}}{2\pi^2} - i\frac{V}{b\omega}\frac{T_{11} T_{12}}{2\pi^2}(F + iG) - \left(\frac{V}{b\omega}\right)^2 \frac{T_5 - T_4 T_{10}}{\pi^2} \\ &-\left(\frac{V}{b\omega}\right)^2 \frac{T_{10} T_{12}}{\pi^2}(F + iG) \end{aligned} , \tag{B1.8}$$

$$T_1 = -\frac{1}{3}\sqrt{1 - c_1^2}\left(2 + c_1^2\right) + c_1 \cos^{-1} c_1 , \tag{B1.9}$$

$$T_2 = c\left(1 - c_1^2\right) - \sqrt{1 - c_1^2}\left(1 + c_1^2\right)\cos^{-1} c + c_1\left(\cos^{-1} c_1\right)^2 , \tag{B1.10}$$

$$T_3 = -\left(\frac{1}{8} + c_1^2\right)\left(\cos^{-1} c_1\right)^2 + \frac{1}{4} c_1 \sqrt{1-c_1^2} \cos^{-1} c_1 \left(7 + 2c_1^2\right) - \frac{1}{8}\left(1 - c_1^2\right)\left(5c_1^2 + 4\right) , \tag{B1.11}$$

$$T_4 = -\cos^{-1} c_1 + c_1 \sqrt{1-c_1^2} \;, \tag{B1.12}$$

$$T_5 = -\left(1 - c_1^2\right) - \left(\cos^{-1} c_1\right)^2 + 2c_1 \sqrt{1-c_1^2} \cos^{-1} c_1 \;, \tag{B1.13}$$

$$T_6 = T_2 \;, \tag{B1.14}$$

$$T_7 = -\left(\frac{1}{8} + c_1^2\right)\cos^{-1} c_1 + \frac{1}{8} c_1 \sqrt{1-c_1^2}\left(7 + 2c_1^2\right) , \tag{B1.15}$$

$$T_8 = -\frac{1}{8}\sqrt{1-c_1^2}\left(2c_1^2 + 1\right) + c_1 \cos^{-1} c_1 \;, \tag{B1.16}$$

$$T_9 = \frac{1}{2}\left[\frac{1}{3}\left(\sqrt{1-c_1^2}\right)^3 + aT_4\right] , \tag{B1.17}$$

$$T_{10} = \sqrt{1-c_1^2} + \cos^{-1} c_1 \;, \tag{B1.18}$$

$$T_{11} = \cos^{-1} c_1 \left(1 - 2c_1\right) + \sqrt{1-c_1^2}\left(2 - c_1\right) , \tag{B1.19}$$

$$T_{12} = \sqrt{1-c_1^2}\left(2 + c_1\right) - \cos^{-1} c_1 \left(2c_1 + 1\right) , \tag{B1.20}$$

$$T_{13} = \frac{1}{2}\left[-T_7 - \left(c_1 - a\right)T_1\right] , \tag{B1.21}$$

$$T_{14} = \frac{1}{16} + \frac{1}{2} a c_1 \;. \tag{B1.22}$$

Note that,

$$V = U_\infty \;. \tag{B1.23}$$

B.2 Theodorsen's function

Consider the integral

$$\int_1^\infty e^{-i2k(\sigma-1)} \frac{\sigma}{\sqrt{(\sigma-1)\sigma}} \, d\sigma \;, \tag{B2.1}$$

By substituting $\sigma = (\zeta + 1)/2$ into this integral, one obtains

$$\int_1^\infty e^{-i2k(\sigma-1)} \frac{\sigma}{\sqrt{(\sigma-1)\sigma}} \, d\sigma = \frac{1}{2}\int_1^\infty e^{-ik(\zeta-1)} \frac{\zeta+1}{\sqrt{\zeta^2-1}} \, d\zeta \;, \tag{B2.2}$$

Note that Hankel's integrals are defined by,

$$\int_1^\infty e^{-ik\zeta}\frac{\zeta}{\sqrt{\zeta^2-1}}d\zeta=-\frac{\pi}{2}H_1^{(2)}(k)\,, \tag{B2.3}$$

$$\int_1^\infty e^{-ik\zeta}\frac{1}{\sqrt{\zeta^2-1}}d\zeta=-i\frac{\pi}{2}H_0^{(2)}(k)\,. \tag{B2.4}$$

where $H_0^{(2)}(k)$ and $H_1^{(2)}(k)$ are Hankel's functions [137, 200] of second kind of zero and first order.

The function $C(k)$ is called Theodorsen's function, the exact expression of it is given by,

$$C(k)=F+iG=\frac{H_1^{(2)}(k)}{H_1^{(2)}(k)+iH_0^{(2)}(k)}\,. \tag{B2.5}$$

The standard notations for the real and imaginary parts of $C(k)$ are *F* and *G*, which are tabulated in Table B.1.

Table B.1 Theodorsen's function $C(k)=F+iG$.

k	$1/k$	F	$-G$
∞	0.000	0.5000	0
10.00	0.100	0.5006	0.0124
6.00	0.16667	0.5017	0.0206
4.00	0.250	0.5037	0.0305
2.00	0.500	0.5129	0.0577
1.50	0.66667	0.5210	0.0736
1.00	1.000	0.5394	0.1003
0.80	1.250	0.5541	0.1165
0.66	1.51516	0.5699	0.1308
0.60	1.66667	0.5788	0.1378
0.56	1.78572	0.5857	0.1428
0.50	2.000	0.5979	0.1507
0.44	2.27273	0.6130	0.1592
0.40	2.500	0.6250	0.1650
0.34	2.94118	0.6469	0.1738
0.30	3.33333	0.6650	0.1793
0.24	4.16667	0.6989	0.1862
0.20	5.000	0.7276	0.1886
0.16	6.250	0.7628	0.1876
0.12	8.33333	0.8063	0.1801
0.10	10.000	0.8320	0.1723
0.08	12.500	0.8604	0.1604
0.06	16.66667	0.8920	0.1426
0.05	20.000	0.9090	0.1305
0.04	25.000	0.9267	0.1160
0.025	40.000	0.9545	0.0872
0.01	100.000	0.9824	0.0482
0	∞	1.000	0

Appendix C: Special Complex Functions

C.1 The complex function $\widetilde{G}(s,z)$

Consider the following complex function,

$$\widetilde{G}(s,z)=\cosh^{-1} R \ , \tag{C1.1}$$

where,

$$R=\sqrt{\frac{(1-z)s}{(s-z)}} \ . \tag{C1.2}$$

The derivative of the complex function is given by,

$$\frac{d\widetilde{G}}{dz}=\frac{1}{\sqrt{R^2-1}}\frac{dR}{dz} \ , \tag{C1.3}$$

where,

$$\frac{dR}{dz}=\frac{1-s}{2(s-z)\sqrt{(1-z)(s-z)}}\sqrt{s} \ , \tag{C1.4}$$

$$\sqrt{R^2-1}=\sqrt{\frac{(1-s)z}{(s-z)}} \ . \tag{C1.5}$$

The derivative is given by,

$$\frac{d\widetilde{G}}{dz}=\frac{\sqrt{(1-s)s}}{2(s-z)\sqrt{(1-z)z}} \ . \tag{C1.6}$$

At $z=x>s$,

$$R=jR^* \qquad \text{where, } R^*=\sqrt{\frac{(1-z)s}{(z-s)}} \ . \tag{C1.7}$$

The complex function can be expressed by,

$$\widetilde{G}=\cosh^{-1} R=\ln\left(R+\sqrt{R^2-1}\right), \tag{C1.8}$$

At $R=jR^*$,

$$\widetilde{G}=\ln\left(jR^*+\sqrt{(jR^*)^2-1}\right)=\ln j+\ln\left(R^*+\sqrt{(R^*)^2+1}\right) , \tag{C1.9}$$

$$\widetilde{G}^{*} = J\frac{\pi}{2} + \sinh^{-1} R^{*} \ . \tag{C1.10}$$

where,

$$\widetilde{G}^{*} = \sinh^{-1} R^{*} = \ln\left(R^{*} + \sqrt{\left(R^{*}\right)^{2} + 1} \right) \ . \tag{C1.11}$$

The derivative of the complex function is given by,

$$\frac{d\widetilde{G}^{*}}{dz} = \frac{1}{\sqrt{\left(R^{*}\right)^{2} + 1}} \frac{dR^{*}}{dz} \ , \tag{C1.12}$$

The derivative is given by,

$$\frac{d\widetilde{G}^{*}}{dz} = \frac{\sqrt{(1-s)s}}{2(s-z)\sqrt{(1-z)z}} \ . \tag{C1.13}$$

From the above derivations, one concludes,

$$\frac{d\widetilde{G}}{dz} = \frac{d\widetilde{G}^{*}}{dz} \ . \tag{C1.14}$$

At $z = x > 1$,

$$R = \overline{R} = \sqrt{s}\,\frac{(-j)\sqrt{z-1}}{(-j)\sqrt{z-s}} = \sqrt{\frac{s(z-1)}{(z-s)}} \ . \tag{C1.15}$$

Note that,

$$\overline{R}^{2} < 1 \ , \tag{C1.16}$$

$$\widetilde{G} = \ln\left(R + \sqrt{R^{2} - 1}\right) = \ln\left(\overline{R} + j\sqrt{1 - \overline{R}^{2}}\right) = \pm j \cos^{-1} \overline{R} = \pm j\overline{G} \ . \tag{C1.17}$$

Note that,

$$\overline{G} = \cos^{-1} \overline{R} \ , \tag{C1.18}$$

$$\frac{d\overline{G}}{dz} = \frac{-1}{\sqrt{1 - \overline{R}^{2}}} \frac{d\overline{R}}{dz} = \frac{\sqrt{(1-s)s}}{2(s-z)\sqrt{(z-1)z}} \ . \tag{C1.19}$$

By comparing the derivatives, one concludes,

$$\frac{d\widetilde{G}}{dz} = +j\frac{d\overline{G}}{dz} \ , \tag{C1.20}$$

$$\widetilde{G} = +j\overline{G} \ . \tag{C1.21}$$

For $z = x < s < 1$,

$$R = \hat{R} = \sqrt{\frac{(1-z)s}{(s-z)}}, \ \bar{R} > 1 \tag{C1.22}$$

$$\frac{d\tilde{G}}{dz} = \frac{-j\sqrt{s(1-s)}}{2(s-z)\sqrt{(1-z)(-z)}} \ . \tag{C1.23}$$

The complex function in this domain is expressed by,

$$\tilde{G} = \cosh^{-1} R = \ln\left(\hat{R} + j\sqrt{1-\hat{R}^2}\ \right) = +j\cos^{-1}\hat{R} = +j\hat{G} \ . \tag{C1.24}$$

Note that,

$$\frac{d\hat{G}}{dz} = \frac{d}{dz}\left(\cos^{-1}\hat{R}\right) = \frac{-1}{\sqrt{1-\hat{R}^2}}\frac{d\hat{R}}{dz} = \frac{-\sqrt{(1-s)s}}{2(s-z)\sqrt{(-z)(1-z)}} \ . \tag{C1.25}$$

By comparing the derivatives, one concludes,

$$\frac{d\tilde{G}}{dz} = j\frac{d\hat{G}}{dz} \ , \tag{C1.26}$$

$$\tilde{G} = j\hat{G} \ . \tag{C1.27}$$

Note that for $s < z = x < 1$,

$$\oint_{z \to s} \frac{d\tilde{G}}{dz}dz = \frac{1}{2}\oint \frac{dz}{s-z} = -\frac{1}{2}\ln(z-s)\Big|_{\theta=\pi}^{\theta=0} = j\frac{\pi}{2} \ , \tag{C1.28}$$

$$\text{IMAG}\left(\tilde{G}\right) = j\frac{\pi}{2} \ . \tag{C1.29}$$

The following are special cases of the complex function $\tilde{G}(s,z)$,

$$\tilde{G}(1,z) = 0 \ , \tag{C1.29}$$

$$\tilde{G}(0,z) = \left\{ \begin{array}{ll} j\dfrac{\pi}{2} + \lim\limits_{s \to 0}\left(\sinh^{-1}\sqrt{\dfrac{(1-z)s}{(z-s)}}\right) = j\dfrac{\pi}{2} & 0 < z < 1 \\ j\lim\limits_{s \to 0}\left(\cos^{-1}\sqrt{\dfrac{(1-z)s}{(z-s)}}\right) = j\dfrac{\pi}{2} & 1 < z < \infty \\ j\dfrac{\pi}{2} & -\infty < z < 0 \end{array} \right\} , \tag{C1.30}$$

One concludes,

$$\tilde{G}(0,z) = j\frac{\pi}{2}, \ \text{for any } z \ , \tag{C1.31}$$

$$\tilde{G}(1,\infty)=0\ , \tag{C1.32}$$

$$\tilde{G}(0,\infty)=j\frac{\pi}{2}\ . \tag{C1.33}$$

C.2 The complex function $\tilde{H}(\sigma,z)$

Consider the complex function $\tilde{H}(\sigma,z)$ given by,

$$\tilde{H}(\sigma,z)=\cos^{-1}R\ , \tag{C2.1}$$

where,

$$R=\sqrt{\frac{(1-z)\sigma}{(\sigma-z)}}\ . \tag{C2.2}$$

The derivative of the above complex function is given by,

$$\frac{d\tilde{H}}{dz}=\frac{-1}{\sqrt{1-R^2}}\frac{dR}{dz}\ , \tag{C2.3}$$

where,

$$\frac{dR}{dz}=\frac{1-\sigma}{2(\sigma-z)\sqrt{(1-z)(\sigma-z)}}\ , \tag{C2.4}$$

$$\sqrt{1-R^2}=\sqrt{\frac{(\sigma-1)z}{(\sigma-z)}}\ , \tag{C2.5}$$

The derivative is given by,

$$\frac{d\tilde{H}}{dz}=\frac{\sqrt{(\sigma-1)\sigma}}{2(\sigma-z)\sqrt{(1-z)z}}\ . \tag{C2.6}$$

For $\sigma>z=x>1$,

$$\frac{d\tilde{H}}{dz}=j\frac{\sqrt{(\sigma-1)\sigma}}{2(\sigma-z)\sqrt{(z-1)z}}=j\frac{dH^*}{dz}\ , \tag{C2.7}$$

$$R=-j\sqrt{\frac{(z-1)\sigma}{(\sigma-z)}}=-jR^*\ , \tag{C2.8}$$

The complex function in this range is expressed as,

$$\tilde{H}=\cos^{-1}R=\cos^{-1}\left(-jR^*\right)=j\ln\left(\left(-jR^*\right)+j\sqrt{1-\left(-jR^*\right)^2}\right)\ , \tag{C2.9}$$

$$\widetilde{H} = j\ln(-j)\left(R^{*} + \sqrt{1+\left(R^{*}\right)^{2}}\right) = \frac{\pi}{2} + j\sinh^{-1} R^{*} \ . \tag{C2.10}$$

Note that,

$$H^{*} = \sinh^{-1} R^{*} \ . \tag{C2.11}$$

The derivative of the above complex function is given by,

$$\frac{dH^{*}}{dz} = \frac{1}{\sqrt{1+\left(R^{*}\right)^{2}}}\frac{dR^{*}}{dz} \ , \tag{C2.12}$$

where,

$$\frac{dR^{*}}{dz} = \frac{\sigma - 1}{2(\sigma - z)\sqrt{(\sigma - z)(z-1)}}\sqrt{\sigma} \ , \tag{C2.13}$$

$$\sqrt{1+\left(R^{*}\right)^{2}} = \sqrt{\frac{(\sigma-1)z}{(\sigma - z)}} \ , \tag{C2.14}$$

The derivative is given by,

$$\frac{dH^{*}}{dz} = \frac{\sqrt{(\sigma-1)\sigma}}{2(\sigma - z)\sqrt{(z-1)z}} \ . \tag{C2.15}$$

By comparing the derivatives in this range, one concludes,

$$\frac{d\widetilde{H}}{dz} = j\frac{dH^{*}}{dz} \ . \tag{C2.16}$$

$$\oint_{|z-\sigma|<\varepsilon} \frac{d\widetilde{H}}{dz}dz = j\oint\frac{dH^{*}}{dz}dz = -j\frac{1}{2}\oint\frac{dz}{z-\sigma} \ , \tag{C2.17}$$

$$\oint\frac{d\widetilde{H}}{dz}dz = -j\frac{1}{2}\left[\ln|z-\sigma| + i\theta\right]_{\theta=0}^{\theta=\pi} = \frac{\pi}{2} \ . \tag{C2.18}$$

For $z = x > \sigma > 1$, one obtains,

$$R = \sqrt{\frac{(z-1)\sigma}{(z-\sigma)}} = \overline{R} \ , \tag{C2.19}$$

The complex function is expressed by,

$$\widetilde{H} = \cos^{-1} R = j\ln\left(\overline{R} + \sqrt{\overline{R}^{2} - 1}\right) = j\cosh^{-1}\overline{R} \ , \tag{C2.20}$$

$$\widetilde{H} = \cos^{-1} R = j\cosh^{-1}\overline{R} = j\overline{H} \ . \tag{C2.21}$$

The above conclusion is supported by comparing the derivatives,

$$\frac{d\overline{H}}{dz}=\frac{\sqrt{(\sigma-1)\sigma}}{2(\sigma-z)\sqrt{(z-1)z}} \ , \tag{C2.22}$$

For $z=x>\sigma>1$, one obtains

$$\frac{d\widetilde{H}}{dz}=\frac{\sqrt{(\sigma-1)\sigma}}{2(\sigma-z)(-j)\sqrt{(z-1)z}}=j\frac{d\overline{H}}{dz} \ . \tag{C2.23}$$

For $z=x<0<1<\sigma$, one obtains

$$\widetilde{H}=\sqrt{\frac{(1-z)\sigma}{(\sigma-z)}}=\hat{H} \ , \tag{C2.24}$$

$$\frac{d\widetilde{H}}{dz}=-j\frac{\sqrt{(\sigma-1)\sigma}}{2(\sigma-z)\sqrt{(1-z)(-z)}} \ , \tag{C2.25}$$

The complex function is expressed by,

$$\widetilde{H}=\cos^{-1}\hat{R}=\pm j\ln\left(\hat{R}+\sqrt{\hat{R}^2-1}\right)=\pm j\cosh^{-1}\hat{R}=\pm j\hat{H} \ . \tag{C2.26}$$

The derivative of the complex function in this range is given by,

$$\frac{d\hat{H}}{dz}=\frac{1}{\sqrt{\hat{R}^2-1}}\frac{d\hat{R}}{dz}=-\frac{\sqrt{(\sigma-1)\sigma}}{2(\sigma-z)\sqrt{(1-z)(-z)}} \ . \tag{C2.27}$$

By comparing the derivatives, one concludes,

$$\frac{d\widetilde{H}}{dz}=j\frac{d\hat{H}}{dz} \ , \tag{C2.28}$$

$$\widetilde{H}=j\hat{H} \ . \tag{C2.29}$$

The following are special cases of the complex function $\widetilde{H}(\sigma,z)$,

$$\widetilde{H}(\sigma,z)=\cos^{-1}\sqrt{\frac{(1-z)\sigma}{(\sigma-z)}} \ , \tag{C2.30}$$

$$\widetilde{H}(1,z)=0 \ , \tag{C2.31}$$

$$\tilde{H}(\infty,z)=\left\{\begin{array}{ll}\cos^{-1}\sqrt{1-z} & 0<z<1\\ \dfrac{\pi}{2}+j\lim\limits_{\sigma\to\infty}\left(\sinh^{-1}\sqrt{\dfrac{(z-1)\sigma}{(\sigma-z)}}\right) & 1<z<\infty\\ j\lim\limits_{s\to-\infty}\left(\cosh^{-1}\sqrt{\dfrac{(1-z)\sigma}{(\sigma-z)}}\right) & -\infty<z<0\end{array}\right\}, \qquad \text{(C2.32)}$$

The final expression of the complex function for this special case is given by,

$$\tilde{H}(\infty,z)=\left\{\begin{array}{ll}\cos^{-1}\sqrt{1-z} & 0<z<1\\ \dfrac{\pi}{2}+j\sinh^{-1}\sqrt{z-1} & 1<z<\infty\\ j\cosh^{-1}\sqrt{1-z} & -\infty<z<0\end{array}\right\}. \qquad \text{(C2.33)}$$

Appendix D: Numerical Method Validation

D.1 Method validation for flows with multiple separation regions past a downstream-facing step

Before using it for the analysis of the flows past airfoils at very low Reynolds numbers, for which there are no experimental results available, the numerical method presented in Chapter 4 has been first validated by comparison with experimental and previous numerical results [D1-D7] for the two-dimensional flows over a downstream-facing step shown in Figure D1.1. For a meaningful comparison with these previous results, computations have been performed for the value of the channel expansion ratio, $H / h = 2$ (the step height being in this case equal to the upstream channel height, $h_S = h = H / 2$), and for various Reynolds numbers, including $\mathrm{Re} = 800$ which has been most commonly used in the previous theoretical and experimental investigations. A fully-developed laminar flow defined by a parabolic velocity profile is considered at the channel inlet:

$$U(y)=24\, U_0\, y\,(0.5 - y)\,, \tag{D1.1}$$

where U_0 is the mean flow velocity and y is in this case the physical coordinate nondimensionalized with respect to H. The following two cases of the channel inlet geometry have been considered, again for meaningful comparisons:

(i) Case in which the upstream portion of the channel is missing, that is $l_0 = 0$, and the fully-developed velocity profile (D1.1) is assumed just above the downstream-facing step (at $x=0$), at the entrance of the downstream channel. This case is considered for comparison with the benchmark numerical solution given by Gartling (1990), as well as with other previous numerical solutions.

(ii) The physical case in which the fully-developed velocity profile (D1.1) is assumed at the inlet of the upstream portion of the channel having the nondimensional length $l_0=2$ with respect to the downstream channel height, H . This value resulted after a detailed study of the effect of the upstream length of the channel on the numerical solution obtained, which has shown that increasing the nondimensional length, l_0 , above 2 did not further affect the numerical solution for the range of Reynolds numbers considered.

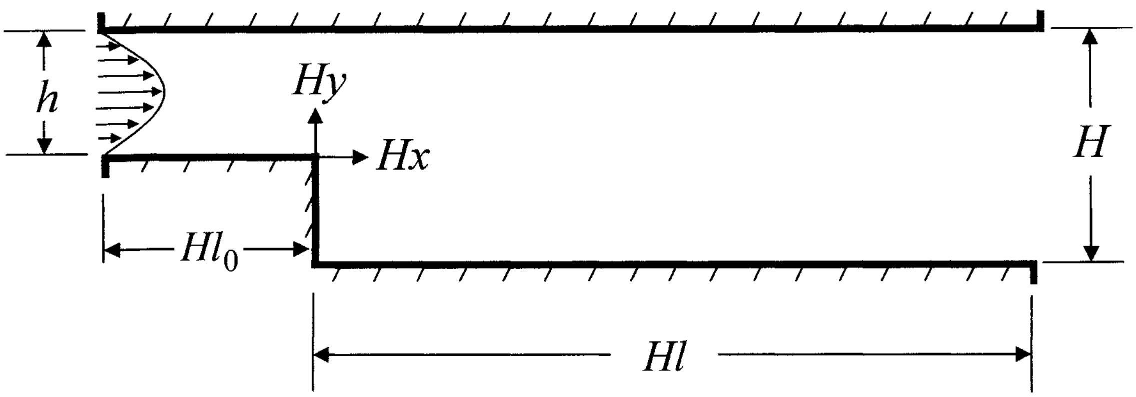

Figure D1.1 Geometry of a channel with a downstream-facing step.

The present numerical results for the flow past the backward step were obtained using a stretched staggered grid with 1001 × 201 grid points for each variable (that is 2001 × 401 grid points in total) in the case $l_0 = 0$, and 1097 × 201 grid points in the case $l_0 = 2$ (obviously in his case there was no need for the coordinate transformation mentioned in Chapter 4). The mesh spacing in the x-direction was minimum at the step, $\Delta x_{\min} = 0.0104$ (for the staggered grid), and maximum at the outlet boundary, $\Delta x_{\max} = 0.0252$, while in the y-direction the minimum mesh spacing was at the walls and the step corner, $\Delta y_{\min} =$ 0.00182. Computations were performed for a nondimensional length of the downstream channel, $l_1 = 30$, with $\delta = 0.8$ and $\Delta\tau = 0.4$, and convergence was considered reached when all of the r. m. s. residuals were less than 10^{-9}.

At low Reynolds numbers, the flow over the downstream-facing step is characterized by two separation regions, one at the lower wall just behind the step and the other at the upper wall. This is shown in Figure D1.2 which presents a graphical illustration of the computed cross-channel velocity profile at various axial locations along the computational domain ($-2 < x < 30$) for Re = 800 and an expansion ratio $H / h = 2$. The streamline contours, illustrating the recirculation regions near the upper and lower walls, are also shown in background in this figure.

The present results for the nondimensional lengths of separation on the lower and upper walls, L_l and $L_u = x_r - x_s$, and for the locations of the separation and reattachment points on the upper wall, x_s and x_r , respectively, are compared in Table D1.1 with previous numerical and experimental results. One can notice good agreement with the previous numerical solutions obtained for the case $l_0 = 0$. The agreement with the benchmark solution obtained by Gartling [D1] is excellent.

For Re = 800 the agreement with the experimental results was not as good for this Reynolds number. Thus, the experimental results obtained by Armaly *et al.* [D2] by using a laser-Doppler velocimetry technique, displayed differences of the order of 20% with respect to the theoretical results. More recently, T. Lee and D. Mateescu [D3] performed very thorough experimental investigations using a non-intrusive technique based on multi-element hot-film sensors glued on the wall surface. As shown in Table D1.1, their experimental results were much closer to the numerical predictions, although the agreement can not be considered satisfactory for this Reynolds number.

As suggested by Gartling [D1], Armaly *et al.* [D2], and Kim & Moin [D4], these discrepancies between the experimental results and the numerical predictions are due to the three-dimensional effects in the experimental channel flows (as compared to the rigorous two-dimensional computational solutions), which appear to become significant for $\mathrm{Re} > 600$. This explanation seems to be confirmed by a very good agreement between the present numerical solutions and the experimental results for lower Reynolds numbers, such as Re = 400 and Re = 600. This can be seen for the lower wall separation length in Table D1.2, as well as in Figure D1.3, which shows the variation with the Reynolds number of the separation and reattachment locations on both the upper and lower walls.

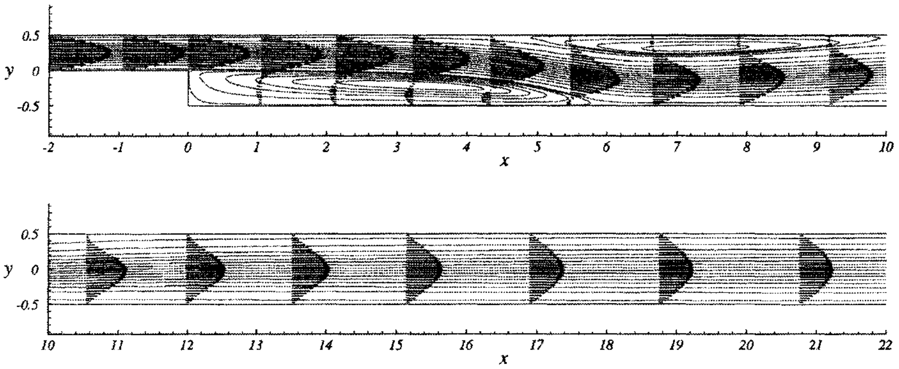

Figure D1.2 *Steady flow over a downstream-facing step* ($H / h = 2$ and $\mathrm{Re} = 800$). Typical cross-channel velocity profiles at various axial locations along the computational domain ($-2 < x < 30$), as well as the streamline contours illustrating the recirculation regions near the upper and lower walls.

Table D1.1 Computed nondimensional lengths of separation on the lower and upper walls and the upper wall separation and reattachment positions compared with previous numerical and experimental results.

	Lower wall	Upper wall		
	Length of separation L_l	Length of separation $L_u = x_r - x_s$	Separation position x_s	Reattachment position x_r
Computational solutions (for Re = 800 and $H/h = 2$)				
Present solution for $l_0 = 2$ (with upstream channel)	5.90	5.65	4.66	10.31
Present solution for $l_0 = 0$ (without upstream channel)	6.09	5.63	4.85	10.47
Gartling (1990) ***($l_0 = 0$)***	6.10	5.63	4.85	10.48
Sohn (1988) ***($l_0 = 0$)***	5.8	4.7	–	–
Kim and Moin (1985) ***($l_0 = 0$)***	6.0	5.75	–	–
Experimental results (* for Re = 805 and $H/h = 2$; ** for Re = 805 and $H/h = 1.94$)				
T. Lee and Mateescu (1998) *	6.45	5.1	5.15	10.25
Armaly* et al. *(1983) **	7.0	4.3	5.7	10.0

Table D1.2 Computed nondimensional length of separation on the lower wall, L_l ,compared with previous numerical and experimental results for various Reynolds numbers.

	Re = 400	**Re = 600**	**Re = 800**	**Re = 1000**	**Re = 1200**
Computational solutions for $H/h=2$					
Kim and Moin (1985) **($l_0 = 0$)**	4.3	5.3	6.0	–	–
Sohn (1988) **($l_0 = 0$)**	4.1	5.2	5.8	–	–
Present solution for $l_0 = 0$ (without upstream channel)	4.32	5.37	6.09	6.71	7.29
Present solution for $l_0 = 2$ (with upstream channel)	4.12	5.17	5.90	6.53	7.11
Experimental results for: * $H/h=2$; ** $H/h=1.94$					
T. Lee and Mateescu (1998) *	4.1	5.21	6.45	7.4	8.4
Armaly **et al.** ***(1983)*** **	4.3	5.8	7.1	8.1	8.9

*,**The experimental Reynolds numbers were slightly different in some cases (see also Figure D1.3).

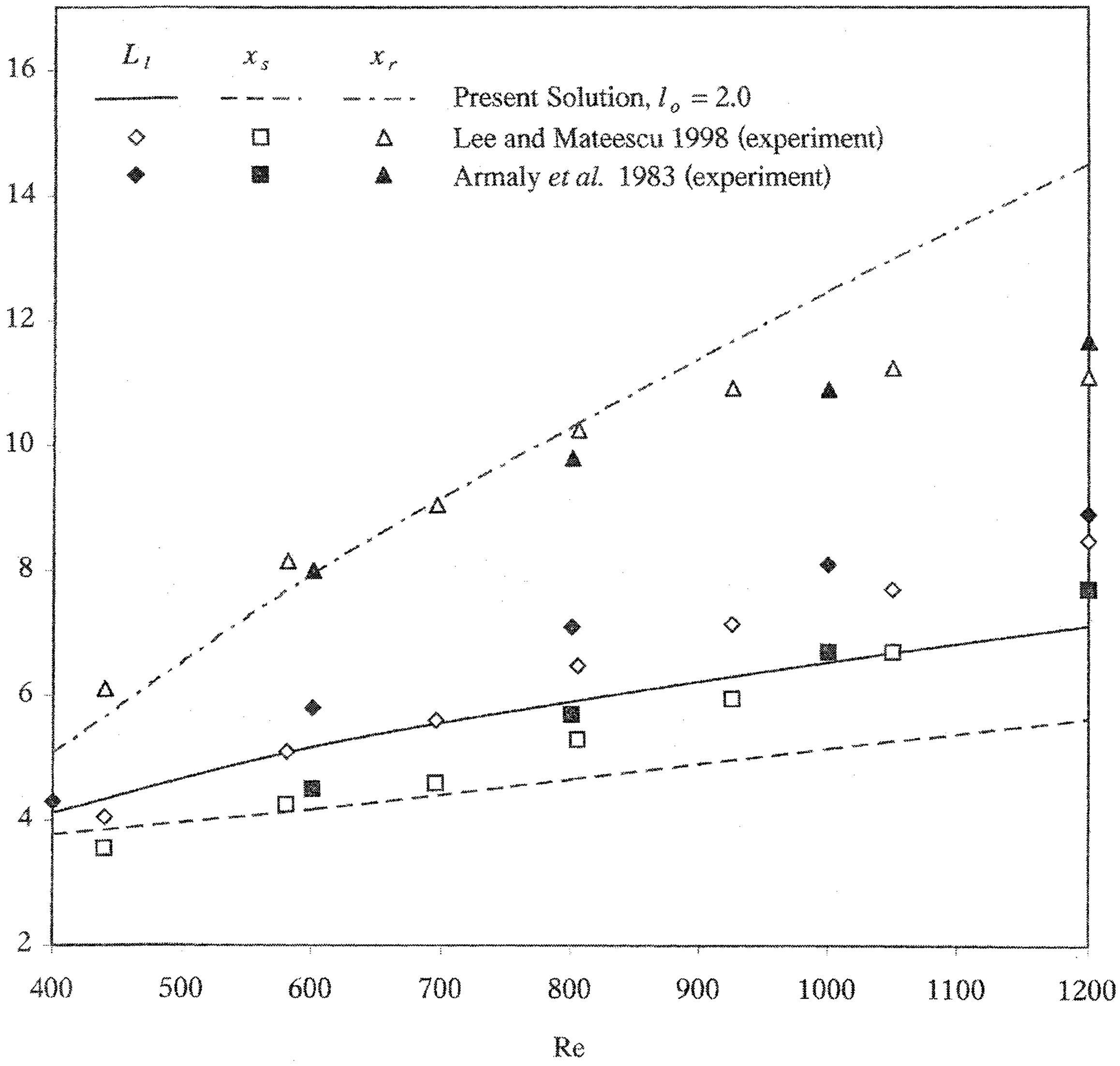

Figure D1.3 *Steady flow over a downstream-facing step* ($H / h = 2$). Variation with the Reynolds number of the location of the separation and reattachment points on the upper and lower walls. Comparison between the present theoretical solutions (——— , lower wall reattachment; – – – , upper wall separation; – · – · –, upper wall reattachment) and experimental results: ◊ , □ , Δ - Lee & Mateescu (1998); ◊ , □ , Δ - Armaly *et al.* (1983).

D.2 Additional references related to the downstream-facing step

[D1] Gartling, D. K. "A test problem for outflow boundary conditions- Flow over a backward-facing step," *International Journal for Numerical Methods in Fluids*, 11, 953-967, 1990.

[D2] Armaly, B. F., Durst, F., Pereira, J. C. F. and Schonung, B. "Experimental and theoretical investigation of backward-facing step flow," *Journal of Fluid Mechanics*, 127, 1026-1033, 1983.

[D3] Lee, T. and Mateescu, D. "Experimental and numerical investigations of 2_D backward-facing step flow," *Journal of Fluids and Structures* 12, pp. 703-716, 1998.

[D4] Kim, J. and Moin P. "Application of a fractional-step method to incompressible Navier-Stokes equations," *Journal of Computational Physics*, 59, 308-323, 1985.

[D5] Soh, W., and Goodrich, J. "Unsteady solution of incompressible Navier-Stokes equations," *Journal of Computational Physics*, 79, 113-134, 1988.

[D6] Sohn, J. L. "Evaluation of FIDAP on some classical laminar and turbulent benchmarks," *International Journal for Numerical Methods in Fluids*, 8, 1469-1490, 1988.

[D7] Mateescu, D. and Venditti, D. "Unsteady confined viscous flows with oscillating walls and multiple separation regions over a downstream-facing step," *Journal of Fluids and Structures*, 15, pp. 1187-1205, 2001.